Final Report

on

NASA Grant NAG-1-657

entitled

Reynolds Stress Closure in Jet Flows Using Wave Models

Sponsored by

NASA Langley Research Center

Technical Monitor: Dr. J. M. Seiner

Submitted by

Philip J. Morris

Department of Aerospace Engineering

The Pennsylvania State University

University Park, PA 16802

September 1990

Table of Contents

1. Introduction

This report provides a detailed final summary of research conducted under NASA Grant NAG–1–657 entitled,"Reynolds Stress Closure in Jet Flows Using Wave Models."

The goal of the research has been to develop turbulence closure schemes, free of model constants, that predict the development of jet flows. In particular, the unsteady characteristics at the large scale were to be modeled and the models were to be applicable to jets of arbitrary geometry. In addition, the modeling scheme had to be computationally inexpensive. This eliminated the possibility of Direct Numerical Simulations or Large Eddy Simulations.

The models developed under this program have achieved the goals of being free of model constants and being computationally inexpensive but the closure schemes were not applied to jet flows. Instead, the closure scheme was developed for a two–dimensional mixing layer. Extensions of the closure scheme to circular and non–circular jets flows is the subject of ongoing research activity under separate funding. However, the numerical procedures to apply the closure scheme to non–circular jets have been developed. This permits the local characteristics of the large scale structures to be calculated. In addition, the shock cell structure in non–circular jets, operating off–design, has been calculated.

The modeling procedure is described in detail in the subsequent chapters. However it may be summarized as the response to the following questions.

1) *If the time–averaged flow properties are known, can the most likely unsteady flow field be deduced?*
2) *If the time–averaged turbulent stresses associated with this unsteady flow field are calculated, are they compatible with the original time–averaged velocity and temperature fields?*

The answer to both these questions appears to be "yes" for the free shear flows examined. Such flows are dynamically unstable and are dominated by their most unstable, linear instabilities. The advantage of such an approach is that it models the unsteady flow field directly using a phenomenological model. It has no need to

resort to model constants to close the higher order equations that are encountered in traditional models. However, the models have yet to be tested in more complex configurations. It is likely that models such as the one described in this report will act as guides for the modeling procedures in conventional Reynolds–averaged models. This will enable more physically realistic models to be incorporated in these closure schemes.

The chapters of this report represent either publications or manuscripts submitted for publication by the principal investigator and the research assistants. The three research assistants who have worked on this project each earned a Ph.D. degree. Many details of the research are given in their theses. The student names and their thesis titles are:

Roy S. Baty, "Reynolds Stress Closure in Jet Flows Using Instability Wave Modeling," *Ph.D. thesis*, Department of Aerospace Engineering, The Pennsylvania State University, 1989.

Thonse R. S. Bhat, "Linear Models for the Shock Cell Structure of Supersonic Jets with Noncircular Exit Geometries," *Ph.D. thesis*, Department of Aerospace Engineering, The Pennsylvania State University, 1990.

William W.–W. Liou, "Weakly Nonlinear Models for Turbulent Free Shear Flows," *Ph.D. thesis*, Department of Aerospace Engineering, The Pennsylvania State University, 1990.

The outline of this report is as follows. Chapter 3 contains a description of the weakly nonlinear turbulence model developed by Liou. An essential part of the application of such a closure scheme to general geometry jets is the solution of the local hydrodynamic stability equation for a given jet cross–section. Chapter 4 describes the conformal mapping schemes used by Baty to map such geometries onto a simple computational domain. Chapter 5 describes Baty's solution of the stability problem for circular, elliptic and rectangular geometries. In Chapter 6 Bhat's use of linear models for the shock cell structure in non–circular jets is given. The Appendices contain reprints of papers also published during this study. Appendix I describes the instability of elliptic jets. Appendix II provides a technique for

predicting the shock cell structure in non–circular jets using a vortex sheet model. Finally, Appendix III describes the resonant interaction between twin supersonic jets.

Each of the component parts of this research program provide progress toward the prediction of the development of jets from arbitrary geometry nozzles including their unsteady turbulent structure at the large scale. It also provides the basis for the prediction of their near–field pressure fluctuations and their radiated noise.

2. Acknowledgements

The principal investigator and research assistants gratefully acknowledge the support of NASA Langley Research Center. In particular, the guidance and flexibility of the technical monitor, Dr. J. M. Seiner are appreciated. In addition, experimental data has been provided by Messrs. M. Ponton and J. Manning. The use of this data has been valuable to the project and its availability is greatly appreciated.

[illegible] INTENTIONALLY [illegible]

Chapter 3

Wave Models for Turbulent Free Shear Flows

Whai-Wai Liou and P. J. Morris

WAVE MODELS FOR TURBULENT FREE SHEAR FLOWS

W. W. Liou and P. J. Morris
The Pennsylvania State University
University Park, PA 16802

ABSTRACT

New predictive closure models for turbulent free shear flows are presented in this paper. They are based on an instability wave description of the dominant large–scale structures in these flows using a quasi–linear theory. Three models have been developed to study the structural dynamics of turbulent motions of different scales in free shear flows. The local characteristics of the large–scale motions are described using linear theory. Their amplitude is determined from an energy integral analysis. The models have been applied to the study of an incompressible free mixing layer. In all cases, predictions are made for the development of the mean flow field. In the last model , predictions of the time–dependent motion of the large–scale structure of the mixing region are made. The predictions show good agreement with experimental observations.

I.INTRODUCTION

Though the presence and importance of large–scale coherent structures to the mixing process in free shear flows has been recognized for many years, turbulence models that incorporate these observations have been very limited. The use of direct numerical or large eddy simulations provide a detailed prediction of the large–scale motions in low and high Reynolds number turbulent flows respectively. But these predictions are computationally expensive and are still limited in general to simple boundary conditions. The present model makes use of experimental observations in excited turbulent flows or conditional sampling measurements to provide a simple model of the large scale motions which is computationally inexpensive.

Most current turbulent flow calculations for practical applications use the long time-averaged Navier–Stokes equations. Turbulence models are needed to evaluate the unknown correlation terms, the Reynolds stresses, that appear when the statistical averaging process is applied to the nonlinear convective terms in the equations. This is the closure problem. There are closure models of various orders that have been proposed. These models are usually based on the notion that the high–order moments of fluctuations can be represented reasonably well as functionals of moments of lower order. Work in this regard is voluminous and will not be elaborated on here. Some models are quite successful and have become very popular in engineering flow calculations. However, they usually involve a large number of model constants determined by comparison with experimental data.

Thus, these models are not entirely predictive but, in some ways, represent a sophisticated correlation of experimental data.

The present models are based on observations of large–scale coherent structures in free mixing layers. Brown and Roshko (1974), among others, observed that these orderly motions dominate the dynamics and the structure of free shear flows like wakes, jets and mixing layers. The structures appear in both low– and high–speed flows. They have also been observed in many flow geometries.

This paper is concerned with new, predictive turbulence models for free shear flows. The models simulate the propagating large–scale structures as spatially travelling instability waves. In this paper, we focus on the validation of the wave models as well as a determination of their limitations. Predictions are made for a two–dimensional incompressible free mixing layer. This will provide guidelines for applications of the models to more complex configurations.

II.THE WAVE MODELS

The wave models presented here are used to make a direct calculation of the large–scale, characteristic structures. The fundamental idea is that the large–scale structures may be modeled using a quasi–linear theory. The local characteristics of these structures may be described by linear instability theory. This has been demonstrated by the experiments of Gaster, Kit and Wygnanski (1985) and Petersen and Samet (1988), among others. In their experiments they compared predictions of the amplitude and phase of the axial velocity fluctuations, based on linear stability theory, with phase–averaged measurements in an excited shear layer and a jet. The agreement between predictions and experiment was very good though only normalized distributions of amplitude and phase, not the absolute amplitude, were predicted. This close agreement between the predictions of linear stability theory and the properties of the large–scale coherent sturctures has formed the basis for theories of turbulent mixing and supersonic jet noise generation and radiation. For example, Tam and Morris (1980) and Tam and Burton (1984) predicted the noise radiation from instability waves in supersonic shear layers and jets and obtained very good agreement with experiment. Their analyses showed that the behavior of the large–scale disturbances could be modeled satisfactorily using a quasi–linear theory, even though the waves were not infinitesimal in magnitude. However, an important element of these calculations, the velocity profiles of the mean flow, that are needed for the linear stability calculations, are obtained from experiments. Their approaches provide a closure, but are not predictive. The models proposed here establish a complete closure model using a simple quasi–linear theory for the large–scale motion. In the present model both the mean flow and the time–dependent turbulent motions at the large–scale are obtained simultaneously as a solution.

II.a Analysis

Turbulent flows generally contain broadband fluctuations and are traditionally treated as random processes. These processes are then described by statistical averages. The observation and justification of the occurrence of orderly and coherent large-scale turbulent fluctuations in turbulent free flows encourage an interpretation of these turbulent flows using a quasi-deterministic description.

In light of the existence of coherent structures, it is appropriate to decompose an instantaneous flow property into three parts. That is,

$$\tilde{f}_i = F_i + f_i + f_i' \tag{1}$$

The fluctuation with respect to the mean quantity, F_i, is separated into two components: one representing the dominant large-scale motion, f_i, and the other representing the small-scale fluctuation, f_i'. The mean flow component is obtained from a long time-average of its instantaneous value and is given by

$$\bar{\tilde{f}}_i = F_i = \frac{1}{T_1}\int_0^{T_1} \tilde{f}_i dt \tag{2}$$

A short time-average may be defined by

$$< \tilde{f}_i > = F_i + f_i = \frac{1}{T_2}\int_0^{T_2} \tilde{f}_i dt \tag{3}$$

where T_2 is much smaller than T_1, but much larger than the characteristic time scale of the background small-scale fluctuation. The mean flow represents an average over many realizations for a long period of time and thus is the profile that is most probably seen by the large-scale structures which occur randomly in space and time. In this approach, mean flow properties and large-scale fluctuations can be obtained explicitly. The small-scale turbulence which provides additional mixing at smaller scales compared to the mean and the large-scale motions is treated separately. The governing equations for the mean flow can be derived by long time-averaging the Navier-Stokes equations. Equations governing the large-scale fluctuations can then be obtained by subtracting the resulting mean equations from the short time-averaged Navier-Stokes equations. The governing equations for the mean flow are

$$\frac{\partial U_i}{\partial x_i} = 0 \tag{4.b}$$

$$U_j\frac{\partial U_i}{\partial x_j} + \frac{\partial}{\partial x_j}(\overline{u_i u_j} + \overline{u_i' u_j'}) = -\frac{\partial P}{\partial x_i} + \frac{1}{Re}\frac{\partial^2 U_i}{\partial x_j \partial x_j} \tag{4.a}$$

where the interactions between motions of disparate scales are assumed to be negligible. The equations can be simplified further by applying the boundary-layer approximation. For two-dimensional flows, the resulting equations are

$$\frac{\partial U}{\partial x} + \frac{\partial V}{\partial y} = 0. \tag{5.a}$$

$$U\frac{\partial U}{\partial x} + V\frac{\partial U}{\partial y} + \frac{\partial}{\partial x}(\overline{u^2} - \overline{v^2}) + \frac{\partial}{\partial y}(\overline{uv}) + \frac{\partial}{\partial y}(\overline{u'v'}) = \frac{1}{Re}\frac{\partial^2 U}{\partial y^2} \qquad (5.b)$$

In order to close the governing equations, the long time-averaged one-point correlations of the large- and small-scale motions in the mean equation have to be provided. Here, the large-scale motions are calculated by solving their governing equations. These equations can be obtained by subtracting the mean equations from the short time-averaged Navier-Stokes equations:

$$\frac{\partial u_i}{\partial x_i} = 0 \qquad (6.a)$$

$$\frac{\partial u_i}{\partial t} + U_j\frac{\partial u_i}{\partial x_j} + u_j\frac{\partial U_i}{\partial x_j} + \frac{\partial}{\partial x_j}(\overline{u_i u_j} - u_i u_j) = -\frac{\partial p}{\partial x_i}$$

$$+ \frac{1}{Re}\frac{\partial^2 u_i}{\partial x_j \partial x_j} - \frac{\partial}{\partial x_j}(< u_i' u_j' > - \overline{u_i' u_j'}) \qquad (6.b)$$

Gaster et al. (1985) argued that the nonlinear terms can be neglected and showed that the local characteristics of the large-scale fluctuations in mixing layers can be described surprisingly well by linear theory. In fact, some weakly nonlinear solutions in hydrodynamic stability, for example, Stuart (1958), assume that the local shapes of the finite amplitude disturbances are those obtained by linear theory. Therefore, it is assumed here that locally the large-scale turbulent structures may be described by linear analysis and that their behavior is only weakly nonlinear. Hence, all the nonlinear interaction terms are neglected in the present formulation.

The next assumption is that molecular viscous effects are unimportant. Davis and Moore (1985), in a numerical study of plane and axisymmetric mixing layers, found that the effect of decreasing the Reynolds number is to smear the vorticities without altering the dynamics of the large-scale structures. This phenomenon can also be observed in the experimental results of Brown and Roshko (1974) and Konrad (1976). In a mixing layer calculation, Tam and Chen (1979) showed that for a Reynolds number over 300, based on the local width, the unstable waves are not affected by the Reynolds number. In fact, increasing the Reynolds number produces more small-scale structures without significantly altering the dynamics of the structure of large scales. Viscous effects are thus of minor importance in the development of the large-scale structure and are, therefore, neglected in the present approach. Computationally, this approximation also means a huge saving in computer time.

The equations for the large-scale fluctuations can be simplified further by assuming that the mean flow is locally parallel. For free shear flows like mixing layers, wakes and jets, mean flows diverge slowly and this renders the locally parallel flow assumption applicable. For two-dimensional problems, the equations governing the large-scale unsteady turbulent motions, after introducing the above three physical assumptions, become

$$\frac{\partial u}{\partial x} + \frac{\partial v}{\partial y} = 0 \qquad (7.a)$$

$$\frac{\partial u}{\partial t} + v\frac{\partial U}{\partial y} + U\frac{\partial u}{\partial x} = -\frac{\partial p}{\partial x} \qquad (7.b)$$

$$\frac{\partial v}{\partial t} + U\frac{\partial v}{\partial x} = -\frac{\partial p}{\partial y} \qquad (7.c)$$

These equations, when solved, provide not only the information that is necessary to close the system of equations for the mean flow, but also the behavior of the large-scale turbulent motion.

Since the coefficients in equation (7) are functions of y only, a simple separable form of solutions may be assumed,

$$\{\mathrm{u},\ \mathrm{v},\ \mathrm{p}\} = A(x)\ \Re\{[\hat{u}(y), \hat{v}(y), \hat{p}(y)]\ exp\ [i(\alpha x - \omega t)]\} \qquad (8)$$

where bold face quantities indicate a complex solution whose real parts lead to real quantities and $\Re$ denotes the real part of a complex number. α is a complex wavenumber and ω represents the frequency. These are the normal mode representations generally used in hydrodynamic stability. The amplitude function $A(x)$ appears as a parameter for local calculations and is determined by the large-scale kinetic energy equation. This weakly nonlinear approach is usually referred to as a "wave envelop" method. In free shear flows, large-scale structures occur randomly in space and time and propagate downstream in the form of quasi-periodic travelling waves. The wave-like solutions, equation (8), thus represent physical phenomena as well. The resulting equations obtained by substituting these expressions into the linearized inviscid equations for the large-scale disturbances can be reduced further to a second order ordinary differential equation in terms of $\hat{v}$:

$$\left\{ (\alpha U - \omega)\left(\frac{\mathrm{d}}{\mathrm{d}y^2} - \alpha^2\right) - \alpha\frac{\mathrm{d}^2 U}{\mathrm{d}y^2} \right\} \hat{v} = 0 \qquad (9)$$

Equation (9) is the incompressible Rayleigh equation, Rayleigh (1880).

For a given mean velocity profile and appropriate homogeneous boundary conditions, equation (9) forms an eigenvalue problem. In the present analysis, the complex wavenumber, α, of the disturbance is the eigenvalue. Note that the wavenumber appears nonlinearly in the problem. In addition to a traditional shooting procedure, three global approximation methods are applied in the solution of equation. These include the Chebyshev spectral approximation, a psuedospectral Chebyshev collocation method and a finite difference method.

The amplitude function $A(x)$ introduced in equation (8) along with the conventional normal mode representation determines the amplitudes of the coherent fluctuations. In the present analysis, the amplitude is determined by the kinetic energy equations for the large-scale fluctuations. Therefore, instead of growing exponentially, $\exp(-2\alpha_i)$, as would be predicted by linear theory, the development of the amplitude function is determined by the conservation of the kinetic energy of the large structures. Equations for the kinetic energy of the large-scale fluctuations can be obtained by multiplying the momentum equations

for u_i, equation (6.b), by u_i and long time-averaging the resulting equation. The energy equation for the large-scale fluctuations can be written as:

$$U_j \frac{\partial k}{\partial x_j} = -\overline{u_i u_j} \frac{\partial U_i}{\partial x_j} - \frac{\partial}{\partial x_j}\left(\overline{u_j k} + \frac{\overline{p u_j}}{\varrho}\right) - \overline{(- < u_i' u_j' >) \frac{\partial u_i}{\partial x_j}}$$

$$- \frac{\partial}{\partial x_j} \overline{(u_i < u_i' u_j' >)} + \text{viscous terms} \qquad (10)$$

where $k = \frac{1}{2}\overline{u_i u_j}$. Since the large-scale structures are inviscid in nature, the terms involving viscosity are negligible. Production of the large structure kinetic energy is positive if $-\overline{u_i u_j}$ and $\partial U_i / \partial x_j$ are of the same sign, negative otherwise. Regions of "negative production" associated with the large-scale coherent structures have been observed, Komori and Udea (1985) and Hussain and Zaman (1985). Conventional eddy viscosity models fail to predict this phenomenon. Since the basic assumption of these models is that momentum exchanges are proportional to local mean flow gradients. That is, eddy viscosity models predict co-gradient momentum transport, or positive production of turbulent kinetic energy by their nature. In fact, the dominant structures in free shear flows are of large scale. The large-scale structures transport fluid elements across the flow unmixed and this is not directly related to local mean flow gradients. Energy is subsequently extracted from the large-scale motion and dissipated at the high frequency end of the wave number spectrum. The terms containing the residual stress tensor, $- < u_i' u_j' >$, describe the draining of energy from the waves. Very little information, experimentally or numerically, is currently available regarding these stresses.

In the following section, three models are derived from the weakly nonlinear theory described above. The weakly nonlinear theory is formulated for turbulent free shear flows in general. As a test of the theory, these three models are derived for turbulent free mixing layers. The large-scale structures observed in mixing layers present most of the features of organized structures observed in turbulent free shear flows. A sketch of a turbulent mixing layer is shown in Figure 1.

II.b Model I

Free shear layers that possess inflectional-point instability, are inherently unstable. As the flow develops, turbulence and/or background random noise provide perturbations necessary to excite these unstable waves and promote initial vortex formation. Therefore, the large-scale structures are made up of all modes residing in the flow. A complete simulation of the large-scale turbulence spectrum would require the inclusion of a broad range of frequency and spanwise wavenumber components. This was accomplished in the local solution of Tam and Chen (1979) and the integral model of Morris and Giridharan (1990). Figure 2 shows the unnormalized Reynolds shear stress distributions from Liou (1986) for waves of various frequencies. The velocity profile of the basic flow is a hyperbolic tangent function and the most unstable frequency for this flow is 0.2. The stress distributions are normalized by their peak amplitudes. It can be seen that for a wide range of frequencies

around the least stable mode, the distributions of flow quantities due to the large-scale fluctuation are similar. However, the mode that interacts most strongly with the mean flow is the one that has the largest spatial growth rate: the most unstable wave. Thus, for efficiency, instead of including all the unstable waves, it is assumed here that the locally least stable modes are most effective in extracting energy from the mean flow. The most unstable waves are then used to describe the overall behavior of the coherent, large-scale motions. In other words, the large-scale motions are described by the locally most amplifying disturbances in the flow. The method used here to locate the most unstable modes can be found in Liou (1986).

The Rayleigh equation, equation (9), governs the local distribution of the large-scale velocity fluctuation in the y direction. The equation is solved locally at each streamwise location. The amplitude function $A(x)$ is determined from the energy equation for the large-scale structures, equation (10).

The equation for the amplitude function is obtained by substituting the wave form expressions, equation (8), for the fluctuation components into the wave kinetic energy equation and integrating across the flow. The resulting equation is

$$\frac{\mathrm{d}G_1 A^2}{\mathrm{dx}} = G_2\, A^2 + G_3\, A^3 \tag{11}$$

where

$$G_1 = \frac{1}{4}\int_{-\infty}^{+\infty} \left[U(\hat{u}\hat{u}^* + \hat{v}\hat{v}^*) + 2.0\, \Re(\hat{u}\hat{p}^*)\right] \mathrm{d}y$$

$$G_2 = -\frac{1}{2}\int_{-\infty}^{+\infty} \left[\frac{\partial U}{\partial y}\Re(\hat{u}\hat{v}^*)\right] \mathrm{d}y$$

where an asterisk denotes the complex conjugate. The terms containing the residual stresses in G_3 are responsible for draining energy from the waves. G_3 is of crucial importance in determining the wave amplitude and has to be considered carefully. However, very little experimental or theoretical results are available regarding these stresses. In the following analysis, we assume that the energy transferred out of the large-scale fluctuations is proportional to

$$\frac{u^3}{l} \tag{12}$$

where u and l are the characteristic velocity and length scales of the large-scale motions. This model assumes that the turbulence is in an equilibrium state for the small-scale fluctuations. That is, the rate at which energy is transferred from the large scales is equal to the rate at which the energy is dissipated by viscosity at the small scales. The net effect of these terms may thus be modeled by

$$C_1\, \frac{k^{3/2}}{l} \tag{13}$$

where C_1 is a model constant. The energy drain integral, G_3, becomes:

$$G_3 = -\frac{C_1}{8\, l}\int_{-\infty}^{+\infty} \left[(\hat{u}\hat{u}^* + \hat{v}\hat{v}^*)^{3/2}\right] \mathrm{d}y \tag{14}$$

The amplitude of the wave structures can be calculated using an explicit fourth order Runge-Kutta method or the implicit Euler method.

To solve the mean flow equations, the small-scale Reynolds shear stress $-\overline{u'v'}$ has to be modeled. Since it is mainly the motion at the large scale that is considered here, a simple zero-equation model is employed. That is,

$$-\overline{u'v'} = C_2 \, l^2 \, |\frac{\partial U}{\partial y}|(\frac{\partial U}{\partial y} \tag{15}$$

The model introduces an additional parameter, C_2.

Thus, Model I contains two model constants: C_1 used in the modeling of the energy transfer term in the amplitude equation for the wave structures and C_2 used in the simple eddy viscosity model for the small-scale Reynolds stress, $-\overline{u'v'}$.

II.c Model II

The large-scale structures in turbulent mixing layers are dynamically active and dominant. Thus the development of the flow is mostly affected by turbulent motions of large scale. Consequently, in this approach, only fluctuations at the large scale are included. Thus, there is no direct interaction between the small-scale structures and the development of the mean flow. This is also suggested by the analyses of Tam and Chen (1979) and Morris and Giridharan (1989). The characteristics of the locally most unstable mode is still considered to be representative of that of the large-scale structures. The energy gained by the large-scale structures from the mean flow is prevented from becoming unbounded through the energy transfer terms in their energy equation. Thus, the influence of the small-scale turbulence on the mean flow is indirectly through the energy balance of the large-scale motion. In this model, the equations for the mean flow and the large-scale structures are the same as those in Model I. The model contains only one model constant , C_1, that describes the transfer of energy from the large to the small scales. Nevertheless, both Model I and II predict the average behavior of the shear layers.

II.d Model III

Model III simulates the time-dependent motion, at the large scale, associated with the passage of a train of large-scale structures. Experimental observations suggest that, even if initially there exists a continuous spectrum of infinitesimal disturbances upstream of the splitter plate, a disturbance emerges dominating over other neighboring perturbations in the early stages of the flow development. As the flow evolves; however, there is a continuous shift of the dominant component toward lower and lower frequencies. In fact, the growth of an initially small periodic disturbance is often followed by the development of subharmonics. In numerical simulations, however, the initial conditions can be conceived in a much simplier way. Instead of monitoring the disturbances in the initial continuous spectrum, a hierarchy of disturbances made up of the initially most unstable mode, according to linear theory, and its subharmonics may be chosen. This reflects the "subharmonic evolution model" proposed by Ho and Huang (1981). Thus, the unsteady turbulent

large-scale fluctuations are described by the superposition of the instability waves in this hierarchy. This enables the time-dependent flow field at the large scale to be simulated. The solution methods for these equations are the same as in Model I and II. The equation for the amplitude function, however, has to be modified. Firstly, it is assumed that interactions between harmonics are negligible as there should be sufficient phase jitter in the unexcited shear layer. In addition, the details of the process of energy transfer from the large to the small scales is not modeled explicitly. At each axial location where a given instability wave saturates, or begins to decay, the energy is immediately removed from the system. Consequently, there is no need to specify either a constant associated with the energy transfer process or the effects of the interaction between the small-scale motion and the mean flow. It should be noted that the energy equation is only solved for each instability wave during its period of growth. For amplifying waves the comparison between linear theory and experiments by Gaster et al. (1985) showed that an inviscid analysis is adequate. Thus, the interaction between the large and small scales will be neglected during the growing or unstable region for each instability wave.

The solution for the turbulent fluctuations is then fed back into the iteration process to get the corrected mean flow solutions. A visualization of the unsteady flow field predicted by Model III is made by means of streaklines. The streaklines are produced by injecting passive marker particles at the initial location, $x = x_0$ at various points across the shear layer. The positions of these particles at subsequent times can be calculated using the equations:

$$\frac{\mathrm{d}}{\mathrm{d}t}x(t) \;=\; U \,[\, x(t)\,,\; y(t)\,] \;+\; u \,[\, x(t)\,,\; y(t)\,,\; t\,] \tag{16}$$

and

$$\frac{\mathrm{d}}{\mathrm{d}t}y(t) \;=\; V \,[\, x(t)\,,\; y(t)\,)\,] + \; v \,[\, x(t)\,,\; y(t)\,,\; t\,], \tag{17}$$

with

$$x(0) = x_0,\; y_k(0) = y_0\;,\quad k = 1, \ldots . m$$

Particles thus move at each time step according to the local instantaneous velocity field.

This concludes the description of the wave models. The dominant large-scale coherent turbulent structures in turbulent free shear flows are modeled in a weakly nonlinear manner. Three models are derived to simulate the development of turbulent free mixing layers. These models connect the development of the mean flow field with the dynamics of the large-scale turbulent fluctuations. The equations governing the mean flow field and the unsteady large-scale turbulent motions form a closed system of equations.

III. Numerical Procedure

The boundary–layer approximation renders the system of equations governing the mean flow parabolic. A fourth order Keller–Box scheme is applied to solve the resulting equations. The equation for the instability wave, which is the Rayleigh equation in the present formulation, has been solved using various methods, including a traditional shooting, two spectral and a finite difference methods. For spatial instability, the system of equations

generated by the global approximations of the Rayleigh equation forms an eigenvalue problem which is nonlinear in its parameter, the wave number. It may be solved using the Linear Companion Matrix method or a method based on matrix factorization, Bridges and Morris (1984). Details of the various solution schemes can be found in Liou (1986,1990) The Rayleigh equation and the equations for the mean flow are solved iteratively at each streamwise location. The convergence criterion for the iterations is

$$\frac{1}{M}\sum_{j}\left|U_{i,j}^{(k+1)} - U_{i,j}^{(k)}\right| \leq \epsilon_1, \tag{18}$$

where ϵ_1 is a small number and M is the total number of grid points at each streamwise location. The amplitudes of the waves are calculated explicitly using a fourth order Runge–Kutta method applied to the wave energy equation (11)

IV. RESULTS AND DISCUSSIONS

The models have been tested in an incompressible free mixing layer. A hyperbolic tangent distribution is taken as the shape of the initial streamwise mean velocity, $U(x_0, y)$, i.e.,

$$U\ (\ x_0\ ,\ y\ )\ =\ \frac{1}{2}\ (\ 1\ +\ \tanh\ (\ 30\ y\ ))\ . \tag{19}$$

The initial cross–stream mean velocity, $V(x_0, y)$, can be set to a small number or zero. The boundary conditions for the mean flow are

$$U\ (\ x\ ,\ y_u(x)\ )\ =\ 1.0,\quad U\ (\ x\ ,\ y_l(x)\ )\ =\ 0.0,\ \ V\ (\ x\ ,\ y_u(x)\ )\ =\ 0.0. \tag{20}$$

where $y_u(x)$ and $y_l(x)$ are the upper and the lower boundaries of the physical domain shown in Figure 3. As a test of the ability of the instability wave model to describe large–scale structures and the associated Reynolds stresses, the model was first applied in the self–similar region of the flow with a mean velocity profile from Patel (1973). Figure 4 shows the calculated and experimental Reynolds shear stress distributions. Calculated results using a traditional shooting method compare favorably with that using global approximations of various order. Note that all the calculated results have been normalized by the peak experimental value. The discrepancy at the low–speed side of the layer suggested that the momentum exchanges due to the small–scale turbulent motions might not be negligible in this region. It should be noted that this negative value of Reynolds shear stress disappears for small values of velocity in the lower stream. The structures obviously contribute negative shear stress at the low–speed edge of the flow. This counter–gradient transport of momentum gives negative energy production in this region. A similar phenomenon was observed experimentally by Komori and Ueda (1985) in the self–similar region of a jet. In fact, regions of negative shear stress can be easily observed if the large–scale structures are excited artificially, for example, see Wygnanski, Oster and Fiedler (1979) This counter–gradient momentum transfer decelerates and subsequently reverses the flow on the low–speed side of the mixing layer as the shear layer develops.

IV.a Model I

As noted above, Model I proposes that a contribution from the small–scale Reynolds stresses is required to describe the total turbulent forces that determine the development of the mean flow. The model introduces a new parameter, C_2. Latigo (1979) argued that the turbulent shear stress contributed by the small–scale, incoherent motions is about a half of the total shear stress. An estimate of C_2 based on the value that is used in the classical eddy–viscosity models is then obtained. In addition, the force terms associated with the large–scale normal stresses in the mean momentum equations are also retained, since they are found to be of the same order as the other Reynolds stress gradient terms on the low–speed edge of the shear layer. The normal stresses associated with the large–scale structures can be calculated directly by the wave models and involve no further empiricism.

In the numerical calculations, the local solution of the Rayleigh equation is found to be time–consuming. To accelerate the axial marching an adaptive grid has been devised. The grid size in the cross–stream direction in the transformed domain are fixed. The axial step sizes are chosen such that the convergence indices of the first iteration at a downstream station are greater than a fixed number ϵ_2.

$$\frac{1}{M}\sum_j \left| U^1_{i+1,j} - U_{i,j} \right| \geq \epsilon_2, \tag{21}$$

The grids are found to cluster in a region where there are large changes of flow properties, for example, when the flow is developing initially.

The initial wave amplitude represents the initial strength of the instability waves or large–scale motions for which there are no quantitative experimental measurements. An estimate of the initial wave amplitude can be made based on the initial energy flux of the turbulence. From a sequence of numerical experiments, however, it is found that flows with relatively strong initial amplitude saturate early. Subsequently the flow develops in a similar manner; only the virtual origin of mixing is changed. The initial amplitudes for the cases presented in this paper are fixed at 5×10^{-3}. The corresponding initial turbulence intensity is about 1%. The model constant C_1 of the energy transfer term in the wave kinetic energy equation is taken from a conventional Prandtl energy model, Launder, et. al. (1979). It is found that its value has no significant influence on the results of the mixing layer calculations.The values of C_1 and C_2 used here are

$$C_1 = 2.8 \quad , \quad C_2 = 0.08 \tag{22}$$

Again, in Model I, turbulent forces associated with the wave shear and normal stresses as well as the small-scale motions are considered. Figure 5 shows the axial forces acting on fluid elements across the layer at various axial stations. Negative or retarding forces associated with the wave Reynolds shear stress appear near the zero speed side early in the developing stages of the layer and never change sign as the flow develops. Nevertheless,

the other two mechanisms, which are the gradients of the normal stresses of the turbulent large-scale structures and of the shear stress of the small-scale turbulent fluctuations, contribute positive driving forces. The net effect is the co-gradient momentum transport near the zero velocity side of the layer. It can also be seen that the $-(\overline{u^2} - \overline{v^2})_x$ terms plays a significant role in the dynamics of the mixing layer development, especially near the zero velocity side of the layer.

The growth of the layer measured by δ is shown in Figure 6 δ is the distance between the points where the local mean velocity is 0.9 and 0.1 of the main stream mean velocity, $\overline{U}$. The calculated rate of growth, $\mathrm{d}\delta/\mathrm{d}x$, agrees reasonably well with the value that is an average taken over various experiments in the self-similar region of the flow.

Figure 7 shows the predicted axial mean velocities at a sequence of downstream stations as functions of the self-similar coordinate, η. The agreement between the predictions and experimental data is good except near the low speed side of the shear layer. The layer has not reached self-similar state at $x = 0.72$ and local velocity profile differs from Patel's self-similar velocity profile. Note that for a free mixing layer, the accuracy of the measured mean flow data in the low speed region is poor due to the rapid variations in the instantaneous flow direction. Any agreement between results on the zero speed edge is likely to be fortuitous.

As can be seen from Figure 8, which shows the shear stress distributions across the mixing layer at various stations, the sum of the shear stresses from the large-scale and the small-scale motions agrees well with experimental data. The experimental measurements are the long time-averaged correlations of the turbulent fluctuations. Model I thus not only predicts the mean velocity profiles but also appears to model correctly the turbulent momentum transport in the layer. The latter is usually achieved only by using higher order moment closure models, which includes a large number of model constants.

The amplitude of the large-scale fluctuations is plotted in Figure 9. The large-scale structures extract energy from the mean flow and grow as the flow develops. However, energy is also being transferred to the smaller scales and subsequently dissipated by viscosity. The final equilibrium of the large-scale motions amplitude is reached when the energy gained from the mean flow balances the energy lost to the small scales.

IV.b Model II

Model I assumes that the large-scale and the small-scale turbulent fluctuations play a direct role in the momentum transport process in the mixing region. Therefore, in Model II only the fluctuations at the large scale are included. This eliminates the need to specify a model, equation (15), to describe the momentum exchanges due to the small-scale fluctuations. Model II thus involves only one model constant for the energy dissipation model in the kinetic energy equation for the large-scale turbulent fluctuations. It can be seen from Figure 10 that the forces associated with the large-scale normal stresses are apparently able to counter-balance the decelerating effects of the wave shear stress gradients. Thus, a prediction of the development of the layer is possible considering only the dynamics associated with the large-scale turbulent fluctuations in the layer.

The predicted mean velocity profiles are presented in Figure 11. It shows that the mean flow can be satisfactorily predicted by modeling only the dominant large-scale structures. Figure 12 compares the calculated axial mean velocity profiles using Models I and II. Note that the predicted development of the mixing layer has reached equilibrium state at both $x = 6.19$ using Model I and $x = 7.26$ using Model II. Thus, Figure 12 is comparing the mean velocity profiles at the equilibrium state of a mixing layer using two different turbulence closure schemes. The agreement between these predictions is more than satisfactory. Both of the predicted mean velocity profiles deviate from Patel's data near the low speed side of the layer. However, as noted previously, the accuracy of the measured data may be suspected in that region due to the rapid variations in the instantaneous flow direction. This phenomenon, in fact, is predicted in the application of Model III to the turbulent mixing layer.

As is shown in Figure 13, the predicted shear stress distributions do not match the total shear stress distributions measured by Patel (1973). However, as noted above, this difference does not necessarily mean that the small-scale stresses should be included. It must be remembered that the present model simulates the entire large-scale spectrum with a single frequency wave that is locally most unstable. Tam and Chen (1979), in their local model, included a broad range of instability waves and found good agreement with experiments without the inclusion of contributions from the small scales. In fact, it is shown here that the time average characteristics of a turbulent mixing layer can be predicted satisfactorily using only the most unstable waves, provided that all the momentum transport mechanisms associated with the wave are included.

The evolution of the large-scale amplitude using Model II follows a similar behavior to that using Model I and is shown in Figure 14. Once again an equilibrium condition is reached where the rate of energy transfer from the mean flow to the large-scale structures balances the rate at which energy is lost by the structures to small scales for eventual dissipation. The little kink near $x = 6.0$ is due to the fact that at this region there are relatively large changes of marching step sizes required by the adaptive grid generation scheme. Since the marching step sizes are selected based on the global variation of the mean flow, this kink has little effect on the predictions of the flow development.

Figure 15 gives the growth of the mixing layer in terms of momentum thickness, θ, predicted by Model II. In the present analysis, the momentum thickness is defined as

$$\theta = \int_{2y_l}^{2y_u} g(1-g)\mathrm{d}y \tag{23}$$

θ_0 is the initial momentum thickness and the straight line represents the rate of growth of the layer, which is an average over experimental data at the equilibrium state of mixing layers. In the early stages of the development of the mixing layer, the large-scale structures in the flow are relatively weak and momentum exchanges are mainly due to the effect of molecular viscosity. The strengthening of the large-scale structures increases drastically the mass and momentum exchanges across the layer and, consequently, the width of the mixing region. This reflects the same phenomenon predicted using Model I.

Figure 16 shows the Strouhal number, St_θ, of the large-scale structures based on the local momentum thickness. That is,

$$St_\theta = \frac{f\theta}{\overline{U}} = \frac{\omega\theta}{2\pi\overline{U}} \tag{24}$$

where f and ω denote the frequency and the angular frequency. After the mixing layer reaches an equilibrium state, the Strouhal numbers of the large-scale distur- bances approach a constant (≈ 0.012). The Strouhal number of the large-scale structures, based on the average passage frequency and the local momentum thickness, in an unforced, initially fully turbulent mixing layer is $\approx$0.024, Hussain and Zaman (1985). In a spatially developing mixing layer, unstable waves or large-scale structures are continuously amplified as they propagate downstream. The amplification of the unstable waves continues until they become neutral. Thus, a wave at its neutrally stable stage reaches maximum amplitude and dominates over waves of other frequencies. Consequently, the detected average passage frequency of the large-scale structures is associated with that of the locally neutral mode, which is about two times of that of the locally most unstable mode. The present calculation, which predicts that the Strouhal numbers of the locally most unstable mode reflects this phenomenon.

IV.c Model III

Model III simulates the time-dependent turbulent motion associated with the passage of a train of large-scale turbulent structures. The large-scale turbulent structures are represented by a superposition of hydrodynamic instability waves. As the flow develops axially, these hydrodynamic waves become damped because of the growth of the shear layer. Since it is assumed that energy associated with a given wave is removed immediately after it becomes neutral, there is no need to obtain damped inviscid solutions by analytic continuation in the complex plane, Tam and Morris (1980).

The initial wave amplitudes of this calculation are

$$A_{0j} = 10^{-2}, \qquad j = 1,....6 \tag{25}$$

The initial mean velocity profiles and the boundary conditions are the same as those used in the previous calculations. In the preliminary calculations, it was found that an abnormality in the mean velocity distributions appeared near the critical points of saturating waves. Also, most of the shear layer growth occurred on the low speed side of the layer. This gives a non-monotonic velocity distribution near the critical layers of saturating waves and another inflection point appears. Saturating waves thus have to be removed before they become neutral during the axial marching. Wygnanski and Petersen (1987) suggested that this abnormality is due to nonlinearity. Composite expansion techniques have been applied to investigate the effect of critical-layer nonlinearity, for example, see Goldstein and Leib (1988) and Goldstein and Hultgren (1988). Another approach to resolve this issue is to include viscous effects; that is to solve the Orr-Sommerfeld equation. Since the present

investigation is directed toward developing simple turbulence models, instead of including other computationally expensive approaches, the effects of the critical point is accounted for by incorporating a small amount of eddy viscosity in the analysis of the mean flow. The additional mixing at the fine scale is diffusive and able to smooth out humps in the flow. In the present calculation, the extra mixedness provided accounts for about 10% of the amount of turbulent momentum exchange that is suggested by conventional models.

With this modification the mean velocity distributions predicted at several downstream stations are shown in Figure 17. There are six waves in the hierarchy in this calculation. Since waves are removed successively during the axial marching, the number of waves included depends on the distance the calculation is to be carried downstream. There are some small differences between the calculated results and Patel's measurements.

It should be noted that Model III simulates the development of the mixing layer associated with the realization of a single event, which is the passage of a train of well-defined large-scale structures. In physical experiments, such as that reported in Patel (1973), external disturbances or noise from various sources may modify the initial conditions of the flow. which cause events that affect the subsequent development of the layer. Therefore, the differences between predictions using Model III and experimental data will vanish if these randomizing events are taken into account. On the other hand, it might be expected that Model III should resemble the behavior of that of an externally excited mixing layer, in which the layer is excited at particular frequency and cleaner flow pictures can be observed.

Figure 18 shows the development of the wave amplitudes. The additional small-scale mixing increases the initial growth of the layer so that the fundamental mode is removed at a lower amplitude than its subharmonics before its amplitude reaches equilibrium level.

The axial width of the layer is shown in Figure 19 and is compared with the prediction using Model I. As was noted earlier, the presence of this stepwise evolution is characteristic of excited flows and would be smoothed out if many waves with slightly different amplitudes and frequencies were included. However, the global evolution of the width of the layer agrees closely with that using Model I. Figure 20 compares the predicted evolution of the momentum thickness of the shear layer, using Model II and Model III. Note that the initial momentum thickness for the cases using Model I, II and III are the same. The only differences are the values of the initial amplitudes. The case using Model III assumes stronger initial large-scale structures than that used in Model II. As the flow develops downstream, Model III predicts a greater amount of large-scale mixing of mass and momentum than Model II. Consequently, the predicted growth of the mixing region using Model III is faster than that using Model II. However, the predicted rates of growth, $d\theta/dx$, using these two models are virtually the same. Since both of these models provide predictions by modeling the intrinsic characteristic structures in the free mixing layer, it is not surprising to find some family resemblance between the results predicted by these three models.

Figure 21 shows the unsteady velocity profiles in the axial direction at x/δ_0=30 before, during and after the passage of a large-scale structure. At this location, the dominating mode has the period of approximately 4. Reverse flow occurs at the low speed side of

the layer during the passing of a large-scale structure. At the same time, the streamwise velocity increases instantaneously at the high speed side of the layer. These instantaneous velocity variations show the passage of a clock-wise rotating structure. Note that the instantaneous reverse flow at the low speed side of the layer gives rise to instantaneous changes of flow angles and makes velocity measurements extremely difficult in that region. The visualization of the flow can also be assisted by streakline plots such as those shown in Figure 22. The roll-up of vortices into larger vortex-like structures can be observed clearly. The initial roll-up is dominated by the fundamental mode. As time progresses, the initial structures convect downstream and roll around each other. These regions of concentrated vorticity then form a single large structure. As the passive particles travel downstream, their motion becomes dominated by lower subharmonics. Vortex-like structures of increasing scale are formed. Subsequently, the rolling process between two adjacent structures repeats as the flow develops further downstream. Careful examination of the figures also shows how the structures are convecting downstream as they form and roll. Large tongues of unmixed fluid are swept across the layer and reach the opposite side of the layer as observed by Brown and Roshko (1974). The engulfed fluid elements from the two sides of the layer mix and are drawn into the leading and trailing vortices when passing through the high-strain braid region between the vortices. This provides the environment for further fine-scale mixing.

Figure 23 and Figure 24 show the flow pictures frozen at $t = 6.5$ and 5.0, respectively. In these cases, harmonic waves in the wave hierarchy are in phase. The distribution of momentum thickness in the streamwise direction at $t = 6.5$ is shown in Figure 23.b. At $t = 6.5$, three full-grown large-scale structures centered at roughly, $x/\delta_0 = 10, 18$ and 40 can be observed. These large-scale structures are essentially vortices rotating in a clock-wise manner. The mean and transient velocity profiles at x/δ_0=18 and 40 are shown in Figure 23.c. The turbulent large-scale structures, which appear as clock-wise rotating vortices, contribute velocity excess/deficit on the high/low speed side of the layer, relative to their respective mean velocity distributions. Therefore, the instantaneous momentum thickness of the flow in the region occupied by the fully-grown large-scale structures is smaller than the mean value. This can be clearly seen in Figure 22.b. Note that for a vortex sheet with a velocity profile given by

$$g = \begin{cases} 1, & y > 0 \\ 0 & y \leq 0, \end{cases} \tag{26}$$

the momentum thickness is zero. The mean (or instantaneous) momentum thickness at any axial station is obtained by substituting $\overline{\tilde{u}}$ (or $< \tilde{u} >$) into the g in equation (26). In Figure 23.b, three dips can be observed clearly in the instantaneous momentum thickness distribution. The positions of the dips correspond to the centers of the three fully-grown structures. On the other hand, the instantaneous velocity profile at $x/\delta_0 = 27$ shows velocity deficit/excess on the high/low speed side of the layer. At $t = 6.5$, the high-strain braid region between two structures passes through $x/\delta_0 = 27$. Therefore it is not surprising to observe that the instantaneous momentum thickness is greater than the mean momentum thickness at $x/\delta_0 = 27$. If there is a very strong velocity excess/deficit on the

high/low speed side, a shear flow may have negative momentum thickness. The case shown in Figure 24 reflects the situation. At $t = 5$, two vortices are merging at $x/\delta_0 = 30$. The two merging vortices deform as they roll around each other. The instantaneous velocity profile at the center of the merging is shown in Figure 24.c. It shows clearly the footprints of these two deformed structures. This results in high velocity excess/deficit on the high/low speed side of the layer. The local instantaneous momentum thickness becomes negative and reaches a minimum at x/δ_0=30 before picking back up downstream. The following increase in momentum thickness in the axial direction is the effect of further mixing of the low and high speed fluid. Similar to the case at $t = 6.5$ and x/δ_0=27, the instantaneous momentum thickness at x/δ_0=30 and 50 are much higher than the respective mean values. As mentioned earlier in the analysis, harmonic waves have to be cut off before they saturate to avoid the problem associated with nonlinearity. Therefore, the rather abrupt variations in the instantaneous momentum thickness distributions in Figure 23.b and Figure 24.b can be observed at the axial locations where the waves are cut off. The second and the third harmonics are cut off at $x/\delta_0 = 18$ and 30, respectively. The dotted lines in Figure 23.b and 24.b show the projected distributions of the instantaneous momentum thickness should the harmonic waves be carried through their neutral points in the calculations.

V. SUMMARY

Three models based on a quasi–linear theory, that describes the dynamics of the dominant large–scale structures in a free mixing layer have been presented. The closure schemes incorporating the models are able predict the development of the turbulent free mixing layer accurately, even though they contain some assumptions and simplifications. The predicted averaged properties of the incompressible turbulent mixing layer agree well with experiments. The transient turbulent motions at the large scale in the layer mapped out using Model III possess many features that are apparent in flow visualization experiments, such as the convective nature of the large–scale structures, the large–scale transport of unmixed fluid elements and the roll–up of vortices. The models involve less empiricism than most conventional models. Since large–scale coherent structures appear also in shear flows of other geometries, the closure schemes presented here should be applicable to those cases as well. It is hoped that these models, which originate from observed physical phenomena, will provide efficient tools to model other free shear flows.

ACKNOWLEDGMENT

This work was supported by NASA Langley Research Center under grant NAG–1–657. The technical monitor is Dr. John Seinor.

REFERENCES

1. Brown, G. L. and Roshko, A., "On Density Effects and Large Structure in Turbulent Mixing Layers," *J. Fluid Mech.*, 64, 775–816 (1974).

2. Gaster, M., Kit, E. and Wygnanski, I., "Large-scale Structures in a Forced Turbulent Mixing Layer," *J. Fluid Mech.*, **150**, 23–39 (1985).
3. Petersen, R. A. and Samet, M. M., "On the Preferred Mode of Jet Instability," *J. Fluid Mech.*, **194**, 153–173 (1988).
4. Tam, C. K. W. and Morris, P. J., "The Radiation of Sound by the Instability Waves of a Compressible Plane Shear Layer," *J. Fluid Mech.*, **98**, 349–381 (1980).
5. Tam, C. K. W. and Burton, D. E., "Sound Generated by Instability Waves of Supersonic Flows. Part 1. Two-dimensional Mixing Layers," *J. Fluid Mech.*, **138**, 249–271 (1984).
6. Tam, C. K. W. and Burton, D. E., "Sound Generated by Instability Waves of Supersonic Flows. Part 2. Axisymmetric Jets," *J. Fluid Mech.*, **138**, 273–295 (1984).
7. Tam, C. K. W. and Chen, K. C., "A Statistical Model of Turbulence in Two-dimensional Mixing Layers," *J. Fluid Mech.*, **92**, 303-326 (1979)
8. Morris, P. J. and Giridharan, G., "On the Turbulent Mixing of Compressible Free Shear Layer," (accepted) *Proc. Roy. Soc. Lond.* (1990) Models for Turbulent Mixing in Compressible Shear Layers," to be published.
9. Ho, C.-M. and Huang, L.-S., "Subharmonics and Vortex Merging in Mixing Layers," *J. Fluid Mech.*, **119**, 443–473 (1982).
10. Bridges, T. J. and Morris, P. J., "Differential Eigenvalue Problems in which the Parameter Appears Nonlinearly," *J. Comp. Phys.*, **55**(3), 437–460 (1984).
16 Liou, W. W., "The Computation of Reynolds Stress in an Incompressible Plane Mixing Layer," M.S. Thesis (1986), Department of Aerospace Engineering, Penn State.
11. Liou, W. W. and Morris, P. J., "A Comparison of Finite Difference and Spectral Solutions of the Rayleigh Equation of Hydrodynamic Stability," in preparation.
12. Patel, R. P., "An Experimental Study of a Plane Mixing Layer," *AIAA J.* **11**, 67–71 (1973).
13. Komori, S. and Ueda, H., "The Large-scale Coherent Structure in the Intermittent Region of the Self-preserving Round Free Jet," *J. Fluid Mech.*, **152**, 337–359 (1985).
14. Wygnanski, I., Oster, D. and Fiedler, H., "A Forced, Plane, Turbulent Mixing-layer; A Challenge for the Predictor," in *Turbulent Shear Flows 2*, (ed. by J. L. S. Bradbury et. al.), 314–326, Springer, Berlin (1979).
15. Latigo, B., "Large-scale Sturcture Interactions in a Two-dimensional Trubulent Mixing Layer," *Ph. D. Thesis*, University of Southern California, 1979.
16. Launder, B. E., Morse, A., Rodi, W. and Spalding, D. B., "Prediction of Free Shear Flows; A Comparison of the Performance of Six Turbulence Models," *NASA SP-321*, 1972.
17. Tam, C. K. W. and Morris, P. J., "The Radiation of Sound by the Instability Waves of a Compressible Plane Turbulent Shear Layer," *J. Fluid Mech.*, **98**, 349–381 (1980).
18. Wygnanski, I. J. and Petersen, R. A., "Coherent Motion in Excited Free Shear Flows," *AIAA J.*, **25**, 201–213 (1987).

19. Goldstein, M. E. and Leib, S. J., "Nonlinear Roll-up of Externally Excited Free Shear Layers," *J. Fluid Mech.*, **191**, 481–515 (1988).

20. Goldstein, M. E. and Hultgren, L. S., "Nonlinear Spatial Evolution of an Externally Excited Instability Wave in a Free Shear Layer," *J. Fluid Mech.*, **197**, 295–330 (1988).

20. Davis, R. W. and Moore, E. F., "A Numerical Study of Vortex Merging in Mixing Layers," *Phys. FLuids,*, **28**, pp. 1626–1635. (1985).

20. Hussain, A. K. M. F. and Zaman, K. B. M. Q., "An Experimental Study of Organized Motions in the Turbulent Plane Mixing Layer," *J. Fluid Mech.* , **159**, 85–104 (1985)

20 Konrad, J. H., "An Experimental Investigation of Mixing in Two-dimensional Turbulent Shear Flows with Application to Diffusion-limited Chemical Reactions," Ph.D. Thesis (1976), California Institure of Technology.

Rayleigh, L., "On the Stability, or INstability of Certain Fluid Motions," *Proc. London Math. Soc.* **11** (1880), pp. 57–70.

Stuart, T. J., "On the Nonlinear Mechanics of Hydrodynamic Stability," *J. Fluid Mech.*, **4**, 51–79 (1975).

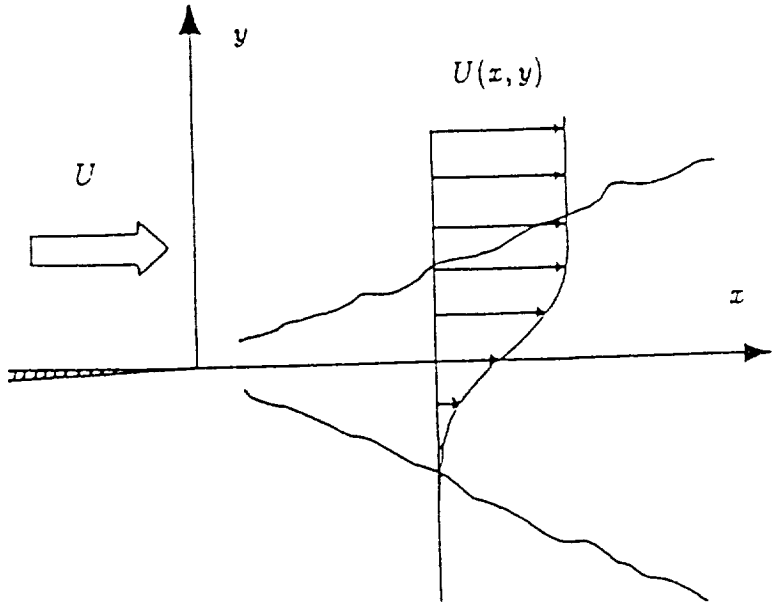

Figure 2.1. Sketch of a free mixing layer.

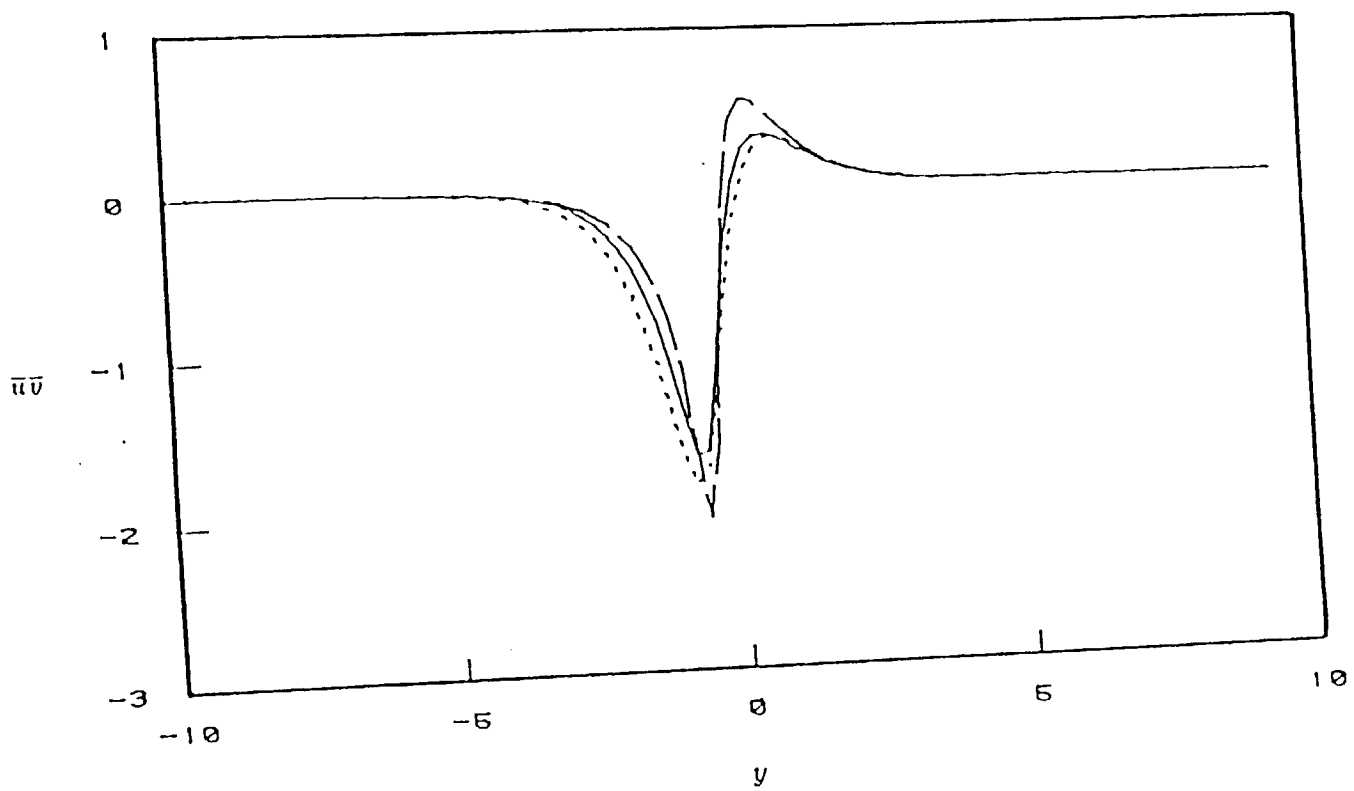

Figure 2.2 Unnormalized Reynolds stresses. - - - - , $\omega = 0.1$; ——— , $\omega = 0.14$; — — , $\omega = 0.2$.
Source: Liou (1986).

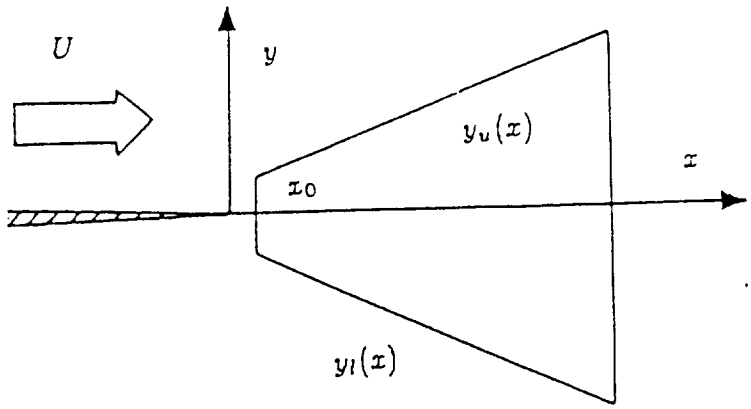

Figure 3.1. Physical domain

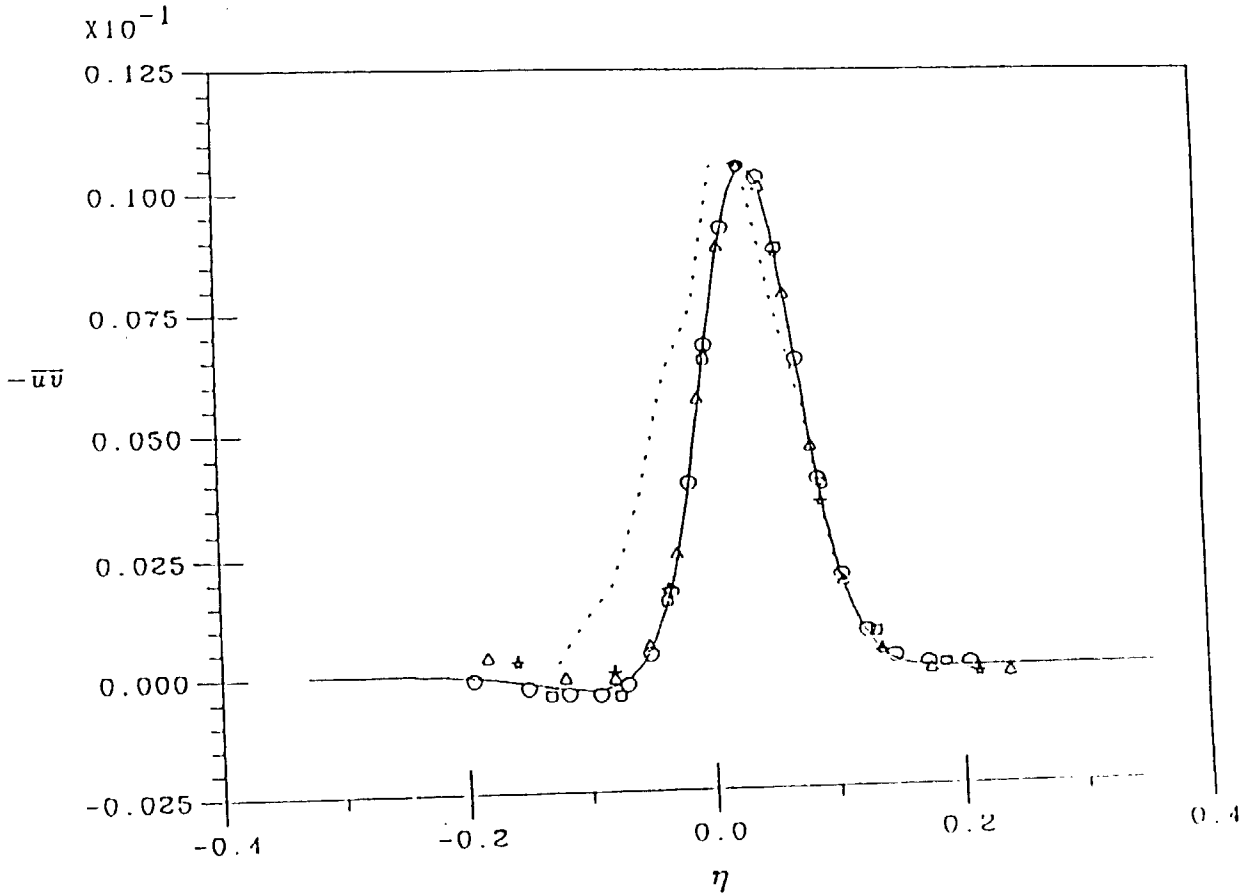

Figure 4.2. $-\overline{uv}$ in the self-similar region. ☆ , Chebyshev Collocation (N=11); △ , Chebyshev Collocation (N=19); □ , finite difference (N=11); ○ , finite difference (N=25); ——— , shooting; – – –, Patel.

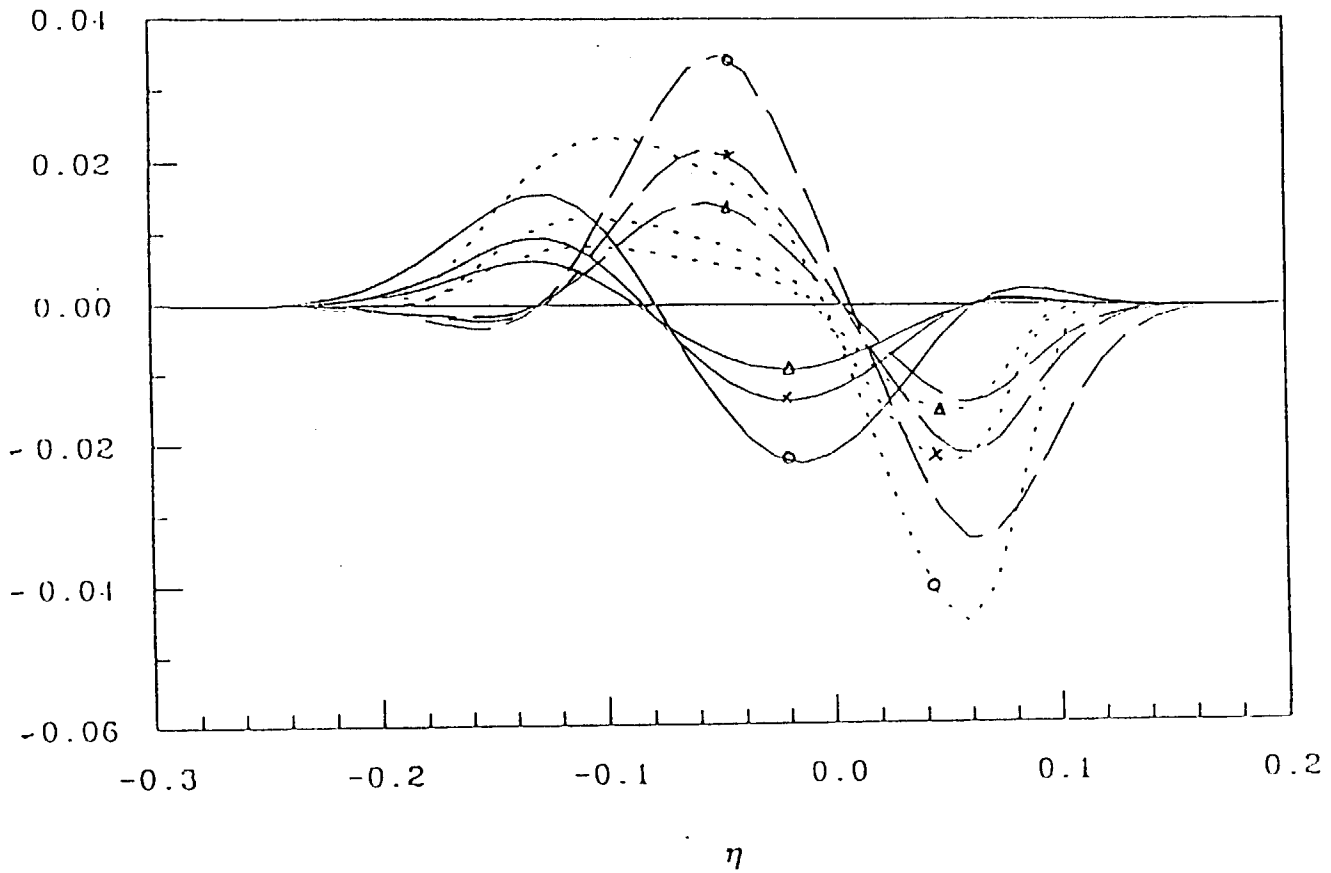

Figure 4.4. Driving forces across the mixing layer using Model I at ○ , x=2.37; × , 4.35; △ , 6.19. ——— , $-(\overline{u^2}-\overline{v^2})_x$; — — , $-(\overline{uv})_y$; – – – – , $-(\overline{u'v'})_y$.

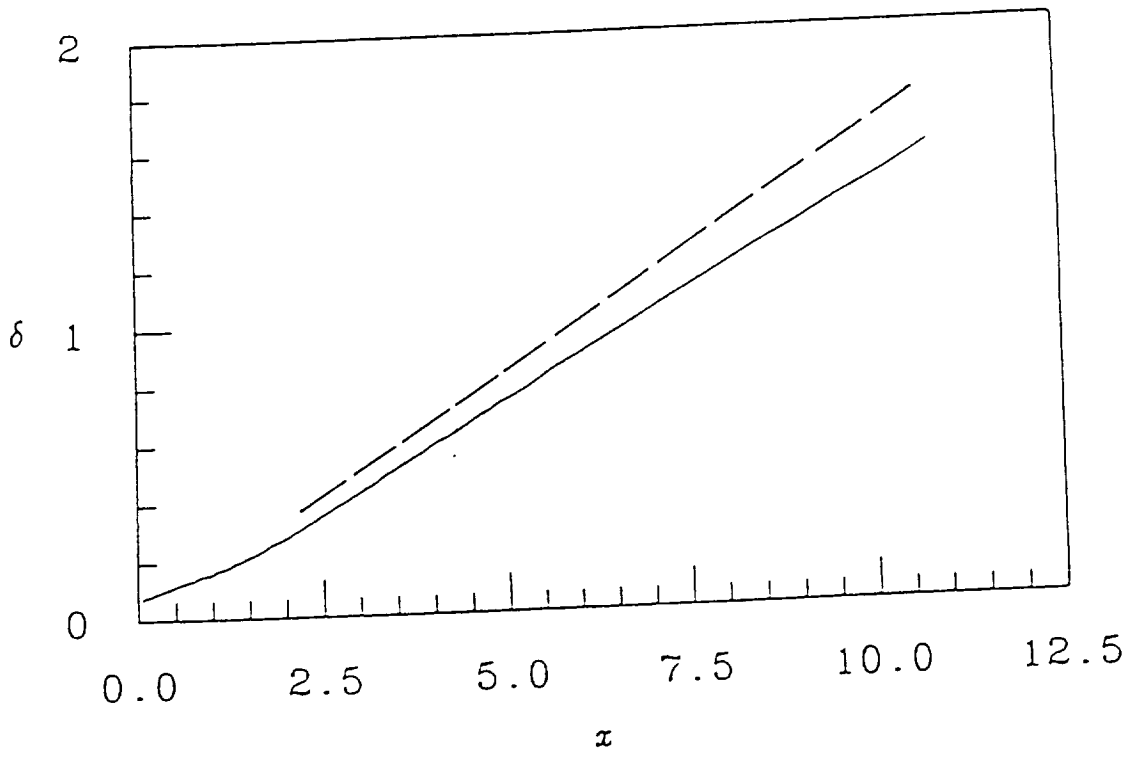

Figure 4.5 Growth of the mixing layer. —— , Model I; – – , experiments.

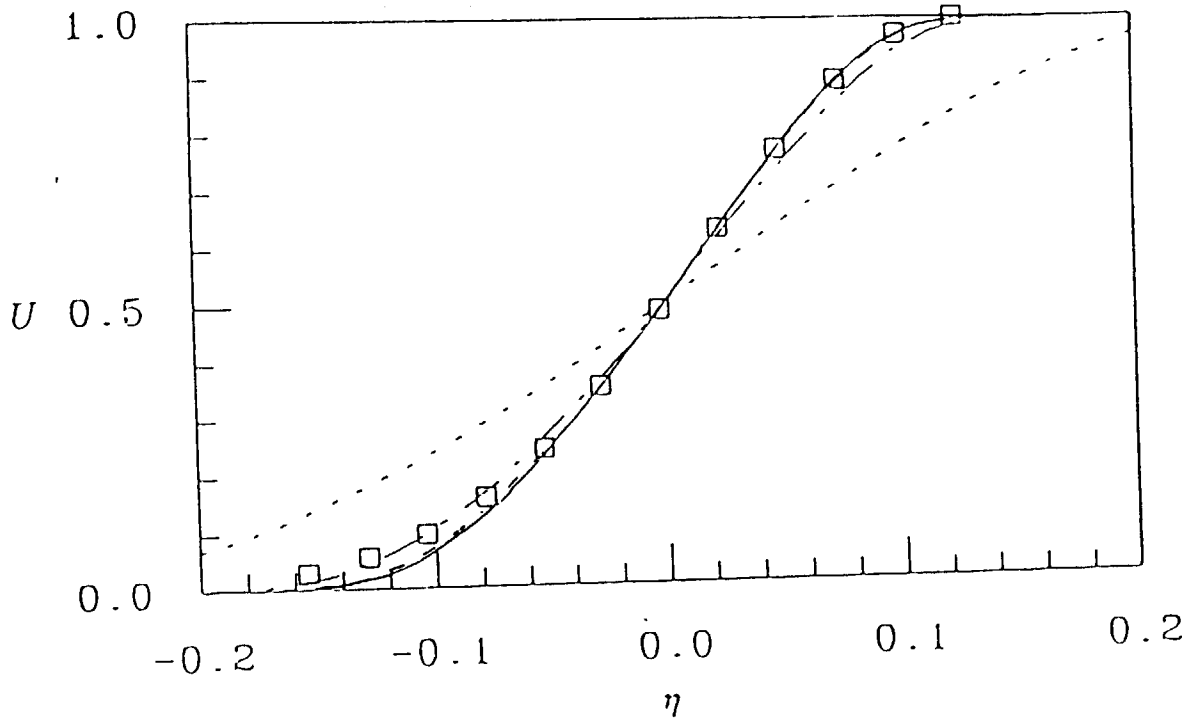

Figure 4.6. Mean velocity profiles using Model I at – – –, x=0.72; – — , 1.45; — — —, 2.37; — — , 3.25; — — , 4.35; —— , 6.19. □ , Patel.

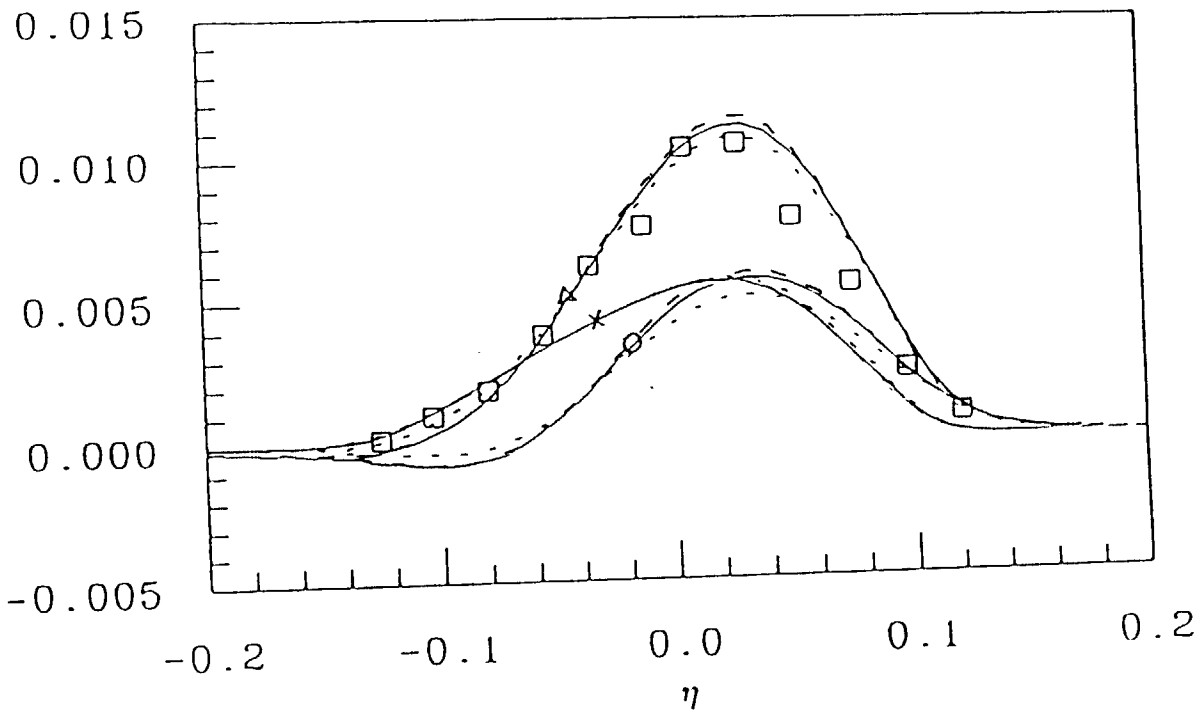

Figure 4.7. Distributions of the Reynolds shear stresses using Model I at - - - - , x=2.37; – –, 4.35; ——— , 6.19. □ , Patel; ○ , $-\overline{uv}$; × , $-\overline{u'v'}$; △ , $-\overline{uv} - \overline{u'v'}$.

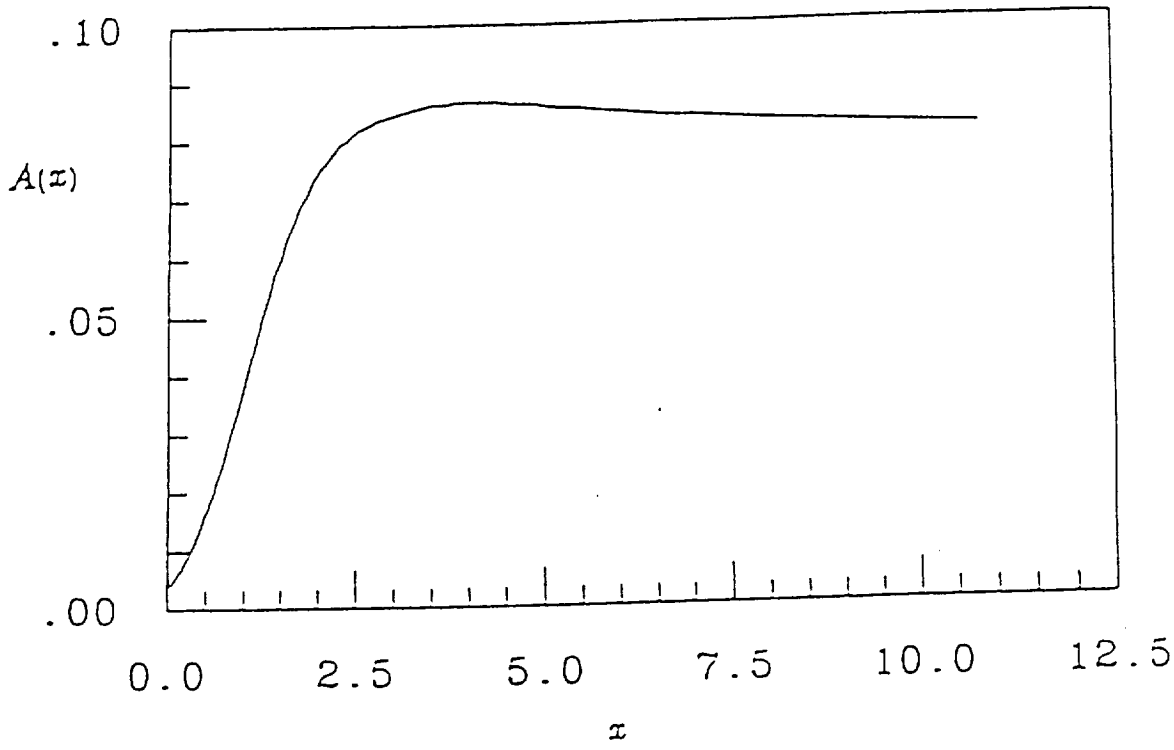

Figure 4.8. Evolution of the large–scale structure amplitude using Model I.

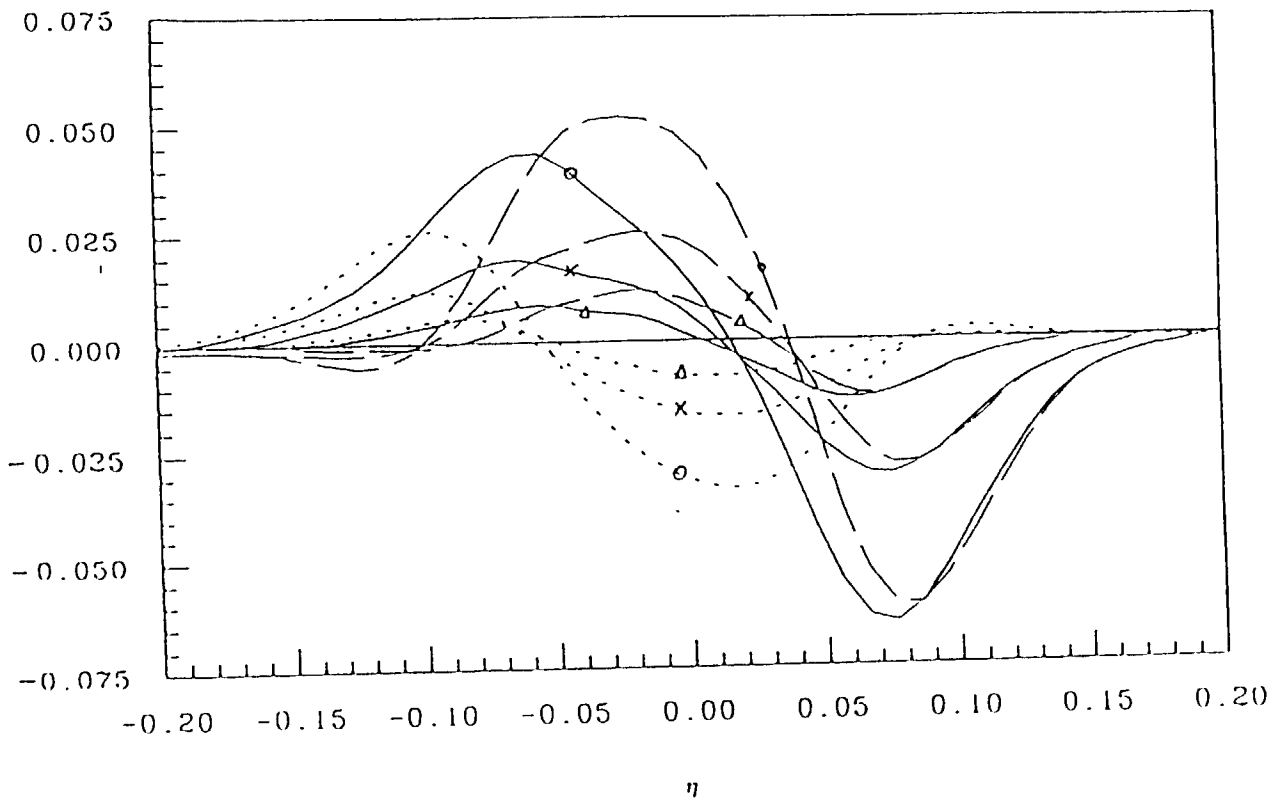

Figure 4.9. Driving forces across the mixing layer using Model II at ○ , x=2.95; × , 5.36; △ , 11.36. - - - - -, $-(\overline{u^2}-\overline{v^2})_x$; — — —, $-(\overline{uv})_y$; ——— , $-(\overline{uv})_y$ $-(\overline{u^2}-\overline{v^2})_x$.

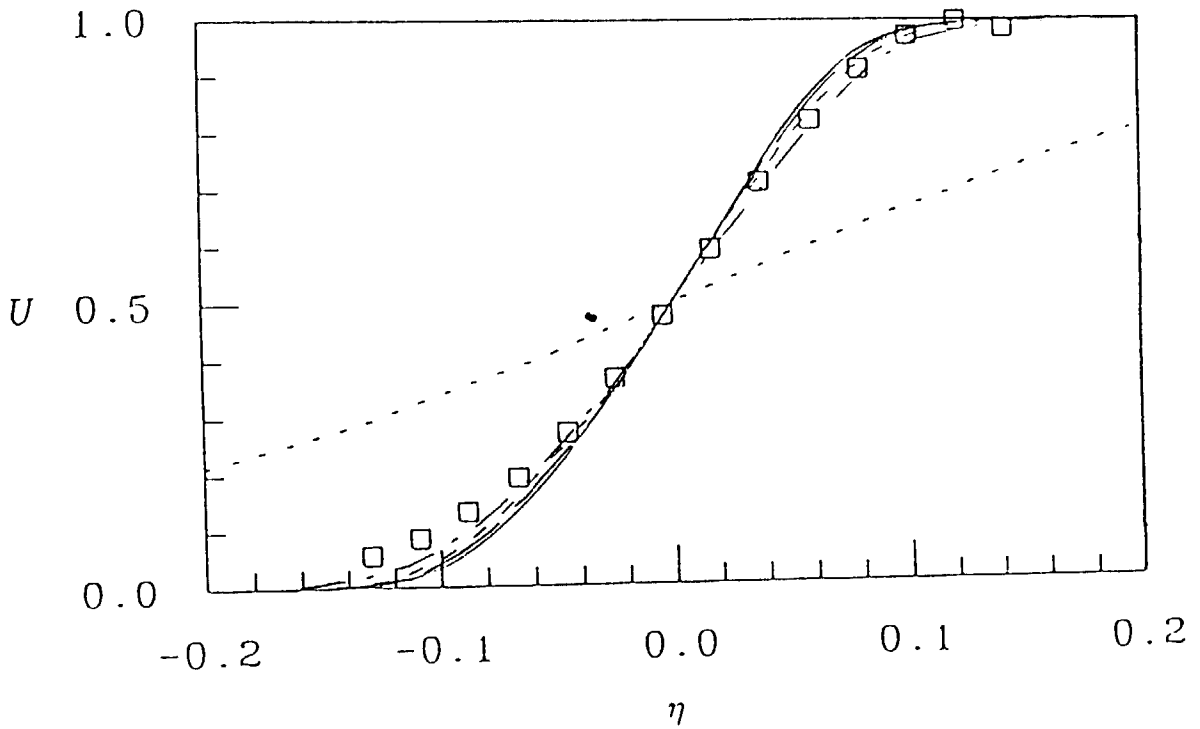

Figure 4.10. Mean velocity profiles using Model II at – – –, x=0.63; - —— , 2.96; ———, 7.36; — —, 9.36; ——— , 11.36. □ , Patel.

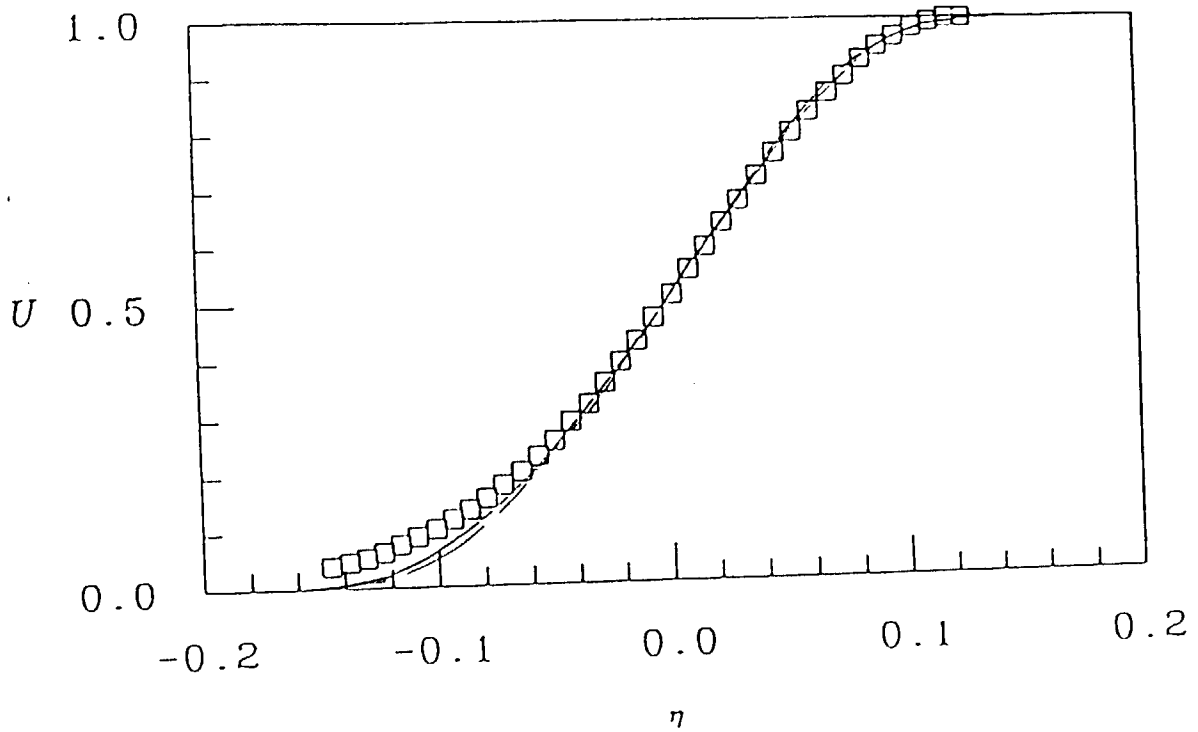

Figure 4.11. Comparison of the velocity profiles using —— Model I (x=6.19); – – Model II (x=7.36); □ Patel.

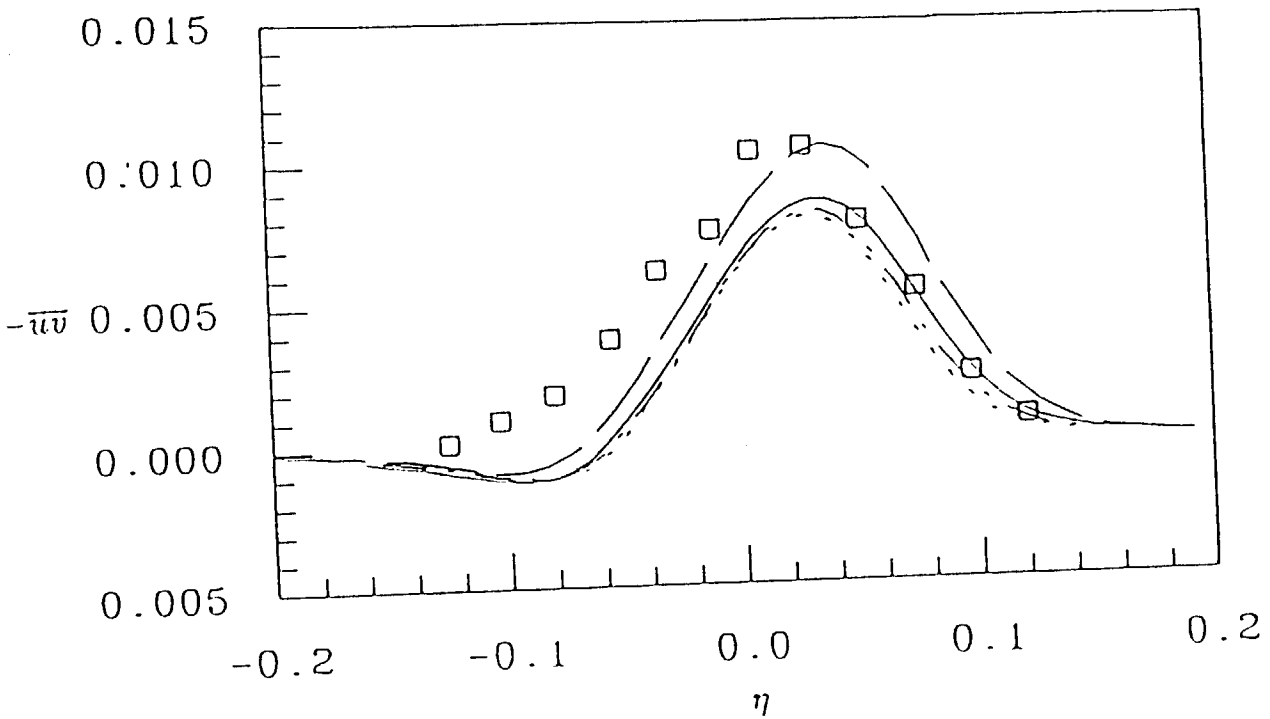

Figure 4.12. Distributions of wave shear stress using Model II at — — —, x=2.96; ——— , 7.36; — — —, 9.36; - - - - -, 11.36. □ , Patel.

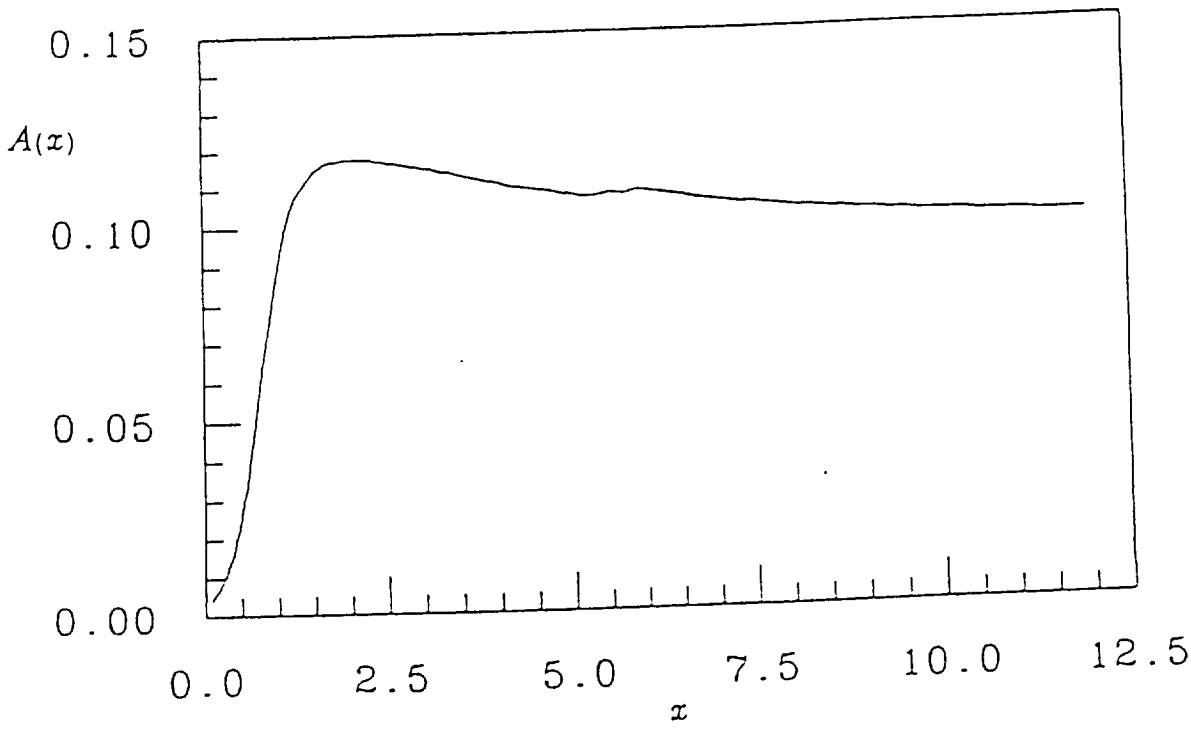

Figure 4.13. Evolution of the large-scale structure amplitude using Model II.

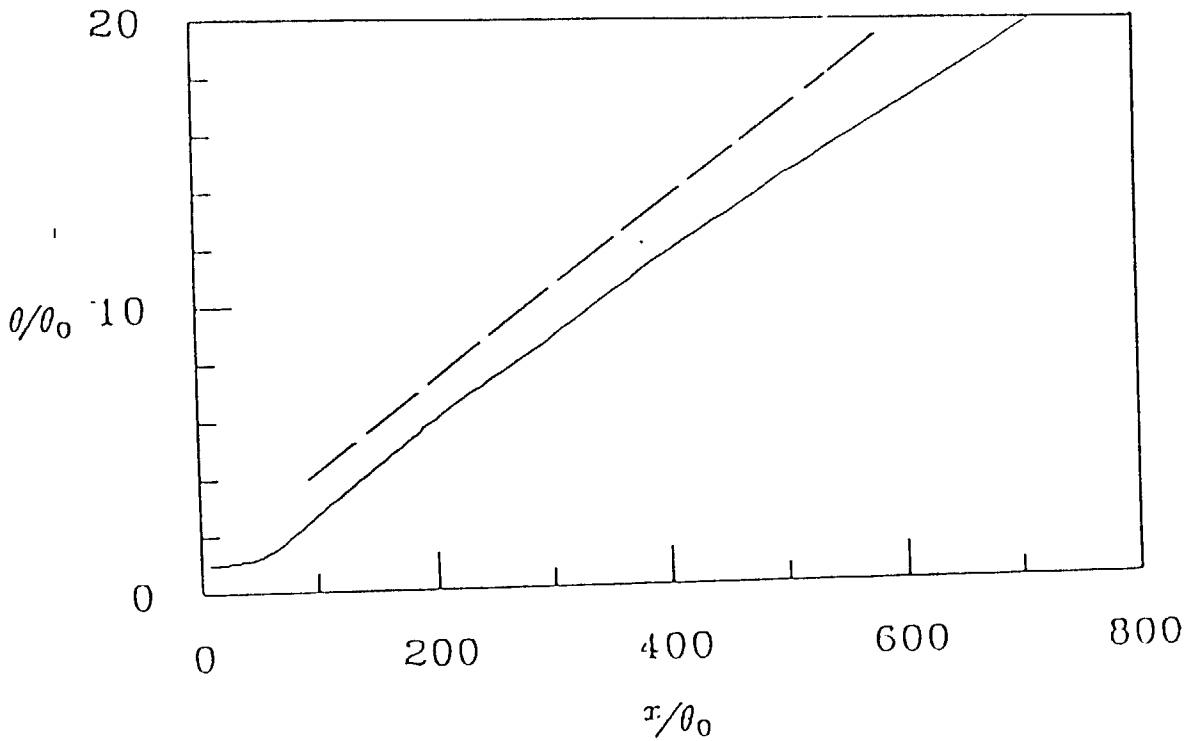

Figure 4.14 Evolution of the momentum thickness. ——, Model II; – –, experiments.

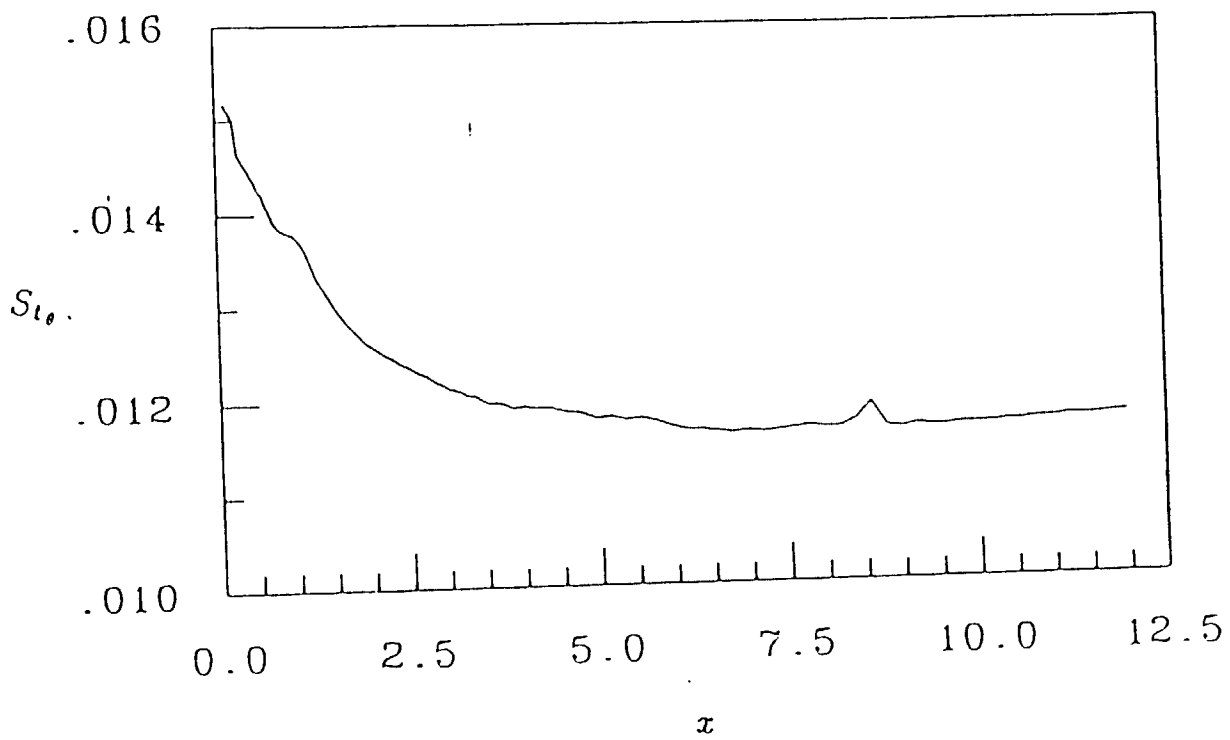

Figure 4.15. Evolution of the Strouhal number using Model II.

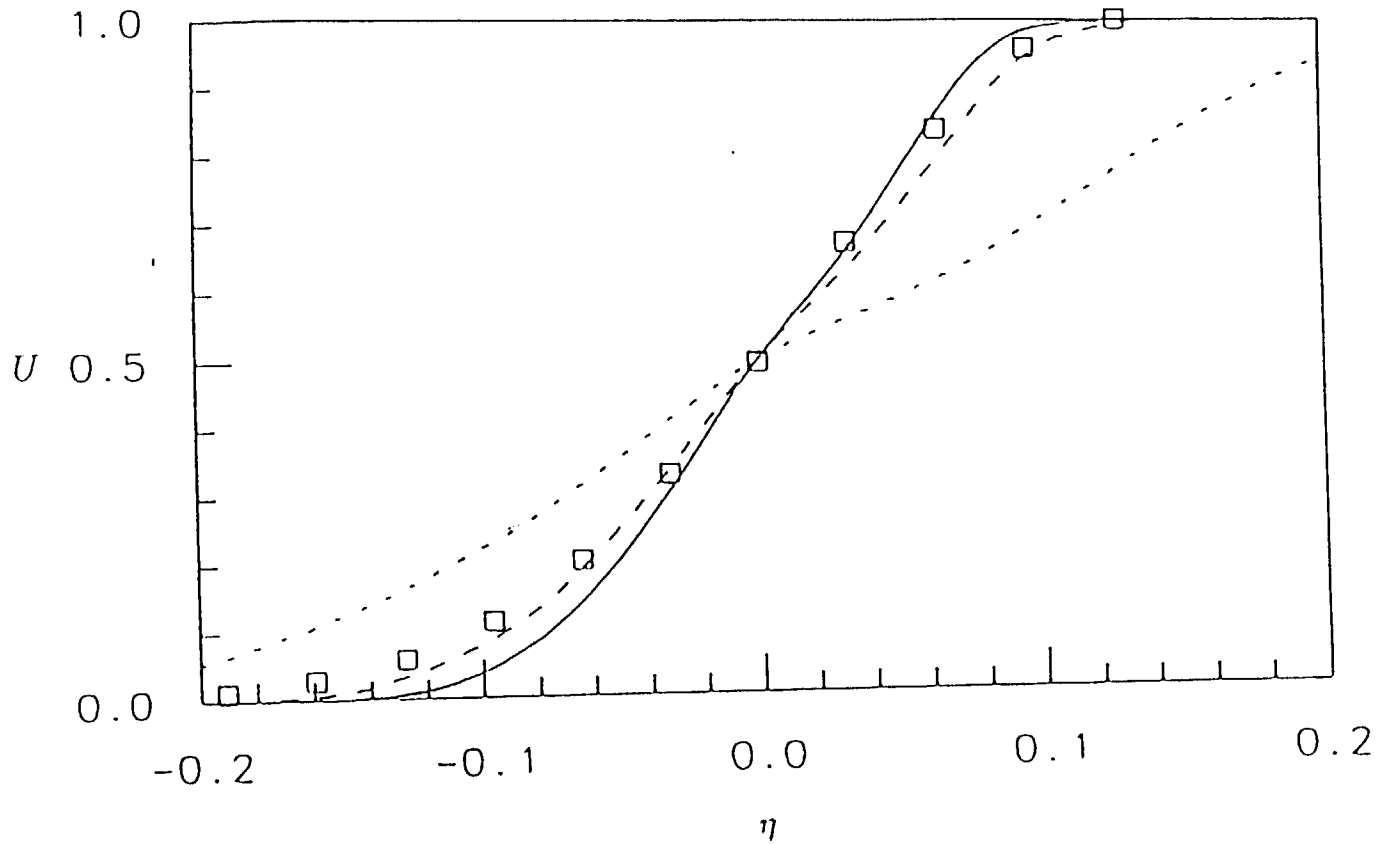

Figure 4.16. Mean velocity profiles using Model III at - - - - -, x=1.0; — — —, 2.96; ———, 5.96. □ , Patel.

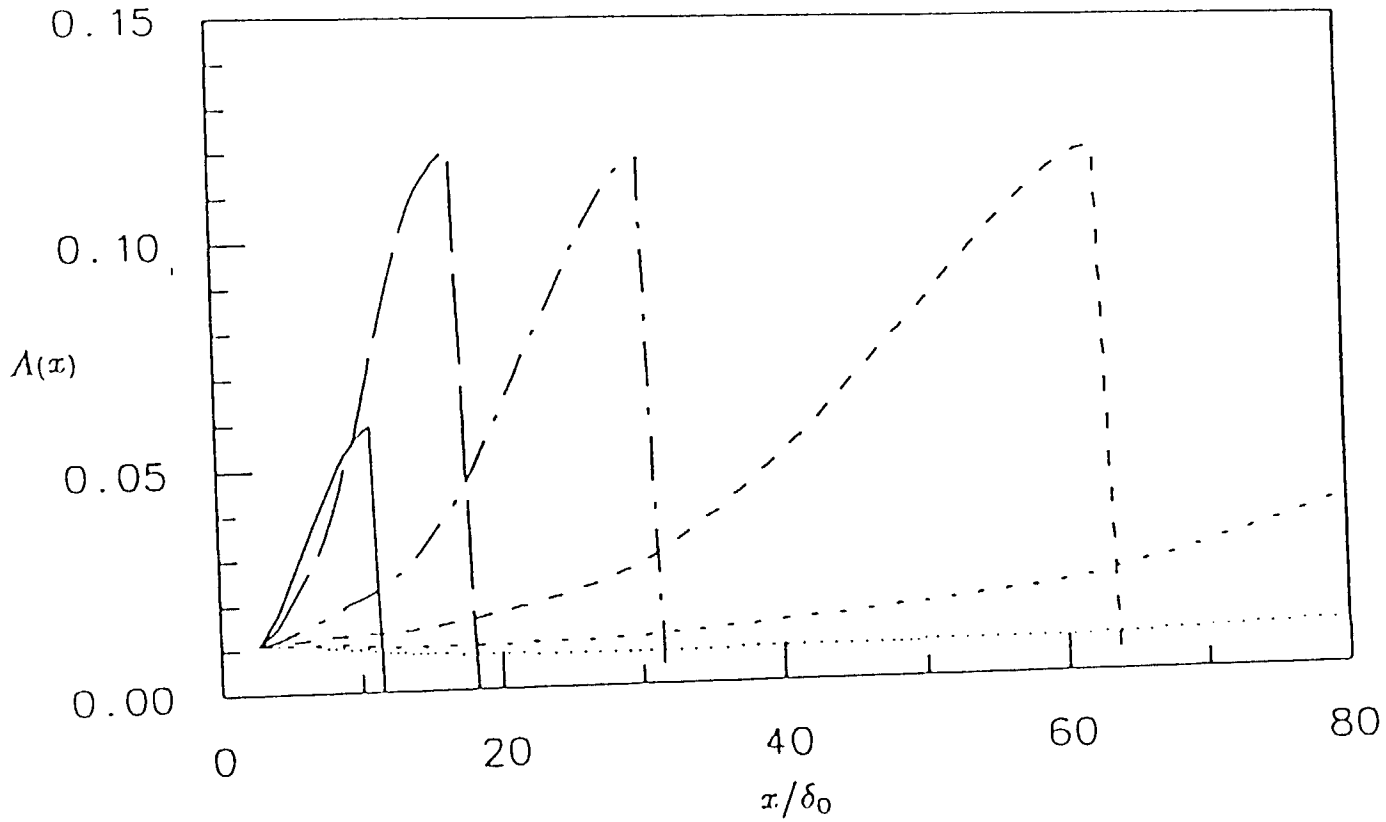

Figure 4.17. Evolutions of the large-scale structure amplitudes using Model III. ——— , fundamental; — —, 1st subharmonic; - ——, 2nd; — — —, 3rd; - - - - -, 4th; ·····, 5th.

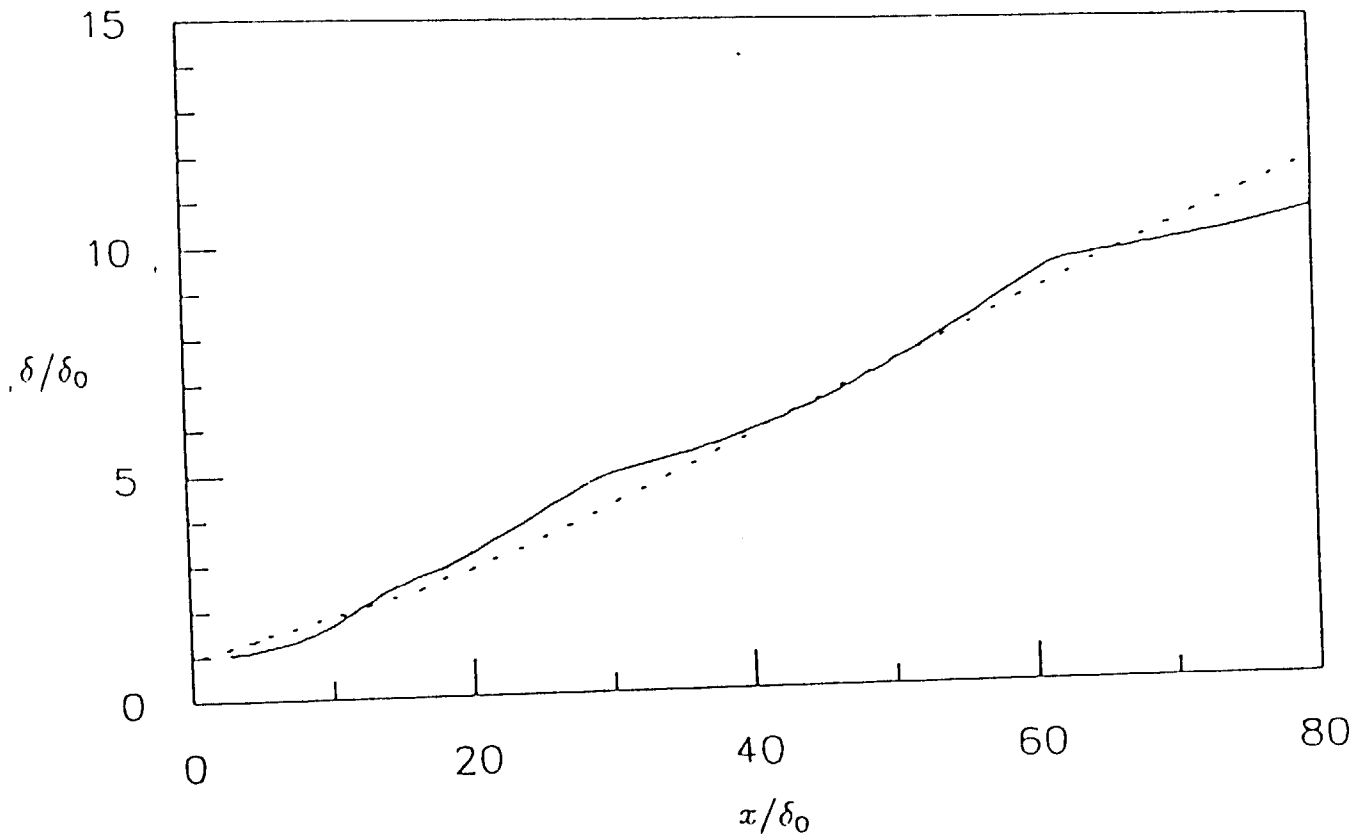

Figure 4.18. Growth of the mixing layer. - - - - -, Model I; ——— , Model III.

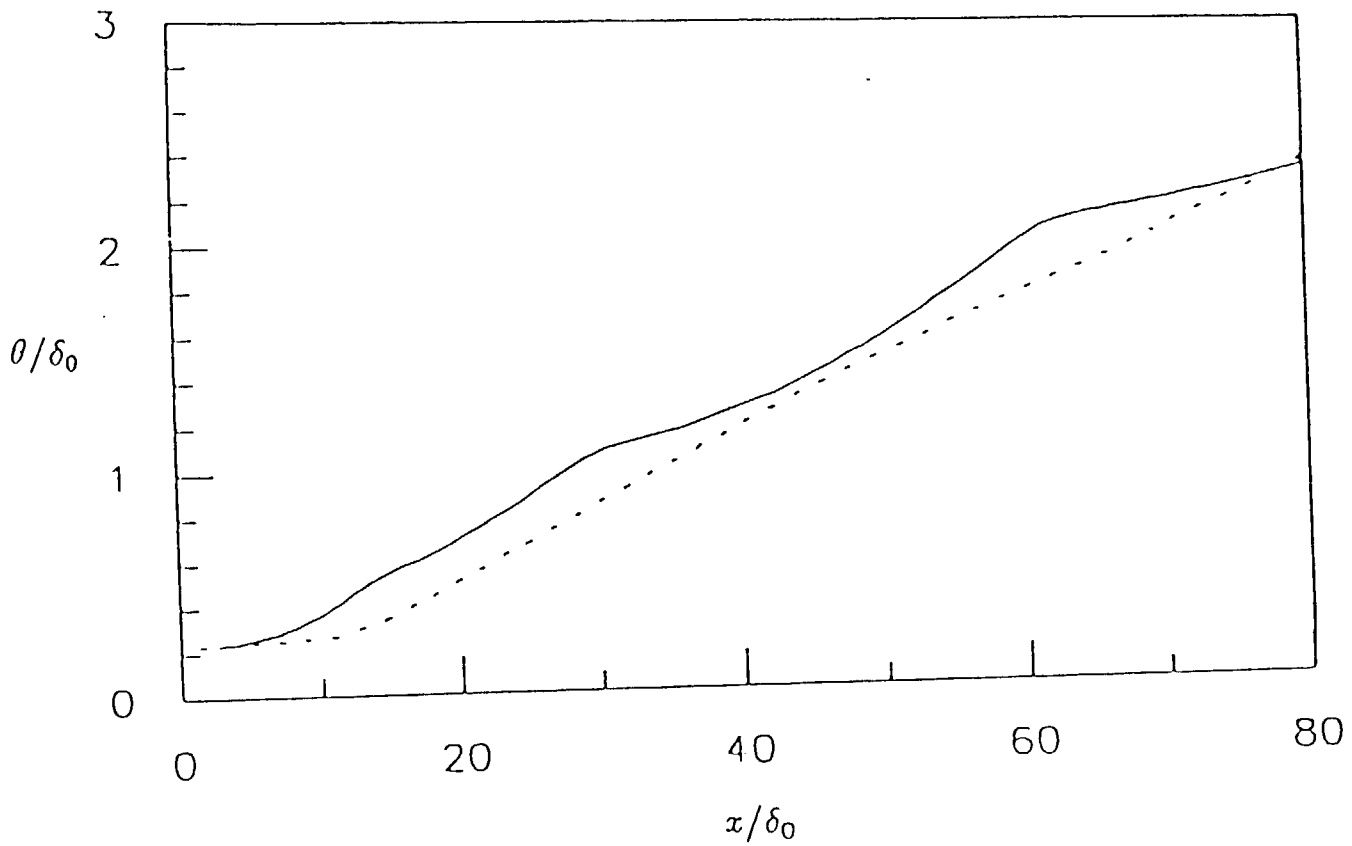

Figure 4.19. Momentum thickness - - - - -, Model II; ——— , Model III.

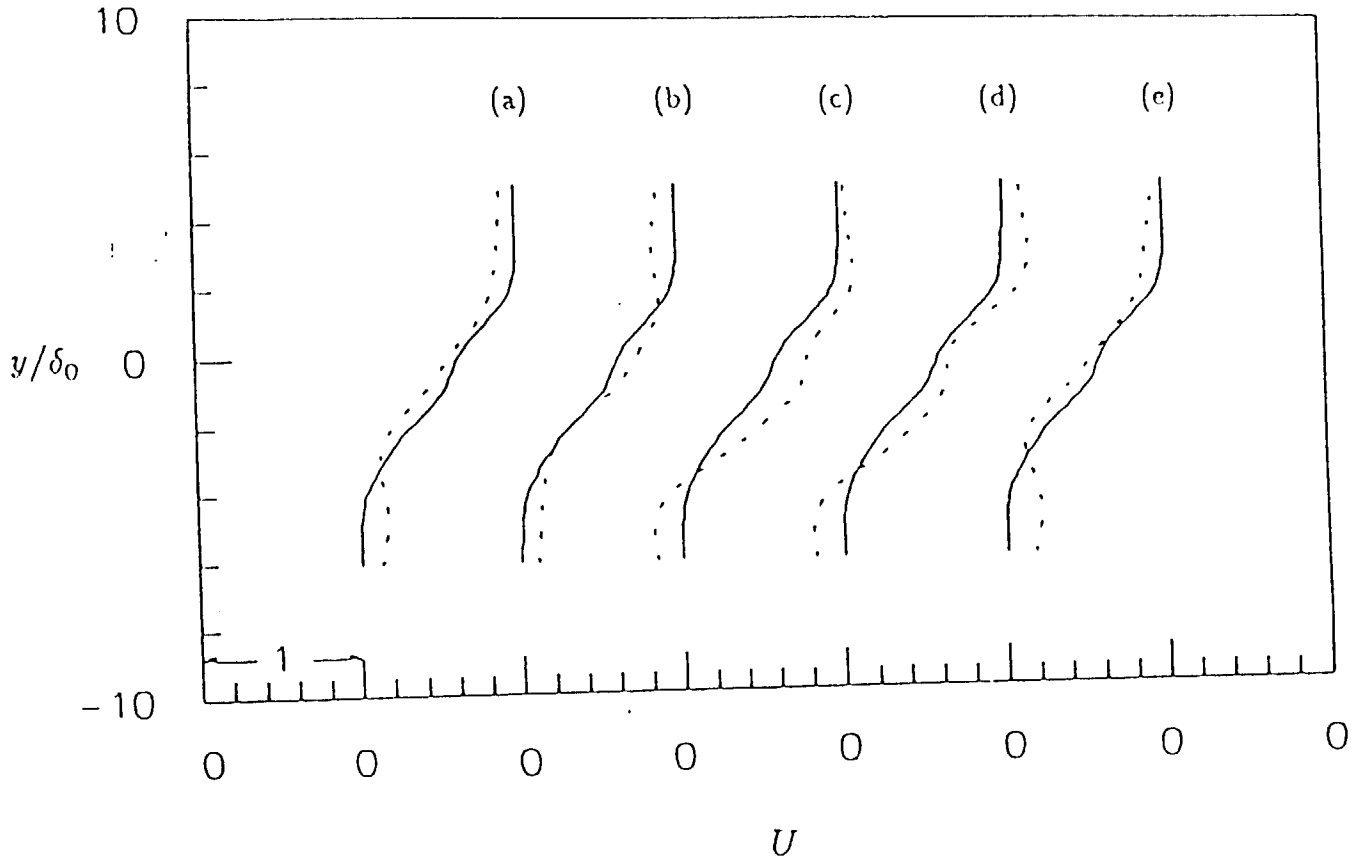

Figure 4.21. Velocity profiles at $x/\delta_0 = 30.$ for (a) t=2.5, (b) 3.5, (c) 4.5, (d) 5.5, (e) 7.0; —— Mean, - - - -Transient.

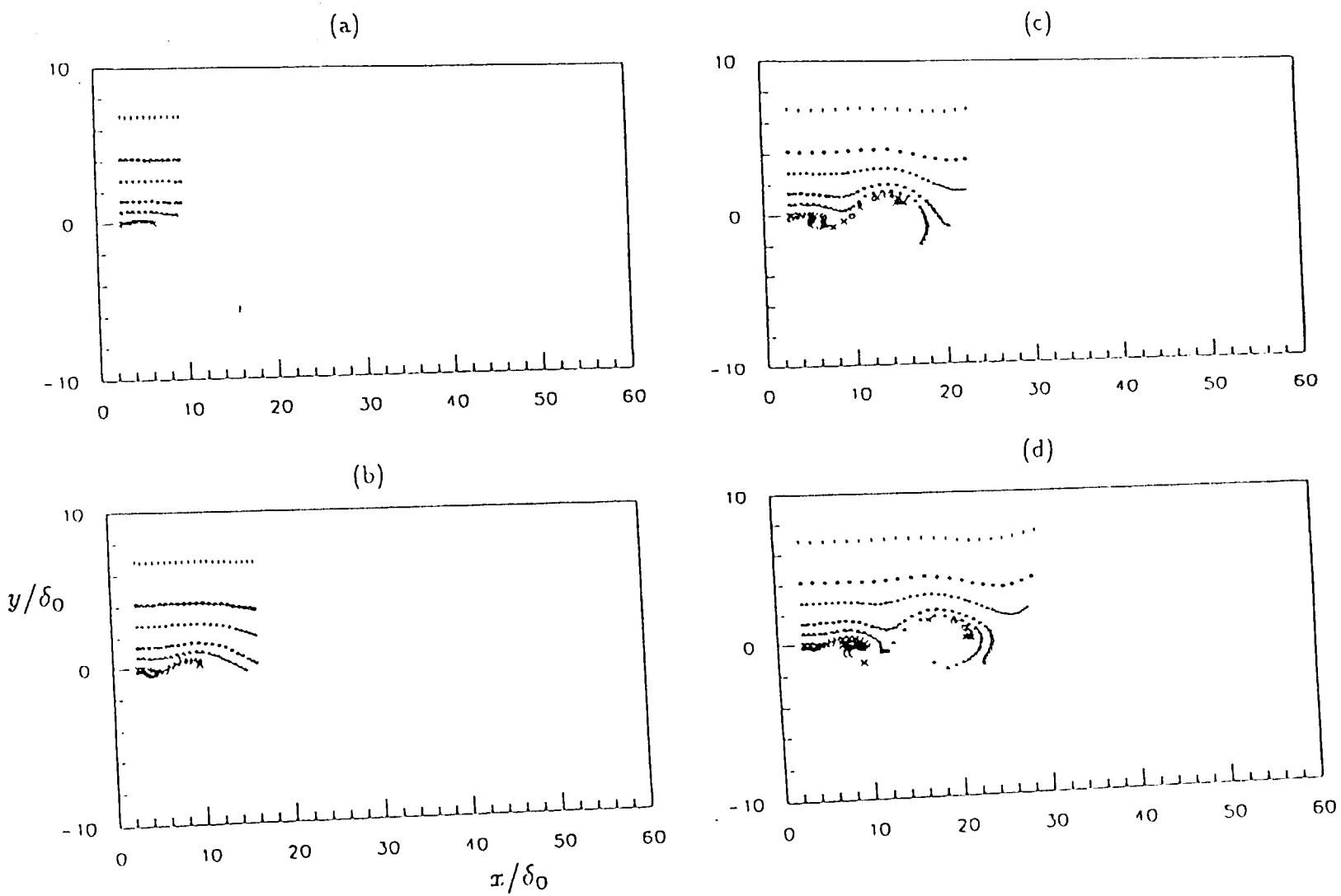

Figure 4.22. Streakline plots at (a) t=0.5, (b) 1.0, (c) 1.5 (d) 2.0, (e) 2.5, (f) 3.0, (g) 3.5, (h) 4.0, (i) 4.5, (j) 5.0, (k) 5.5, (l) 6.0, (m) 6.5, (n) 7.0, (o) 7.5, (p) 6.5.

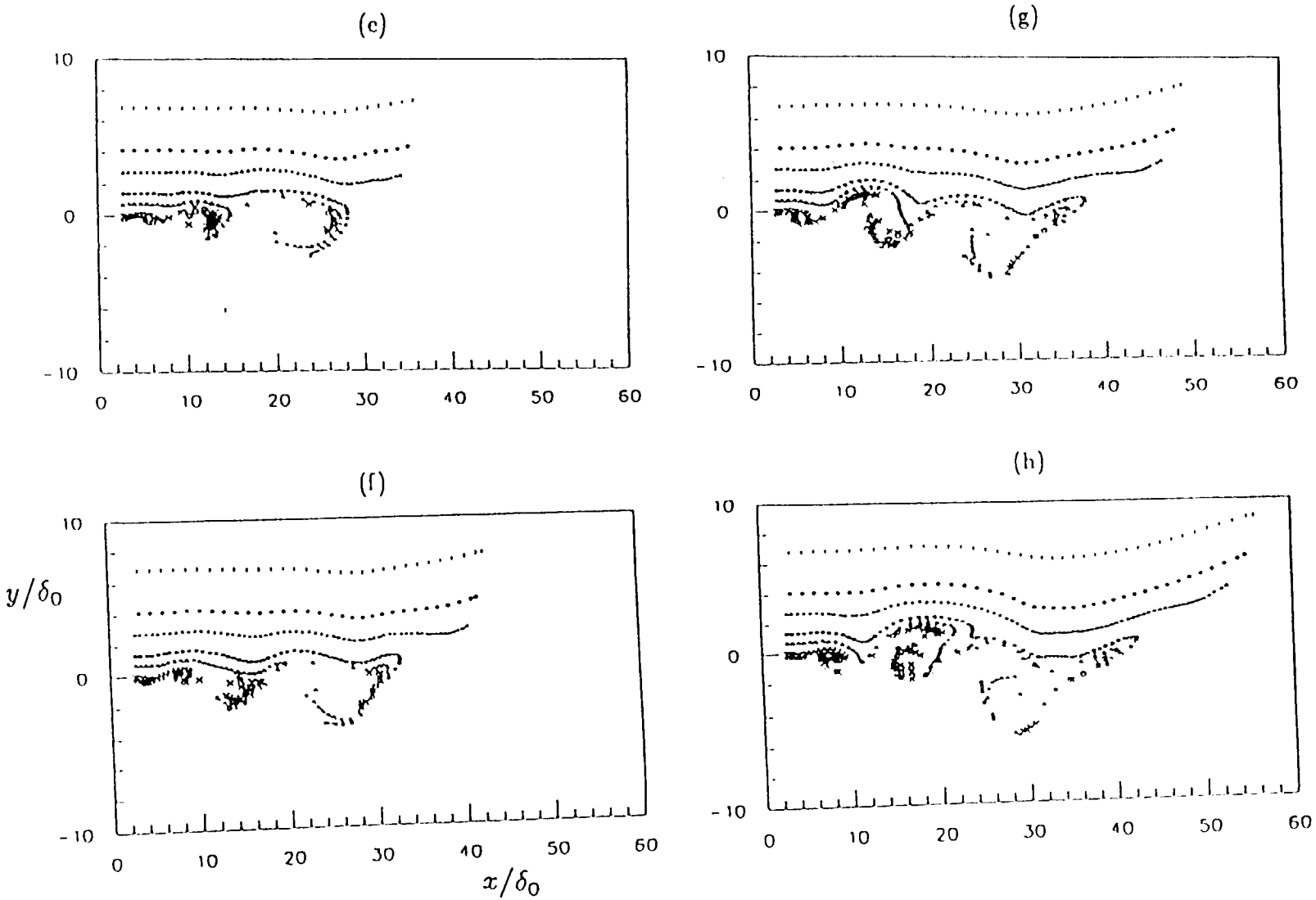

Figure 4.22. (continued)

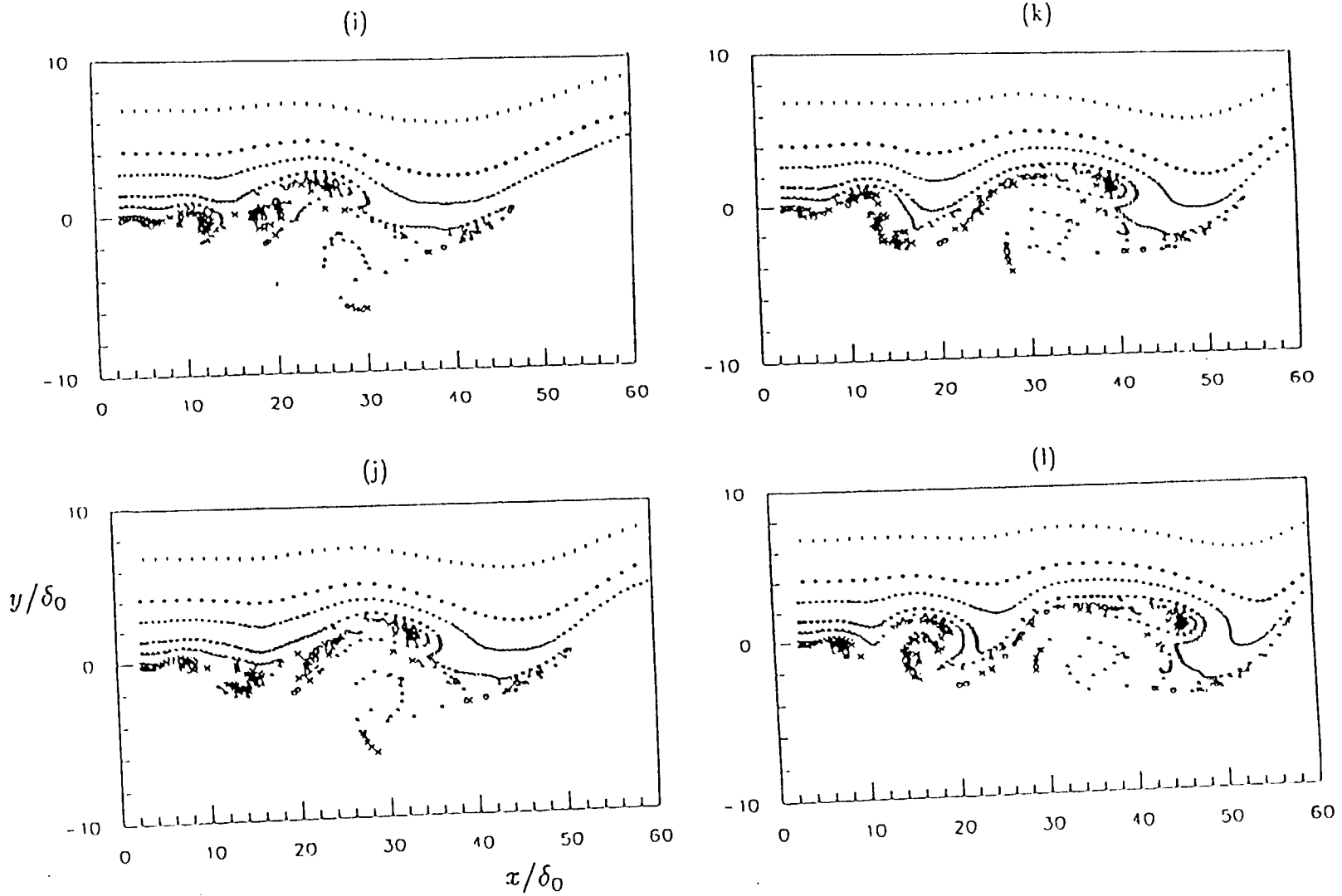

Figure 4.22. (continued)

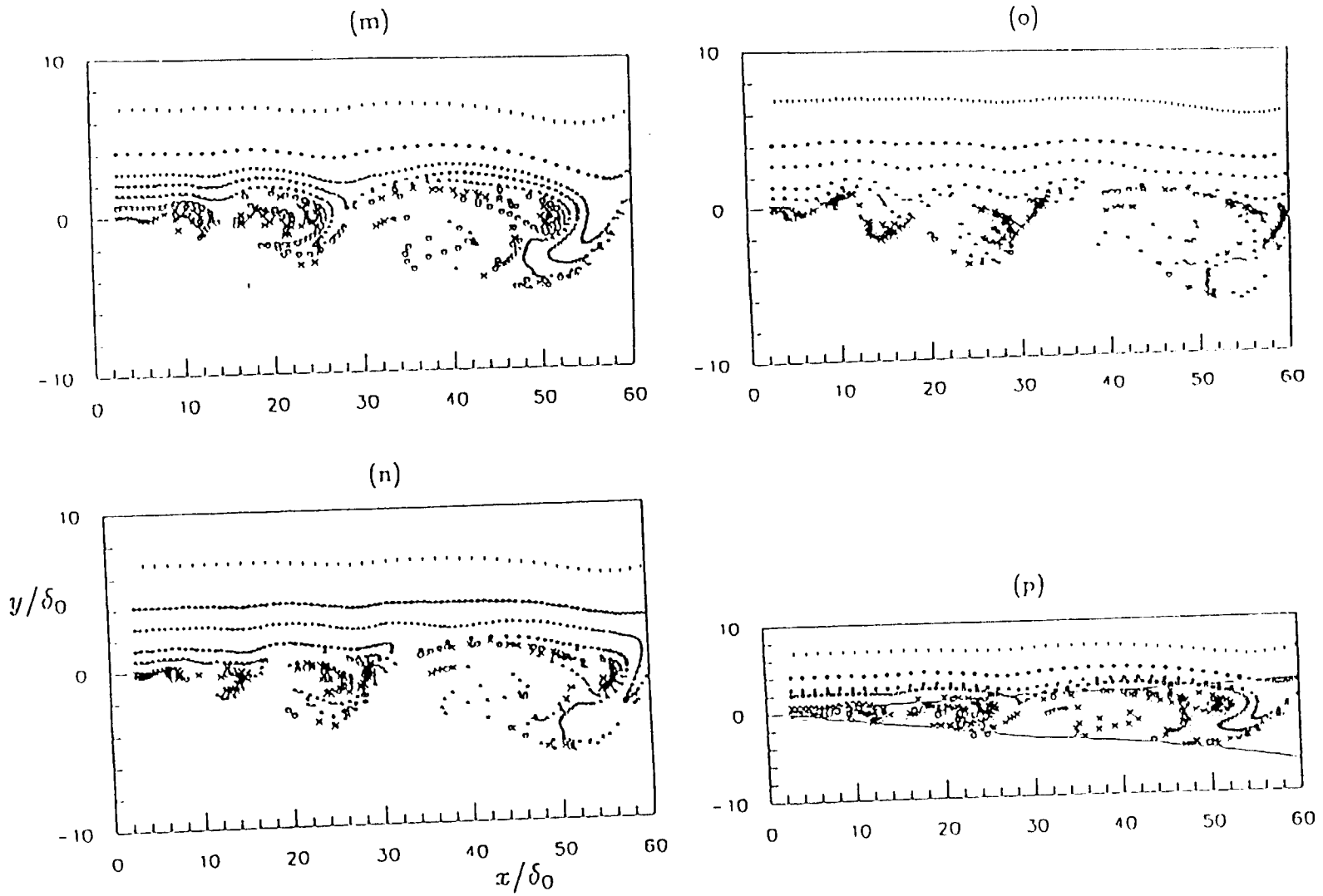

Figure 4.22. (continued)

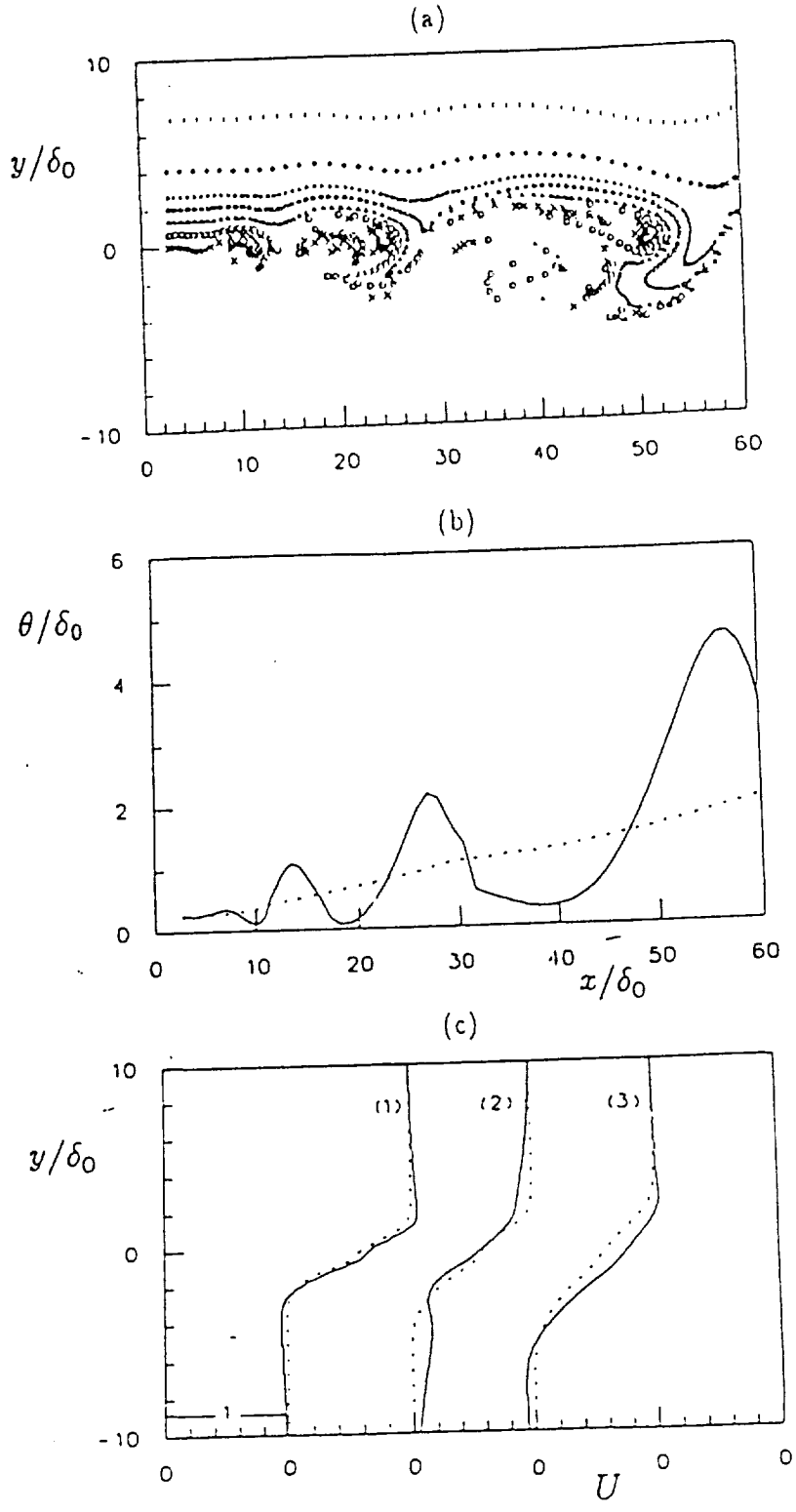

Figure 4.28. Flow visualization using Model III at $t = 6.5$. (a) Streakline plot; (b) Evolution of momentum thickness, - - - -, mean; ——, Model III; (c) Velocity profiles at (1) $x/\delta_0 = 18$, (2) 27, (3) 40, – – – –, mean, ——, transient.

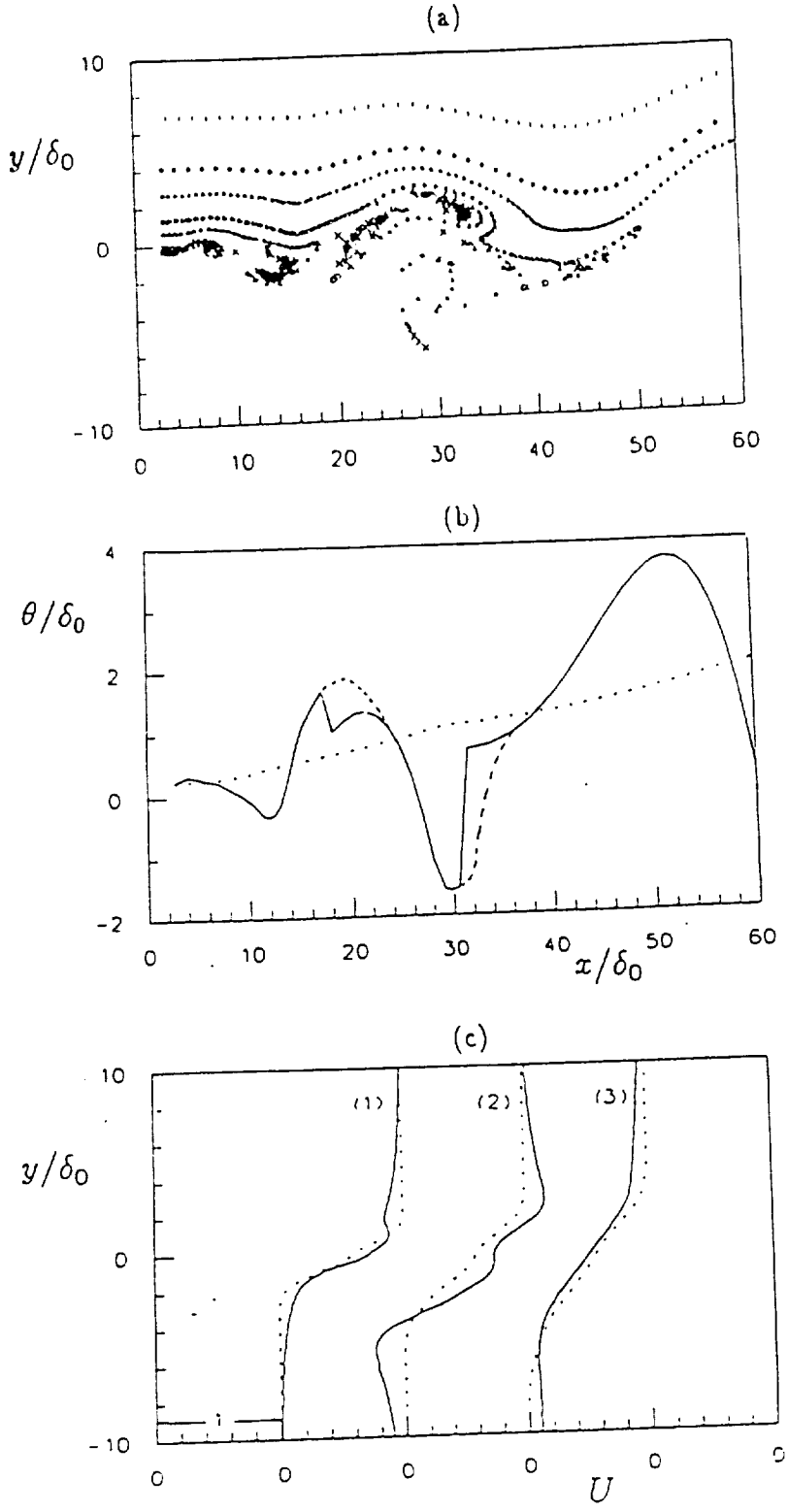

Figure 4.29. Flow visualization using Model III at $t = 5.0$. (a) Streakline plot; (b) Evolution of momentum thickness, - - - - , mean; —— , Model III; (c) Velocity profiles at (1) $x/\delta_0 = 16$, (2) 30, (3) 50, - - - - , mean, —— , transient.

Chapter 4

Conformal Grid Generation Using Wegmann's Methods

Roy S. Baty and P. J. Morris

ABSTRACT

Conformal coordinate transformations are used to map simple computational domains onto arbitrary simply and doubly connected regions with smooth boundaries. Efficient schemes involving the solution of the inverse boundary correspondence function problems associated with mapping the unit disc or circular annulus onto simply or doubly connected domains respectively are employed. The numerical implementation of these schemes is emphasized. Examples are generated for regions with elliptic inner and outer boundaries. Additional examples are used to demonstrate the accuracy and convergence of the schemes and their practical limitations. The techniques are found to converge well if holomorphic functions are used to describe the boundaries. The use of preconditioning maps is also discussed.

1.0 INTRODUCTION

Many problems of practical interest in engineering involve the solution of differential problems in complex geometries. In such problems the boundaries may not conform to coordinate lines in an orthogonal coordinate system. Alternatively, the coefficients in the differential problem may not be constant along coordinate lines making a separable form of solution impossible. Several numerical techniques are available to overcome these difficulties. Finite element or boundary element methods may be used. If a finite difference or spectral approximation is sought the physical domain must be transformed into a simple computational domain. Once again, several alternative approaches exist. The use of conformal maps is very desirable. Such maps simplify the governing differential equations in the mapped regions since the metric tensors are diagonal. However, these maps are difficult, and sometimes inefficient, to generate computationally and often lead to ill-posed numerical problems.

Recently, Wegmann [1,2] developed a very efficient scheme to determine the conformal map from a standard computational domain onto an arbitrary simply connected region in the plane. This scheme solves the inverse boundary correspondence problem associated with mapping the unit disc onto a region with a smooth boundary. Wegmann [3] also extended this technique to determine the boundary values for the transformation mapping the circular annulus onto a doubly connected region with smooth boundaries. In both cases, the entire conformal map may be generated from the solution of the boundary correspondance problem using the Cauchy Integral Theorem.

The present study of conformal maps is motivated by the authors' interest in the spatial stability of jets of arbitrary cross section. The characteristics of the

instability waves play an important role in the jet mixing process and the radiation of noise by high speed jets. The growth of these instabilities is governed by the linearized, inviscid equations of motion. These may be simplified to a single linear, elliptic, second- order partial differential equation for the instability wave pressure. In general, the coefficients in this equation vary arbitrarily in the cross section plane and no separable solutions may be found. Thus a numerical solution must be obtained in the regions of non- constant coefficients.

There are two characteristic regions in a jet flow. The first is the annular mixing region surrounding the potential core of the jet and the second is the developed jet flow region downstream of the potential core. Once a map is generated for either of these doubly or simply connected regions onto a simple computational domain, the homogeneous boundary value problem for the instability wave pressure fluctuations may be solved. Such a solution, using a hybrid pseudospectral and finite difference algorithm is described by Baty and Morris [4].

In this paper we apply Wegmann's techniques to compute the conformal coordinate transformations for simply and doubly connected regions. Examples are given for regions appropriate for the study of jets issuing from elliptic nozzles. Simply and doubly connected elliptic regions of aspect ratios 2 and 3 are considered. The conformal maps for such regions are difficult to compute and provide a good numerical test case. The numerical implementation of the mapping techniques is emphasized. The elliptic and additional maps are generated to establish the convergence and accuracy of the techniques. In addition, the practical limitations of these techniques and some methods to overcome these difficulties are presented.

In the next section some preliminary mathematics is developed. Sections 3 and 4 describe the simply and doubly connected Wegmann methods. Details of the

numerical implementation of the techniques and several examples are given. Some practical limitations of the techniques and a discussion of convergence and efficiency is given in Section 5.

2.0 PRELIMINARY MATHEMATICS

The regions of interest in the present study are the annular and disc-like regions. Therefore, the canonical regions are the unit annulus (with some inner radius $0 < \mu < 1$) and the unit disc. Let C denote either canonical region, let P denote a given physical region, and let W denote the conformal mapping satisfying:

$$W : C \rightarrow P \tag{2.1}$$

Consider a rectangular region, $\mathcal{R}$, defined by

$$\mathcal{R} := \left[(y^1, y^2) \in \mathbf{R}^2 | a \leq y^1 \leq b, 0 \leq y^2 \leq c\right] \tag{2.2}$$

where a, b, and c are finite real numbers and where $c > 0$. The exponential mapping, $\exp(iz)$, then carries $\mathcal{R}$ onto an annular region, C:

$$\exp : \mathcal{R} \rightarrow C \tag{2.3}$$

Composing the mappings given by 2.1 and 2.3 yields a map from a rectangular domain onto the region of interest:

$$W \circ \exp : \mathcal{R} \rightarrow P \tag{2.4}$$

The exponential map carries an infinite strip onto the unit disc. Thus, any finite rectangle will be carried onto an annulus.

The following discussion considers the analysis required for simply connected geometries. The analysis needed for the doubly connected geometries may be generalized from this case.

Let $\mathcal{D}$ be the unit disc. Let $\mathcal{E}$ be a simply connected region with a smooth closed boundary parameterized by,

$$z(t) \quad \text{on} \quad 0 \leq t \leq \beta. \tag{2.5}$$

Here, z is assumed to be a smooth regular curve. By the Riemann mapping theorem there exists a unique function g such that,

$$g : \mathcal{D} \rightarrow \mathcal{E}. \tag{2.6}$$

It should be noted that the uniqueness of g follows from the imposition of normalizing conditions, for example see [5]. For simply connected regions the following conditions are imposed:

$$g(0) = 0, \qquad g'(0) > 0. \tag{2.7}$$

The goal of the simply connected Wegmann method is to determine the map g on the boundary of the unit disc. This requires determining the image of a point on the unit circle. Since $g(\mathcal{D}) = \mathcal{E}$, it follows that a point on the unit circle is carried to a point on the boundary of $\mathcal{E}$. Now, since the boundaries of $\mathcal{D}$ and $\mathcal{E}$ are known smooth functions, only the angle of a point on the boundary of $\mathcal{D}$ or $\mathcal{E}$ needs to be known in order to determine its location on the boundary. Therefore, if the angle θ of a point is given, the problem becomes to determine the angle $\tau(\theta)$ of its image satisfying:

$$g(e^{i\theta}) = z(\tau(\theta)) \tag{2.8}$$

Any real function $\tau(\theta)$ such that,

$$\tau(\theta) - \frac{\beta}{2\pi}\theta, \tag{2.9}$$

is 2π periodic and 2.8 is satisfied is called an inverse boundary correspondence function, IBCF.

The Wegmann method solves for the function, τ, so that equations 2.8-9 are satisfied. The technique assumes that a good guess, $\hat{\tau}$, for τ is known and then computes a small correction factor, η, such that:

$$\tau = \hat{\tau} + \eta \qquad 2.10$$

To simplify the construction of τ, an approximation of η is calculated. Substitution of 2.10 into 2.8 and linearization of the result yields:

$$g(e^{i\theta}) = z(\hat{\tau}(\theta)) + z'(\hat{\tau}(\theta))\eta(\theta) \qquad 2.11$$

where the prime denotes differentiation with respect to τ. Equation 2.11 can then be recast as a function–theoretic boundary value problem allowing the explicit determination of η. In the numerical solution of the IBCF, equation 2.11 is solved iteratively becoming:

$$g_{k+1}(e^{i\theta}) = z(\tau_k(\theta)) + z'(\tau_k(\theta))\eta_k(\theta) \qquad 2.12$$

Therefore, at each step of the iteration the function τ as well as the boundary of the smooth domain $\mathcal{E}$ are approximated. Once the IBCF, τ, has been computed, 2.8 may be used to construct the function, g, on the interior of the unit disc from the Cauchy Integral Theorem.

3.0 THE SIMPLY CONNECTED WEGMANN METHOD

Wegmann's technique solves the inverse boundary correspondence problem, introduced in the last section, by iterative computation of the correction factor, η, defined by 2.10. This method generates simultaneously two sequences of functions.

The first sequence of functions, g_k, is analytic on the interior of the unit disc and satisfies the normalization conditions 2.7. The second sequence of functions, z_k, maps continuously the unit circle onto the boundary of the physical region. If these sequences converge, they may be used to compute the boundary correspondence function, τ.

The basic strategy of the Wegmann method is to construct the real part of the desired conformal map, g_k, on the boundary of the physical regions and then use a conjugate integral operator, K, to determine the imaginary part. Here K is defined by the equation,

$$Ku(\tau) = \frac{1}{2\pi}\text{P.V.}\int_0^{2\pi} u(t)\cot(\frac{\tau - t}{2})dt \qquad 3.1$$

where P.V. stands for the principal value of the integral.

Equation 3.1 defines a general operator which generates the conjugate periodic function, v, of a real 2π periodic function, u. Furthermore, the operator K is easy to evaluate numerically. If the functions on which this operator acts are expressed as a Fourier series, K simply multiplies the coefficients of the Fourier series by $\pm i$ or by 0. The mathematical and numerical details are given in Henrici [6].

Wegmann's method [3], constructs the real part of the conformal map by recasting 2.12 as a Riemann–Hilbert problem given by:

$$\Im\left(\frac{g_{k+1}(e^{i\theta})}{z'(\tau_k(\theta))}\right) = \Im\left(\frac{z(\tau_k(\theta))}{z'(\tau_k(\theta))}\right) \qquad 3.2$$

This Riemann–Hilbert problem has a unique solution, Henrici [5]. Furthermore, the solution of the Riemann-Hilbert problem may be used iteratively to compute the desired conformal map on the boundary of the physical region. The $k+1$–th approximation of the map is given by :

$$\omega_k(\theta) = K(\beta(\tau_k(\theta)) - \theta) \qquad 3.3$$

$$q_k(\theta) = \Im[z(\tau_k(\theta))\exp(\omega_k(\theta) - i\phi(\tau_k(\theta)))] \quad 3.4$$

$$g_{k+1}(e^{i\theta}) = (iq_k(\theta) - \chi_k - Kq_k(\theta))\exp(i\phi(\tau_k(\theta)) - \omega_k(\theta)) \quad 3.5$$

where ϕ is the tangent angle of the curve defined by:

$$z'(\xi) = |z'(\xi)|\exp(i\phi(\xi)) \quad 3.6$$

Furthermore, the constant, χ_k, is defined by:

$$\chi_k = \hat{q}_k \cot \hat{\alpha}_k \quad 3.7$$

where,

$$\hat{q}_k = \frac{1}{2\pi}\int_0^{2\pi} q_k(\xi)d\xi, \quad 3.8$$

and

$$\hat{\alpha}_k = \frac{1}{2\pi}\int_0^{2\pi} (\phi(\tau_k(\xi)) - \xi)d\xi. \quad 3.9$$

The constant χ_k insures that the normalizing conditions 2.7 are satisfied.

The update of the correction factor, η_k, is then determined by 2.12 and 3.5, which yield,

$$\eta_k(\theta) = -\Re\left(\frac{z(\tau_k(\theta))}{z'(\tau_k(\theta))}\right) - \frac{\chi_k + Kq_k(\theta)}{|z'(\tau_k(\theta))|\exp(\omega_k(\theta))} \quad 3.10$$

Then using 3.8, the next iteration of the inverse boundary correspondence function becomes:

$$\tau_{k+1}(\theta) = \tau_k(\theta) + \eta_k(\theta). \quad 3.11$$

Equations 3.3-11 constitute the simply connected Wegmann method.

3.1: Numerical implementation of the Wegmann method

The Wegmann method has been implemented numerically using FFT's to approximate the Fourier series and the necessary periodic functions and their conjugate integral operators. The FFT's have been computed using the standard IMSL subroutines DFFTRF and DFFTRB.

The present calculations have been performed on a Vax 11/780, in double precision, using the following steps:

[1] An initial guess for the inverse boundary correspondence function, τ_0, is made.

[2] The boundary functions z, z' and the argument of z', ϕ, as defined by 3.6 are computed at the values of τ_k.

[3] The integral equation 3.3 is then computed. This is accomplished using an FFT to approximate the integrand of 3.3. Then the conjugate integral operator is applied. Finally an inverse FFT is applied to obtain a discrete representation of the function ω_k.

[4] Using the results of steps 2 and 3, q_k is then computed from 3.4.

[5] The conjugate integral operator is then applied to q_k.This is accomplished using an FFT and its inverse is also obtained as outlined in step 3.

[6] The normalization constant, defined by 3.7, is then computed, using 3.8 and 3.9.

[7] The final step is to use the results of steps 2 through 6 to compute η_k, given by 3.10, and then update the inverse boundary correspondence function, 3.11.

If a good initial guess is provided, the Wegmann method converges quadratically. For the present application of grid generation, the scheme requires typically 5 iterations. Therefore, the coupling of the FFT's with the quadratic convergence

rate makes this scheme very efficient.

3.2: Validation of the simply connected Wegmann method

The code has been validated by computing the inverse boundary correspondence function for an inverted ellipse defined by:

$$z(s) = (1-(1-p^2)\cos^2 s)^{\frac{1}{2}} \exp(is) \qquad 3.12$$

for $0 < p < 1$. In this case the boundary correspondence function may be determined exactly. From Gaier [6], the solution of the inverse boundary correspondence function is given by:

$$\tan(\theta) = p\tan(\tau) \qquad 3.13$$

Table I shows the maximum value of the absolute errors for the inverse boundary correspondence function defined by setting $p = 0.6$ in 3.12. Here, N and k represent the number of points used to discretize the circle and the number of iterations respectively. These error results have the characteristic properties of the results found by Wegmann [1], for the inverted ellipse. Table I also illustrates the quadratic convergence rate of the scheme.

The Wegmann scheme has also been used to compute the inverse boundary correspondence functions for regions bounded by ellipses. The boundary curves defining the ellipses are written in terms of holomorphic functions. These are given in Section 5. The sensitivity of the scheme to the functional form of description of the boundaries is also discussed in Section 5. Once the IBCF's are determined, the conformal maps are computed using the Cauchy Integral Theorem, see Henrici [5], given by:

$$g(z) = \int_0^1 \frac{g(e^{2\pi it})}{1-e^{-2\pi it}z}dt \qquad 3.14$$

Equation 3.14 is approximated by a series, using an FFT to compute the coefficients of the series. The series is then evaluated at the grid points in the computational domain by applying the Horner summation technique: Burden and Faires [7].

Figures 1 and 2 show the grids generated using the Wegmann method for simply connected elliptic regions of aspect ratio 2 and 3. Figure 3 shows the computational domain for these examples. Recall that this rectangle is mapped onto the elliptical regions by composing the exponential map with the Wegmann map.

4.0 DOUBLY CONNECTED WEGMANN METHOD

The doubly connected Wegmann method [3] is a generalization of the simply connected scheme. In this case, the canonical region for the conformal map is the unit annulus, with interior radius μ. This scheme requires the solution of two inverse boundary correspondence problems computed simultaneously, one for each boundary of the physical region. Furthermore, the value of the interior radius of the canonical annulus must be determined.

Since the Wegmann method for annular regions is a generalization of the simply connected method, the iterative steps are not outlined in the present study, but may be found in reference [3]. It should be noted, however, that Wegmann tested two versions of the scheme. These versions differ in the iterative method used to compute the inner radius of the annulus, μ. All the numerical experiments presented in this section are based on Wegmann's first scheme. The first method is applied since its convergence properties have been justified rigorously, while there is less mathematical justification for the convergence properties of the second scheme.

The doubly connected scheme has been implemented numerically using FFT's to approximate the periodic functions and their corresponding conjugate integral

operators. As with the simply connected method, the calculation is initiated by providing a guess for the IBCF's, $\tau_{1,0}$, and $\tau_{2,0}$. The subscripts 1 and 2 denote the outer and inner inverse boundary correspondence functions respectively. With good initial guesses for the IBCF's and the interior radius, the doubly connected Wegmann method converges quadratically.

To validate the doubly connected Wegmann method, the inverse boundary correspondence functions have been computed for the annular region defined by the curves:

$$z_1(s) = \exp(is), \tag{4.1}$$

and,

$$z_2(s) = A + B\exp(is) \tag{4.2}$$

for $0 < A, B < 1$. The conformal map carrying the unit annulus onto this region is given by

$$f(z) = \frac{jz + \ell}{mz + n} \tag{4.3}$$

where the constants j, ℓ, m, and n may be determined from the coordinates of the center of the circles. Thus, the inverse boundary correspondence functions for this example may be computed easily from 4.3.

Table 2 shows the maximum value of the absolute errors for the IBCF's defined for the non--concentric region for $A = 0.2$ and $B = 0.5$. These results are again similar to the results of Wegmann [3] for this region. As in Table 1, N and k represent the number of points used to discretize the boundaries and the number of iterations respectively. The error results are presented in pairs: the first number corresponds to the error on the outer boundary, while the second number corresponds to the error on the inner boundary.

The Wegmann method has also been applied to compute the boundary correspondence functions for annular elliptic regions. The functions used to define the boundaries of the elliptic regions are given in Section 5. Once the IBCF's are computed, the conformal maps are computed using the Cauchy Integral Theorem. For the annular domains, two Cauchy integrals are needed to approximate the conformal map on the interior of the annulus. One integral is defined on each boundary of thc canonical annulus. These integrals are approximated using series, computing the coefficients with FFT's. The Horner summation scheme is then applied to evaluate the truncated series at the grid points in the computational domain.

Figure 4 shows an annular elliptic region with outer boundary of aspect ratio 2. The corresponding region in the computational domain is rectangular with $a = 0$, $b = \pi/2$, and $c = 0.42$, in 2.2. Recall that the conformal map from the rectangular computational domain onto the elliptic region is obtained by composing the exponential map with the Wegmann map. Figure 5 shows a thin annular elliptic region with outer boundary of aspect ratio 3. In this case $a = 0$, $b = \pi/2$, and $c = 0.09$ in 2.2.

5.0 PRACTICAL LIMITATIONS OF THE WEGMANN METHOD

In the preceding sections, the Wegmann methods were shown to be extremely powerful techniques to generate the conformal coordinate transformations for simply and doubly connected regions. Using FFT's and the Horner summation scheme, the overall Wegmann grid generation method requires $O(N \log N)$ computations, where N is the number of discretization points on the boundary of the computational domain. (The operation bound is based on the assumption that the total number of grid points is less than the value of N.) This order of computations is an improvement over standard integral techniques which typically require $O(N^3)$ computations. The

standard integral approach is to compute the inverse coordinate map, and then approximate the desired map using an interpolative process. As an example of an integral approach for the inverse map, see Symm [8].

The Wegmann technique is also more efficient than the numerical method developed by Fornberg, [9], [10], and [11]. For simply connected domains the Wegmann scheme is approximately seven times more efficient than the Fornberg scheme (Wegmann [11]). For doubly connected domains, the Wegmann method is even more efficient than this, since it converges quadratically while the Fornberg method converges linearly. It may be the case that the Fornberg method is easier to code than the Wegmann method. It may also be the case that the Fornberg method is easier to apply to an arbitrary region with a smooth boundary, since the Wegmann method is sensitive to the initial guess for the inverse boundary correspondence function.

Some limitations of the Wegmann method determined during the numerical experiments will now be discussed. A basic limitation of the Wegmann method is in the choice of functions used to describe the boundaries of physical regions. In general, Wegmann [1, 2, 3] showed that a function with Hölder continuous derivatives may be used to generate the inverse boundary correspondence function needed to construct the desired conformal mapping. However, if simple smooth polar expressions of the form:

$$z(\theta) \;=\; \rho(\theta)\exp(i\theta), \tag{5.1}$$

are used to represent the boundary of the physical region, the Wegmann method does not necessarily converge. The difficulty is that, although the first three derivatives of z are Hölder continuous, they may become large. This forces the initial guess for the Wegmann technique to be very good and, in general, a very good

initial guess is not available.

The polar form of the boundary functions has been implemented for simply and doubly connected elliptic regions. Several initial guesses based on linear and non-linear functions for the inverse boundary correspondence function have been tried in conjunction with the polar representation. In all cases the Wegmann method fails to converge.

In order for the Wegmann method to converge without a good initial guess, holomorphic (complex, analytic) functions are used to describe the boundaries of the physical region. In the case of the simply and doubly connected elliptic regions the map:

$$\alpha \sin(-\theta + i\rho) \tag{5.2}$$

has been used to represent the boundaries of the regions. Here α and ρ are real numbers and the variable θ is defined in the interval $[0, 2\pi]$. Figure 6 shows the first derivative with respect to θ of the holomorphic and polar representations for an aspect ratio 2 ellipse. Clearly, the derivative of the holomorphic function does not fluctuate as much as the derivative of the polar representation. It should be noted that the holomorphic representation must satisfy the Cauchy–Riemann equations whereas the polar representation does not.

In contrast to the polar form, the holomorphic form with an initial guess of:

$$\tau(\theta) \;=\; \theta, \tag{5.3}$$

almost always converges. For the simply connected method, regions with aspect ratio up to 4 have been run successfully.

In the case of the doubly connected method, an initial guess for the inner radius, μ, of the canonical annulus is also required. When a good guess for μ is

given the doubly connected Wegmann method works very well. However, for a case where the outer ellipse had an aspect ratio of 2 and the inner ellipse had an aspect ratio of 10 the scheme failed to converge.

In an attempt to improve the performance of the Wegmann method in such cases an intermediate conformal mapping, J, is introduced to precondition the physical space. Let P denote the doubly connected physical region. Let I denote the image of P under the map J. The goal is to use the Wegmann method to construct the conformal map from a canonical annular region, C, onto I, and then apply the inverse map J^{-1} to obtain the desired conformal map from the canonical domain onto the physical region. This preconditioning has been used successfully. For the present example, the preconditioning map is the inverse Joukowski map defined by

$$J(z) = \frac{z}{2} \pm \sqrt{\frac{z^2}{2} + \gamma^2} \qquad 5.4$$

where γ is a function of the dimensions of the inner elliptic boundary. The inverse Joukowski map carries the inner elliptic boundary onto a circle. The outer ellipse is mapped onto a curve which is closer to a circle than the initial outer curve. Figure 7 shows the image of the annular region under the inverse Joukowski map.

The second limitation of the Wegmann method involves the number of discretization points needed for regions bounded by high aspect ratio curves. The problem of determining a conformal mapping numerically generally leads to an ill-posed computation. One cause of this is the local angle preservation of conformal maps. In simply connected regions bounded by high aspect ratio curves, the local orthogonality forces evenly spaced discretization points in the computational domain to be crowded together in the given region. The crowding phenomenon causes the ill-posed numerical properties seen in computing the conformal maps.

Figures 8 and 9 show the crowding of the boundary discretization points for the simply connected elliptic regions of aspect ratio 2 and 3, respectively. Clearly, as the aspect ratio of the boundary curve for a simply connected domain increases, the crowding phenomenon becomes more severe.

The Wegmann method works well in determining the solution of the boundary correspondence problem for simply connected elliptic regions. However, as the aspect ratio increases, the number of terms needed in the series approximation of the desired conformal map also increases. Table 3 shows the maximum error found on the boundaries of the ellipses as a function of aspect ratio, and the number of terms used in the series approximation. The error shown in Table 3 is defined by evaluating the series approximation of the conformal map at points on the boundary of the canonical domain and substituting the result into the expression:

$$\text{Error} \quad = \quad |F(x,y) - 1|, \tag{5.5}$$

where $F(x,y)$ is defined by,

$$F(x,y) \quad := \quad \frac{x^2}{a} + \frac{y^2}{b}. \tag{5.6}$$

Table 3 shows that a large number of terms are required in the approximating series as the aspect ratio of the domain increases. Therefore, these error results suggest that the Wegmann grid generation technique is practical to apply to simply connected elliptic regions of aspect ratio less than 4. For elliptic regions of aspect ratio greater than 4, it may be possible to apply preconditioning to reduce the number of terms required in the approximating series. However, this form of preconditioning has not been attempted in the present study.

The severe crowding phenomenon exhibited by the conformal maps for simply connected regions has not been observed for the doubly connected regions. The

elliptic annular regions for which the Wegmann method has been tested show little or no crowding effects. Figure 10 shows the image of the discretized points for a typical annular elliptic region. The lack of crowding suggests that the annular elliptic regions may be approximated with fewer terms than required by a simply connected region of the same outer aspect ratio.

6.0 SUMMARY

This paper has presented numerical experiments for the implementation of the mapping techniques of Wegmann. Through the use of FFT's this method requires $O(N \log N)$ operations. In addition, the technique is quadratically convergent. Several examples for both simply and doubly connected regions have been examined. In particular elliptic regions have been considered. The Wegmann techniques have been shown to work for high aspect ratio elliptic regions. However, the main practical limitation of these methods for both simply and doubly connected regions has been found experimentally to be the functional form used to represent the boundaries. For general regions, the Wegmann method works well if the boundaries are represented by holomorphic functions. However, the methods may not converge at all if a general smooth polar representation is used without a very good initial guess.

In spite of these limitations the Wegmann method is more efficient than other conformal mapping techniques. A further application of this scheme is in the development of conformal maps for single and double elements airfoils. For this case it is necessary to compute the maps on the exterior of a domain. A comparison between the Wegmann technique and other existing methods for this problem is being undertaken by the authors.

7.0 ACKNOWLEDGEMENTS

This work was supported by NASA Langley Research Center under NASA Grant NAG–1- -657. The technical monitor is Dr. J. M. Seiner. The authors are grateful to Mr. Paolo Dini of the Pennsylvania State University for providing the graphical representations of the grids.

REFERENCES

[1] WEGMANN, R., "An Iterative Method for Conformal Mapping," *Numerical Conformal Mapping*, (ed. Trefethen, L. N.), North-Holland (1986), pp. 7-18.

[2] WEGMANN, R., "Convergence Proofs and Error Estimates for an Iterative Method for Conformal Mapping," *Numer. Math.*, Vol. 44 (1986), pp. 435–446.

[3] WEGMANN, R., "An Iterative Method for the Conformal Mapping of Doubly Connected Regions," *Numerical Conformal Mapping* (ed. Trefethen, L. N.), North- Holland (1986), pp. 79-98.

[4] BATY, R. S. and MORRIS, P. J. "Instability of Jets of Arbitrary Geometry," *AIAA Paper* 89–1796 (1989).

[5] HENRICI, P., *Applied and Computational Complex Analysis, Vol. 3*, John Wiley and Sons (1986).

[6] GAIER, D., *Konstruktive Methoden der Konformen Abbildung*, Springer– Verlag (1964).

[7] BURDEN, R. L. and FAIRES, J. D., *Numerical Analysis*, 3rd Edition, Prindel, Weber and Schmidt (1985).

[8] SYMM, G.T., "An Integral Equation Method in Conformal Mapping," *Numer. Math.*, Vol. 9 (1966), pp. 250–258.

[9] FORNBERG, B., "A Numerical Method for Conformal Mappings," *SIAM J. Sci. Stat. Comput.*, Vol. 1 (1980), pp 386–400.

[10] FORNBERG, B., "A Numerical Method for Conformal Mapping of Doubly Connected Regions," *SIAM J. Sci. Stat. Comput.*, Vol. 5 (1984) pp. 771-783.

[11] WEGMANN, R., "On Fornberg's Numerical Method for Conformal Mapping," *SIAM J. Numer. Anal.*, Vol. 23 (1986) pp. 1199–1213.

k	$N = 64$	$N = 128$	$N = 256$	$N = 512$
1	2.6(-2)	2.6(-2)	2.6(-2)	2.6(-2)
2	2.7(-4)	2.8(-4)	2.8(-4)	2.8(-4)
3	8.0(-8)	3.2(-8)	3.2(-8)	3.3(-8)
4	9.4(-9)	6.0(-14)	4.5(-15)	3.5(-15)
5	1.6(-9)	1.0(-14)	8.5(-15)	6.5(-15)

Table 1: Error results for the inverse boundary correspondance function of the inverted ellipse based on the simply connected Wegmann scheme.

k	$N = 64$	$N = 128$	$N = 256$	$N = 512$
1	2.2(-1), 1.8(-1)	2.2(-1), 1.8(-1)	2.2(-1), 1.8(-1)	2.2(-1), 1.8(-1)
2	1.4(-2), 6.9(-3)	1.4(-2), 6.9(-3)	1.4(-2), 6.9(-3)	1.4(-2), 6.9(-3)
3	8.3(-5), 4.1(-5)	8.4(-5), 4.1(-5)	8.4(-5), 4.1(-5)	8.4(-5), 4.1(-5)
4	2.1(-9), 2.5(-7)	2.1(-9), 2.6(-7)	2.2(-9), 2.6(-7)	2.2(-9), 2.6(-7)
5	1.4(-9), 3.4(-7)	1.4(-9), 3.6(-7)	1.4(-9), 3.6(-7)	1.4(-9), 3.6(-7)

Table 2: Error results for the boundary correspondance functions of the non–concentric annular region based on the doubly connected Wegmann scheme.

N	AR = 2	AR = 3	AR = 4
16	1.68(-1)	NC	NC
32	3.52(-2)	NC	NC
64	4.49(-3)	2.21(-1)	NC
128	1.62(-4)	1.18(-1)	NC
256	1.95(-7)	4.68(-2)	NC
512	1.30(-12)	7.31(-3)	1.81(-1)
1024	NC	1.06(-3)	1.10(-1)
2048	NC	4.81(-5)	5.60(-2)

Table 3: Maximum error found on the boundaries of simply connected regions of aspect ratio AR as a function of the number of terms in the series approximation. NC denotes not computed.

Figure Captions

Figure 1. An example grid for a simply connected region bounded by an aspect ratio 2 ellipse.

Figure 2. An example grid for a simply connected region bounded by an aspect ratio 3 ellipse.

Figure 3. The computational space for the Wegmann maps for the aspect ratio 2 and 3 ellipses.

Figure 4. An example grid for a doubly connected region with an outer boundary defined by an aspect ratio 2 ellipse.

Figure 5. An example grid for a doubly connected thin region with an outer boundary defined by an aspect ratio 3 ellipse.

Figure 6. Comparison of the derivatives of the boundary representations. The holomorphic case is denoted by the dot–line curve. The polar case is denoted by the dotted curve.

Figure 7. The image of an annular region with an elliptic outer boundary of aspect ratio 2 and an elliptic inner boundary with aspect ratio 10, under the action of the J map.

Figure 8. Plot of the IBCF for the aspect ratio 2 ellipse with $N = 64$.

Figure 9. Plot of the IBCF for the aspect ratio 3 ellipse with $N = 64$.

Figure 10. Plot of the IBCF for the ellipses of aspect ratio 2 and 3 with $N = 64$.

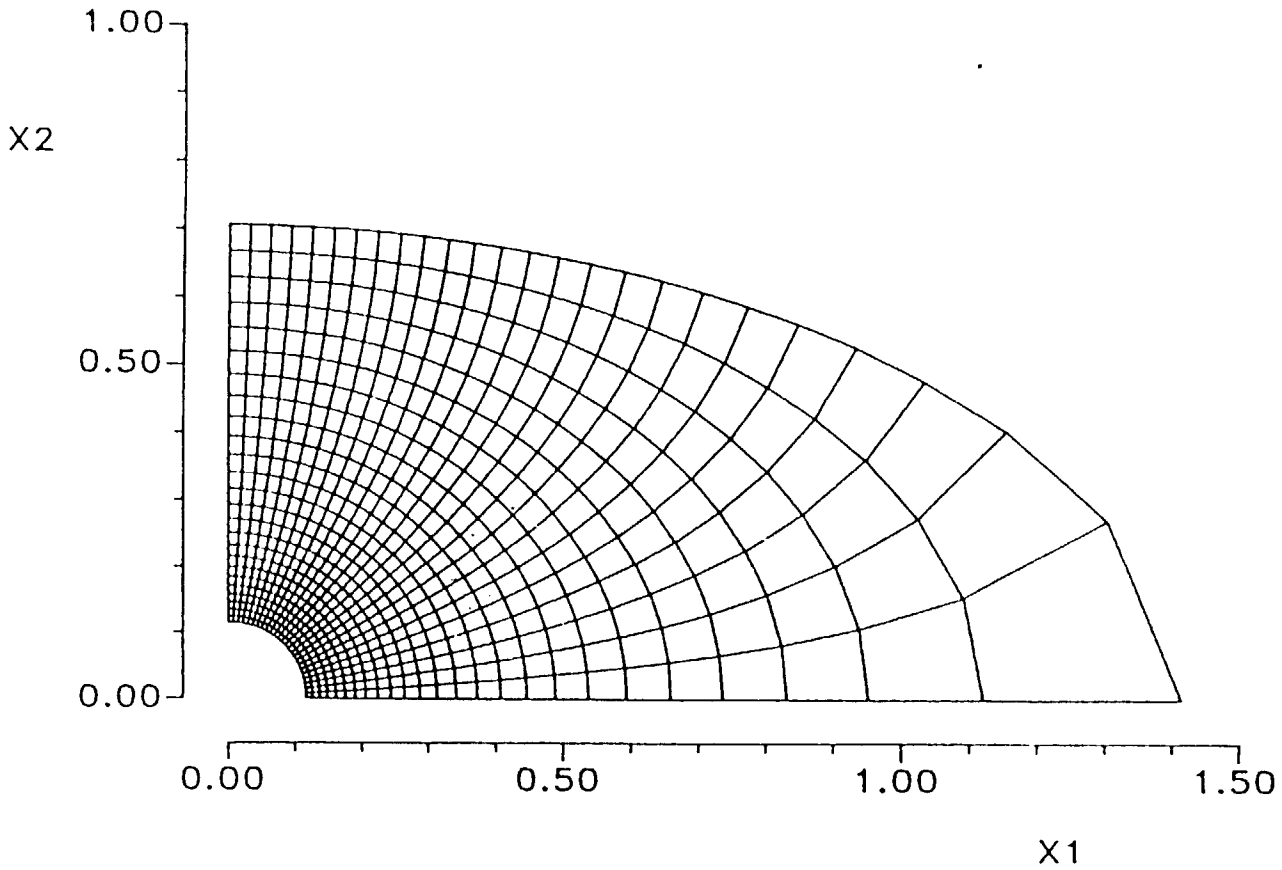

Figure 1. An example grid for a simply connected region bounded by an aspect ratio 2 ellipse.

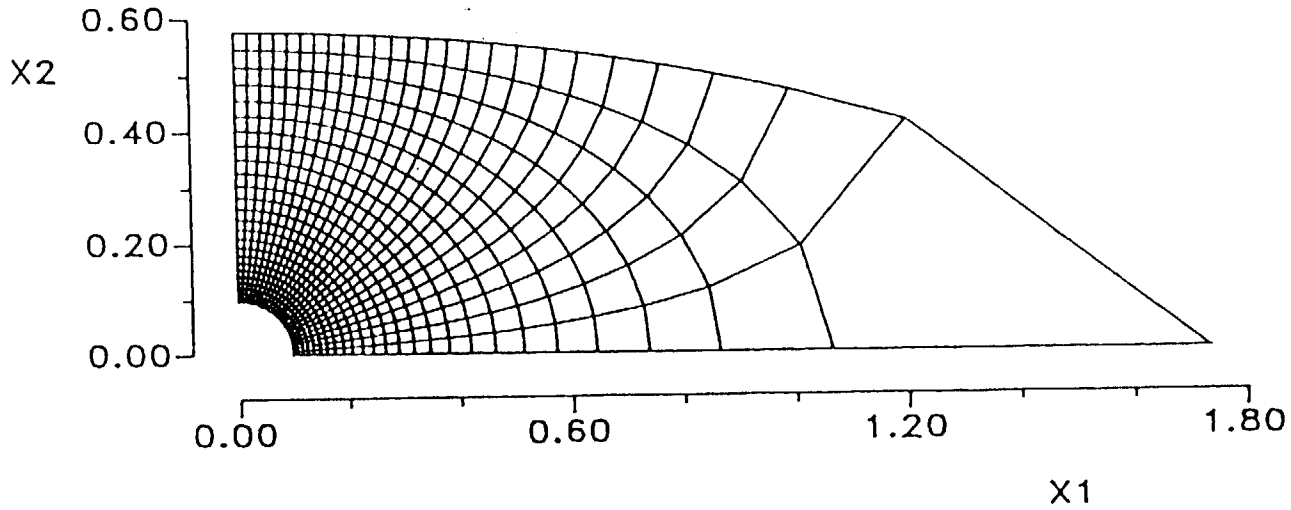

Figure 2. An example grid for a simply connected region bounded by an aspect ratio 3 ellipse.

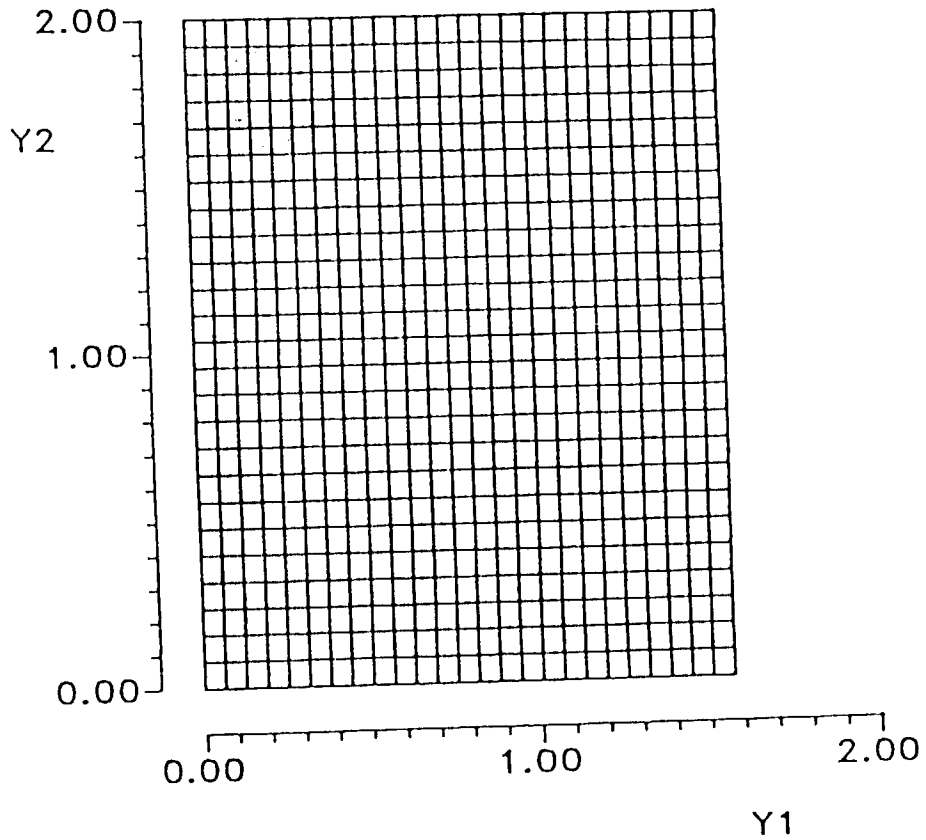

Figure 3. The computational space for the Wegmann maps for the aspect ratio 2 and 3 ellipses.

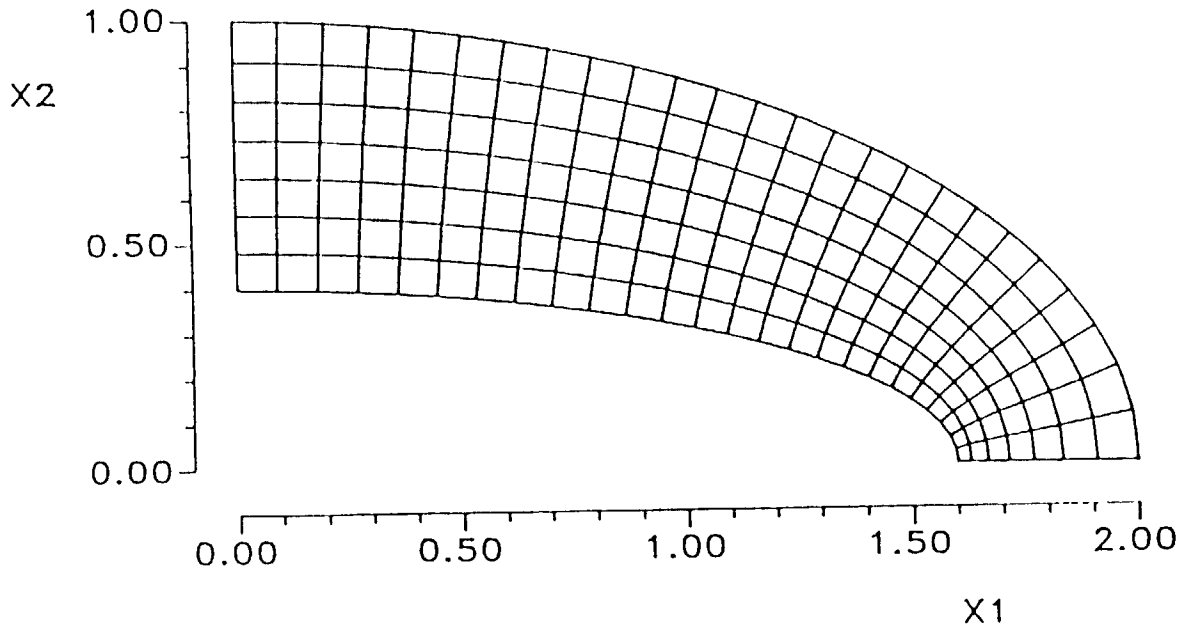

Figure 4. An example grid for a doubly connected region with an outer boundary defined by an aspect ratio 2 ellipse.

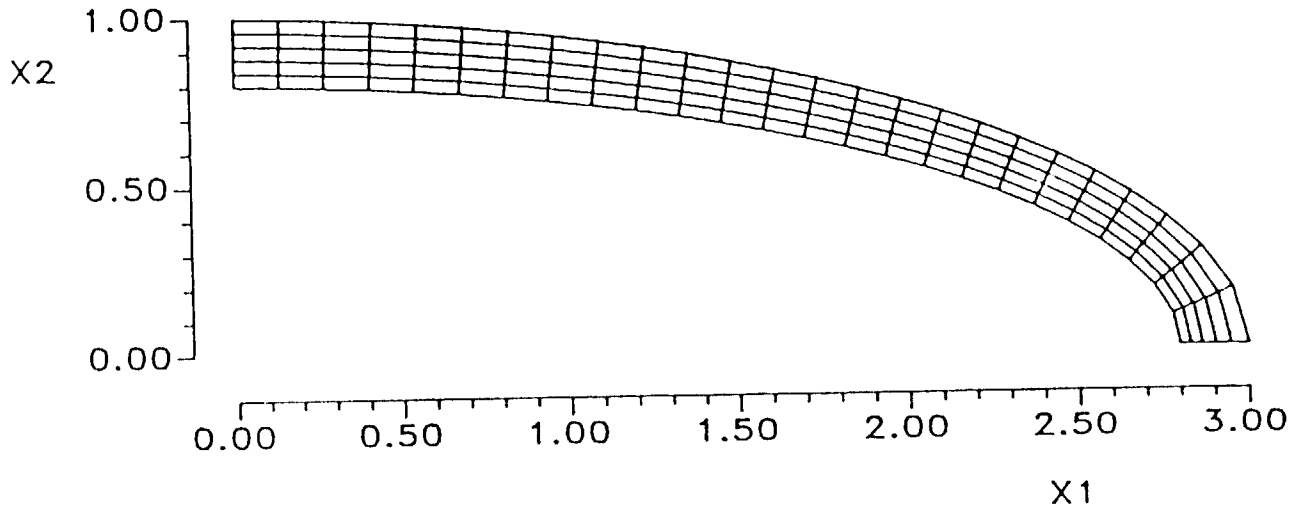

Figure 5. An example grid for a doubly connected thin region with an outer boundary defined by an aspect ratio 3 ellipse.

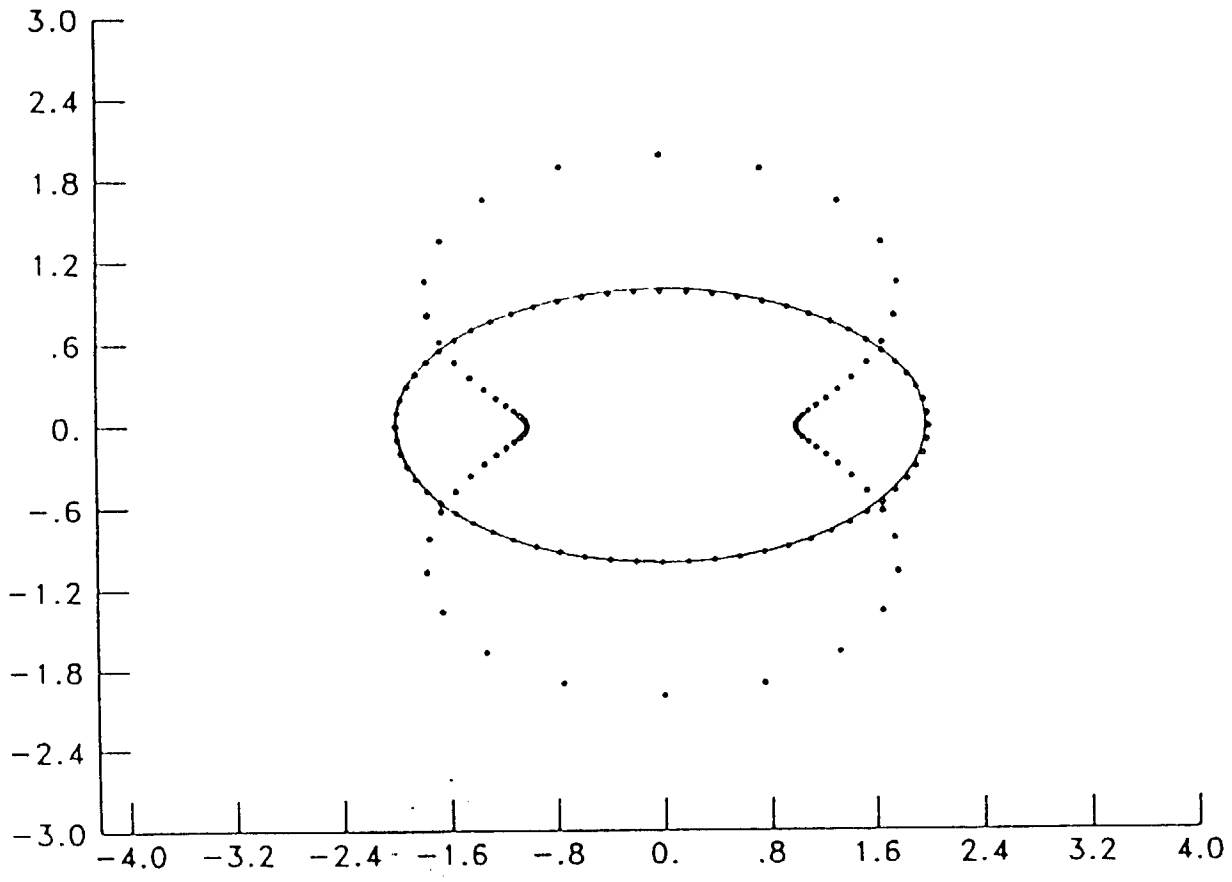

Figure 6. Comparison of the derivatives of the boundary representations. The holomorphic case is denoted by the dot–line curve. The polar case is denoted by the dotted curve.

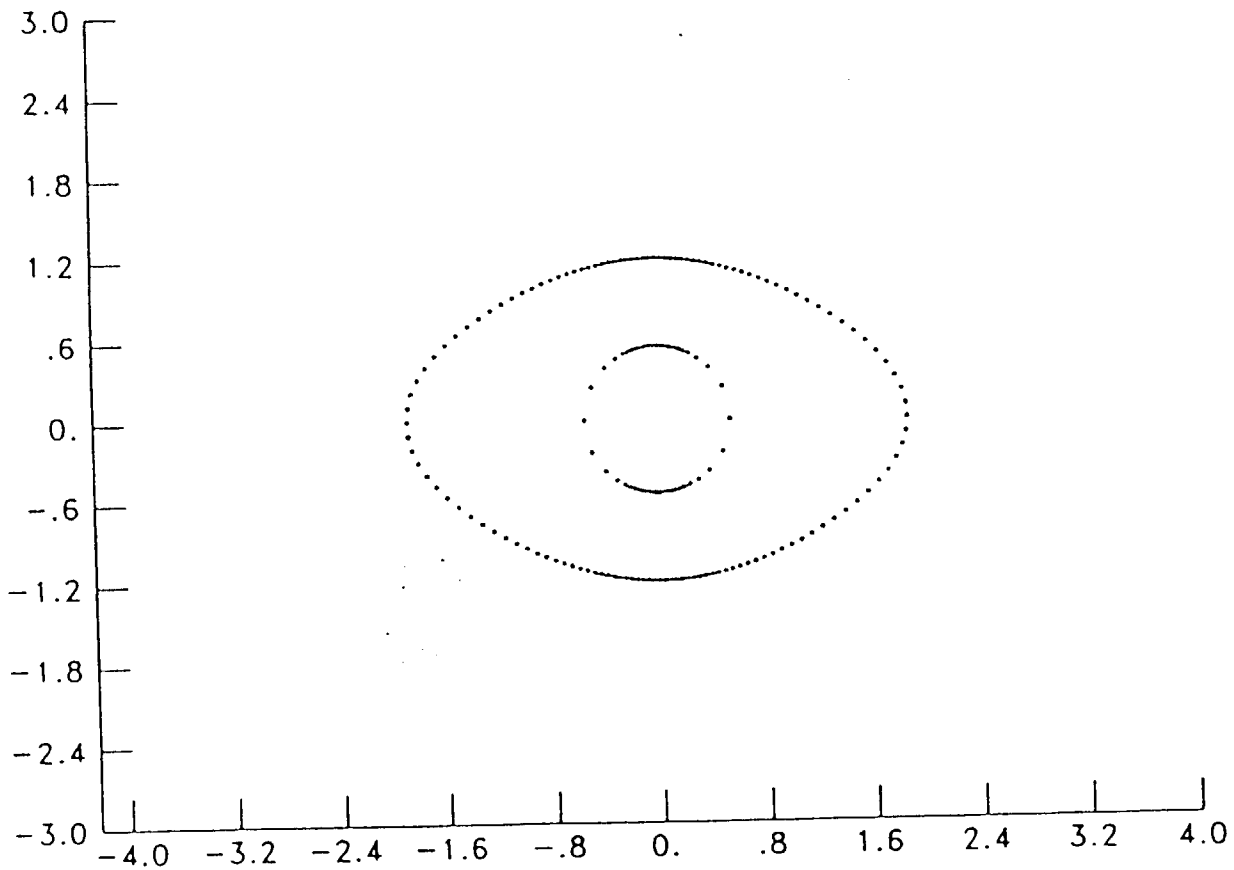

Figure 7. The image of an annular region with an elliptic outer boundary of aspect ratio 2 and an elliptic inner boundary with aspect ratio 10, under the action of the J map.

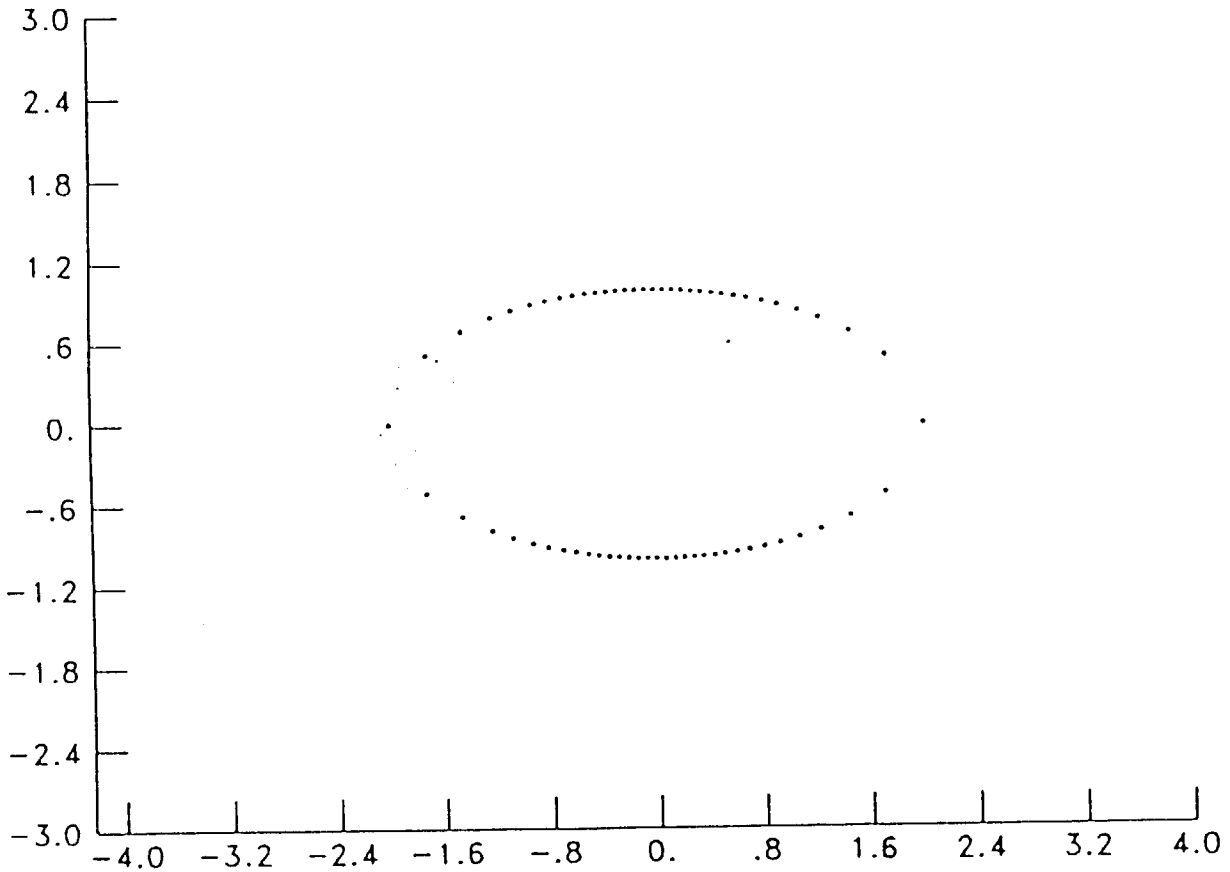

Figure 8. Plot of the IBCF for the aspect ratio 2 ellipse with $N = 64$.

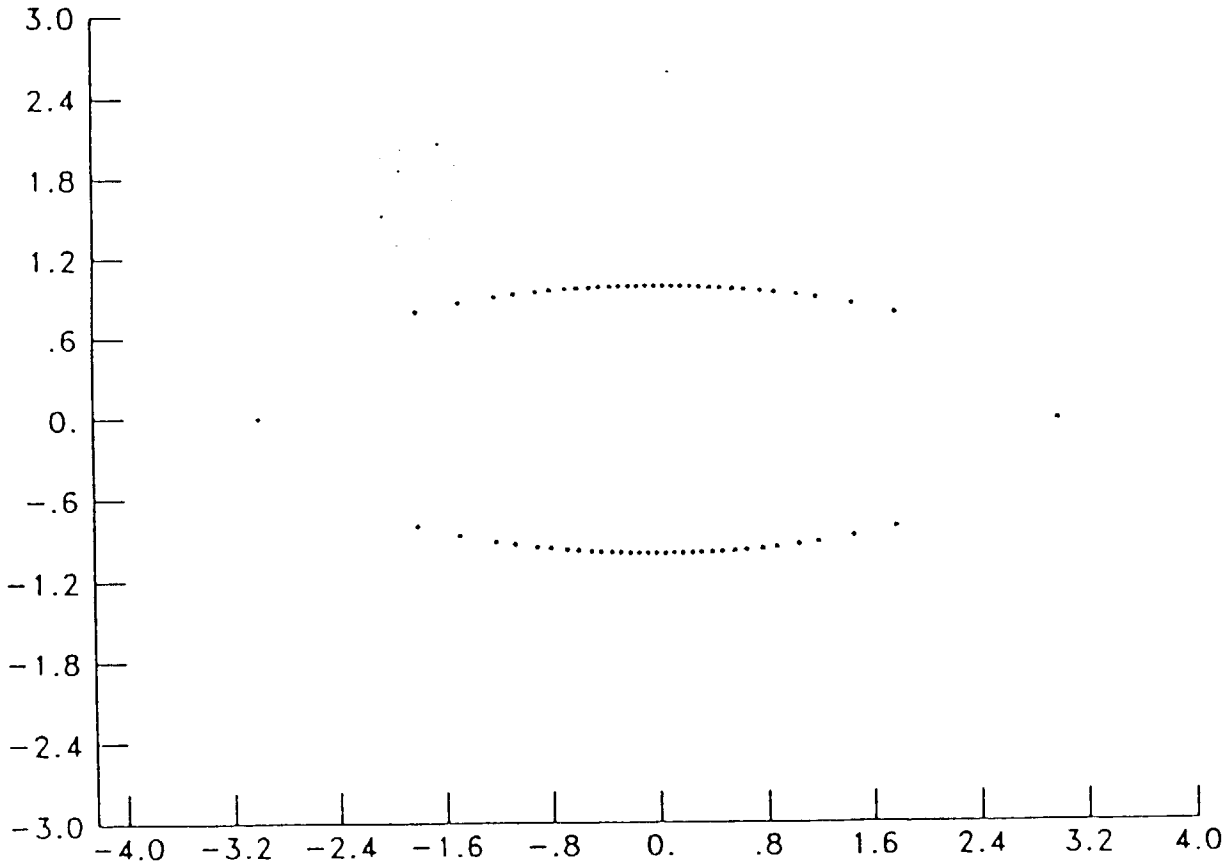

Figure 9. Plot of the IBCF for the aspect ratio 3 ellipse with $N = 64$.

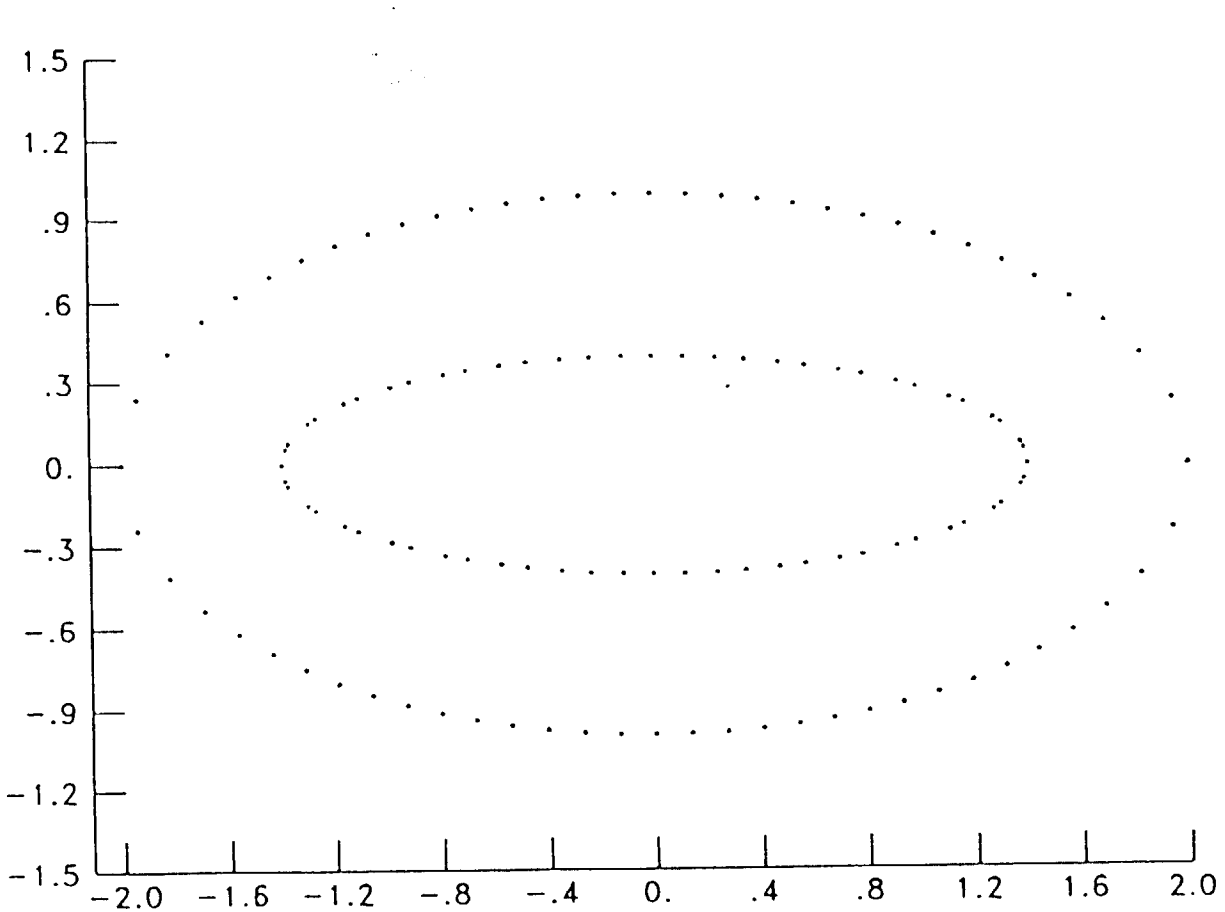

Figure 10. Plot of the IBCF for the ellipses of aspect ratio 2 and 3 with $N = 64$.

Chapter 5

Instability of Jets of Arbitrary Geometry

Roy S. Baty and P. J. Morris

INTENTIONALLY

INSTABILITY OF JETS OF ARBITRARY GEOMETRY

Roy S. Baty† and Philip J. Morris*
The Pennsylvania State University, University Park, PA 16802

ABSTRACT

This paper describes a calculation technique for determining the stability of jets of arbitrary cross section. In particular, elliptic and rectangular jets are considered. The numerical procedure involves both a conformal transformation between the computational domain and the physical plane and a solution of the transformed stability equation in the computational domain. Modern, efficient, conformal mappings are used for both simply and doubly connected domains. The numerical solution is based on a finite difference/pseudospectral discretization of the stability equation. The technique is verified by comparison with previous calculations for circular and elliptic jets. Calculations are performed for the stability of elliptic and rectangular jets of aspect ratio 2. Growth rates, phase velocities, and pressure eigenfunctions are calculated.

1. INTRODUCTION

This study is motivated by the authors' interest in turbulent mixing in free shear flows. It is now generally acknowledged that the mixing process is dominated by the dynamics of large scale coherent structures. In addition, the local properties of these structures may be modeled by a linearized analysis. This has been demonstrated in the experiments and analysis of excited free shear layers and jets by Gaster, Kit and Wygnanski[1] and Petersen and Samet[2]. Tam and Morris[3,4] made use of instability wave models of the large scale structures to predict the noise radiation from supersonic shear layers and the development of excited jets. In addition, Liou[5] and Morris and Giridharan[6] have developed Reynolds stress closure schemes in which the unknown turbulent stresses are described by solutions of the local stability equation.

The present paper is concerned with the instability of jets of arbitrary cross sections. This analysis is an essential component in the extension of some of the analyses of turbulent flows described above to more complex geometries. Non–circular jets have been observed to have enhanced mixing properties over circular jets. This makes their use attractive as injectors in combustors. Schadow et al[7] demonstrated this improved mixing using an elliptical jet in a dump combustor. Rectangular jets have applications in thrust–vectoring/thrust–reversing engine nozzles for future fighter aircraft.

The stability of elliptic jets has been studied by Crighton[8] and Morris[9]. In the former case a vortex sheet representation of the jet flow was used. In the latter case more realistic, finite thickness, shear layers were considered where the analytic description of the mean flow enabled separable solutions of the stability equation to be found in elliptic cylindrical coordinates. Koshigoe and Tubis[10,11] used both a finite element and finite difference approach to consider the stability of jets of elliptic and triangular cross sections.

In the present paper we describe efficient algorithms to compute the stability of non–circular jets. These techniques are applied to elliptic and rectangular jets. These results are a partial summary of a doctoral dissertation of one of the authors (RSB)[12]. In the next section the numerical methods are described. This involves a conformal mapping technique for simply and doubly connected domains and a hybrid finite–difference/pseudospectral solution of the stability equation. The stability characteristics of elliptic and rectangular jets are then given in the form of the variation of the growth rates and phase velocities with instability wave frequency and eigenfunctions for the most unstable modes.

2.0 ANALYSIS AND COMPUTATIONS

A jet flow is considered issuing from a nozzle of arbitrary cross section. The governing equation is given in Cartesian coordinates, (x, y, z). The axis of the jet is aligned with the z direction and the axial mean velocity is denoted by $W(x, y)$. The mean velocity components in the x and y directions are neglected. This is the parallel flow approximation of hydrodynamic stability. If the parallel flow assumption is not applied and the effects of flow divergence are considered, a problem results which requires a multiple–scales analysis. These effects are not considered in the present study.

A linear, elliptic, partial differential equation for the pressure is obtained by taking the divergence of the

---

† NASA Graduate Student Researcher, Department of Aerospace Engineering, Student Member, AIAA

* Professor, Department of Aerospace Engineering, Member AIAA.

momentum equation and using the equation of continuity. The resulting equation is linearised about the mean flow. The velocity fluctuations are eliminated in favor of the pressure fluctuation using the linearised momentum equations. If the pressure fluctuation is written in the form:

$$p(x,y,z,t) = \hat{p}(x,y)e^{i\gamma}, \qquad (2.1)$$

where,

$$\gamma = \alpha z - \omega t,$$

and α is the axial wavenumber and ω is the instability wave frequency, then the equation for $\hat{p}$ may be written as:

$$(\Delta - \alpha^2)\hat{p} + \frac{2\alpha}{\omega - \alpha W}\nabla W \cdot \nabla \hat{p} = 0 \qquad (2.2)$$

Eqn. (2.2) is the Rayleigh equation governing the inviscid, incompressible, spatial stability of jets of arbitrary cross section. In order to determine the pressure $\hat{p}$, in eqn. (2.2), boundary conditions must be added. In this case, $\hat{p}$ satisfies:

$$\hat{p} \to 0 \quad \text{as} \quad |x| \to +\infty \qquad (2.3)$$

and

$$\hat{p} \quad \text{is finite as} \quad |x| \to 0 \qquad (2.4)$$

The computational goal in solving the stability problem defined by eqns. (2.2)–(2.4) is to determine the complex wavenumber spectrum for a given frequency, ω. Several difficulties arise in computing the wavenumbers or eigenvalues associated with the Rayleigh problem. Firstly, the wavenumber, α, appears nonlinearly in (2.2). This nonlinearity prevents the direct use of standard matrix eigenvalue calculation schemes. Secondly, if the stability analysis is used to model turbulent mixing in jet flows, the stability problem must be solved at a large number of cross sections in a given jet flow. Therefore, any scheme developed must be computationally very efficient.

2.1 The Generalized Rayleigh Equation

To consider jets of arbitrary geometry, conformal mappings are used to map standard computational domains onto realistic jet flow cross sections. Conformal mapping is analytically a very desirable technique, since these maps simplify the governing differential equation by generating a diagonal metric tensor. Therefore, conformal maps are applied to simplify the Rayleigh problem for a jet of arbitrary geometry.

Recently, very efficient schemes have been developed to determine the conformal maps from standard computational domains onto arbitrary regions in the plane. Wegmann[13,14,15] proposed a scheme to compute the conformal maps from canonical domains onto simply and doubly connected regions with smooth boundaries. This technique has been applied to determine the coordinate maps needed for a realistic elliptic jet flow cross section. For polygonal regions, Trefethen[16,17] has developed an efficient software package, SCPACK, to determine the conformal map and its inverse from the interior of a polygon onto the unit disc. SCPACK has been applied to determine the conformal maps needed in the study of a rectangular jet flow cross section. The details of the conformal grid generation techniques are given by Baty[12]. To apply conformal maps, the Rayleigh problem must be recast in general conformal coordinates. Let Cartesian coordinates be denoted by (x^1, x^2), and let the computational coordinates be denoted by (y^1, y^2). Now, let f denote a conformal map satisfying the following relations:

$$x^1 = Re(f(y^1 + iy^2)) \qquad (2.5)$$

and

$$x^2 = Im(f(y^1 + iy^2)) \qquad (2.6)$$

Applying eqns. (2.5)–(2.6), the Cauchy–Riemann equations, and the general tensor form of (2.2) then yields the generalised Rayleigh equation in terms of (y^1, y^2):

$$(\Delta - \hat{g}\alpha^2)\hat{p} + \frac{2\alpha}{\omega - \alpha W}\nabla W \cdot \nabla \hat{p} = 0 \qquad (2.7)$$

where

$$\hat{g} = |f'(y^1 + iy^2)|^2$$

2.2 The Hybrid Method

This section develops a hybrid numerical scheme to solve the inviscid, incompressible stability problem defined by eqn. (2.2). Hybrid techniques are numerical methods which combine series approximations with finite difference calculations. For two dimensional partial differential equations, such as the stability problem, hybrid methods generate discretisation matrices whose order varies linearly with the approximating series summation bound, N. This implies that the number of operations required to compute an eigenvalue of equation (2.2) is on the order of:

$$O(N^3) \qquad (2.8)$$

The estimate given by (2.8) is a great improvement over the number of operations required by spectral and pseudospectral methods. These series methods generate discretisation matrices from two dimensional series approximations and produce matrices whose size is proportional to:

$$(N+1)^2 \qquad (2.9)$$

Equation (2.9) implies that these methods require a number of operations on the order of:

$$O((N+1)^6) \tag{2.10}$$

to compute an eigenvalue of the Rayleigh problem. Furthermore, hybrid techniques have the advantage of increased accuracy over purely finite difference approaches. The accuracy of a hybrid scheme depends on the properties of the approximating series and on the accuracy of the finite difference scheme. The present study uses a pseudospectral series to develop a hybrid scheme.

A pseudospectral series assumes that the function to be approximated is known, or may be computed, on a fixed set of points in the computational domain. This information is then used with an appropriate set of basis functions to form a finite series approximating the function. Basing the function's approximation on a known set of points defines a grid in the computational domain.

The hybrid method presented here is defined using a pseudospectral series based on the Chebyshev polynomials. The details of the pseudospectral technique come from the one dimensional pseudospectral theory in Gottlieb et al[18].

To outline the method, consider the Rayleigh eqn. (2.8). Assume that the function to be approximated may be represented in a series of the form:

$$\hat{p}(y^1, y^2) \approx \sum_{i=0}^{N} a(y_i^1, y^2) f_i(y^1) \tag{2.11}$$

Here y^1 represents the azimuthal variation, while y^2 represents the radial variation in an arbitrary jet cross section. In eqn. (2.11), the coefficients $a(y_i^1, y^2)$, are functions of the grid points defined by:

$$y_j^1 = \cos(\frac{\pi j}{N}) \quad \text{for} \quad j = 0, 1, 2, \ldots, N \tag{2.12}$$

and the radial direction, y^2. Moreover, the basis functions, f_i, are rational functions defined by:

$$f_j(y^1) = \frac{((1-(y^1)^2)T_N'(y^1)(-1)^{j+1})}{c_j N^2 (y^1 - y_j^1)} \tag{2.13}$$

with

$$c_0 = c_N = 2$$

and

$$c_j = 1 \quad \text{otherwise.}$$

Here, $T_N'(y^1)$ is the derivative of the N^{th} order Chebyshev polynomial. Evaluating (2.13) at the grid points leads to the relation:

$$f_j(y_i^1) = \delta_{ji} \tag{2.14}$$

where δ_{ji} is the Kronecker delta.

Next, substituting eqn. (11) into the Rayleigh equation, yields:

$$\sum_{i=0}^{N} a(y_i^1, y^2) f_i''(y^1) + \sum_{i=0}^{N} a''(y_i^1, y^2) f_i(y^1) + \beta\left\{ \frac{\partial W}{\partial y^1} \sum_{i=0}^{N} a(y_i^1, y^2) f_i'(y^1) + \frac{\partial W}{\partial y^2} \sum_{i=0}^{N} a'(y_i^1, y^2) f_i(y^1) \right\} - \alpha^2 \sum_{i=0}^{N} a(y_i^1, y^2) f_i(y^1) = 0 \tag{2.15}$$

where

$$\beta = \frac{2\alpha}{\omega - \alpha W}$$

To simplify this equation, the derivatives of the approximating basis functions at the grid points must be determined. Reference 18 gives these derivatives as:

$$\left. \frac{d^p f_i(y^1)}{d(y^1)^p} \right|_{y^1 = y_j^1} = (D^p)_{ji} \tag{2.16}$$

where

$$(D^1)_{ji} = \frac{c_j(-1)^{i+j}}{c_i(y_j^1 - y_i^1)} \quad \text{if} \quad j \neq i \tag{2.17}$$

$$(D^1)_{jj} = \frac{-y_j^1}{2(1-(y_j^1)^2)} \tag{2.18}$$

$$(D^1)_{00} = \frac{2N^2+1}{6} \tag{2.19}$$

$$(D^1)_{NN} = -(D^1)_{00} \tag{2.20}$$

and where

$$(D^p) = (D^1)^p \tag{2.21}$$

Now, combining eqns. (2.16)–(2.21), eqn. (2.15) and applying eqn. (2.14) produces a system of linear, second ordinary differential equations in terms of the coefficients:

$$a''(y_k^1, y^2) + \{\frac{2\alpha}{\omega - \alpha W}\} \frac{\partial W}{\partial y^2} a'(y_k^1, y^2) - \hat{g}\alpha^2 a(y_k^1, y^2) + \sum_{i=0}^{N} a(y_i^1, y^2)(D^2)_{ki} + \{\frac{2\alpha}{\omega - \alpha W}\} \frac{\partial W}{\partial y^1} \sum_{i=0}^{N} a(y_i^1, y^2)(D^1)_{ki} = 0 \tag{2.22}$$

The eqns. (2.22) are then recast as a collection of first order systems. This collection of systems of first order equations can then be recast as a matrix equation with the unknown vector being the coefficients of the approximating series. The resulting matrix equation may be integrated once the boundary conditions are determined and added to the matrix equation.

2.3 The Boundary Conditions

In order to evaluate numerically the discretisation matrix associated with the Rayleigh equation, the boundary conditions must be included. In the region outside of the mixing layer, the velocity is constant, reducing the Rayleigh equation into the Helmholtz equation:

$$(\Delta - \hat{g}\alpha^2)\hat{p} = 0 \qquad (2.23)$$

Following Batchelor and Gill[19], the general solution of eqn. (2.23) in polar coordinates for the exterior region is given by:

$$\sum_{n=0}^{\infty} \left(A_n H_n^1(i\alpha r) + B_n H_n^2(i\alpha r)\right) \exp(in\theta) \qquad (2.24)$$

where H_n^1 and H_n^2 denote Hankel functions of the first and second kind respectively. Using the condition, (2.3), that the pressure must approach zero as r approaches infinity, implies that the boundary condition on the outer edge of the jet flow cross section is of the form:

$$\hat{p} = \sum_{n=0}^{\infty} A_n H_n^1(i\alpha r) \exp(in\theta) \qquad (2.25)$$

Moreover, since the pressure must be bounded as r approaches zero, condition (2.4), the boundary condition at the inner edge of the jet flow cross section becomes:

$$\hat{p} = \sum_{n=0}^{\infty} B_n J_n(i\alpha r) \exp(in\theta) \qquad (2.26)$$

where J_n is the Bessel function of the first kind. Next, the physically realisable azimuthal terms are determined in order to simplify eqns. (2.25)–(2.26). All the jet geometries to be computed in this study are symmetrical about both the horizontal and vertical axes in the plane. Thus, from Morris[9], the possible pressure variations in the azimuthal direction correspond respectively to four classes of functions depending on symmetries about the major and minor axes. This then gives the general solution for the physically possible boundary solutions. The resulting infinite series defining the pressure boundary conditions on the edges of the shear layer cross section become:

$$\sum_{n=0}^{\infty} A_n C_n(i\alpha r) \cos(2n\theta) \qquad (2.27)$$

$$\sum_{n=0}^{\infty} A_n C_n(i\alpha r) \sin((2n+1)\theta) \qquad (2.28)$$

$$\sum_{n=0}^{\infty} A_n C_n(i\alpha r) \sin((2n+2)\theta) \qquad (2.29)$$

$$\sum_{n=0}^{\infty} A_n C_n(i\alpha r) \cos((2n+1)\theta) \qquad (2.30)$$

where C_n represents either J_n or H_n^1. Now, recalling that the jet flow cross section is assumed to be symmetrical about both axes, allows the computation to be restricted to the first quadrant in the physical plane. The standard computational domain for this physical region will be a rectangle. On the edges of the computational rectangle which correspond to a constant radial value, the functions defined by eqns. (2.27)–(2.30) will be applied. Before these boundary conditions are evaluated in computational space, they are transformed in terms of the computational coordinate system using the metric generated by the conformal mapping. On the vertical edges of the computational domain, which represent lines of constant angle, the boundary conditions are determined by the sysmmetry conditions. If the pressure fluctuation is not symmetrical about an axis, that is, if it changes sign across an axis, then the corresponding boundary condition becomes:

$$\hat{p} = 0 \qquad (2.31)$$

However, if the pressure fluctuation is symmetrical about an axis, that is, the sign does not change, the pressure boundary condition becomes:

$$\frac{\partial \hat{p}}{\partial \theta} = 0 \qquad (2.32)$$

Notice that the boundary conditions defined by eqns. (2.27)–(2.30) for the horisontal edges of the computational domain are consistent with the boundary conditions imposed on the vertical edges of computational domain.

The matrix equation may be integrated explicitly in the radial direction once the boundary conditions have been converted into the appropriate initial conditions. The boundary conditions on the horisontal edges of the computational domain are converted into initial conditions using a generalised shooting method. Let N denote the summation bound for the approximating series. Then there are $N-1$ interior grid points. On the lower edge of the computational domain, the first term and its derivative from the exact series solution as given above are evaluated. This becomes the initial condition on the

lower boundary. The matrix containing the system of differential equations is then integrated to the geometric center of the computational domain, yielding V_1^l. At each step in the explicit integration procedure the boundary conditions on the vertical edges of the computational domain are satisfied by solving for the first and last coefficients of the approximating series or its derivative.

On the upper edge, the first term in the exact series solution and its derivative are evaluated also. Then these values are used to integrate the matrix equation to the center of the computational domain, producing V_1^u. This process is repeated for each term in the series using $N-1$ terms from the exact series solutions on the horizontal edges of the computational domain.

The resulting integrated solutions and their derivatives are then matched at the center of the domain. The matching is accomplished by requiring that a linear combination of the $2(N-1)$ solutions be equated to zero:

$$\sum_{i=1}^{N-1} (R_i V_i^u + S_i V_i^l) = 0 \qquad (2.33)$$

Requiring that eqn. (2.33) have a non-trivial solution then forces the determinant of the matrix of integrated solutions to be zero. Recalling that the solution vectors are implicit functions of a fixed real frequency and some guessed complex wavenumber implies that a local scheme may be used to determine the wavenumbers. In this study the Newton-Raphson scheme was used.

Once a wavenumber or eigenvalue of the Rayleigh problem has been computed, its corresponding eigenfunction may be determined. The hybrid method computes an eigenfunction as it integrates the initial conditions from the edges of the shear layer to its geometric center. However, the relative weights of the integrated solutions are not known. These weights are precisely the coefficients which force the solutions and their derivatives to match in the shear layer.

Recall that this matching is given mathematically by eqn. (2.33), where R_i and S_i are the unknown coefficients. These coefficients may be determined by recasting (2.33) in the form:

$$(V_i^u, V_j^l) \begin{pmatrix} R_i \\ S_j \end{pmatrix} = 0 \qquad (2.34)$$

After the matching coefficients are determined they are used to scale the initial conditions. The Rayleigh problem is then integrated a final time using the scaled initial conditions and the pseudospectral amplitudes, $a(y^1_i, y^2)$, are stored along each radial grid line. Therefore, the eigenfunction is approximated discretely in the radial direction, and by a series in the azimuthal direction.

2.4 The Mean Velocity Profile

The mean velocity profile used in the computations is based on a generalisation of the profile given by Michalke[20]. For the round jet Michalke chose a velocity profile in the mixing layer of the form:

$$W(r) = \frac{1}{2}\left(1 + \tanh\left(\frac{R}{2\theta}\left[1 - \frac{r}{R}\right]\right)\right), \qquad (2.35)$$

$$\text{for } R - \frac{\delta}{2} < r < \infty$$

where R is the jet radius, θ is the momentum thickness and δ is a fixed real number satisfying:

$$\tanh\left(\frac{\delta}{4\theta}\right) \approx 1 \qquad (2.36)$$

Notice that the velocity profile defined by eqn. (2.35) is only a function of the radial direction. Furthermore, since conformal maps are being applied to generate the computational coordinates, (y^1, y^2), the radial coordinate, y^2, will be uncoupled from the azimuthal coordinate, y^1, allowing a general velocity profile to be expressed in terms of y^2. To generalise eqn. (2.35), let f denote a conformal map carrying a standard computational rectangle onto the first quadrant of a jet flow cross section. Also, let $f(y^1 + iy^2)$ denote the minor axis of the jet cross section in terms of the computational coordinate system. Then in terms of f the generalized velocity profile is defined as:

$$W(y^2) = \frac{1}{2}\left(1 + \tanh\left(\frac{B}{2\theta_B}\left[1 - \frac{f(y^1 + iy^2)}{f(y^1 + iy_o^2)}\right]\right)\right), \qquad (2.37)$$

$$\text{for } y_i^2 \le y^2 < \infty,$$

where y_o^2 is the half velocity point, B is the length of the minor axis, θ_B is the momentum thickness on the minor axis, and y_i^2 is a real value satisfying:

$$\tanh\left(\frac{B}{\theta_B}\left[1 - \frac{f(y^1 + iy_i^2)}{f(y^1 + iy_o^2)}\right]\right) \approx 1 \qquad (2.38)$$

The momentum thickness used in the generalized mean velocity profile is defined on the minor axis by:

$$\theta_B = \int_0^\infty \rho W(1 - W)dy \text{ for } x = 0 \qquad (2.39)$$

As an example of a non–circular mean velocity profile, if the function $a\cos(y^1 + iy^2)$ is used to generate the physical coordinates, the mean velocity profile defined by eqn. (2.37) reduces to:

$$W(y^2) = \frac{1}{2}\left(1 + \tanh\left(\frac{B}{2\theta_B}\left|1 - \frac{\sinh(y^2)}{\sinh(y_o^2)}\right|\right)\right), \quad (2.40)$$

$$\text{for } y_i^2 \le y^2 < \infty.$$

The next section will outline test results for the stability code using the velocity profiles defined in this section.

3.0 NUMERICAL RESULTS

In this section the generalised Rayleigh problem governing the linear inviscid stability of incompressible jets of arbitrary geometry is solved using the hybrid scheme described in the previous section. To consider jets of arbitrary geometry, conformal transformations have been used to map standard computational domains into jet flow cross sections in physical space. Calculations are performed for the stability of the annular shear layer region of rectangular and non–confocal elliptic jets of aspect ratio 2. These calculations are performed for azimuthal normal modes corresponding to the flapping and varicose instabilities observed in non–circular jets. In addition, examples of the eigenfunctions for these cases are shown. Firstly, the validation of the stability code, by comparison of its results to benchmark calculations for the round and confocal elliptic geometries, is given.

3.1 Code Verification

The stability code has been validated numerically for several different geometries and boundary conditions. The series of numerical tests performed involved computing the eigenvalues associated with the maximum rate of growth for the flapping and varicose azimuthal normal modes of incompressible circular and confocal elliptic jets. These results have been compared to the results of Morris[9], who computed the wavenumbers associated with the maximum growth rate for incompressible confocal elliptic jets.

In order to compare the present computation with Morris'[9] results, a relative error is introduced. Define:

$$\%\text{Error} = \frac{|\alpha_p - \alpha_b|}{|\alpha_b|} \quad (3.1)$$

where α_p are the current results and α_b are the published results.

For the circular case, the complex exponential map is used to generate the grid for the generalized Rayleigh problem. The mean velocity profile used in this computation is given by eqn. (2.35) above. In all the test cases the momentum thickness on the major axis, θ_A, is taken to be 0.02, as in ref. 9. Also, all the computations assumes geometries such that the velocity profile satisfies:

$$.001 \le W \le .999 \quad (3.2)$$

in the shear layer. Table 1 compares the wavenumbers computed using the hybrid technique, for the aspect ratio 1 case, with those of ref. 9 for the aspect ratio of 1.001.

Mode	Freq	Hybrid	Morris	%Error
V	5.441	10.207-5.687i	10.199-5.685i	0.07
F_A	5.453	10.244-5.652i	10.238-5.649i	0.06
F_B	5.456	10.253-5.652i	10.243-5.651i	0.08

Table 1 Aspect ratio 1.0 results for the hybrid method compared to previous calculations[9].

In Table 1, F_A and F_B represent asimuthal flapping modes about the major and minor axes respectively, while V represents the varicose asimuthal mode. The results of the stability code are approximately independent of the number of collocation points in the asimuthal direction. For the circular case, a Runge–Kutta integration scheme is used with a fixed step–size of 0.004.

For the confocal elliptic case, the complex cosine function is used to calculate the grid for the generalised Rayleigh equation. This coordinate transformation generates elliptic cylindrical coordinates in the physical plane, as used in ref. 9. The confocal elliptic thin shear layer calculations have been performed for the aspect ratio 2 case. The mean velocity profile used in both calculations is a special case of the general profile of the last section and is given by eqn. (2.40). Table 2 compares the results of the hybrid method to the results of ref. 9 for the aspect ratio 2 confocal elliptic shear layer.

Mode	Freq	Hybrid	Morris	%Error
V	5.657	10.156-4.496i	10.135-4.507i	0.21
F_A	5.010	9.307-3.664i	9.322-3.677i	0.19
F_B	5.657	10.045-4.472i	10.027-4.507i	0.35

Table 2 Aspect ratio 2 results for the hybrid method compared to previous calculations[9].

The step size is 0.006 for the aspect ratio 2 case. For the aspect ratio 2 confocal elliptic shear layer, the results shown are computed with 7 interior collocation points. If less than 4 interior collocation points are used the

computed wavenumbers exhibit a large error in comparison with the benchmark values. Conversely, if a large number of interior collocation points are used, say above 9, it becomes very difficult to locate the wavenumbers associated with the maximum growth rate. By adding more interior points to the computation, two distinct limiting processes are affected. Firstly, the approximation of the eigenfunction becomes more accurate because more geometric information about the physical domain is supplied to the approximation. Secondly, the functions defining the boundary conditions on the edges of the shear layer become more accurate by including terms which fluctuate more rapidly in the azimuthal direction. It is believed that adding solutions which represent the rapidly fluctuating azimuthal terms to the integrated discretization leads to a determinant minimization problem which is ill-conditioned. Presently, this represents the main difficulty found in solving the Rayleigh problem with the hybrid method. Since the generalised shooting technique couples the geometry and the boundary conditions, one possible way of correcting the problem would be to normalise appropriately the determinant equation before it is minimised. No further work on this problem has been attempted in the present study.

In the analysis of the instability of jets of arbitrary geometry the eigenfunctions associated with the computed wavenumbers may also be determined. Recall that in this case the eigenfunctions correspond to the pressure function, $\hat{p}$. All the other field variables may be related to this function. Thus, once the pressure eigenfunction is known, the distributions of the velocity components associated with instability waves or large scale coherent structures are determined completely.

The technique for the evaluation of the eigenfunctions was described in Section 2.3. Two numerical checks have been performed in analysing the results of the eigenfunction calculation for the round jet. Firstly, the stored integrated solutions have been shown to match at the geometric center of the computational domain. Secondly, the computed constants, given in eqn. (2.34) which weight the initial conditions have been checked to verify that the code is predicting the fundamental instabilities for the varicose and flapping modes. For both of these numerical tests the code performed well. Further numerical checks have shown that the code also predicts correctly the higher order modes.

As a verification of the eigenfunction calculation procedure the eigenfunctions for the varicose (axisymmetric) and flapping (helical) instabilities of the round jet have been computed. The corresponding eigenvalues are given in Table 3. The eigenfunctions are shown in Figs. 1 and 2 in the form of iso-pressure contours. The contours are plotted for the fundamental varicose and flapping instabilities given by eqn. (2.1) with γ equal to 0. All the contours shown are for positive values as there are no negative values for the zero phase case. Below, when the eigenfunctions are shown for the elliptic and rectangular cases the positive and negative contours are shown separately. These plots further assume that the pressure field is normalised by the modulus of its maximum value.

Mode	Freq	Wavenumber
V	5.44	10.20-5.68i
F_A	5.45	10.24-5.65i

Table 3 The frequencies and wavenumbers used to compute the eigenfunctions associated with the round jet.

The eigenfunction for the fundamental varicose mode is shown in Fig. 1. In this case the derivative of the pressure with respect to the azimuthal direction is zero on both axes. Moreover, as expected, the pressure contours show little azimuthal variation. The minor azimuthal variation in the pressure eigenfunction indicates that the eigenfunctions contain very small contributions from higher order modes.

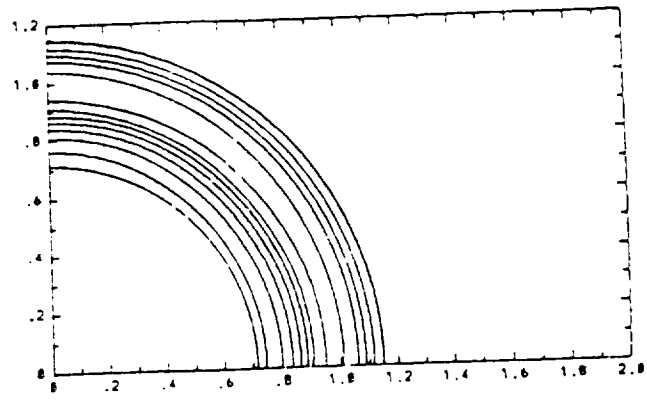

Fig. 1 Iso-pressure contours for the varicose mode: circular jet case, $\gamma = 0$. (Positive contours only shown)

The contour plot for the fundamental flapping instability about the horizontal axis is shown in Fig. 2. For this mode, the pressure contours should be symmetrical about the vertical axis and zero along the horizontal axis. For both of these examples, the hybrid method works well in predicting the properties of the normalised pressure shape function.

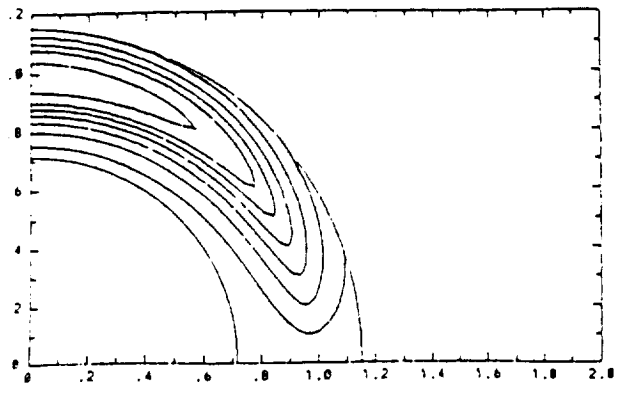

Fig. 2 Iso-pressure contours for the flapping mode: circular jet case, $\gamma = 0$. (Positive contours only shown)

3.2 Stability Calculations

For the numerical experiments, a non-confocal elliptic shear layer and a rectangular shear layer of aspect ratio 2 are chosen. Both of the jet shear layers are non-dimensionalised by requiring that the semi-major and semi-minor axes, A and B, satisfy:

$$\frac{A}{B} = 2 \tag{3.3}$$

and

$$\sqrt{AB} = 1 \tag{3.4}$$

along the half velocity line in the shear layer. Furthermore, both cases assume the hyperbolic tangent mean velocity profile defined by eqn. (2.37). All numerical tests have been performed assuming a constant momentum thickness of 0.02 in the computational domain. In the physical plane this results in a non-uniform azimuthal variation in the momentum thickness: the momentum thickness on the minor axis being greater than that on the major axis. This corresponds to the experimental profiles observed by Seiner et al[21] for an elliptic, aspect ratio 2, supersonic jet.

The first step in analysing the instability of the non-circular jets is to compute the complex wavenumbers or eigenvalues for a set of real frequencies. The cases considered are the varicose and flapping azimuthal modes. The flapping case is for flapping about the major axis. The wavenumbers are computed by fixing a frequency and then making an initial guess for the wavenumber. A Newton-Raphson iterative scheme is used to locate the eigenvalues. The computed wavenumbers and their corresponding frequencies are used to determine the local growth rate and phase velocity for the instability waves.

For the shear layers considered, the hybrid method was run with both 5 and 7 interior collocation points. The difference between wavenumbers for these cases is typically in the second and third decimal places. All the calculations for the elliptic shear layer are based on 7 interior collocation points, while those for the rectangular shear layer are based on 5 interior collocation points. Figure 3 shows the variation of the axial growth rate with frequency for the varicose mode of the aspect ratio 2 elliptic jet. The maximum growth rate is slightly lower than that determined for the confocal elliptic shear layer: see Table 2. The variation of the phase velocity, given by ω/α_r, for this case is shown in Fig. 4. This result is typical of all the calculations for both the varicose and flapping instabilities in the elliptic and rectangular jet cases. For the varicose instability there is generally a slight decrease in the phase velocity at low frequencies. However, in all the cases considered, the phase velocities of the instability waves are approximately 60 percent of the centerline velocity. These results are in agreement with those of Koshigoe and Tubis[10,11].

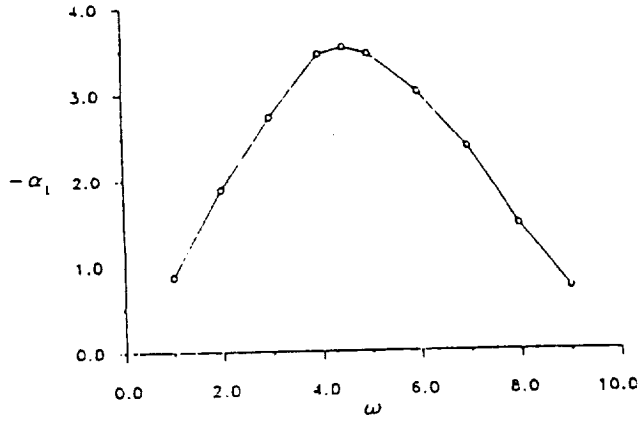

Fig. 3 Variation of the axial growth rate with frequency. Elliptic jet, aspect ratio 2, varicose mode.

To determine the most unstable mode the three largest growth rates were interpolated using a second order polynomial. Table 4 shows the frequencies of the maximum growth rates for the elliptic jet.

Mode	Freq	Wavenumber
V	4.49	7.86-3.50i
F_A	4.16	7.75-2.95i

Table 4 The frequencies and wavenumbers used to compute the eigenfunctions associated with the non-confocal elliptic jet.

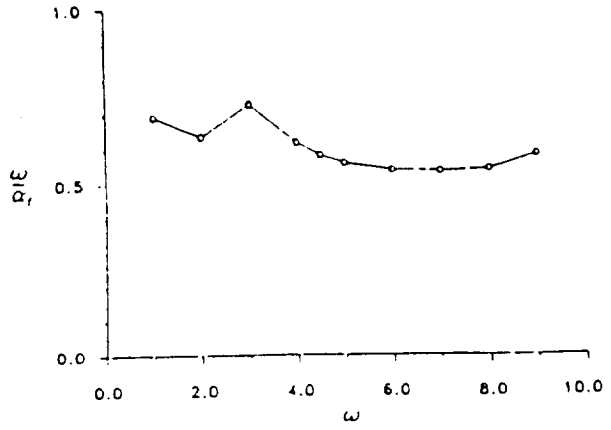

Fig. 4 Variation of the phase velocity with frequency. Elliptic jet, aspect ratio 2, varicose mode.

Figure 5 shows the variation of the axial growth rate with frequency for the varicose mode of the aspect ratio 2 rectangular jet. The maximum growth rate is much lower than that for the elliptic jet. In addition, the frequency for the maximum growth rate is also reduced. Table 5 shows the frequencies for the maximum growth rates for the varicose and flapping instabilities. This frequency should give an indication of the initial vortex shedding frequency for the jet. It is not clear whether the calculated reduction in this frequency for the rectangular jet is due to the change in the geometry or to the distribution of momentum thickness around the jet. This question is being addressed by the authors in additional calculations.

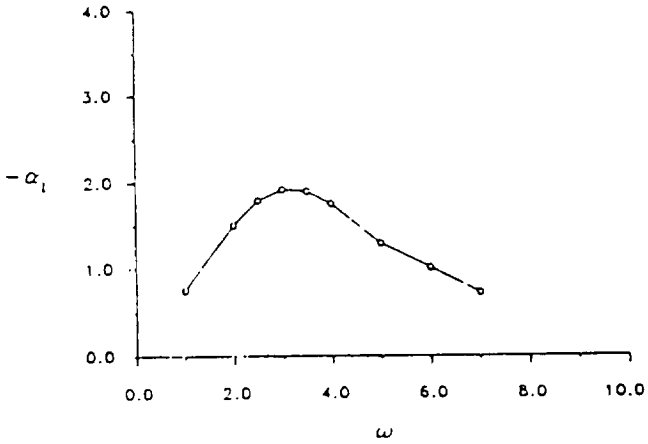

Fig. 5 Variation of the axial growth rate with frequency. Rectangular jet, aspect ratio 2, varicose mode.

As a final calculation we consider the pressure eigenfunctions for the elliptic and rectangular jets. Figure 6 shows the iso–pressure contours for the most unstable varicose instability in the elliptic jet and Fig. 7 shows the corresponding contours in the rectangular jet case. Positive contours are shown in the upper half of the figure and negative contours are shown in the lower half. The zero contour appears in both. The most notable feature in both figures is the lack of regularity, compared to the circular jet contours shown above. The pressure fluctuations are confined to several regions with no apparent relationship to the particular geometry. Very similar distributions are found for the flapping modes so that they are not shown here.

Mode	Freq	Wavenumber
V	3.16	5.71-1.92i
F_A	2.90	5.46-1.98i

Table 5 The frequencies and wavenumbers used to compute the eigenfunctions associated with the rectangular jet.

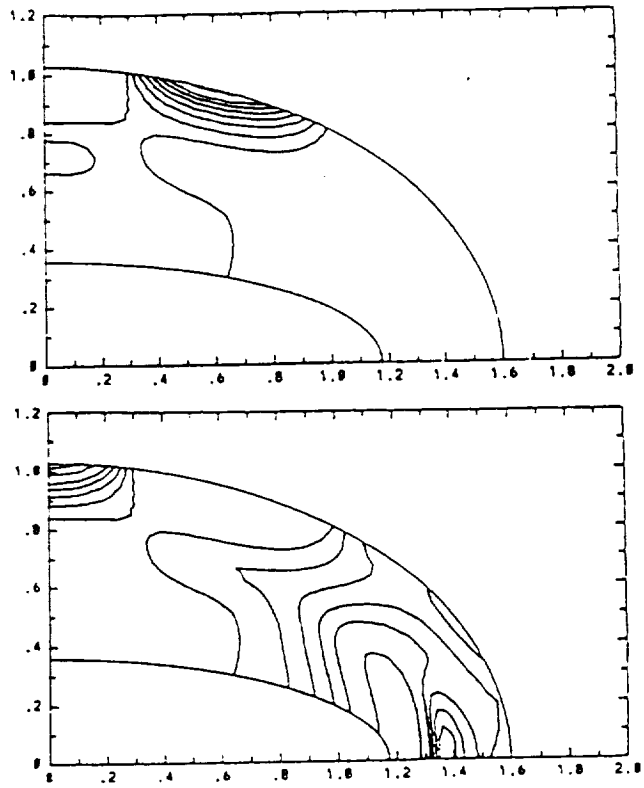

Fig. 6 Iso–pressure contours for the elliptic nonconfocal jet. Aspect ratio 2, varicose mode, $\gamma = 0$. (a) positive contours, (b) negative contours.

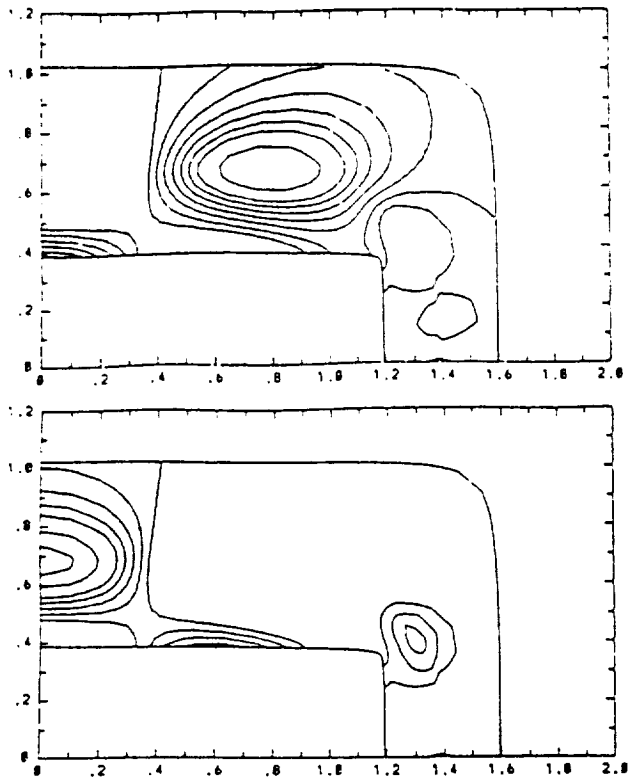

Fig. 7 Iso–pressure contours for the rectangular jet. Aspect ratio 2, varicose mode, $\gamma = 0$. (a) positive contours, (b) negative contours.

Though the contours of equal pressure level show no apparent structure this is not the case for the contours of equal Reynolds stresses and their gradients. In the rectangular jet case the distributions indicate that the jet is developing initially as two independent two–dimensional shear layers. Whereas, in the elliptic jet case there is a continuous variation from the major to the minor axes with the dominant fluctuations, for the modes considered being close to the major axis. Further details are contained in ref. 12 and will be reported elsewhere.

4.0 Summary

This paper has presented a calculation procedure to determine the stability of jets of arbitrary cross sections. Calculations have been performed for elliptic and rectangular jets. Both eigenvalues and eigenfunctions for the pressure have been calculated. The velocity components may be obtained from the pressure using the linearized equations of continuity and momentum. In turn this enables the second–order statistics, including the normal and shear stresses, associated with the instability waves to be calculated. If it is argued that the mixing process in free shear layers is dominated by large scale structures and that, locally, they may be modeled as instability waves, these second–order statistics are all that is needed to provide a turbulence closure scheme. This technique is presently being developed by the authors.

The calculations presented here are for incompressible flow. They are readily extended to the compressible flow case and examples of this calculation are contained in ref. 12. In addition, this reference contains details of the conformal mapping techniques as well as calculations of the velocity, Reynolds stress, and Reynolds stress gradient distributions. These calculations are being used by the authors to help understand the axial development of non–circular jets. The results of this analysis will be presented later.

This work was supported by NASA Langley Research Center under NASA Grant NAG–1–657. The technical monitor is Dr. J. M. Seiner

5. REFERENCES

[1]Gaster. M., Kit, E. and Wygnanski, I., "Large Scale Structures in a Forced Turbulent Mixing Layer," *Journal of Fluid Mechanics*, Vol. 150, 1985, pp. 23–39.

[2]Petersen, R. A. and Samet, M. M., "On the Preferred Mode of Jet Instability," *Journal of Fluid Mechanics*, Vol. 194, 1988, pp. 153–173.

[3]Tam, C. K. W. and Morris, P. J., "The Radiation of Sound by the Instability Waves of a Compressible Plane Turbulent Shear Layer," *Journal of Fluid Mechanics*, Vol. 98, 1980, pp. 349–381.

[4]Tam, C. K. W. and Morris, P. J., "Tone Excited Jets, Part V: A Theoretical Model and Comparison With Experiment," *Journal of Sound and Vibration*, Vol. 102, 1985, pp. 119–151.

[5]Liou, W.–W., "The Computation of Reynolds Stress in an Incompressible Plane Mixing Layer," *M.S. thesis*, Pennsylvania State University, 1986.

[6]Morris, P. J. and Giridharan, M. G., "On the Turbulent Mixing of Compressible Free Shear Layers," submitted to *Proc. Roy. Soc. Lond.*, 1989.

[7]Schadow, K. C., Wilson, K. J., Lee, M. J., and Gutmark, E., "Enhancement of Mixing in Ducted Rockets with Elliptic Gas–Generator Nozzles," AIAA Paper 84–1260, 1984.

[8]Crighton, D. G., "Instability of an Elliptic Jet," *Journal of Fluid Mechanics*, Vol. 59, 1973, pp. 665–672.

lorris, P. J., "Instability of Elliptic Jets," *A.I.A.A. urnal*, Vol. 26, No. 2, 1988, pp. 172–178.

Koshigoe, S. and Tubis, A., "Wave Structures in Jets Arbitrary Shape. I. Linear Inviscid Spatial Stability nalysis," *Physics of Fluids*, Vol. 29, 1986, pp. 3982–)92.

[1]Koshigoe, S. and Tubis, A., "Wave Structures in ets of Arbitrary Shape. II. Application of a Gener- lized Shooting Method to Linear Instability Analysis," *hysics of Fluids*, Vol. 30, 1987, pp. 1715–1723.

[2]Baty, R. S., "Reynolds Stress Closure in Jet Flows ısing Instability Wave Modeling," *Ph.D. thesis*, Penn- sylvania State University, 1989.

[13]Wegmann, R., "An Iterative Method for Conformal Mapping," *Numerical Conformal Mapping*, ed. L. N. Trefethen, North- Holland, 1986, pp. 7–18.

[14]Wegmann, R., "An Iterative Method for Conformal Mapping of Doubly Connected Regions," *Numerical Conformal Mapping*, ed. L. N. Trefethen, North-Holland, 1986, pp. 79–98.

[15]Wegmann, R., "Convergence Proofs and Error Estimates for an Iterative Method for Conformal Mapping," *Numer. Math.*, Vol. 44, 1986, pp. 435–446.

[16]Trefethen, L. N., "Numerical Computation of the Schwartz-Christoffel Transformation," *SIAM J. Sci. Stat. Comput.*, Vol. 1, 1980, pp. 82–102.

[17]Trefethen, L. N., "SCPACK User's Guide," *ICASE Internal Report No.*, 24, 1983.

[18]Gottlieb, D., Hussaini, M. Y. and Orszag, S. A., "Introduction: Theory and Application of Spectral Methods," *Spectral Methods for Partial Differential Equations*, ed. R. G. Voigt, SIAM, 1984, pp. 1–54.

[19]Batchelor, G. K. and Gill, A. E., "Analysis of the Stability of Axisymmetric Jets," *Journal of Fluid Mechanics*, Vol. 14, 1962, pp. 529–551.

[20]Michalke, A., "Instabilitat eines kompressiblen runded Freistrahls unter Berucksichtigung des Einflusses der Strahlgrenzschichtdicke," *Z. Flugwiss.*, Vol. 19, 1971, pp. 319–328.

[21]Seiner, J. M., Ponton, P. K. and Baty, R. S., "An Experimental Study of a Supersonic Elliptic Jet," private communication, 1989.

Chapter 5

A Linear Shock Cell Model for Non-Circular Jets Using Conformal Mapping with a Pseudospectral Hybrid Scheme

Thonse R. S. Bhat and P. J. Morris

AIAA-90-3960-CP

A LINEAR SHOCK CELL MODEL FOR NON-CIRCULAR JETS USING CONFORMAL MAPPING WITH A PSEUDO-SPECTRAL HYBRID SCHEME

Thonse R. S. Bhat*, Roy S. Baty† and Philip J. Morris**
The Pennsylvania State University, University Park, PA 16802

ABSTRACT

The shock structure in non-circular supersonic jets is predicted using a linear model. This model includes the effects of the finite thickness of the mixing layer and the turbulence in the jet shear layer. A numerical solution is obtained using a conformal mapping grid generation scheme with a hybrid pseudo-spectral discretization method. The uniform pressure perturbation at the jet exit is approximated by a Fourier-Mathieu series. The pressure at downstream locations is obtained from an eigenfunction expansion that is matched to the pressure perturbation at the jet exit. Results are presented for a circular jet and for an elliptic jet of aspect ratio 2.0. Comparisons are made with experimental data.

1.Introduction

Broadband shock associated noise is one of the major components of the noise of supersonic jets operating at off-design conditions. As a result, in recent years, effort has been focussed on understanding the characteristics and the generation mechanisms of broadband shock associated noise. The early work of Harper-Bourne and Fisher[1] has been followed by a number of experimental and theoretical studies on this topic. Investigations have been conducted by Tanna[2], Seiner and Norum[3,4], Seiner and Yu[5], Norum and Seiner[6,7] and Tam and Tanna[8] among others. The noise generation mechanism proposed by Tam and Tanna[8] was used by Tam[9] to develop a stochastic model for broadband shock associated noise. He obtained very good agreement with experiments for the near and far field noise spectra and directivity. In his study the shock cell structure was modelled using the method of multiple-scales of Tam, Jackson and Seiner[10].

Recently there has been considerable interest in non-circular supersonic jets with a view of achieving better mixing characteristics and a reduction in radiated noise. There has been some progress in the development of supersonic jet noise theories for non- circular jets. Tam[11] used a vortex-sheet model for the jet and predicted the screech tone frequencies in rectangular and elliptic jets. Morris, Bhat and Chen[12] used a boundary element method to predict the shock cell structure and screech tone frequencies in jets of arbitrary geometry. Once again, a vortex-sheet model was used to describe the jet. Morris and Bhat[13] extended their analysis of non-circular geometry jets to include the effects of finite mixing layer thickness using realistic and continuous mean velocity and density profiles. They also included the dissipative effects of the small-scale turbulence through the addition of eddy-viscosity terms in the momentum equations. However, they encountered some convergence problems with their numerical technique.

In this paper, the shock cell structure of non-circular supersonic jets is modelled using a linearized analysis. In the present study a new numerical scheme is introduced. This method uses conformal mapping with a pseudo-spectral hybrid discretization scheme. This work is an attempt by the authors to develop models with a robust numerical scheme to predict the shock cell structure in an efficient manner. The physical model used here is similar to the one used earlier by Tam, Jackson and Seiner[10] and Morris and Bhat[13]. In the latter case a body-fitted coordinate system was used to set up the problem for non-circular geometry jets. However, this scheme had convergence problems. The new numerical method uses the conformal mapping technique developed by Wegmann[14] and used by Baty[15] in his analysis of the inviscid instability of arbitrary geometry jets. This method transforms the physical space to a rectangular computational domain using a series of conformal mappings. In the computational space, the flow variables are represented in a series form using a hybrid pseudo-spectral approximation.

The next section outlines the development of the governing equations in terms of a general conformal coordinate system. A description is also given of the implementation of the conformal mapping technique. The discretization of the model differential equations using a hybrid pseudo-spectral scheme is also described. Section 3 describes the application of these numerical techniques to the shock cell problem. In section 4, predictions are

---

* Graduate Assistant, Department of Aerospace Engineering, Student Member AIAA.

† Present Address, Senior Member of Technical Staff, Sandia National Laboratories, Albuquerque, NM 87185, Member AIAA.

** Professor, Department of Aerospace Engineering, Senior Member AIAA.

C-2

presented for a circular jet and an elliptic jet of aspect ratio 2.0. Also, comparisons are made with experimental data.

2. ANALYSIS

The cross-section of the initial region of a jet consists of three regions: the potential core of the jet, the annular mixing region and the ambient fluid surrounding the jet. In the potential core and in the ambient fluid, the solutions to the linearized governing equations can be obtained analytically. However, in the annular mixing region, where the mean velocity and density of the jet vary, the solution must be obtained numerically.

The model used here for the shock cell structure is that developed by Tam, Jackson and Seiner[10] for circular jets. This model takes into account the finite thickness of the mixing region and the effects of turbulence in the jet shear layer. A finite-difference technique using a pseudo-spectral hybrid scheme in conjunction with conformal mapping is used here to extend the model to a study of the shock cell structure in non-circular supersonic jets.

2.1 Governing Equations

The non-dimensional linearized governing equations for the shock cell structure, in Cartesian tensor notation, are given by:

$$\frac{\partial}{\partial x_i}(\bar{\rho}u_i^S) + W\frac{\partial \rho^S}{\partial x_3} = 0 \tag{2.1}$$

$$\bar{\rho}W\frac{\partial u_i^S}{\partial x_3} + \bar{\rho}u_j^S\frac{\partial W}{\partial x_j}\delta_{i3} = -\frac{1}{\gamma M_j^2}\frac{\partial p^S}{\partial x_i} + \frac{1}{Re}\frac{\partial^2 u_i^S}{\partial x_j \partial x_j} \tag{2.2}$$

$$W\frac{\partial p^S}{\partial x_3} + \gamma\frac{\partial u_i^S}{\partial x_i} = 0 \tag{2.3}$$

The reference scales are r_j, the equivalent radius of the fully expanded jet and U_j, ρ_j, and p_j, the fully expanded jet velocity, density and pressure, respectively. $\bar{\rho}$ and W are the mean density and axial velocity of the jet. The quantities with a superscript S correspond to the perturbations associated with the shock cell structure. M_j is the fully expanded jet Mach number. The assumptions made in deriving the linearized equations given above are discussed in detail by Bhat[16]. The mean velocity is assumed to be known, either from experiments or predictions. It is also assumed that the mean flow is independent, locally, of the axial distance. The turbulent Reynolds stresses in the momentum equations have been modelled using a simple eddy viscosity model. The turbulent Reynolds number is given by, $Re = U_j r_j/\nu_t$ where ν_t is the turbulent eddy viscosity. The shock cell structure is modelled as spatially periodic waves that are time-independent. Using the locally parallel flow approximation, the perturbation quantities associated with the shock cell structure can be represented in a separable form with a periodic variation in the axial direction. This is given by,

$$f^S(x_1, x_2, x_3) = \hat{f}(x_1, x_2)\exp(i\alpha x_3) \tag{2.4}$$

where f^S is any flow perturbation quantity and α is the complex axial wavenumber.

The linearized eqns. (2.1)-(2.3) are written in terms of a Cartesian coordinate system. These equations must be transformed in terms of a general, nonsingular curvilinear coordinate system, (y_1, y_2) in the cross-sectional plane. This coordinate change can be performed by expressing the differential operators in (2.1)-(2.3) in general tensor form. These are obtained using the approach of Eiseman[17], with the axial coordinate given by, $x_3 = y_3$. The shock cell structure equations in a general coordinate system are then given by,

$$\frac{\partial}{\partial y_k}(\bar{\rho}u_i^S)\frac{\partial y_k}{\partial x_i} + W\frac{\partial \rho^S}{\partial y_3} = 0 \tag{2.5}$$

$$\bar{\rho}W\frac{\partial u_i^S}{\partial y_3} + \bar{\rho}u_j^S\frac{\partial W}{\partial y_k}\delta_{i3}\frac{\partial y_k}{\partial x_j} = -\frac{1}{\gamma M_j^2}\frac{\partial p^S}{\partial y_k}\frac{\partial y_k}{\partial x_i} + \frac{1}{Re}\frac{1}{\sqrt{g}}\frac{\partial}{\partial y_i}(g^{ki}\frac{\partial u_i^S}{\partial y_k}\sqrt{g}) + \frac{1}{Re}\frac{\partial^2 u_i^S}{\partial y_3^2} \tag{2.6}$$

$$W\frac{\partial p^S}{\partial y_3} + \gamma\frac{\partial u_i^S}{\partial y_k}\frac{\partial y_k}{\partial x_i} = 0 \tag{2.7}$$

where, $g = \det(g_{ij})$ and g_{ij} is the metric tensor. The metric tensor and its inverse g^{ij} are defined as,

$$g_{ij} = \frac{\partial x_k}{\partial y_i}\frac{\partial x_k}{\partial y_j} \tag{2.8}$$

$$g^{ij} = \frac{\partial y_i}{\partial x_m}\frac{\partial y_j}{\partial x_m} \tag{2.9}$$

and

$$g^{ij} = 1/g_{ij} \tag{2.10}$$

The transformation of eqns. (2.5)-(2.7) in physical space to a simple computational domain is accomplished using a inverse conformal mapping technique. The formulation is similar to that given by Baty[15] and is outlined briefly here. Consider a computational domain, $\mathcal{R}$, in the complex plane (y_1, y_2). Let f be an analytic mapping which maps $\mathcal{R}$ onto a given jet flow cross-section in the physical space (x_1, x_2). It is assumed that f has a nonzero derivative, i.e.

$$f'(z) = f'(y_1 + iy_2) \neq 0 \quad \text{for all} \quad z \in \mathcal{R} \tag{2.11}$$

The relation between the coordinates (y_1, y_2) and $x_1, x_2)$ generated by $f(z)$ is given by,

$$f(z) = f(y_1 + iy_2) = x_1 + ix_2 \qquad (2.12)$$

The analytic mapping f satisfies the Cauchy-Riemann quations,

$$\frac{\partial x_1}{\partial y_1} = \frac{\partial x_2}{\partial y_2} \quad \text{and} \quad \frac{\partial x_1}{\partial y_2} = -\frac{\partial x_2}{\partial y_1}. \qquad (2.13)$$

The derivative of f can then be written as,

$$f'(z) = \frac{\partial x_1}{\partial y_1} - i\frac{\partial x_1}{\partial y_2} = \frac{\partial x_2}{\partial y_2} + i\frac{\partial x_2}{\partial y_1}. \qquad (2.14)$$

The components of the metric tensor, g_{ij} are given by,

$$g_{11} = g_{22} = |f'(z)|^2, \quad g_{12} = g_{21} = 0 \qquad (2.15)$$

The components of g^{ij}, the inverse of g_{ij}, are given by,

$$g^{11} = g^{22} = \frac{1}{g_{11}} \quad \text{and} \quad g^{12} = g^{21} = 0 \qquad (2.16)$$

Then, the resulting equations for the shock cell tructure in general conformal coordinates can be written,

$$\frac{\partial}{\partial y_k}(\bar{\rho}\hat{u}_i)\frac{\partial y_k}{\partial x_i} + i\alpha\bar{\rho}W = 0 \qquad (2.17)$$

$$i\alpha W\bar{\rho}\hat{u}_i + \bar{\rho}\hat{u}_j\frac{\partial W}{\partial y_k}\delta_{i3}\frac{\partial y_k}{\partial x_j} = -\frac{1}{\gamma M_j^2}\frac{\partial \hat{p}}{\partial y_k}\frac{\partial y_k}{\partial x_i} + \frac{1}{Re}\left\{\frac{1}{g_{11}}\Delta\hat{u}_i - \alpha^2\hat{u}_i\right\} \qquad (2.18)$$

$$i\alpha W\hat{p} + \gamma\frac{\partial \hat{u}_i}{\partial y_k}\frac{\partial y_k}{\partial x_i} = 0 \qquad (2.19)$$

here Δ is the standard Cartesian Laplacian in terms the coordinates (y_1, y_2). The conformal mapping is enerated numerically and the method is described in e next section.

.2 Conformal Mapping

Let $\mathcal{P}$ denote a given jet flow cross-section in the ysical space and $\mathcal{C}$ be the unit annulus with some inior radius, μ, such that $0 < \mu < 1$. Let $\mathcal{W}$ be the nformal mapping such that $\mathcal{C}$ is mapped onto $\mathcal{P}$. As e desired computational domain is rectangular, anher mapping must be used to map the rectangular gion $\hat{\mathcal{R}}$ onto the annular region $\mathcal{C}$. This is given by the ponential mapping $\exp(iz)$. The rectangular computional domain in coordinates (y_1, y_2) is given by,

$$\hat{\mathcal{R}} = \{(y_1, y_2) \in \mathbb{R}^2 : \alpha \le y_1 \le \eta, 0 \le y_2 \le \beta\}. \qquad (2.20)$$

α, η and β are finite real numbers and β is positive.

The discretization for the finite-difference scheme, discussed below, involves an approximating function defined on the interval $[-1, 1]$ in the "azimuthal" direction, y_1. This requires a linear coordinate transformation of the form

$$y_1 = As_1 + B, \quad \text{and} \quad y_2 = s_2 \qquad (2.21)$$

with the transformed rectangular computational domain defined by:

$$\hat{\mathcal{R}} = \{(s_1, s_2) \in \mathbb{R}^2 : -1 \le s_1 \le 1, 0 \le s_2 \le \beta\} \qquad (2.22)$$

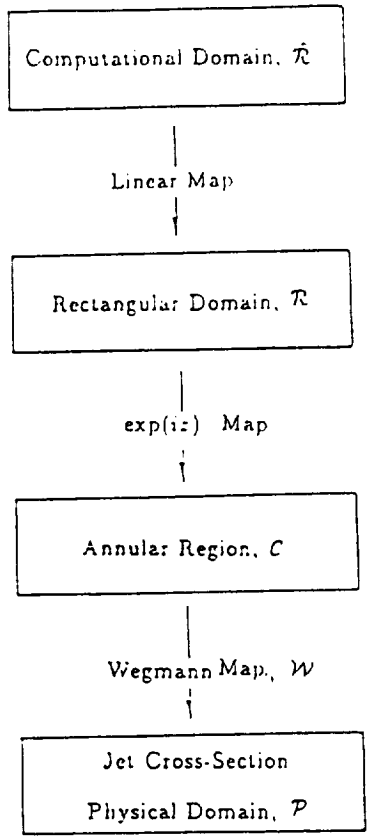

Fig. 1 Schematic of the transformation from the computational domain $\hat{\mathcal{R}}$ to the physical space $\mathcal{P}$

A and B may be determined once the dimensions of the rectangular domain $\mathcal{R}$ are known. The various steps involved in mapping the rectangular domain $\hat{\mathcal{R}}$ onto the physical space $\mathcal{P}$ are shown schematically in Fig. 1. The Wegmann mapping, $\mathcal{W}$, needs to be determined next.

Let ϵ_i (i=1,2) denote the doubly connected region with smooth closed boundaries. Here, the subscript i refers to the inner ($i = 1$) and outer ($i = 2$) boundaries of the given jet flow cross-section. It is assumed that ϵ_i can be parameterized by

$$z_i(t) \quad \text{on} \quad 0 \le t \le \beta_i \quad \text{for} \quad i = 1, 2 \tag{2.23}$$

where z_i is a smooth regular curve. The aim of the method is to determine a mapping g_i such that the boundaries of the annulus C are mapped onto ϵ_i. This involves determining the image of a point on the unit annulus on the boundary of the jet cross-section. As both the jet cross-section and the annulus are known smooth functions, only the angle θ of a point on the annulus needs to be known to determine the angle, say $\tau(\theta)$, of its image satisfying:

$$g_i(e^{i\theta}) = z_i(\tau_i(\theta)) \tag{2.24}$$

The Wegmann method[14] solves for the function, τ, which is also known as the boundary correspondence function. Any real function $\tau(\theta)$ satisfying eqn. (2.24) and

$$\tau(\theta) - \frac{\beta_i}{2\pi}\theta, \ \beta_i \in \mathrm{R} \tag{2.25}$$

that is 2π periodic is defined to be a boundary correspondence function. The image $\tau(\theta)$ is determined by satisfying eqns. (2.24)-(2.25). This is obtained iteratively starting from a good guess $\hat{\tau}$ and determining the correction factor η such that,

$$\tau = \hat{\tau} + \eta \tag{2.26}$$

For the doubly connected region, there will be two boundary correspondence functions for the two edges of the shear layer. The interior radius of the annulus is also unknown, and must be determined. It is found that good initial guesses for both the boundary correspondence functions and the interior radius are required to obtain quadratic convergence. The details of the iterative scheme can be found in Wegmann[14] and Baty[15]. The conformal mapping is generated numerically using the Cauchy Integral Theorem after the boundary correspondence problem is solved.

Once the mapping is completed it is necessary to discretize the governing equations given by (2.17)-(2.19) in the computational domain. A hybrid technique which combines a series approximation with a finite-difference technique is used here. Let the functions to be approximated, in the present case the perturbations associated with the shock cell structure, be represented in a series of the form:

$$\phi(y_1, y_2) \approx \sum_{i=0}^{N} a(y_{1i}, y_2) f_i(y_1), \tag{2.27}$$

with the coefficients $a(y_{1i}, y_2)$ taken to be functions of y_2 and the basis functions, f, represented in terms of Chebyshev polynomials defined by,

$$f_i(y_1) = \frac{[(1-y_1^2)T_N'(y_1)(-1)^{i+1}]}{c_i N^2 (y_1 - y_{1i})}. \tag{2.28}$$

$T_N'(y_1)$ is the derivative of the N^{th} order Chebyshev polynomial and the constants c_i are given by,

$$c_0 = c_N = 2 \quad \text{and} \quad c_i = 1 \quad \text{otherwise.} \tag{2.29}$$

The grid in the y_1 coordinate direction is defined by,

$$y_{1j} = \cos\frac{\pi j}{N} \quad \text{for} \quad j = 0, 1, 2, ..., N \tag{2.30}$$

The model equations can be discretized readily as the basis function, evaluated at the grid points, satisfies relation

$$f_i(y_{1j}) = \delta_{ij} \tag{2.31}$$

where δ_{ij} is the Kronecker delta. In the present model the derivatives of the approximating basis functions at the grid points must also be determined. These derivatives can be obtained using the relations given by Gottlieb et al.[18]

The flow variables are all approximated by a series of the form given by (2.27). The approximating series are substituted into the governing eqns. (2.17)-(2.19). These equations are then evaluated at the interior grid points. With the use of eqn. (2.31) a system of linear ordinary differential equations in the unknown series coefficients is produced. The full form of the equations is given by Bhat[16].

3. Calculation Procedure

When the jet shear layer is of finite extent a numerical solution to the governing equations must be obtained in that region. In order to obtain the numerical solution, the solution of the governing equations in regions of constant mean flow properties must be found first. The separable solutions for the flow variables in a polar coordinate system may be found using the technique described by Morris[19]. The solutions for the flow variables are found to be of the form:

Inner region:

$$\tilde{p}(r,\theta) = \sum_{n=-\infty}^{\infty} -A_n \frac{\gamma M_j^2 Re}{(Re + i\alpha M_j^2)} J_n(i\lambda^* r)\exp(in\theta) \tag{3.1}$$

$$\hat{u}_r(r,\theta) = \sum_{n=-\infty}^{\infty} [A_n J_n(i\lambda^* r) + B_n J_n(i\lambda r)]\exp(in\theta) \tag{3.2}$$

$$\hat{u}_r(r,\theta) = \sum_{n=-\infty}^{\infty} [-A_n \frac{i}{\alpha}\frac{d}{dr}\{J_n(i\lambda^* r)\} - B_n \frac{\alpha}{\lambda} J_{n+1}(i\lambda r) - C_n \frac{in}{r} J_n(i\lambda r)] \exp(in\theta) \quad (3.3)$$

$$\hat{u}_\theta(r,\theta) = \sum_{n=-\infty}^{\infty} [A_n \frac{n}{\alpha r} J_n(i\lambda^* r) + B_n \frac{i\alpha}{\lambda} J_{n+1}(i\lambda r) + C_n \frac{d}{dr}\{J_n(i\lambda r)\}] \exp(in\theta) \quad (3.4)$$

here,

$$\lambda^{*2} = \frac{(\alpha^2 Re + i\alpha\lambda^2 M_j^2)}{(Re + i\alpha M_j^2)} \quad (3.5)$$

nd,

$$\lambda^2 = \alpha^2 + i\alpha Re \quad (3.6)$$

uter region:

$$\hat{p}(r,\theta) = \sum_{n=-\infty}^{\infty} D_n \frac{2\gamma M_j^2}{Re} H_n^{(1)}(i\alpha r) \exp(in\theta) \quad (3.7)$$

$$\hat{u}_z(r,\theta) = \sum_{n=-\infty}^{\infty} [D_n r H_{n+1}^{(1)}(i\alpha r) + E_n H_n^{(1)}(i\alpha r)] \exp(in\theta) \quad (3.8)$$

$$\hat{u}_r(r,\theta) = \sum_{n=-\infty}^{\infty} [\frac{iD_n}{\alpha}\{H_{n+1}^{(1)}(i\alpha r) - r\frac{d}{dr}[H_{n+1}^{(1)}(i\alpha r)]\} - E_n H_{n+1}^{(1)}(i\alpha r) - \frac{inF_n}{\alpha r} H_n^{(1)}(i\alpha r)] \exp(in\theta) \quad (3.9)$$

$$\hat{u}_\theta(r,\theta) = \sum_{n=-\infty}^{\infty} [\frac{(n+2)}{\alpha} D_n H_{n+1}^{(1)}(i\alpha r) + iE_n H_{n+1}^{(1)}(i\alpha r) + \frac{F_n}{\alpha}\frac{d}{dr}\{H_n^{(1)}(i\alpha r)\}] \exp(in\theta) \quad (3.10)$$

ere, $(\hat{u}_z, \hat{u}_r, \hat{u}_\theta)$ are the components of the velocity fluctuations in the (z, r, θ) coordinates. J_n is the Bessel nction of the first kind of order n, $H_n^{(1)}$ is the Hankel function of the first kind of order n. These solutions erve as the initial conditions to the governing equations. he boundary conditions along the two bounding radial nes of the shear layer must also be specified. These nditions depend on whether the solutions sought are id or even about the boundaries. In the present case, r a uniform pressure perturbation at the jet exit, solutions are sought that are even about both the minor nd major jet axes. The boundary and initial conditions are applied in the rectangular computational domain. The initial conditions are satisfied on the upper and lower boundaries of the rectangle, which correspond to the inner and outer edges of the shear layer. The initial conditions in (r,θ) coordinates are transformed in terms of the computational coordinates using the metric generated by the conformal mapping. The boundary conditions on the other edges of the computational domain, which represent the two bounding radial lines, are satisfied by solving for the first and last coefficients of the approximating series or its derivative.

The system of differential equations, derived in the last section, may be written as six first- order coupled ordinary differential equations in the unknown coefficients. These equations are integrated from the boundaries for each value of n in the series (3.1)-(3.10). A linear superposition of these solutions is matched at some intermediate location in the computational domain. This results in a system of homogeneous equations in the unknown series coefficients. The axial wavenumbers are determined by zeroing the determinant of the coefficient matrix using a Newton-Raphson iterative technique.

The mean velocity profile is assumed to be given by:

$$W(r) = W_j \exp[-\ln(2)\eta^2] \quad (3.11)$$

where $\eta = n/b$, where n is measured normal to the edge of the potential core and b is the local half-width of the jet mixing layer. For a circular jet, $n = r - h$ and the relationship between the potential core radius h and b is obtained from the condition of conservation of axial momentum. This is given by Tam and Morris[20]. In the case of the elliptic jet, these values are obtained from the measured mean velocity profiles[21] for an elliptic nozzle of aspect ratio 2 operating at its design condition of M_d=1.52. These data include the mean velocity profiles along the major- and minor-axes for several downstream locations. By fitting the half-Gaussian velocity profile, given by eqn. (3.11), the location of the potential core, h_1 (along the major-axis) and h_2 (along the minor-axis), the half-velocity point, b_1 (along the major axis) and b_2 (along the minor axis) are obtained at the various downstream locations. The experimental values of the half- widths and the potential core radii are shown in Figure 2.

The half-widths and the potential core radii are taken to be a linear function of the axial distance. In the calculations for the circular jet, the growth rate of the shear layer is taken from the data of Birch and Eggers[22] which is 1.266 times the inverse of the spreading rate of the mixing layer, σ.

The mean density $\bar{\rho}$ may be calculated from the mean velocity using a Crocco's relationship. The turbulent Reynolds number, based on b, the half-width, is

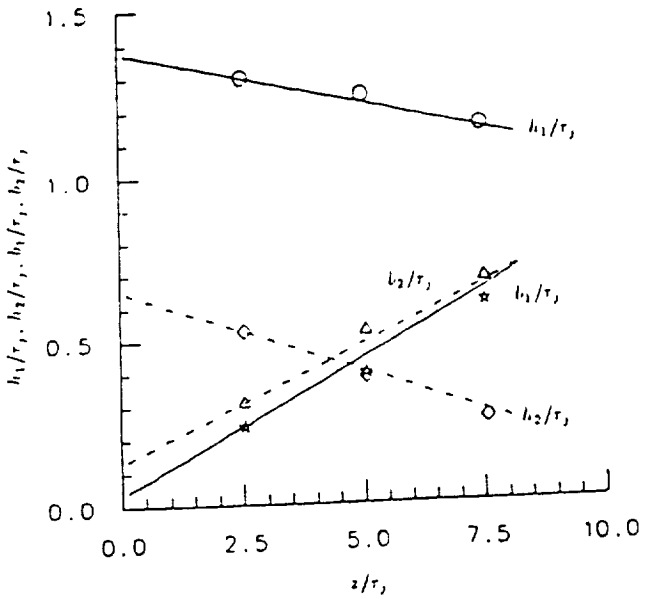

Fig. 2 Variation of Shear Layer Parameters with Axial Distance of a 2:1 Elliptic Jet. $*, b_1/r_j$; $\Delta, b_2/r_j$; $\circ, h_1/r_j$; $\circ, h_2/r_j$. $M_j = M_d = 1.52$.

set equal to 300. The numerical integration is performed using a fixed step size fourth-order Runge-Kutta scheme with 32 steps in the domain of integration. Calculations are performed in one quadrant only based on the assumed symmetry of the mean velocity profile about the major- and minor-axes. In the case of the circular jet, three interior lines are used, while for the elliptic jet, nine interior collocation points are used. The perturbation pressure as a function of downstream distance is calculated from the pressure perturbation at the nozzle exit and the axial variation of the wavenumber, α, for a given mode. The pressure may be written as

$$p(z) = \sum_{n=0}^{\infty}\sum_{r=1}^{\infty}\Big\{(p_{nr})_0 \exp\Big|\int_0^x i\alpha_{nr}(z_1)dz_1\Big|\Big\}, \quad (3.12)$$

where $(p_{nr})_0$ is the amplitude of the n-r mode at the nozzle exit and (α_{nr}) is the complex axial wavenumber for that mode. These amplitudes are calculated from a vortex- sheet model of the jet.

The vortex-sheet model was proposed by Prandtl[23] and Pack[24], and extended by Tam and Tanna[8]. The weak shock cell structure is modelled as a small-amplitude disturbance superimposed on an otherwise perfectly expanded jet. The assumption of weak shock cells restricts the analysis to supersonic jets operating at slightly off-design conditions given by

$$|M_j^2 - M_d^2| \le 1.0 \quad (3.13)$$

where M_j and M_d are the fully expanded jet and design Mach numbers. The relationship between the fully expanded and design conditions are given by Tam and Tanna[8]. The fully expanded jet is represented by a column of uniform flow bounded by a vortex sheet.

The linearized equation for the pressure perturbation inside the vortex sheet is,

$$\nabla^2 p^S - M_j^2 \frac{\partial^2 p^S}{\partial z^2} = 0 \quad (3.14)$$

Using elliptic cylindrical coordinates, related to Cartesian coordinates by

$$x = a\cosh(\rho)\cos(\theta)$$

$$y = a\sinh(\rho)\sin(\theta)$$

and,

$$z = z$$

eqn. (3.14) becomes

$$\frac{2}{a^2(\cosh 2\rho - \cos 2\theta)}\Big[\frac{\partial^2 p^S}{\partial \rho^2} + \frac{\partial^2 p^S}{\partial \theta^2}\Big] + \alpha^2(M_j^2 - 1)p^S = 0 \quad (3.15)$$

The vortex sheet is bounded by the ellipse $\rho = \rho_0$.

The boundary conditions are

$$p^S = 0 \text{ on the ellipse } \rho = \rho_0 \quad (3.16)$$

and,

$$\text{at } z = 0, p^S = \Delta p \text{ everywhere inside the ellipse } \rho = \rho_0 \quad (3.17)$$

A separable solution is sought in the form,

$$p^S(\rho, \theta) = F(\rho)G(\theta) \quad (3.18)$$

The equations for F(ρ) and G(θ) are found to be,

$$\frac{d^2F}{d\rho^2} - (\lambda - 2q\cosh 2\rho)F = 0 \quad (3.19)$$

and,

$$\frac{d^2g}{d\theta^2} + (\lambda - 2q\cos 2\theta)G = 0 \quad (3.20)$$

where λ is a separation constant and $q = -\alpha^2(M_j^2 - 1)a^2/4$. Equations (3.20) and (3.19) are the Mathieu and the Modified Mathieu equations respectively with parameters λ and q. In general, the solutions of these equations are given by the four classes of Mathieu and Modified Mathieu functions. The only solution which is

symmetric with respect to both x and y axes is given by,

$$p^S(\rho,\theta) = \sum_{n=0}^{\infty} D_n Ce_{2n}(\rho,q)ce_{2n}(\theta,q) \qquad (3.21)$$

where, D_n is a constant to be determined from the initial condition, and ce_{2n} and Ce_{2n} are the Mathieu and the Modified Mathieu functions respectively.

The boundary condition (3.16) requires that $Ce_{2n}(\rho_0,q) = 0$ and this gives the roots q_{nr}. In calculating ρ_0, the dimensions of the fully expanded jet are used. The pressure perturbation at the nozzle exit is then given by,

$$p^S(\rho,\theta) = \Delta p = \sum_{n=0}^{\infty}\sum_{r=1}^{\infty} D_{nr} Ce_{2n}(\rho,q_{nr})ce_{2n}(\theta,q_{nr}) \qquad (3.22)$$

where, Δp is the pressure difference at the nozzle exit, calculated using the one-dimensional isentropic relations, and is given by eqn. (2.3) in Tam, Jackson and Seiner[10]. By means of the orthogonality property of the Mathieu functions, the coefficients D_{nr} are found to be,

$$\begin{aligned} D_{nr} =& \Delta p\Big\{\int_0^{\rho_0}\int_0^{2\pi} Ce_{2n}(\rho,q_{nr})ce_{2n}(\theta,q_{nr}) \\ & |cosh2\rho - cos2\theta|d\theta d\rho\Big\} / \\ & \Big\{\int_0^{\rho_0}\int_0^{2\pi} Ce_{2n}^2(\rho,q_nr)ce_{2n}^2(\theta,q_{nr}) \\ & |cosh2\rho - cos2\theta|d\theta d\rho\Big\}. \end{aligned} \qquad (3.23)$$

The integrals are evaluated using the method suggested in McLachlan[25]. In the limit, as the aspect ratio tends to unity, eqn. (3.23) reduces to eqn. (2.1b) given in Tam, Jackson and Seiner[10]. The initial mode amplitude in eqn. (3.12) is related to D_{nr} by,

$$(p_{nr})_0 = D_{nr} Ce_{2n}(\rho,q_{nr})ce_{2n}(\theta,q_{nr}), \qquad (3.24)$$

for given values of ρ and θ.

The calculation procedure may be summarized as the following steps. (1) The pressure perturbation at the jet exit is obtained as a Fourier-Mathieu series approximation, eqn. (3.22). (2) The axial wavenumber for a given mode at a given axial location is obtained from a solution of eqns. (2.17)-(2.19) using conformal mapping and a hybrid pseudo-spectral discretization. (3) The pressure associated with the shock cell structure is calculated as the superposition of contributions from each mode from eqn. (3.12).

4. Results

This section presents the calculations for the shock cell structure in a circular jet and in an elliptic jet of aspect ratio 2. In the case of the elliptic jet, the predictions are compared with the experimental data obtained recently at NASA Langley[21]. These measurements are for an elliptic jet issuing from a nozzle of aspect ratio 2 and operated at several off-design conditions. The design Mach number of this nozzle is 1.52.

Two different operating conditions have been considered - an underexpanded jet (fully expanded jet Mach number, $M_j = 1.64$, design Mach number, $M_d = 1.52$) and an overexpanded jet ($M_j = 1.36$, $M_d = 1.52$). It should be noted that in the earlier work of Morris and Bhat[13], two different operating conditions (underexpanded and overexpanded) were considered for the circular jet. The predictions obtained for these cases were compared with the experimental measurements of Norum and Seiner[26] and also with the results obtained with the multiple-scales model of Tam, Jackson and Seiner[10]. The comparison showed very favorable agreement. In this study, emphasis is placed on obtaining predictions of the shock cell structure for comparison with the experimental data for the elliptic jet.

Table 1. Initial amplitudes for the various modes of elliptic jet, M_j=1.64, M_d=1.52.

Mode No.	$(p_{nr})_0/p_a$	Mode No.	$(p_{nr})_0/p_a$
01	0.31506	21	0.04636
02	−0.12058	22	−0.03442
03	0.07365	23	0.02305
04	−0.05301	24	−0.01739
11	−0.09432	31	−0.02636
12	0.05190	32	0.02611
13	−0.03351	33	−0.01779
14	0.02475	34	0.01365

Table 2. Initial amplitudes for the various modes of elliptic jet, M_j=1.36, M_d=1.52.

Mode No.	$(p_{nr})_0/p_a$	Mode No.	$(p_{nr})_0/p_a$
01	−0.33231	21	−0.05083
02	0.12597	22	0.03589
03	−0.07692	23	−0.02413
04	0.05534	24	0.01821
11	0.10153	31	0.02967
12	−0.05429	32	−0.02703
13	0.03506	33	0.01859
14	−0.02588	34	−0.01428

In order to obtain a reasonable description of the perturbation pressure, the number of modes to be con-

sidered in eqn. (3.12) has to be determined. This can be achieved by calculating the amplitudes of the Fourier-Mathieu series coefficients representing the perturbation pressure at the nozzle exit, see eqns. (3.22) and (3.23). Henceforth, any given mode is designated by the indices nr. For example, mode 01 corresponds to $n = 0$ and $r = 1$. The initial amplitude of any given mode is a function of both n and r as well as the jet operating condition. This dependence can be seen in Tables 1 and 2. The amplitudes presented here are the perturbation pressure $(p_{nr})_0$ on the jet centerline normalized by the ambient pressure p_a. It can be seen that for a given n, the amplitude decreases as r increases. The amplitudes also decrease as n increases for any given r. It is also clear that many modes would have to be considered to provide a perfectly uniform exit perturbation pressure. The variation of the perturbation pressure at the nozzle exit along the major- and minor-axes is shown in Fig. 3 for the underexpanded elliptic jet, where L_A and L_B are the dimensions of the fully-expanded major-and minor axes, respectively. Here, contribution from the modes $n = 0$, 1, 2 and 3 are considered where for each n, four roots (i.e. $r = 1$, 2, 3 and 4) are considered. This figure reveals that in spite of considering so many modes, there is still some nonuniformity in the pressure variation across the cross-section of the jet. This is characteristic of the difficulty of approximating a step function with Bessel functions, in the circular jet case, and modified Mathieu functions, in the elliptic jet case. However, as the amplitude of the higher modes is reasonably small, it is assumed that a practical approximation can be obtained by considering fewer modes. Hence, in all subsequent calculations for the elliptic jet, the modes considered are 01, 02, 03, 04, 11 and 12. The difference between the sum of the contribution of these modes and the pressure difference at the exit, obtained using isentropic relations, is less than 10% for both the underexpanded jet and the overexpanded jet. Calculations at other operating conditions for both circular and elliptic jets have shown that the number of modes required to obtain a given degree of accuracy is a strong function of the jet operating conditions.

Figure 4 shows the axial pressure distribution obtained for the underexpanded jet along the centerline of the elliptic jet. Figure 5 is for the case of the overexpanded elliptic jet. The sum of the contributions from the six chosen modes is compared with experimental data of ref. 21. Here, the normalized pressure perturbation is given as a function of downstream distance, z, referenced to the equivalent radius of the fully expanded jet, r_j. As can be seen, in both the cases, there is favorable overall agreement between the measured and calculated pressure distributions. The shock cell spacings and

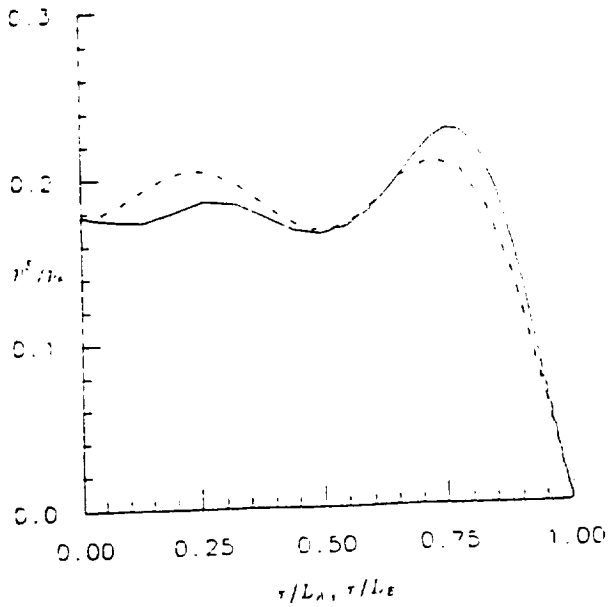

Fig. 3 Variation of Pressure at the Nozzle Exit for Elliptic Jet, M_j=1.64, M_d=1.52. ——, along the major-axis; – – –, along the minor-axis.

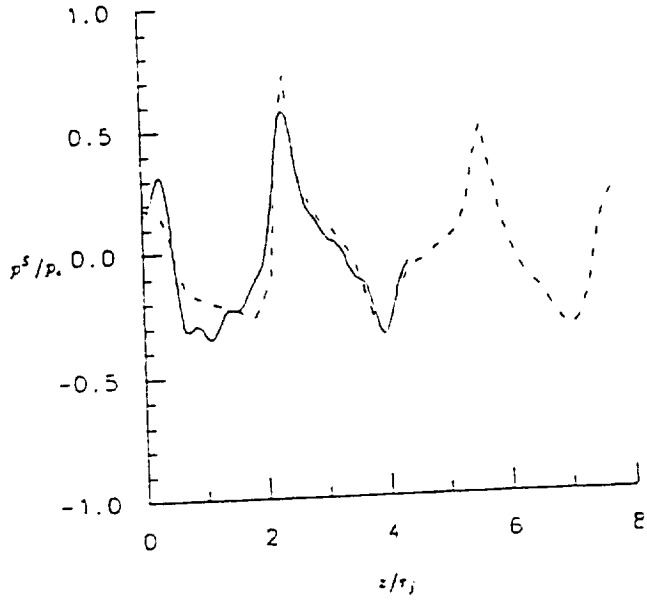

Fig. 4 Centerline Axial Pressure Distribution for Elliptic Jet, M_j=1.64, M_d=1.52. ——, present calculations; – – –, measured data of ref. 21.

the pressure amplitudes are in fairly good agreement. It should be noted that the numerical results presented in Figs. 4 and 5 have been calculated by shifting the results

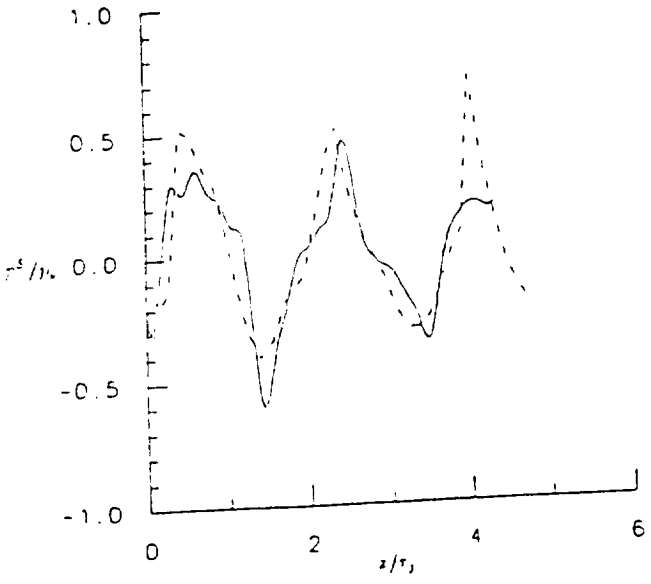

Fig. 5 Centerline Axial Pressure Distribution for Elliptic Jet, M_j=1.36, M_d=1.52. ——, present calculations; – – –, measured data of ref. 21.

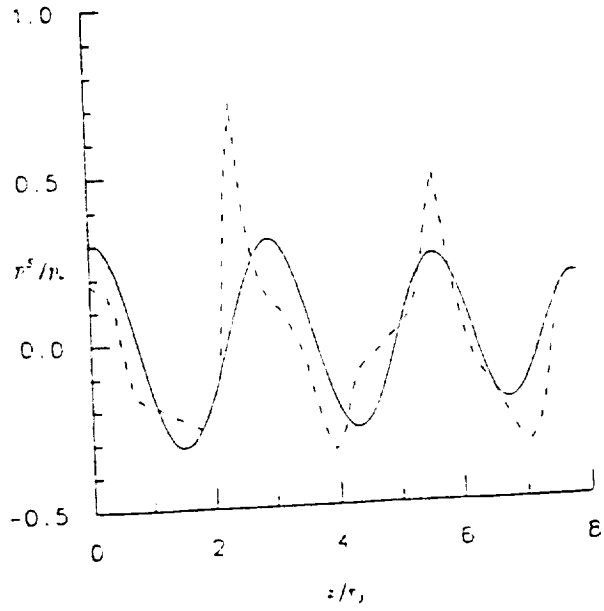

Fig. 6 Centerline Axial Pressure Distribution for Elliptic Jet, M_j=1.64, M_d=1.52. ——, mode 01; – – –, measured data of ref. 21

by about half an equivalent diameter in the axial direction. This is done to account for the unknown location of virtual origin of the shear layer. Clearly, the present model being relatively simple, cannot effectively model the initial development of the jet as the flow transitions from the nozzle dimensions to the fully expanded jet. It should be noted that the potential core is much shorter for the elliptic jet compared to a circular jet at the same operating conditions. For example, from Fig. 2, it can be seen that $h_2 \approx 0$ for $z/r_j \approx 12$. Also, the calculations in Fig. 4 stop at $z/r_j = 4.5$. Beyond that point convergence could not be obtained for the eigenvalues of the higher order modes.

In Figs. 6 and 7, the fundamental mode (mode 01) for the two cases are compared with the measurements. No axial shift has been applied to the predictions in Fig. 7. These figures show that the shock cell spacing can be approximated to a reasonable extent by the fundamental mode alone. However, the amplitudes of the shock cells cannot be predicted by this mode alone. In order to get a better description, a greater number of modes as in Figs. 4 and 5 need to be considered.

As mentioned earlier, non-circular jets have been considered with a view to achieving better aeroacoustic characteristics. Thus, comparisons of the axial pressure distribution of circular and elliptic jets operating under identical conditions have been made. Figures 8 and 9 show this comparison for both the underexpanded and

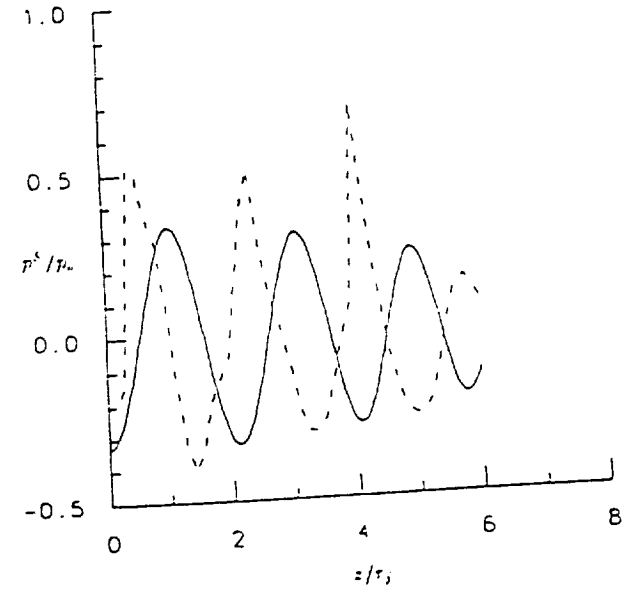

Fig. 7 Centerline Axial Pressure Distribution for Elliptic Jet, M_j=1.36, M_d=1.52. ——, mode 01; – – –, measured data of ref. 21

the overexpanded jets. In the case of circular jet, the axial pressure distributions are made up of a linear combination of the first six modes of the shock cell model.

These modes are given by the various zeroes of the Bessel function, J_0, and their amplitudes at the jet exit is given by eqn. (2.1) in Tam, Jackson and Seiner[10]. These figures show that the shock cell amplitudes as well as the shock cell spacings are less for the elliptic jet case. This suggests that the amplitude of broadband shock associated noise might be reduced in the elliptic jet case. However, since the decrease is relatively small in absolute terms it is likely to have a negligible effect on the radiated noise calculated in decibels.

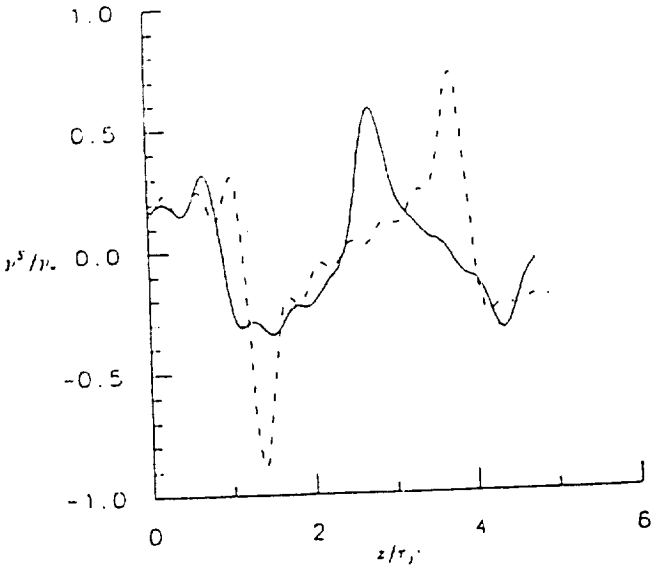

Fig. 8 Variation of Axial Pressure Distribution with Aspect Ratio, r/d=0.0, M_j=1.64, M_d=1.52. ——, 2:1 Elliptic Jet; - - -, Circular Jet.

5. Summary

In this paper a linear model has been used to predict the shock cell structure in non-circular jets. A conformal mapping technique with a pseudo-spectral hybrid scheme has been used to calculate the wavelength and decay rate of the shock cell modes. Predictions have been obtained for a circular jet and an elliptic jet of aspect ratio 2. The numerical scheme used here has been shown to be more successful than the earlier scheme of Morris and Bhat[13] in obtaining converged solutions for the elliptic jet. The axial variation of the various modes contributing to the shock cells for the elliptic jet has been observed to behave in a fashion similar to those of a circular jet. The amplitudes and the shock cell spacings for the elliptic jet have been found to be less than those for a circular jet for identical operating conditions. These changes are likely to result in negligible

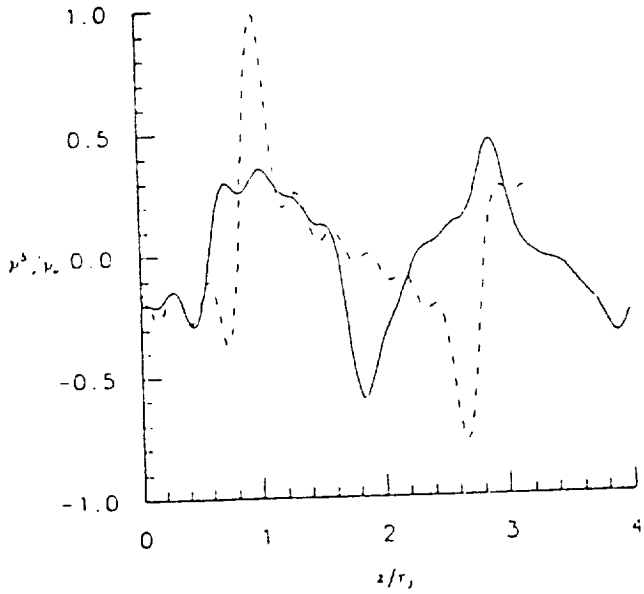

Fig. 9 Variation of Axial Pressure Distribution with Aspect Ratio, r/d=0.0, M_j=1.36, M_d=1.52. ——, 2:1 Elliptic Jet; - - -, Circular Jet.

direct benefits in noise reduction. However, additional benefits of the elliptic geometry could result due to a modification of the jet's turbulent structure or a reduction in the supersonic region of the jet. These mechanisms are being explored by the authors.

Acknowledgements

This work was supported by NASA Langley Research Center under NASA Grant NAG-1-657. The technical monitor is Dr. J. M. Seiner.

References

1. Harper-Bourne, M. and Fisher, M. J., "The Noise from Shock Waves in Supersonic Jets," 1973, Proceedings (No. 131) of the AGARD Conference on Noise Mechanisms, Brussels, Belgium.
2. Tanna, H. K., "An Experimental Study of Jet Noise. Part II: Shock Associated Noise," *Journal of Sound and Vibration*, Vol. 50, 1977, pp. 429-444.
3. Seiner, J. M. and Norum T. D., "Experiments on Shock Associated Noise of Supersonic Jets," *AIAA Paper* 79-1526, 1979.
4. Seiner, J. M. and Norum T. D., "Aerodynamic Aspects of Shock Containing Jet Plumes," *AIAA Paper* 80-1965, 1980.
5. Seiner, J. M. and Yu, J. E., "Acoustic Near and Local Flow Properties Associated with Broadband Shock Noise," *AIAA Paper* 81-1975, 1981.
6. Norum, T. D. and Seiner, J. M., "Broadband Shock

Noise from Supersonic Jets," *AIAA Journal*, Vol. 20, 1982, pp. 68-73.

7. Norum, T. D. and Seiner, J. M., "Measurements of Mean Static Pressure and Far Field Acoustics of Shock containing Supersonic Jets," *NASA TM-84521*, 1982.
8. Tam, C. K. W. and Tanna, H. K., "Shock Associated Noise of Supersonic Jets from Convergent-Divergent Nozzles," *Journal of Sound and Vibration*, Vol. 81(3), 1982, pp. 337-358.
9. Tam, C. K. W., "Stochastic Model Theory of Broadband Shock Associated Noise from Supersonic Jets," *Journal of Sound and Vibration*, Vol. 116, 1987, pp. 265-302.
10. Tam, C. K. W., Jackson, J. A. and Seiner, J. M., "A Multiple-Scales Model of the Shock-Cell Structure of Imperfectly Expanded Supersonic Jets," *Journal of Fluid Mechanics*, Vol. 153, 1985, pp.123-149.
11. Tam, C. K. W., "On the Screech Tones of Supersonic Rectangular Jets, " *AIAA Paper* 86-1866, 1986.
12. Morris, P. J., Bhat, T. R. S. and Chen, G., "A Linear Shock Cell Model for Jets of Arbitrary Exit Geometry," *Journal of Sound and Vibration* , Vol. 132, 1989, pp. 199-211.
13. Morris, P. J. and Bhat, T. R. S., "Shock Structure in Non-Circular Jets," *AIAA Paper* 89-1083, 1989.
14. Wegmann, R., "An Iterative Method for the Conformal Mapping of Doubly Connected Regions," *Numerical Conformal Mapping* (ed. Trefethen, L. N.), North- Holland, 1986, pp. 79-98.
15. Baty, R. S., "Reynolds Stress Closure in Jet Flows using Instability Wave Modeling," Ph.D Dissertation, 1989, The Pennsylvania State University.
16. Bhat, T. R. S., "Linear Models for the Shock Cell Structure of Supersonic Jets with Non-Circular Exit geometries," Ph.D Dissertation, 1990, The Pennsylvania State University.
17. Eiseman, P. R., "Geometric Methods in Computational Fluid Dynamics," *ICASE Report No.* 80-11, 1980.
18. Gottlieb, D., Hussaini, M. Y. and Orszag, S. A., "Introduction: Theory and Applications of Spectral Methods," *Spectral Methods for Partial Differential Equations* (ed. Voigt, R. G., et al.), SIAM, 1984, pp. 1-54.
19. Morris, P. J., "The Spatial Viscous Instability of Axisymmetric Jets," *Journal of Fluid Mechanics*, Vol. 77, 1976, pp. 511-529.
20. Tam, C. K. W. and Morris, P. J., "Tone Excited Jets, Part V: A Theoretical Model and Comparison with Experiment," *Journal of Sound and Vibration*, Vol. 102, 1985, pp. 119-151.
21. Seiner, J. M., Ponton, M. K. and Baty, R. S., Private Communications.
22. Birch, S. F. and Eggers, J. M., "A Critical Review of the Experimental Data for Developed Turbulent Free Shear Layers," *NASA SP*-321, Vol. 1.
23. Prandtl, L., "Uber die Stationaren Wellen in einem Gasstrahl," *Phys. Zeit.*, Vol. 5, 1904, pp. 599-601.
24. Pack, D. C., "A Note on Prandtl's formula for the Wavelength of a Supersonic Gas Jet," *Q. J. Mech. Appl. Maths.*, Vol. 3, 1950, pp. 173-181.
25. Mclachlan, N. W., *Theory and Applications of Mathieu Functions*, Oxford University Press, 1947.
26. Norum, T. D. and Seiner, J. M., "Measurements of Mean Static Pressure and Far Field Acoustics of Shock Containing Supersonic Jets," *NASA TM-84521*, 1982.

Appendix I

The Instability of Elliptic Jets

P. J. Morris

Instability of Elliptic Jets

Philip J. Morris

Pennsylvania State University, University Park, Pennsylvania*

Abstract

This paper presents a detailed account of the hydrodynamic stability characteristics of the initial region of an elliptic jet. A realistic mean velocity profile is used. Calculations of growth rates, phase velocities and eigenfunctions are presented. The growth rates of all modes in the initial mixing region are found to depend on the minimum momentum thickness. Pressure fluctuations are found to be greatest for all modes close to the major axis. An irregular normal mode is found at larger eccentricities. All modes, odd or even about the major axis and with periods of π or 2π have similar growth rates in the initial mixing region.

* Professor, Department of Aerospace Engineering, Member AIAA

Introduction

This paper presents a detailed account of the hydrodynamic stability characteristics of an elliptic jet in the initial mixing region. The results of the analysis serve two purposes. First, they provide a reference case for the verification of analyses that consider jets of arbitrary shape. Second, they provide some insight into the initial development of large-scale coherent structures in a turbulent, elliptic jet. In a previous paper, ref. 1, the author presented some preliminary calculations. The present paper extends those calculations and corrects some misinterpretations.

Purely round jet geometries are the exception rather than the rule in practical applications. Jet engine exhausts are fitted with mixing devices to reduce noise and decrease the length of the exhaust plume. Non-circular exhausts also occur in V/STOL applications in enhanced lift and thrust-vectoring devices. The enhanced mixing properties of non-circular jets make them attractive components for fuel-injection and high-speed combustion. A number of recent experimental investigations have been conducted to examine the properties of non-circular jets[2-8]. At low Reynolds number an elliptic jet develops in an unusual fashion as the major and minor axes of the jet switch several times with downstream distance. This may be associated with the mutual interaction of adjacent elliptic toroidal vortices. At high Reynolds number the number and location of any axis-switching remains unclear. However, in this case, experience has shown that the gross properties of the large-scale structures in the turbulent mixing layer may be modeled as instability waves. This approach has led to a better understanding of jet mixing noise radiation in high speed jets [9], and the effect of acoustic excitation on the development of turbulent jets[10]. Detailed comparisons between the predictions of instability-wave models and turbulence in mixing layers[11] and wakes[12] have also been made.

Thus a knowledge of the stability characteristics of an elliptic jet should provide a description of the gross features of the large-scale structures in such a flow.

Crighton[13] examined the stability of an elliptic jet with a "top-hat" velocity profile. He obtained some solutions for large eccentricity, in which limit the jet had stability characteristics similar to those of a two-dimensional jet. Calculations for a wide range of eccentricities for this vortex sheet representation were obtained by Morris and Miller[1]. Their numerical results supported Crighton's asymptotic solutions. However, the vortex sheet approximation is only valid in the low-wavenumber limit. It indicates instability at all frequencies. The observed limited bandwidth of unstable frequencies is determined by the finite width of the mixing region. Only by using realistic mean velocity profiles can a most-unstable or neutral frequency be obtained. Thus in the present paper the stability of an elliptic jet represented by a continuous axial velocity profile will be considered.

A numerical method for the calculation of the stability characteristics of jets of arbitrary shape has been developed by Koshigoe and Tubis[14]. Their calculations for an elliptic jet compared favorably with the earlier calculations of ref. 1. The integral approach that they use suffers from limitations in accuracy as will be shown below. However, the technique does not depend on the separability of the stability equations and is thus a very attractive approach.

In this paper the stability characteristics of elliptic jets are documented for several eccentricities. The numerical solution requires the evaluation of modified Mathieu functions for arbitrary complex argument. Both eigenvalues and eigenfunctions are presented. In the next section the stability equation in elliptic cylindrical coordinates and the asymptotic forms of solution that satisfy the boundary condi-

tions are developed. The numerical evaluation of these asymptotic solutions is then described. The stability characteristics of an elliptic jet in the initial region are then given. Finally, the relationship between these calculations and the development of a realistic elliptic jet is discussed.

Analysis

A jet flow is considered issuing from an elliptic nozzle. The problem will be developed in elliptic cylindrical coordinates (ρ, θ, z). These are related to the Cartesian system by:

$$\begin{aligned} x &= a \cosh\rho \cos\theta \\ y &= a \sinh\rho \sin\theta \\ z &= z. \end{aligned} \tag{1}$$

The jet axis is aligned with the z direction and the axial mean velocity of the jet $W(\rho, \theta)$ is assumed to be a function of ρ and θ only. This is the parallel flow approximation of hydrodynamic stability. This assumption leads to the leading order problem in a multiple-scales analysis to include the effects of flow divergence. These effects are not considered in the present analysis.

A Poisson equation for the pressure is obtained by taking the divergence of the momentum equation and using the equation of continuity. The resulting equation is linearized about the mean flow. The velocity fluctuations are eliminated in favor of the pressure fluctuation using the linearized momentum equations. If the pressure fluctuation is written in the form,

$$p(\rho, \theta, z, t) = \hat{p}(\rho, \theta) \exp[i(\alpha z - \omega t)], \tag{2}$$

then the equation for $\hat{p}$ may be written,

$$\frac{\partial^2 \hat{p}}{\partial \rho^2} + \frac{\partial^2 \hat{p}}{\partial \theta^2} + \frac{2\alpha}{\Omega}\left\{\frac{\partial W}{\partial \rho}\frac{\partial \hat{p}}{\partial \rho} + \frac{\partial W}{\partial \theta}\frac{\partial \hat{p}}{\partial \theta}\right\} - \frac{\alpha^2 a^2}{2}\left[\cosh(2\rho) - \cos(2\theta)\right]\hat{p} = 0, \qquad (3)$$

where $\Omega = \omega - \alpha W$.

If W is taken to be a function of the "radial" coordinate ρ only then a separable form of solution may be sought. This separation is valuable in that highly accurate stability calculations may be performed without excessive computation. However, as will be seen below, this results in a link between the momentum thickness distribution of the mean flow and the eccentricity of the jet which may not be physically realistic.

If a solution for $\hat{p}$ is sought in the form $\hat{p} = R(\rho)T(\theta)$ then T and R are found to satisfy,

$$\frac{d^2 T}{d\theta^2} + \left[\lambda - 2q\cos(2\theta)\right]T = 0, \qquad (4)$$

and

$$\frac{d^2 R}{d\rho^2} + \frac{2\alpha}{\Omega}\frac{dW}{d\rho}\frac{dR}{d\rho} - \left[\lambda - 2q\cosh(2\rho)\right]R = 0, \qquad (5)$$

where $q = -\alpha^2 a^2/4$ and λ is a separation constant. In general q is complex. Equation (4) is Mathieu's equation. Equation (5) is the Rayleigh equation in elliptic cylindrical coordinates and reduces to the modified Mathieu equation in regions where W is constant.

The solutions of eqn. (4) are of four types that are odd or even in θ and with period π or 2π. Details of the evaluation of the Mathieu and modified Mathieu functions and their characteristic numbers are given in refs. 15 and 16. The notation given by Abramovitz and Stegun[16] is used in the present analysis. The characteristic numbers were obtained numerically as the eigenvalues of the matrix

for the coefficients of the sine or cosine series of the Mathieu functions (see ref. 16, eqns. 20.2.2–20.2.11). The series was truncated after 11 terms. This gave 8 decimal places of accuracy for all the values that could be compared with tabulated values[16]. The modified Mathieu functions were obtained from a series of products of Bessel functions (see ref. 16, eqns. 20.6.7–20.6.10).

Only certain combinations of these functions permit the physical boundary conditions to be satisfied. These were determined by Crighton[13]. In the ambient fluid surrounding the jet the pressure fluctuation must vanish as $\rho \to \infty$. This leads to the following forms of solution.

$$\hat{p}(\rho,\theta) \to \begin{cases} A\ \mathrm{ce}_{2r+p}(\theta)\ \mathrm{Mc}^{(3)}_{2r+p}(\rho) \\ A\ \mathrm{se}_{2r+p}(\theta)\ \mathrm{Ms}^{(3)}_{2r+p}(\rho). \end{cases} \tag{6}$$

$Mc^{(3)}$ and $Ms^{(3)}$ are Mathieu–Hankel functions. If $p = 0$ the solutions are of period π, if $p = 1$ the solutions are of period 2π.

The interfocal line $\rho = 0$ extends from $(x, y) = (-a, 0)$ to $(a, 0)$. If the pressure and velocity components are to be continuous across the interfocal line then the solution for $\hat{p}(\rho,\theta)$ for small ρ must take the form,

$$\hat{p}(\rho,\theta) = \begin{cases} B\ \mathrm{ce}_{2r+p}(\theta)\ \mathrm{Ce}_{2r+p}(\rho) \\ B\ \mathrm{se}_{2r+p}(\theta)\ \mathrm{Se}_{2r+p}(\rho). \end{cases} \tag{7}$$

This gives the asymptotic form of the solution within the potential core of the jet.

Crighton[13] considered the case of a vortex-sheet representation of the jet flow. That is,

$$W(\rho) = \begin{cases} W_0 & \text{for} \quad \rho < \rho_0, \\ 0 & \text{for} \quad \rho > \rho_0. \end{cases} \tag{8}$$

Continuity of pressure and particle displacement at the vortex sheet requires that,

$$\Delta[\hat{p}] = 0 \qquad ; \qquad \Delta\left[\frac{\partial \hat{p}}{\partial \rho}\right] = 0, \tag{9}$$

where $\Delta[\quad]$ denotes the change across the discontinuity. Application of these conditions for the forms of solution given by eqns. (6) and (7) leads to a set of dispersion relationships. For the even modes these take the form,

$$\frac{\mathrm{Ce}'_{2r+p}(\rho_0)\mathrm{Mc}^{(3)}_{2r+p}(\rho_0)}{\mathrm{Ce}_{2r+p}(\rho_0)\mathrm{Mc}^{(3)\,\prime}_{2r+p}(\rho_0)} = \left[1 - \frac{\alpha W_0}{\omega}\right]^2, \tag{10}$$

where primes denote differentiation with respect to ρ. A similar result may be obtained for the odd solutions. Crighton [13] obtained asymptotic solutions for these relationships for large eccentricities. Morris and Miller[1] solved eqn. (10) numerically for a wide range of eccentricities. They showed that as the eccentricity increased the growth rates of the even modes decreased but those of the odd modes, in particular $2r + p = 1$, increased. This could be interpreted to mean that as the jet's eccentricity increases the preferred mode would switch from being in phase around the jet, such as the axisymmetric mode in the round jet, to being out of phase about the major axis, such as the antisymmetric mode in the two-dimensional jet. However, these conclusions should only be valid at very low frequencies in a real jet. These deficiencies are addressed below where a mean velocity profile with finite thickness is considered.

Calculations

The mean velocity profile

The mean velocity profile considered is analogous to that chosen by Michalke[17] to describe the initial mixing region of a circular jet. For the elliptic jet the profile is taken to be

$$W(\rho) = \begin{cases} 1 & 0 \le \rho \le \rho_i \\ \frac{1}{2}\left[1 + \tanh\left\{B(1 - \sinh\rho/\sinh\rho_0)/2\theta_B\right\}\right] & \text{for} \quad \rho > \rho_i \end{cases} \tag{11}$$

A and B are the lengths of the semi-major and semi-minor axes of the ellipse defined by $\rho = \rho_0$ and θ_B is the momentum thickness along the minor axis given by,

$$\theta_B = \int_0^\infty W(1-W)dy \quad : \quad x = 0. \tag{12}$$

In eqn. (12) ρ_i is chosen such that $\tanh\{B(1-\sinh\rho_i/\sinh\rho_0)/2\theta_B\}$ is close to unity and ρ_0 is the half-velocity point. Since the minimum value of ρ is zero this condition can be met if θ_B/B is sufficiently small. The velocity profile given by eqn. (11) reduces to Michalke's[17] profile in the case of a circular jet. The profile was chosen by Michalke on the basis of comparison with experimental data rather than being a solution of the equations of motion. As such it is a local representation, consistent with the parallel flow approximation of the stability analysis. Axial variations are included parametrically through the dependence of θ_B and B on z. The validity of this choice of profile may be seen by comparing with the experimental data of Ho and Gutmark[8]. Figure 1 shows a comparison made at two axial locations $z/A_0 = 0.5$ and 2.0, where A_0 is the semi-major axis length at the jet exit. The local values of A/B based on the locations of the half velocity points are 1.88 and 1.49 respectively. The corresponding values of θ_B/B were found to be 0.044 and 0.223. The agreement between the analytical profile and the experimental data is reasonably good except in the inner part of the mixing region along the minor axis for the downstream location.

The momentum thickness along the major axis is defined by

$$\theta_A = \int_0^\infty W(1-W)dx \quad : \quad y = 0. \tag{13}$$

It can be shown that,

$$A\theta_A = B\theta_B[1 + \text{terms of order } (\theta_B/B)^2]. \tag{14}$$

Thus as the eccentricity of the jet increases the momentum thickness on the minor axis becomes greater than that on the major axis. This is a consequence of requiring that W be a function of ρ only so that a separable solution can be obtained. In practice this linkage between eccentricity and momentum thickness ratio will not exist. In that sense the profile is somewhat unrealistic. However the benefits of obtaining highly accurate solutions to the separable problem are felt to justify the present approach.

Numerical method

The Rayleigh equation (5) was solved numerically using a variable step-size Runge-Kutta algorithm (IMSL routine DVERK modified for complex arithmetic). For a given value of frequency and initial guess for the wavenumber two integrations were performed starting from ρ_1 and ρ_2, at which $W = 0.001$ and 0.999 respectively, toward the center of the mixing region. The starting conditions were based on the asymptotic solutions (6) and (7). The resulting numerical solutions at $\rho = \rho_0$ are denoted by $R_1(\rho_0)$ and $R_2(\rho_0)$. The two solutions and their derivatives much match at $\rho = \rho_0$, that is,

$$\begin{aligned} C_1 R_1(\rho_0) - C_2 R_2(\rho_0) &= 0 \\ C_1 R_1'(\rho_0) - C_2 R_2'(\rho_0) &= 0 \end{aligned} \tag{15}$$

If eqn. (15) is to have a non-trivial solution for C_1 and C_2,

$$\nabla(\omega, \alpha) = R_1(\rho_0) R_2'(\rho_0) - R_1'(\rho_0) R_2(\rho_0) = 0. \tag{16}$$

Newton's method was used to find the zeroes of $\nabla(\omega, \alpha)$ and hence the eigenvalues α.

Calculations were performed for both odd and even modes about the major axis with periods π and 2π. The variables were non-dimensionalized with respect to the

jet exit velocity, the radius of a circular jet of equal exit area $\sqrt{AB}$ and the uniform density. Unless stated otherwise all calculations were for a momentum thickness on the major axis of $\theta_A = 0.02$. However, it should be remembered that the momentum thickness on the minor axis varies according to eqn. (14). Calculations have been performed for three eccentricities: $A/B = 1.001$, $A/B = 2.0$ and $A/B = 4.0$. The first case permits comparison of the results with the circular jet case. The areas within the contours of $\rho = \rho_0$, which are the contours of the half-velocity points, were held constant.

The ce_0 mode

The ce_0 mode corresponds to the axisymmetric $m = 0$ mode in the circular jet case. Figure 2 shows the axial growth rates α_i for the ce_0 mode as the eccentricity changes. The results for $A/B = 1.001$ are very close to the circular jet results[18]. The maximum growth rate decreases as A/B increases. However the frequency for the maximum growth remains nearly independent of eccentricity. Table I gives this frequency and the corresponding wavenumber for several modes and values of A/B. If the frequencies for maximum growth are non-dimensionalized with respect to the major axis momentum thickness θ_A the values for $\omega_{max}\theta_A$ are 0.109, 0.113 and 0.113 for $A/B = 1.001$, 2.0 and 4.0 respectively. This suggests that the initial shedding frequency is controlled by the minimum momentum thickness, along the major axis in the present case, and is nearly independent of eccentricity. This is confirmed by the measurements of Husain and Hussain[2] and Gutmark and Ho[3,4]. In the former experiments the momentum thickness was nearly independent of azimuthal position whereas in the latter experiments $\theta_B = 0.8\theta_A$.

Figure 3 shows the variation of the phase velocity with A/B for the ce_0 mode.

For $A/B = 1.001$ the mode exhibits phase velocities greater than the exit velocity that were discussed by Bechert and Pfizenmaier[19]. In general, increasing the eccentricity makes the phase velocities less dependent on frequency. Table I shows that the phase velocity for ω_{max} increases with increasing A/B.

In the round jet, the amplitude of the azimuthal modes are independent of the azimuthal location. However the behavior of modes for the elliptic jet is different. Firstly, as discussed further below, the modes are not "spinning" but have a fixed phase reference to the major or minor axes. Secondly the azimuthal variation is determined by the behavior of the Mathieu function that is the solution of eqn. (4). As A/B approaches unity q approaches zero, since a goes to zero. Then the solutions to eqn. (4) are either sines or cosines. However for larger values of A/B, q is a complex number with phase determined by the complex wavenumber α. In this case the amplitude of the ce_0 mode is no longer independent of azimuthal location. Figure 4 shows the azimuthal variation of $|T(\theta)|$ for the various eccentricities for the maximum amplifying frequency in each case. For $A/B = 1.001$ the amplitude is nearly independent of θ. This is the axisymmetric mode behavior for the round jet. For $A/B = 2.0$ and 4.0 the amplitude decays rapidly away from the major axis and is essentially zero on the minor axis. This would indicate that close to the jet exit the pressure and velocity fluctuations associated with the ce_0 mode would be greatest near to the major axis. However, because of the form of velocity profile chosen this is also the location of the minimum momentum thickness. For uniform momentum thickness around the jet exit it is not clear that this behavior would be seen. The variation of $R(\rho)$ with eccentricity is shown in Fig. 5. The distribution is plotted along the major axis relative to the half-velocity point and stretched by the major axis momentum thickness θ_A. The distributions, plotted in this way, are

nearly independent of eccentricity. Thus those motions observed in the round jet will be duplicated in the elliptic jet except that the amplitude may vary azimuthally.

The ce_{2r} modes

In addition to the ce_0 mode there are other even modes of period π that are unstable in the initial mixing region. Figure 6 shows the axial growth rates for these ce_{2r} modes for $r = 0$, 1 and 2 for $A/B = 1.001$. From this figure and the numerical values given in Table 1 it is clear that the higher-order modes have similar but smaller growth rates than the ce_0 mode. The azimuthal variation of these modes for $A/B = 1.001$ is given approximately by $\cos(2r\theta)$. The ce_2 mode corresponds to the $n = 2$ double helix in the round jet calculations of Mattingly and Chang[20]. However it should be emphasized that all the modes in the elliptic jet case are phase-locked with respect to the major and minor axes and are not spinning modes. This means that any jet that deviates slightly from axisymmetry in the mean is likely to exhibit "flapping" rather than spinning modes.

Koshigoe and Tubis[14] have also calculated the stability of these higher-order modes. However the accuracy of their technique, designed for non-separable problems, is limited by their two-dimensional grid. In the present calculation the solutions are analytic in the azimuthal direction and use a variable step-size to achieve a prescribed accuracy in the "radial" direction. However, in spite of the relatively crude nature of their grid, the results in ref. 14 show all the qualitative characteristics of the present results.

The se_1 mode

The modes that reduce to the helical, $n = 1$ mode in the round jet case are the se_1 and ce_1 modes. They have azimuthal variations that reduce to $\sin\theta$ and

$\cos\theta$ respectively. The variation of the axial growth rates for the se_1 mode for various eccentricities is shown in Fig. 7. For $A/B = 4.0$ the maximum growth rate for the se_1 mode is slightly less than that of the ce_0 mode. The most-amplifying frequencies for the se_1 mode are also slightly lower than the ce_0 modes. The value of ω_{max} falls from 0.1091 to 0.0704 (when scaled by the momentum thickness θ_A) as A/B changes from 1.001 to 4.0. The phase velocities, shown in Fig. 8 are always less than the jet exit velocity. For $A/B = 1.001$ the results agree closely with the values for the $n = 1$, helical mode in the round jet. At the most amplifying frequency the phase velocities are approximately one half the jet velocity (see Table I). As the eccentricity increases the phase velocities become less dependent on frequency.

For $q = 0$, the round jet limit, the se_1 Mathieu function has its maximum value at $\theta = \pm\pi/2$. However for other values of q this changes. Figure 9 shows the azimuthal variation of $|T(\theta)|$ for various eccentricities. As was found in the ce_0 mode case the amplitude falls to zero at the minor axis as the eccentricity increases. Thus the pressure and velocity fluctuations associated with this mode will also be greater close to the major axis (for the present choice of mean velocity profile).

The se_{2r+1} modes

The higher-order odd modes with period 2π, the se_{2r+1} modes, exhibit an interesting behavior. For real or small q the characteristic numbers of Mathieu's equation are readily classified. However, for complex q pairs of these characteristic numbers are equal. The location of these branch points has been examined by Hunter and Guerrieri[21]. The asymptotic formulae used to calculate the characteristic numbers changes as one crosses a branch cut that extends radially outward from the branch point in the complex plane (see Fig. 4, ref. 21). Across these branch cuts

the characteristic numbers exchange their order. This leads to an unusual behavior for the se_{2r+1} modes for higher eccentricities. The characteristic numbers and the associated normal modes may be classified initially according to the eigenvalue sequence provided by the IMSL routine. Figure 10 shows the complex value of $c = \omega/\alpha$ for the first four characteristic numbers in the sequence. The eigenvalues fall into several groups. There are three continuous sequences associated with the second and first, third and second, and fourth and third characteristic numbers. There is clearly another sequence with a different behavior in the c-plane that has contributions from all the characteristic numbers. This sequence could be thought of as indicating an "irregular" mode, though it does not have the same features as the irregular mode described by Michalke[22]. In the present case the higher-order odd modes have been classified by number if they fall into the smooth sequences shown in Fig. 10 or as irregular if they do not. This leads to the axial growth rates and phase velocities shown in Figs. 11 and 12 respectively for $A/B = 2.0$. The maximum growth rate is still associated with the se_1 mode. All the modes have similar phase velocities in the range 0.5 to 0.8 and the dependence on frequency decreases as the mode number increases. Though it appears likely that the appearance of the irregular mode is associated with the branch points of the characteristic numbers of Mathieu's equation, the mode-switching does not always occur near the branch cuts identified by Hunter and Guerrieri[21]. So the appearance of the irregular mode remains unexplained.

The ce_{2r+1} modes

The ce_{2r+1} modes are even about the major axis and have a period 2π. They may be identified with a flapping motion about the minor axis in the elliptic jet. The ce_1 mode corresponds to the $n = 1$, helical mode in the round jet. From Table

l it can be seen that the ce_1 and se_1 modes have almost identical characteristics, approaching the $n = 1$, helical mode values, as the round jet limit is approached. The ce_1 and se_1 modes behave very similarly as the eccentricity changes with the exception that the frequency of the most-amplifying mode is nearly independent of the eccentricity for the ce_1 mode. In view of the similarity between the two modes the growth rates and phase velocities are not shown but the most-amplifying frequencies and wavenumbers are given in Table I.

Discussion

The present results, subject to the particular mean velocity profile, indicate that no particular mode is dominant in the initial mixing region and that the stability characteristics are controlled by the minimum initial momentum thickness, which in the present case always lies on the major axis. In a given experiment the selection of a particular mode will depend on external influences, such as intended or unintended forcing or a feed-back based on the preferred mode of the entire jet flow field.

Michalke[23] and others have shown how the process of vortex pairing may be simulated qualitatively using linear stability theory. Such calculations can describe the initial mixing region of a low Reynolds number jet or an artificially excited jet at higher Reynolds number. Consider the ce_0 mode which corresponds to the axisymmetric mode in the round jet case. In the preceding section it was shown that the "radial" eigenfunctions for this mode were independent of eccentricity, see Fig. 5. Thus the same processes observed in the round jet should occur in the elliptic jet. However, in the elliptic jet the amplitude of these motions was seen to be dependent on the azimuthal location. For the ce_0 mode the amplitude is a

maximum on the major axis and falls rapidly to zero on the minor axis. Thus it could be speculated that a vortex roll-up would occur on the major axis but no such motions would be seen on the minor axis. Such vortex motions, which resulted in a switching of the jet's major and minor axes, were observed by Husain and Hussain[2] and Gutmark and Ho[6]. However, these processes occur in regions where the jet is developing rapidly and the thickness of the mixing layer is increasing.

The primary purpose of this paper has been to establish the stability characteristics of a non-circular jet. The choice of mean velocity profile enabled the stability equation to be separated so that highly accurate solutions could be obtained to the resulting ordinary differential boundary value problem. The particular choice of velocity profile resulted in an initial momentum thickness that varied around the jet, being a minimum on the major axis and a maximum on the minor axis. This situation could be different in a given experiment as it was in the measurements of Husain and Hussain[2] and Gutmark and Ho[3]. However the results given in the preceding sections should serve as a test of the accuracy of numerical methods that describe the stability of jet flows of arbitrary shape.

Acknowledgements

This work was supported in part by NASA Langley Research Center under NASA Grant NAG-1-657. The co-technical monitors are Drs. J. M. Seiner and R. G. Wilmoth. The author is also grateful to Prof. C.-M. Ho for supplying his experimental data and Dr. S. Koshigoe for copies of his results. The original Mathieu function routines were written by Mr. D. G. Miller.

References

[1]Morris, P. J. and Miller, D. G., "Wavelike Structures in Elliptic Jets," AIAA Paper 84-0399, 1984.

[2]Husain, H. S. and Hussain, A. K. M. F., "Controlled Excitation of Elliptic Jets," *Physics of Fluids*, Vol. 26, October 1983, pp. 2763-2766.

[3]Gutmark, E. and Ho, C.-M., "Near-Field Pressure Fluctuations of an Elliptic Jet," *AIAA Journal*, Vol. 23, 1984, pp. 354-358.

[4]Schadow, K. C., Wilson, K. J., Lee, M. J., and Gutmark, E., "Enhancement of Mixing in Ducted Rockets with Elliptic Gas-Generator Nozzles," AIAA Paper 84-1260, 1984.

[5]Gutmark, E., Schadow, K. C., Parr, D. M., Harris, C. K., and Wilson, K. J., "The Mean and Turbulent Structure of Noncircular Jets," AIAA Paper 85-0543, 1985.

[6]Gutmark, E. and Ho, C.-M., "Visualization of a Forced Elliptic Jet," *AIAA Journal*, Vol. 24, 1985, pp. 684-685.

[7]Schadow, K. C., Wilson, K. J., Parr, D. M., and Gutmark, E., "Mixing Characteristics of a Ducted Elliptical Jet with Dump," AIAA Paper 86-1399, 1986.

[8]Ho, C.-M. and Gutmark, E., "Vortex Induction and Mass Entrainment in a Small Aspect Ratio Elliptic Jet," submitted for publication, 1987.

[9]Tam, C. K. W. and Morris, P. J., "The Radiation of Sound by the Instability Waves of a Compressible Plane Turbulent Shear Layer," *Journal of Fluid Mechanics*, Vol. 98, 1980, pp. 349-381.

[10]Tam, C. K. W. and Morris, P. J., "Tone Excited Jets, Part V: A Theoretical Model and Comparison with Experiment," *Journal of Sound and Vibration*, Vol. 102, 1985, pp. 119–151.

[11]Tam, C. K. W. and Chen, K. C., "A Statistical Model of Turbulence in Two-Dimensional Mixing Layers," *Journal of Fluid Mechanics*, Vol. 92, 1979, pp. 303–326.

[12]Gaster, M., Kit, E., and Wygnanski, I., "Large-Scale Structures in a Forced Turbulent Mixing Layer," *Journal of Fluid Mechanics*, Vol. 150, 1985, pp. 23–39.

[13]Crighton, D. G., "Instability of an Elliptic Jet," *Journal of Fluid Mechanics*, Vol. 59, 1973, pp. 665–672.

[14]Koshigoe, S. and Tubis, A., "Wave Structures in Jets of Arbitrary Shape. I. Linear Inviscid Spatial Stability Analysis," submitted for publication, 1986.

[15]McLachlan, N. W., *Theory and Application of Mathieu Functions*, Oxford University Press, 1947.

[16]Abramowitz, M. and Stegan, I. A., Handbook of Mathematical Functions, Dover, 1965.

[17]Michalke, A., "Instabilitat eines kompressiblen runden Friestrahls unter Berucksichtigung des Einfluses der Strahlgrenzschichtdicke." *Z. Flugwiss.*, Vol. 19, 1971, pp. 319–328.

[18]Morris, P. J., "The Spatial Viscous Instability of Axisymmetric Jets," *Journal of Fluid Mechanics*, Vol. 77, 1976, pp. 511–529.

[19]Bechert, D. and Pfizenmaier, E., "On Wavelike Perturbations in a Freejet Travelling Faster than the Mean Flow in the Jet," *Journal of Fluid Mechanics*, Vol. 72, 1975, pp. 341-352.

[20]Mattingly, G. E. and Chang, C. C., "Unstable Waves on an Axisymmetric Jet Column," *Journal of Fluid Mechanics*, Vol. 65, 1974, pp. 544-560.

[21]Hunter, C. and Guerrieri, B., "The Eigenvalues of Mathieu's Equation and Their Branch Points," *Studies in Applied Math.*, Vol. 64, 1981, pp. 113-141.

[22]Michalke, A., "Survey on Jet Instability Theory," *Progress in Aerospace Sciences*, Vol. 21, 1984, pp. 159-199.

[23]Michalke, A., "Vortex Formation in a Free Boundary Layer According to Stability Theory," *Journal of Fluid Mechanics*, Vol. 22, 1965, pp. 371-383.

Mode	A/B	ω_{max}	α_{real}	α_{imag}
ce_0	1.001	5.4413	10.1992	$-5.6852i$
ce_0	2.0	5.6578	10.1355	$-4.5074i$
ce_0	4.0	5.6518	9.0558	$-2.5470i$
ce_2	1.001	5.4949	10.3593	$-5.5483i$
ce_2	2.0	4.4171	8.3818	$-3.1567i$
ce_4	1.001	5.6203	10.7420	$-5.1763i$
se_1	1.001	5.4537	10.2381	$-5.6491i$
se_1	2.0	5.0106	9.3223	$-3.6778i$
se_1	4.0	3.5184	6.7366	$-2.2132i$
se_3	2.0	3.9380	7.5734	$-2.7856i$
ce_1	1.001	5.4567	10.2432	$-5.6517i$
ce_1	2.0	5.6577	10.0272	$-4.5074i$
ce_1	4.0	5.6517	9.0556	$-2.5470i$

Table I. Frequencies and wavenumbers for maximum rate of growth.

Captions

Fig. 1 Comparison of eqn. (11) with experimental data[8]: $z/A_0 = 0.5$, O , major axis, ◇ , minor axis; $z/A_0 = 2.0$, □ , major axis, △ , minor axis. Equation (11), ——— , $A/B = 1.88$, $\theta_B/B = 0.044$; - - - - - , $A/B = 1.49$, $\theta_B/B = 0.223$.

Fig. 2 Variation of axial growth rate with frequency for the ce_0 mode. ——— , $A/B = 1.001$; — — — —, $A/B = 2.0$; — · — · —, $A/B = 4.0$. $\theta_A = 0.02$.

Fig. 3 Variation of phase velocity with frequency for the ce_0 mode. For legend see Fig. 2.

Fig. 4 Azimuthal variation of the amplitudes of the most unstable ce_0 eigenmodes. For legend see Fig. 2.

Fig. 5 Distributions of most unstable ce_0 eigenmodes along the major axis. For legend see Fig. 2.

Fig. 6 Variation of axial growth rate with frequency for the ce_{2r} modes. ———, $r = 0$; — — — —, $r = 1$; — · — · —, $r = 2$. $A/B = 1.001$, $\theta_A = 0.02$.

Fig. 7 Variation of axial growth rate with frequency for the se_1 mode. For legend see Fig. 2.

Fig. 8 Variation of phase velocity with frequency for the se_1 mode. For legend see Fig. 2.

Fig. 9 Azimuthal variation of the amplitudes of the most unstable se_1 eigenmodes. For legend see Fig. 2.

Fig. 10 Eigenvalues in the c-plane for different characteristic numbers of Mathieu's equation. Eigenvalue sequence number, □ , 1; O , 2; △ , 3; ◇ , 4.

Fig. 11 Variation of axial growth rate with frequency for the se_{2r+1} modes. ——— , $r = 0$; — — — —, $r = 1$; — · — · — , $r = 2$; □———□, irregular mode. $A/B = 2.0$, $\theta_A = 0.02$.

Fig. 12 Variation of phase velocity with frequency for the se_{2r+1} modes. For legend see Fig. 11.

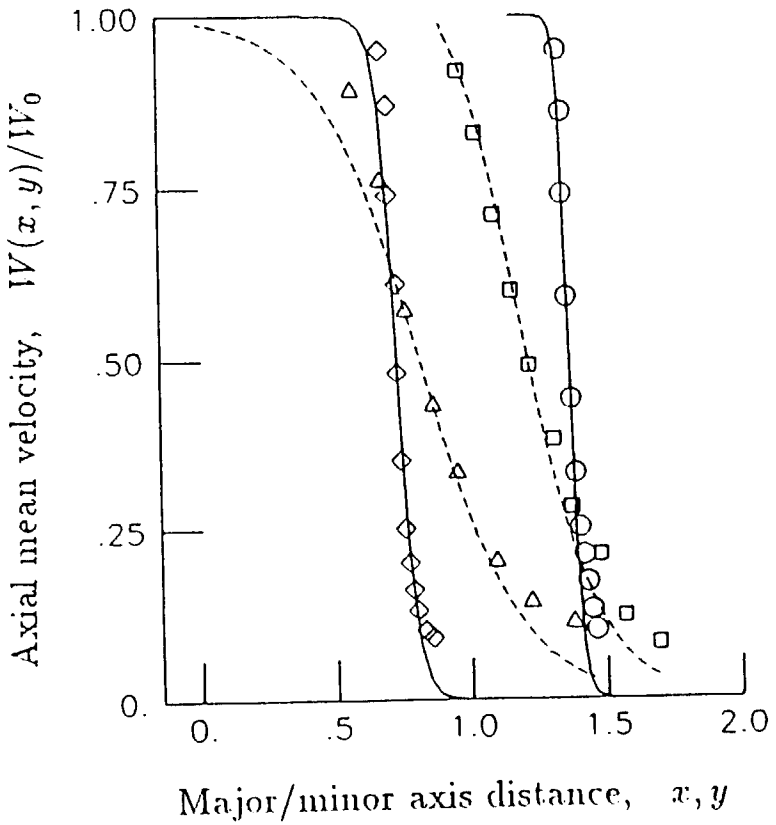
1.00
.75
.50
.25
0.
0.
.5
1.0
1.5
2.0
Axial mean velocity, $W(x,y)/W_0$
Major/minor axis distance, x, y

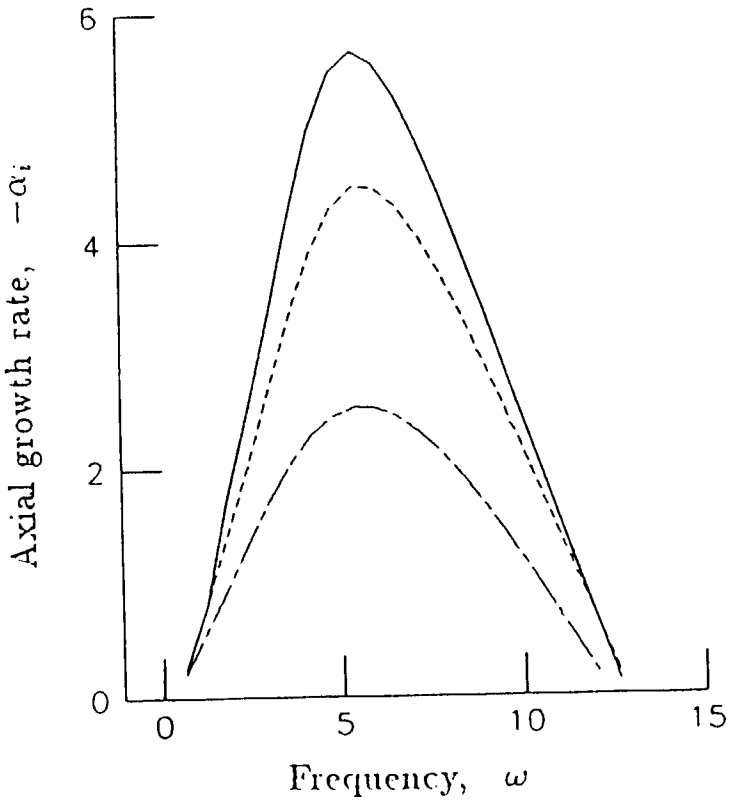
6
4
2
0
0
5
10
15
Axial growth rate, $-\alpha_i$
Frequency, ω

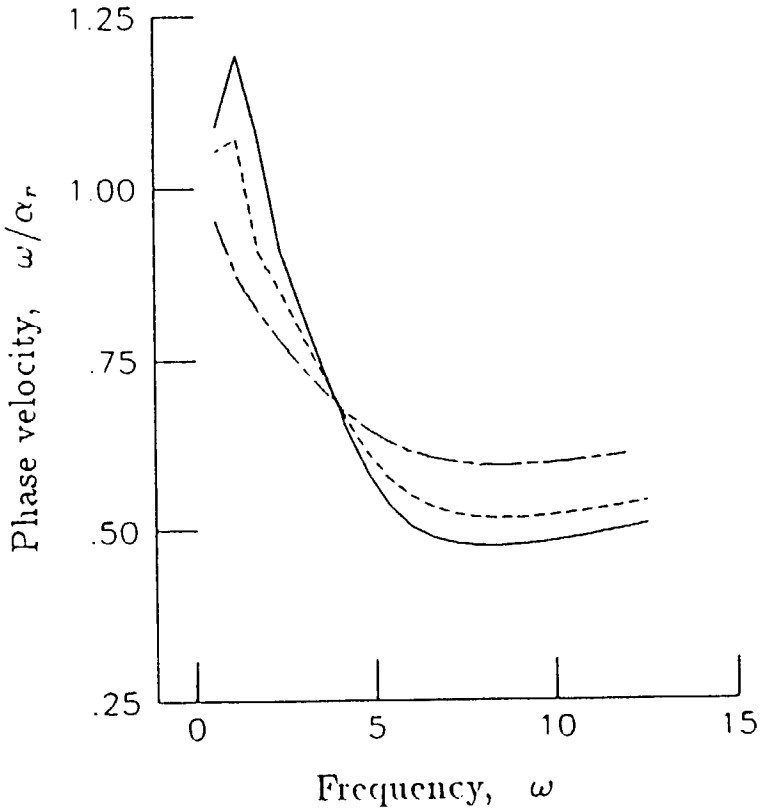
1.25
1.00
.75
.50
.25
Phase velocity, ω/α_r
0
5
10
15
Frequency, ω

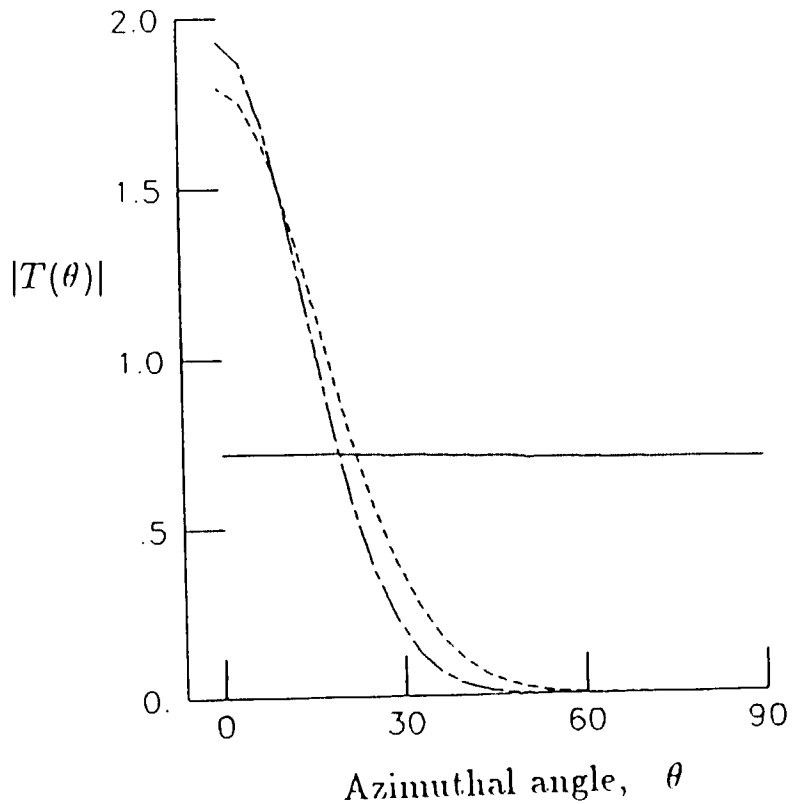
2.0
1.5
$|T(\theta)|$
1.0
.5
0.
0
30
60
90
Azimuthal angle, θ

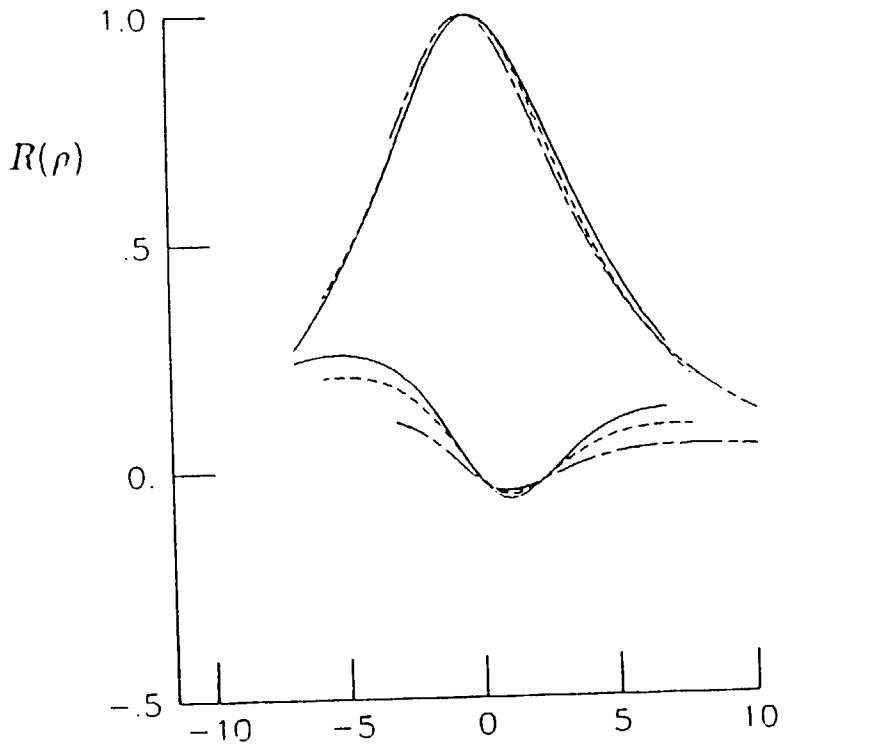
1.0
$R(\rho)$
.5
0.
−.5
−10
−5
0
5
10
Normalized distance along major axis, $(x - x_0)/\theta_A$

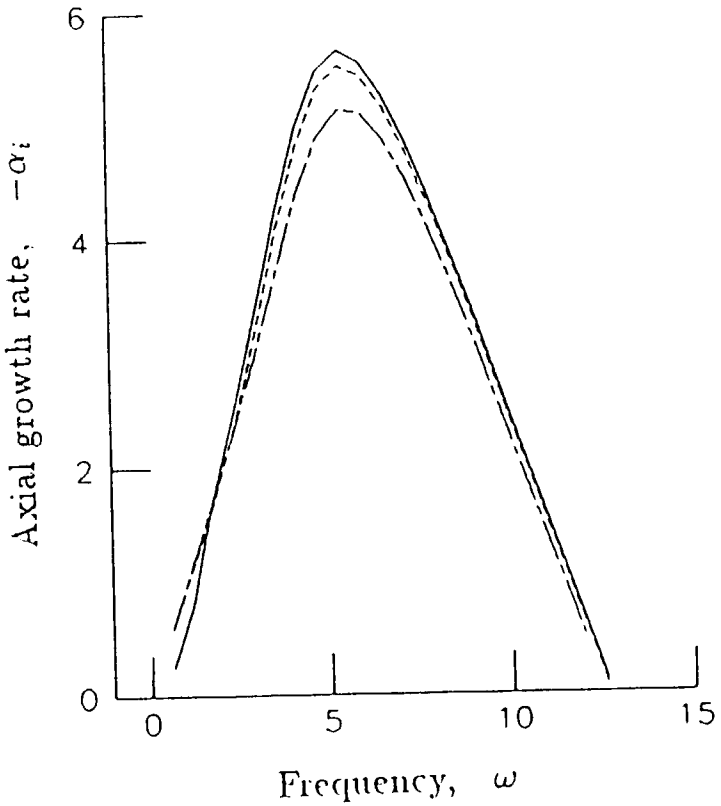
6
4
2
0
0
5
10
15
Axial growth rate, $-\alpha_i$
Frequency, ω

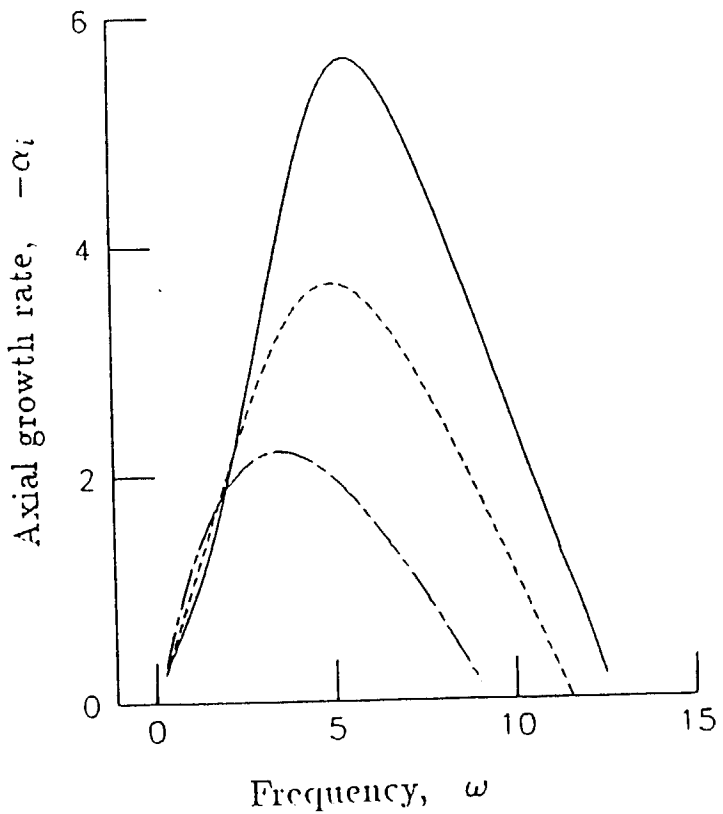
6
4
2
0
0
5
10
15
Axial growth rate, $-\alpha_i$
Frequency, ω

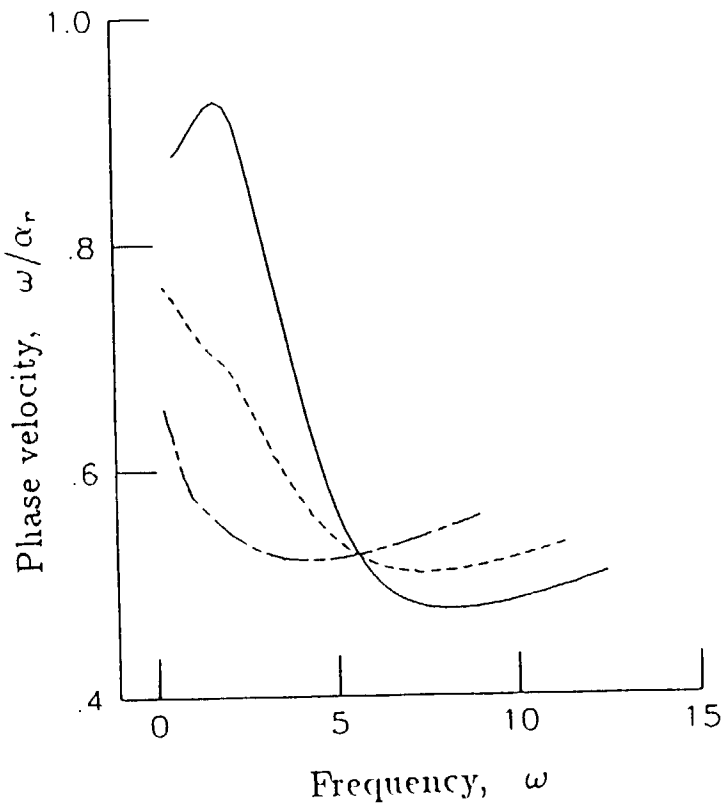
1.0
.8
.6
.4
Phase velocity, ω/α_r
0
5
10
15
Frequency, ω

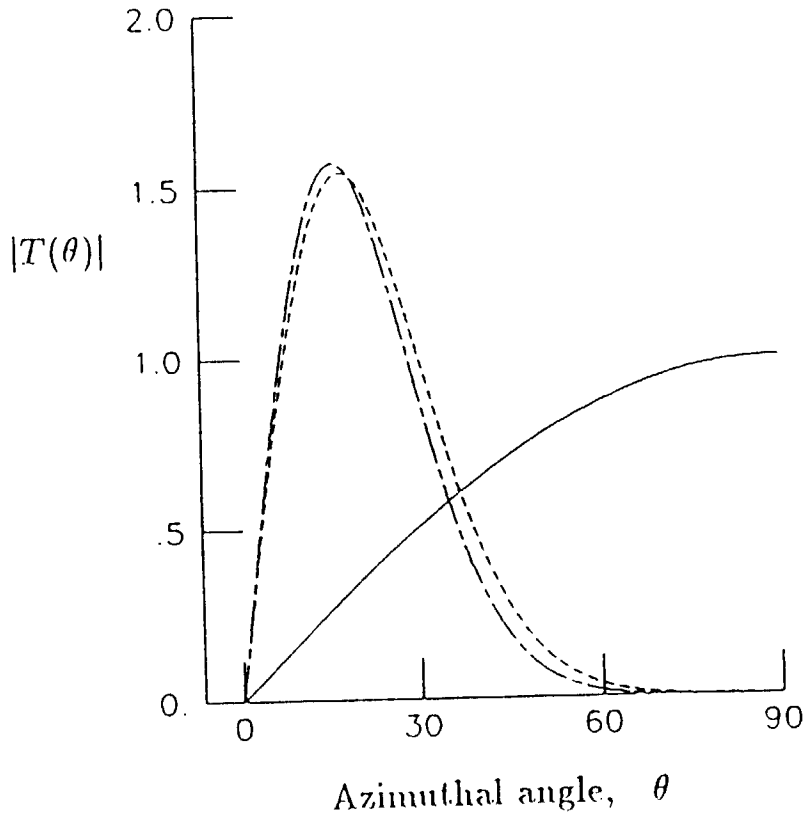
2.0
1.5
1.0
.5
0.
$|T(\theta)|$
0
30
60
90
Azimuthal angle, θ

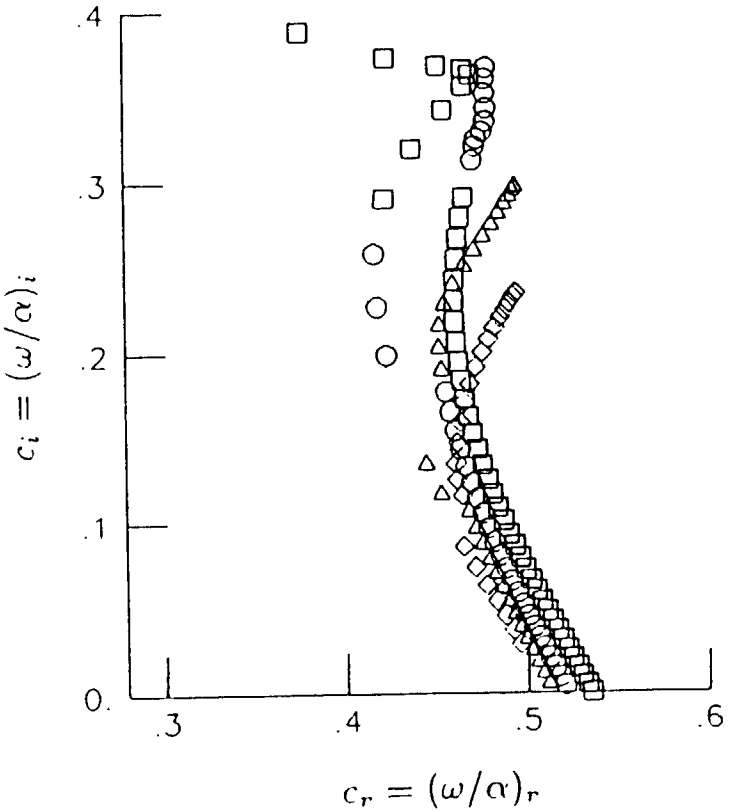
.4
.3
.2
.1
0.
.3
.4
.5
.6
$c_i = (\omega/\alpha)_i$
$c_r = (\omega/\alpha)_r$

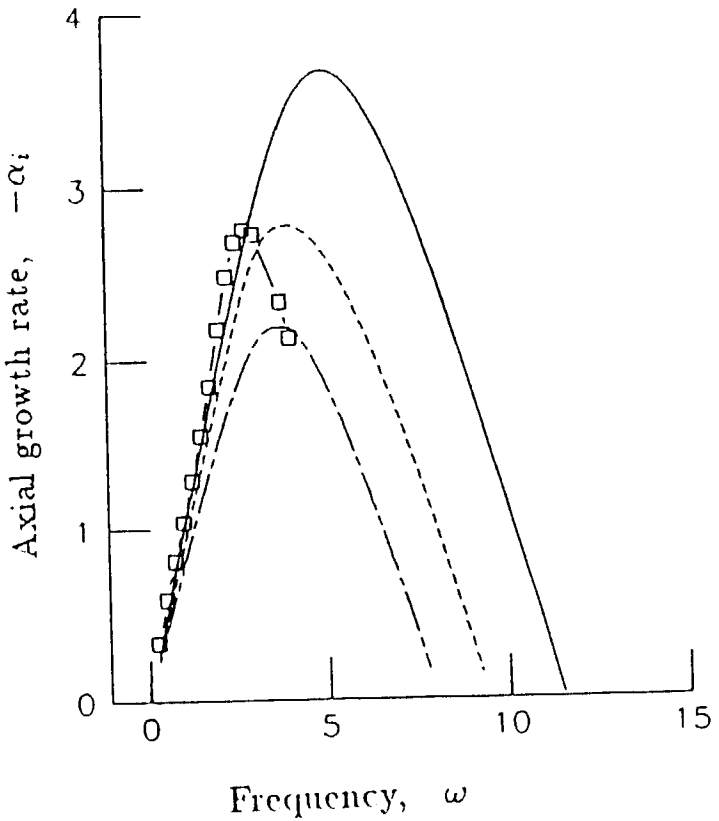
4
3
2
1
0
0
5
10
15
Axial growth rate, $-\alpha_i$
Frequency, ω

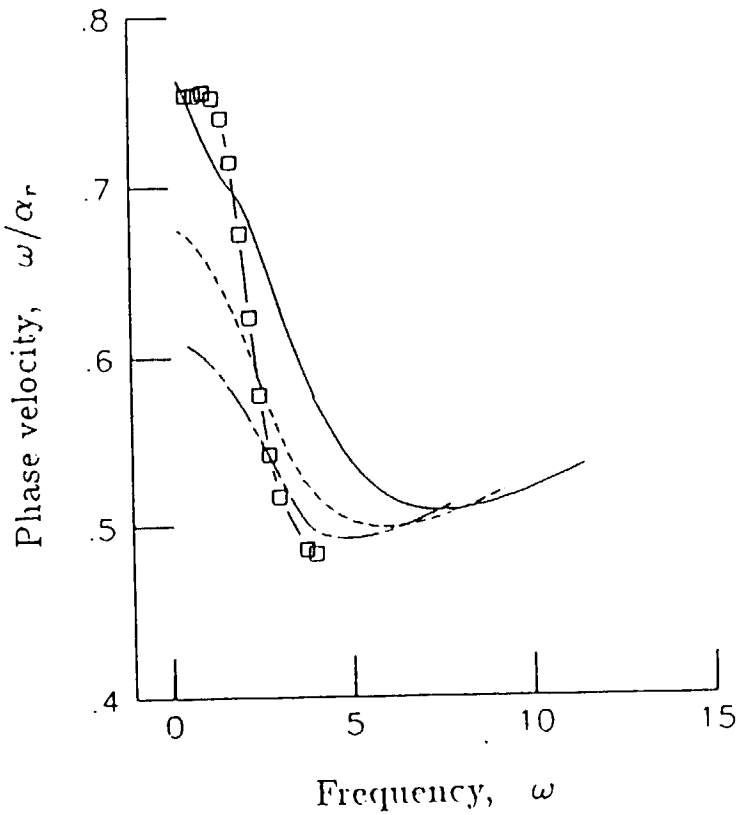
.8
.7
.6
.5
.4
0
5
10
15
Phase velocity, ω/α_r
Frequency, ω

Appendix II

A Linear Shock Cell Model for Jets of Arbitrary Exit Geometry

P. J. Morris, T. R. S. Bhat, and G. Chen

Abstract

The shock cell structure of single supersonic non-ideally expanded jets with arbitrary exit geometry are studied. Both vortex sheets and realistic mean profiles are considered for the jet shear layer. The boundary element method is used to predict the shock spacing and screech tones in a vortex sheet model of a single jet. This formulation enables the calculations to be performed only on the vortex sheet. This permits the efficient and convenient study of complicated jet geometries. Results are given for circular, elliptic and rectangular jets and the results are compared with analysis and experiment. The agreement between the predictions and measurements is very good but depends on the assumptions made to predict the geometry of the fully-expanded jet. A finite difference technique is used to examine the effect of finite mixing layer thickness for a single jet. The finite thickness of the mixing layer is found to decrease the shock spacing by approximately twenty percent over the length of the jet potential core.

1. Introduction

There have recently been considerable advances in our understanding of supersonic jet noise. The results of this work are well summarized by Tam [1]. In this paper he shows how the various mechanisms for noise generation in supersonic jets may be related to the turbulence in the jet shear layer and its interaction with the nearly-periodic shock structure of the jet. The contribution to the noise radiation from the turbulence alone, usually referred to as jet mixing noise, may be modelled as the radiation of sound by instability waves following the work of Tam and Morris [2], and Tam and Burton [3, 4]. The interaction of the instability waves with the periodic shock-structure can result in screech tones as shown by Tam [5]. The broadband shock noise is associated with the interaction between the random turbulence in the jet shear layer and the shock structure. The important features of the random turbulence may be modelled as a random superposition of the normal modes of the jet shear layer, Tam and Chen [6]. These normal modes are simply the solution of the Orr-Sommerfeld equation with mean flow properties given by the jet velocity and temperature fields. The success of this model and prediction scheme is remarkable in its ability to predict both the near and far pressure fields of the jet.

With the exception of reference 5, Tam's work has dealt with jets with a simple geometry. However recent interest has focussed on the behavior of non-circular jets [7-11]. Such jets have enhanced mixing properties. This is important in turbulent combustion, particularly at high speeds, and for jet exhaust plumes. Nearly rectangular nozzles have important uses in STOL applications for lift control and vectored thrust.

In this paper we consider supersonic jets issuing from jet nozzles with arbitrary cross-sections. As noted above, Tam and co-workers have shown that both the large-scale coherent structures and the shock structure of jets may be modelled using a wave analysis. The essential difference between the two cases is that the former are travelling waves while the latter may be modelled as stationary waves. This means that we are concerned with solving the equations of hydrodynamic stability in which the coefficients depending on the mean flow are arbitrary functions in a plane normal to the jet axis. Calculations of the stability of non-circular jets have also been performed by Koshigoe and Tubis [12, 13] and Morris [14]. In the former a Green's function approach was used and in the latter the mean velocity profile for the elliptic jet was chosen such that separable solutions could still be obtained in elliptic cylindrical coordinates.

We will assume that the mean flow properties are slowly-varying functions of the axial distance. Tam, Jackson and Seiner [15], showed that the effect of the slow axial variation could be accounted for using the method of multiple scales, but that the differences in the predicted shock-structure with and without this effect were small. Thus we will assume that the mean flow is locally parallel.

In this paper the shock cell structure and screech tones of a single supersonic jet with arbitrary exit geometry are addressed. The jet mixing layer is modelled by both a vortex sheet and realistic continuous velocity and density profiles. In the former case the area of the vortex sheet cross-section is taken to be that of the fully-expanded jet. This is a jet in which the mass flux is equal to that at the jet exit but the pressure has been equalized with the ambient. This is an approximation, even for the small pressure differences considered in the present case. However, a sample calculation for the two-dimensional jet using linear pressure/turning angle

relationships showed that the vortex sheet had an average location given by the vortex sheet location for the fully- expanded jet. Though the analysis developed in the next sections could be applied to segmented exit geometries, such as the multitube configuration, the rapid development of the flow in such cases would diminuish the validity of the model.

It has been found that the boundary element method is a valuable tool for the study of jets of arbitrary geometry represented by a vortex sheet. Other numerical methods have been employed to consider the cases where the jet mixing layer has finite thickness. In the next section the the analytical development is given for both representations of the jet. This is followed by the calculations and comparison with experiment.

2. Analysis

A typical cross-section of a single jet is shown in Fig. 1. The flow may be divided into three regions. In regions I and III the mean flow properties are constant. These regions correspond to the potential core of the jet and the ambient fluid surrounding the jet respectively. Region II represents the annular mixing region in which the mean velocity and density of the jet vary.

As a first approximation a linear shock cell model can be developed in which the mixing region of the jet is represented by a vortex sheet. Such a model was used by Tam and Tanna [16] in the circular jet case and Tam [5] for arbitrary geometry jets. The next approximation accounts for the finite thickness of the mixing layer and the variation in the mean flow properties. To solve these two problems two methods have been developed. The vortex-sheet problem is analyzed using the boundary-element method. The finite thickness case is solved using a finite-difference solution. The analysis for these two techniques is given in this section.

2.1 Vortex-Sheet Shock Cell Model.

The formulation of the problem is the same as that given by Tam [5], and will be outlined briefly. However Tam used an eigenfunction expansion method to analyze the arbitrary geometry problem. Such an approach is well-suited to problems in which the vortex-sheet conforms to a coordinate line in an orthogonal coordinate system such as the circular, rectangular or elliptic jet. Tam gave solutions to the first two cases and for the elliptic jet in the limiting cases of nearly circular and highly eccentric geometries. However such a method is not suitable for more complicated geometries. Thus in the present analysis the solution is based on the boundary element method. However the eigenfunction expansion method is used in the present

paper to find the solutions in the elliptic jet case for any eccentricity. These results are used to verify the boundary element calculations.

Consider a shock cell system in a jet column bounded by a vortex sheet as shown in Fig. 2. For convenience, a Cartesian coordinate system centered at the nozzle exit with the x-axis in the direction of the jet centerline will be used. The surface of the vortex sheet bounding the fully-expanded jet is given by $S_0(y,z) = 0$. There is no disturbance outside the jet. The linearized equations of motion inside the vortex sheet are:

$$\rho_j \nabla \cdot \mathbf{v} + U_j \frac{\partial \rho}{\partial x} = 0, \tag{2.1}$$

$$\rho_j U_j \frac{\partial \mathbf{v}}{\partial x} = -\nabla p, \tag{2.2}$$

$$p = a_j^2 \rho. \tag{2.3}$$

ρ_j, u_j and a_j are the density, velocity and the speed of sound of the fully expanded jet. ρ, p and $\mathbf{v}$ are the density, pressure and velocity associated with the linear shock cell structure.

From eqns. (2.1) to (2.3) it is found that the pressure p satisfies the equation

$$\nabla^2 p - M_j^2 \frac{\partial^2 p}{\partial x^2} = 0, \tag{2.4}$$

with $p = 0$ on the boundary $S_0(y,z) = 0$ and, at $x = 0$, $p = \Delta p$ inside $S_0(y,z) = 0$ and $\mathbf{v}_\perp = 0$. $\mathbf{v}_\perp$ are the velocity fluctuations normal to the jet axis.

A general solution of the vortex–sheet shock cell boundary value problem can be found by writing the pressure fluctuation as:

$$p(x,y,z) = \phi(y,z)\cos(kx). \tag{2.5}$$

where k is an as yet unknown axial wavenumber. The equation for $\phi(y,z)$ may then be written

$$\nabla_\perp^2 \phi + \beta^2 \phi = 0. \tag{2.6}$$

where

$$\nabla_\perp^2 = \left(\frac{\partial^2}{\partial y^2} + \frac{\partial^2}{\partial z^2} \right)$$

and

$$\beta^2 = (M_j^2 - 1)k^2, \tag{2.7}$$

with $\phi = 0$ on $S_0(y,z) = 0$. This is an eigenvalue problem with k as the eigenvalue, which is to be determined.

Consider an arbitrary domain as shown in Fig. 3 where the boundary is divided into N panels. $\xi = \xi(a_1, a_2)$ are the locations of the node points and $\alpha = \alpha(b_1, b_2)$ are the locations of the mid points of each panel.

Let $F(\mathrm{x} \mid \mathrm{y})$ be the fundamental solution of the Helmholtz equation, i.e.

$$(\nabla_\perp^2 + \beta^2) F(\mathrm{x} \mid \mathrm{y}) = -\delta(\mathrm{x} - \mathrm{y}), \tag{2.8}$$

where, $\mathrm{x} = (x_1, x_2)$ and $\mathrm{y} = (y_1, y_2)$ and x and y are arbitrary, and $\delta(\ )$ is the Dirac delta function. Then,

$$F(\mathrm{x} \mid \mathrm{y}) = \frac{i}{4} H_0^{(1)}(\beta |\mathrm{x} - \mathrm{y}|). \tag{2.9}$$

Application of the divergence theorem and noting that ϕ satisfies eqn. (2.6) and is zero on the boundary yields,

$$\frac{1}{2}\phi(\alpha_i) \doteq \int_{S_0=0} \frac{\partial \phi(\xi)}{\partial \nu} F(\alpha_i \mid \xi) d\sigma. \tag{2.10}$$

Approximating $\partial\phi/\partial\nu$ by a constant, say g_i on each arc Γ_i, we obtain,

$$\frac{1}{2}\phi(\alpha_i) = \sum_{j=1}^{N} g_j \int_{\Gamma_j} F(\alpha_i \mid \xi) d\sigma. \tag{2.11}$$

or,

$$\frac{1}{2}\phi(\alpha_i) = \sum_{j=1}^{N} \mu_{ij}(\beta)\ g_j, \tag{2.12}$$

where,

$$\mu_{ij}(\beta) = \int_{\Gamma_j} F(\alpha_i \mid \xi)\ d\sigma. \tag{2.13}$$

In eqns. (2.10) to (2.13) $i = 1, 2, \ldots, N$.

The approximate eigenvalues β are obtained from,

$$\det[\mu_{ij}]_{N\times N} = 0. \tag{2.14}$$

It now remains to set up the elements of the matrix μ_{ij}. When $i = j$ the integrand contains a singularity and so the evaluation of the integral in μ_{ij} must be performed carefully. We obtain:

$$\begin{aligned}\mu_{ii}(\beta) = \frac{i}{4}\Bigg\{ & L_i H_0^{(1)}\left(\frac{\beta L_i}{2}\right) + \frac{\pi L_i}{2}\Bigg[\mathbf{H}_0\left(\frac{\beta L_i}{2}\right) \\ & \times H_1^{(1)}\left(\frac{\beta L_i}{2}\right) - \mathbf{H}_1\left(\frac{\beta L_i}{2}\right) H_0^{(1)}\left(\frac{\beta L_i}{2}\right)\Bigg]\Bigg\},\end{aligned} \tag{2.15}$$

where L_i is the length of the panel on the arc Γ_i, and $\mathbf{H}_0$ and $\mathbf{H}_1$ are Struve functions of order 0 and 1 respectively, that can be expressed as a series of Bessel functions. When $i \neq j$ the integrand is smooth and the evaluation of the integral in μ_{ij} may be obtained using Simpson's rule.

$$\begin{aligned}\mu_{ij}(\beta) = \frac{i}{4}\Bigg\{ & \frac{L_j}{6}\Bigg[H_0^{(1)}\left(\beta|\alpha_i - \xi_j|\right) \\ & + 4H_0^{(1)}\left(\beta|\alpha_i - \alpha_j|\right) + H_0^{(1)}\left(\beta|\alpha_i - \xi_{j+1}|\right)\Bigg]\Bigg\}.\end{aligned} \tag{2.16}$$

The eigenvalues are obtained by a local iterative scheme which is given by,

$$\beta_{k+1} = \beta_k - 1/f(\beta_k). \tag{2.17}$$

where,

$$f(\beta_k) = \mathrm{Tr}[\mu^{-1}(\beta_k)\mu'(\beta_k)], \tag{2.18}$$

Tr denotes the trace of a matrix and a prime denotes the derivative of the matrix with respect to β_k. This is Newton's method written in a convenient form for matrix operations. Thus the eigenvalues can be determined starting from an initial guess.

2.2 Continuous Mean Profiles

When region II of Fig. 1 is of finite extent a numerical solution must be obtained in the mixing region. The general form of separable solution for the fluctuating pressure when the mean velocity and density are taken to be independent, locally, of the axial distance is given by,

$$p(r,\theta,x,t) = \hat{p}(r,\theta)\exp[i(kx - \omega t)], \tag{2.19}$$

where ω is the radian frequency and a polar coordinate system has been introduced. The shock-structure may be associated with the zero frequency solutions, i.e. $\omega = 0$. The pressure fluctuation is found to satisfy the non-separable form of the Rayleigh equation [12],

$$\begin{aligned}\frac{\partial^2\hat{p}}{\partial r^2} + \frac{1}{r}\frac{\partial\hat{p}}{\partial r} + \frac{1}{r^2}\frac{\partial^2\hat{p}}{\partial\theta^2} + \frac{2k}{(\omega - kU)}\left[\frac{\partial U}{\partial r}\frac{\partial\hat{p}}{\partial r}\right. \\ \left. + \frac{1}{r^2}\frac{\partial U}{\partial\theta}\frac{\partial\hat{p}}{\partial\theta}\right] - \left[k^2 - M_j^2(\omega - kU)^2\right]\hat{p} = 0.\end{aligned} \tag{2.20}$$

For simplicity the flow has been assumed to be isothermal but the variations in mean density may be readily included using a Crocco's relationship.

For an arbitrarily shaped jet U is a function of both r and θ. Thus a separable solution in r and θ is not generally available and one resorts to a numerical solution in region II. Along the interior edge of this region and in region I, the potential core of the jet, the mean velocity is a constant, U_j. In the ambient fluid surrounding the jet the properties are also uniform. In this case we take the external velocity to be zero. Thus on the boundaries between regions I and II, and II and III, a separable form of solution may be obtained and can be written,

$$\hat{p}_j = \sum_{n=-\infty}^{\infty} A_n J_n(i\lambda_j r)\exp(in\theta), \tag{2.21}$$

and,

$$\hat{p}_0 = \sum_{n=-\infty}^{\infty} B_n H_n^{(1)}(i\lambda_0 r)\exp(in\theta), \tag{2.22}$$

where

$$\lambda_j^2 = k^2 - M_j^2(\omega - kU_j)^2, \tag{2.23}$$

and,

$$\lambda_0^2 = k^2 - M_j^2\omega^2. \tag{2.24}$$

The subscripts j and 0 refer to the solutions in regions I and III respectively. J_n is the Bessel function of the first kind and order n, and $H_n^{(1)}$ is the Hankel function of the first kind and order n.

For region II the solution may be obtained numerically using a finite difference scheme. The region is divided by N radial lines. If the mean flow possesses symmetry about any coordinate directions the numerical integration need only be performed in a limited sector. For example, if the mean flow is symmetric about both the y and z axes the numerical integration is performed in the first quadrant. This would be the case for the elliptic or rectangular jets. The derivatives with

respect to θ in eqn. (2.20) are approximated by a three-point central difference formula. Equation (2.20) then gives a system of coupled ordinary differential equations for the values of $\hat{p}$ along the radial lines. The values of $\hat{p}$ along the bounding radial lines depend on whether the modes sought are odd or even about the boundaries. In the the former case $\hat{p}$ is zero on the boundary, in the latter case $\partial\hat{p}/\partial\theta$ is set to zero.

The numerical solution is started at the interior boundary with one term from a finite series of the form (2.21). The values of n are chosen to be compatible with the modes sought. For example, $n = 2m$ for modes that are periodic in π such as the axisymmetric mode in the circular jet case. The solution is repeated for each term in the series as the starting condition. A corresponding set of solutions is started along each of the radial lines at the exterior boundary. The sets of solutions are matched at some intermediate value of radius. For example along any radial line at the matching point,

$$\sum_n A_n \hat{p}_{nI} = \sum_n B_n \hat{p}_{nII}, \tag{2.25}$$

and

$$\sum_n A_n \hat{p}'_{nI} = \sum_n B_n \hat{p}'_{nII}, \tag{2.26}$$

where $\hat{p}_{nI}$ and $\hat{p}_{nII}$ denote the numerical solutions started at the interior and exterior boundaries respectively with starting conditions for the n-th term in the series, and primes denote the derivative with respect to r. Application of these matching conditions along each of the N radial lines gives $2N$ homogeneous equations for the $2N$ unknowns A_n and B_n. These equations may be written in matrix form. The eigenvalue is obtained by minimizing the determinant of the resulting matrix.

3. Calculations

Calculations have been performed for both the vortex sheet case and the jet mixing layer of finite thickness. In the former case the circular, rectangular, and elliptic jets have been considered. Comparisons have been made between the predictions, analytical results and experimental data where possible.

3.1 Vortex-Sheet Shock Cell Model

The shock spacing is given by the wavelength λ_s associated with the lowest eigenvalue k. For a circular jet the analytical result for β, given by eqn. (2.7), was given by Tam and Tanna [16]. It corresponds to the first zero of the J_0 Bessel function. To determine the accuracy of the boundary element method, calculations were performed for the circular jet case with various numbers of panels. The results are given in Table I. The numerical result is within one percent of the analytic result for 20 panels. Thus in all subsequent calculations the number of panels is fixed at 20 unless noted otherwise.

Tam and Tanna [16] noted that the dimensions of the vortex sheet to be used when comparing with experimental data should be those of the fully-expanded jet and not those of the jet nozzle itself. The ratio of the areas of the fully-expanded jet and the nozzle may be obtained from one-dimensional isentropic flow formulas. That is,

$$\frac{A_j}{A_d} = \frac{M_d}{M_j}\left[\frac{1+\frac{\gamma-1}{2}M_j^2}{1+\frac{\gamma-1}{2}M_d^2}\right]^{\frac{\gamma+1}{2(\gamma-1)}}, \tag{3.1}$$

where M_d and M_j are the nozzle design Mach number and fully-expanded jet Mach number respectively and A_d and A_j are the areas of the nozzle exit and the fully-expanded jet respectively. For a circular jet the ratio of the radius of the

fully–expanded jet to the nozzle radius is given by the square root of eqn. (3.1). For non–circular jets further assumptions must be made. Tam [5] assumed that the jet expands or contracts by an equal amount about its perimeter. Approximate formulas may then be found for the dimensions of the fully–expanded jet. For the cases of the rectangular and elliptic jets these formulas are eqns. (2.42) and (2.43) of reference 5. Alternatively the shape of the jet cross–section could be assumed to be unchanged in the expansion so that the ratio of the characteristic dimensions of the fully–expanded jet to the nozzle is once again given by the square root of eqn. (3.1). However, though without any conclusive experimental evidence, the mixing in the initial mixing region near the nozzle might be more likely to move the jet to a more symmetric form, i.e. a lower eccentricity in the elliptic case. This trend is given by Tam's formulation , at least in the under–expanded case. This formulation has been used mostly in the subsequent calculations. However some predictions based on the assumption of no change in the jet geometry have also been made. For the elliptic jet the formula for the fully–expanded jet dimensions should be written correctly as:

$$\frac{L_j}{L_d} = \left[\frac{A_j}{A_d} - 1\right] \frac{\pi L_b}{2E(e^2)L_d} + 1, \tag{3.2}$$

where L_j refers to the fully–expanded jet scales and L_d refers to the nozzle exit scale. $E(s)$ is the complete elliptic integral of the second kind and $e^2 = (1 - L_b^2/L_a^2)$, where L_a and L_b refer to the semi–major and semi–minor axes of the nozzle.

For the elliptic jet the shock spacing is given by [5],

$$\lambda_s = \pi a \sqrt{(M_j^2 - 1)}/\sqrt{q_{01}}, \tag{3.3}$$

where q_{01} is the smallest root of the modified Mathieu function $\mathrm{Ce}_{nm}(\mu_0, q_{mn})$, and

$$a = \sqrt{L_A^2 - L_B^2} \qquad \mu_0 = \tanh^{-1}(L_A/L_B), \tag{3.4}$$

where L_A and L_B are the lengths of the semi-major and semi-minor axes of the fully-expanded jet. Tam [5] gave approximate values for the roots in the limits of very small and very large eccentricity. In the present calculations the roots have been determined numerically using the Mathieu function routines described by Morris [14]. These calculations confirm the asymptotic formulas given by Tam. In addition calulations have been performed for an elliptic jet with nozzle axis ratio $L_A/L_B = 2$. This corresponds to the nozzle used in recent experiments at NASA Langley [17]. Figure 4 shows the calculated shock spacing as a function of fully-expanded jet Mach number for the 2:1 elliptic nozzle. The design Mach number of the jet is 1.5. The shock spacing is referenced to the semi-minor axis of the nozzle. The numerical results (for N=20) agree well with the analytic result given by eqn. (3.3) with the zeroes of the Mathieu function evaluated numerically. It should be noted that an axis ratio of 2:1 only occurs at the ideally-expanded condition. For $M_j = 1.1$ the fully-expanded axis ratio is 2.2278 and for $M_j = 1.8$ the ratio is 1.7753.

A relationship between the shock spacing in the jet and the screech tone frequencies has been developed by Tam, Seiner and Yu [18] based on a "weakest link" hypothesis. The screech tone frequency is given by the simple formula,

$$f_p = \frac{u_c k_1}{2\pi(1 + u_c/a_\infty)}, \tag{3.5}$$

where k_1 is the smallest wavenumber of the shock cell system, u_c is the convection velocity of the excited large scale instability waves of the flow and a_∞ is the ambient speed of sound. The same formula was developed by Powell [19] and Harper-Bourne and Fisher [20] using a different model. In the calculations it has been assumed that the convection velocity is 0.7. This assumption was found to be satisfactory in [18]

though it may not be generally valid. Though other values have been proposed for the convection velocity the present choice is an adequate approximation. It should be noted however that the convection or phase velocity for the instability wave that achieves a maximum amplitude in the jet shear layer may be calculated from the stability analysis (for realistic mean velocity and temperature profiles). Figure 5 compares the predicted screech tone frequencies from eqn. (3.5) with the measured values. The smallest wavenumber was obtained from the boundary element calculations shown in Fig. 4. The agreement between the predictions and measurements is very good. It is interesting that the experimental data and the predictions appear to agree best close to the design Mach number. This would suggest that the discrepancies between the predictions and the experiments are related to the choice of dimensions for the fully-expanded jet. Preliminary measurements [17] of the velocity profiles in the Mach 1.5, 2:1 elliptic nozzle at NASA Langley indicate that the ratio of the axes, based on the half-velocity points, remains constant for the first two potential core lengths. Also shown in Fig. 5 is the predicted screech frequency where the aspect ratio of the fully-expanded jet is taken to be the same as the nozzle. The area of the fully-expanded jet is given by the one-dimensional gas flow equations. The agreement between the predictions and experiment is better in this case particularly at the over-expanded conditions. It is not clear whether this assumption would provide better predictions for all exit geometries.

The circular and elliptic jets have smooth boundaries. As an example of a case with sharp corners we consider the rectangular nozzle. The analytic solutions in this case are obtained very easily using the eigenfunction expansion approach and the formulas for the shock spacing and screech frequencies are given by Tam [5] [eqns. (2.44) and (3.2)]. Figure 6 shows a comparison between the numerical

results for the shock spacing obtained using the boundary element method, Tam's analytic results (based on the assumption of large aspect ratio), and Powell's [21] experimental results. The agreement between the sets of data is quite reasonable. For these calculations, in which the aspect ratio of the jets is large, 34 panels were used in the boundary element calculations.

Figure 7 shows a comparison of the predicted screech frequencies using the analytic and numerical results and the experiments of Krothapalli et al [22]. As expected the agreement between the predictions and experiments is good. Once again 34 panels were used in the calculations.

It should be noted that at the higher pressure ratios strong shocks exist in the plume and the geometry of the plume changes with downstream distance. This results in the eventual switching of the major and minor axes. The good agreement between the predictions of the vortex sheet model and the measurements would suggest that the fundamental wavelength of the jet is relatively insensitive to the effects of finite mixing layer thickness, jet growth, and non–axial velocity components. This is also indicated by the calculations given in the next section.

3.2 Continuous Mean Profiles

As a demonstration of the effect of finite thickness on the shock spacing calculations were performed for a circular jet. Clearly this case could be examined by using the separable form of solution and integrating along a single radial line. In fact this calculation has been performed to test the numerical accuracy of the general scheme. However the purpose of the example was to test the general approach and calculations for other geometries must await mean flow data at high speeds.

The calculations were performed with three evenly spaced radial lines in the first quadrant. The mean velocity profile was taken to be,

$$U(r) = U_j \exp[-\ln(2)\ \eta^2], \tag{3.6}$$

where $\eta = (r - h)/b$, h is the potential core radius and b is the local half-width of the jet mixing layer. The relationship between h and b may be obtained from an integral form of the axial momentum equation (see for example, Tam and Morris [23]). The jet was assumed to be isothermal. The integration of the system of ordinary differential equations in the radial direction was performed using a fixed step size fourth-order Runge-Kutta scheme with only 20 steps in the integration region, $0 \leq \eta \leq 3.0$. This relatively small number of steps appeared to be adequate when compared with the results using a variable step-size scheme that used several hundred steps.

Figure 8 shows the variation of the shock spacing, based on the lowest wavenumber, as a function of the mixing layer thickness. The jet Mach number $M_j = 1.4$. The wavelength is relatively independent of the mixing layer thickness though the shock spacing does decrease as the thickness increases. For small values of b the spacing approaches that given by the vortex sheet model. Only the lowset wavenumber associated with the axisymmetric mode has been sought. Higher axisymmetric modes exist corresponding to the zeroes of the J_0 Bessel function in the limit of the vortex- sheet. Tam, Jackson and Seiner [15] showed that when the contributions from all these modes are superimposed a remarkably detailed prediction of the pressure distribution, associated with the shock structure, may be obtained. A similar result could be obtained with the present method for other jet geometries. However, it should be noted that Tam et al's calculations included the dissipative

effect of the shear layer turbulence through an eddy viscosity. This results in an axial decay of the strength of the shocks. No such decay would be obtained with the present formalism. However the inclusion of the viscous effects would simply convert the equation satisfied by the fluctuations from the Rayleigh equation to an Orr-Sommerfeld equation and the numerical analysis would proceed in a similar fashion.

The method developed in this section is being applied by the authors to other more complicated geometries than the circular jet. There are several modifications to the numerical procedure which make the calculations more efficient in jets with high aspect ratios. However the basic principle of matching the linearly independent solutions along radial lines is the same as described here. These calculations will be presented later. The present calculations have served to validate the basic technique and also to demonstrate the magnitude of the effect of finite mixing region thickness. It can be seen from the present calculations that the vortex–sheet approach provides a remarkably good prediction of the shock spacing when compared with the more realistic results for the finite thickness mixing layer.

4. Summary

This paper has given the formulations for the calculation of the shock cell spacing of single jets of arbitrary geometry. Methods have been given for both vortex sheet models of the jet shear layer and for continuous mean profiles. The vortex sheet calculations for the single jet were performed using the boundary element method. This enabled the shock structure to be predicted in jets of arbitrary geometry. Calculations have been given for circular, rectangular and elliptic jet cases. The effect of finite mixing layer thickness on the shock spacing has been predicted using a finite-difference solution in the mixing layer. The shock wavelength has been found to reduce as the mixing layer thickness increases.

Acknowledgements

This work was supported in part by NASA Langley Research Center under NASA Grant NAG-1-657. The co-technical monitors are Drs. J. M. Seiner and R. G. Wilmoth.

References

1. C. K. W. TAM 1987 *Journal of Sound and Vibration* **116**, 265–302. Stochastic model theory of broadband shock associated noise from supersonic jets.

2. C. K. W. TAM and P. J. MORRIS 1980 *Journal of Fluid Mechanics* **98**, 349–381. The radiation of sound by the instability waves of a compressible plane turbulent shear layer.

3. C. K. W. TAM and D. E. BURTON 1984 *Journal of Fluid Mechanics* **138**, 249–271. Sound generated by instability waves of supersonic flows. Part 1. Two-dimensional mixing layers.

4. C. K. W. TAM and D. E. BURTON 1984 *Journal of Fluid Mechanics* **138**, 273–295. Sound generated by instability waves of supersonic flows. Part 2. Axisymmetric jets.

5. C. K.W. TAM 1986 *American Institute of Aeronautics and Astronautics Paper No.* 86–1866. On the screech tones of supersonic rectangular jets.

6. C. K. W. TAM and K. C. CHEN 1984 *Journal of Fluid Mechanics* **92**, 303–326. A statistical model of turbulence in two-dimensional mixing layers.

7. H. S. HUSAIN, and A. K. M. F. HUSSAIN 1983 *Physics of Fluids* **26**, 2763–2766. Controlled excitation of elliptic jets.

8. K. C. SCHADOW, K. J. WILSON, M. J. LEE and E. GUTMARK 1984 *American Institute of Aeronautics and Astronautics Paper No.* 84–1260. Enhancement of mixing in ducted rockets with elliptic gas-generator nozzles.

9. E. GUTMARK, K. C. SCHADOW, D. M. PARR, C. K. HARRIS and K. J. WILSON 1985 *American Institute of Aeronautics and Astronautics Paper No.* 85–0543. The mean and turbulent structure of noncircular jets.

10. E. GUTMARK and C.-M. HO 1985 *AIAA Journal* **24**, 684–685. Visualization of a forced elliptic jet.

11. K. C. SCHADOW, K. J. WILSON, D. M. PARR, and E. GUTMARK 1986 *American Institute of Aeronautics and Astronautics Paper No.* 86–1399. Mixing characteristics of a ducted elliptical jet with dump.

12. S. KOSHIGOE and A. TUBIS 1986 *Physics of Fluids* **29**, 3982–3992. Wave structures in jets of arbitrary shape. I. Linear inviscid spatial stability analysis.

13. S.KOSHIGOE and A. TUBIS 1987 *Physics of Fluids* **30**, 1715–1723. Wave structures in jets of arbitrary shape. II. Application of a generalized shooting method to linear instability analysis.

14. P. J. MORRIS 1988 *AIAA Journal* **26**, 172–178. Instability of Elliptic Jets.

15. C. K. W. TAM, J. A. JACKSON and J. M. SEINER 1985 *Journal of Fluid Mechanics* **153**, 123-149. A multiple–scales model of the shock–cell structure of imperfectly expanded supersonic jets.

16. C. K. W. TAM and H. K. TANNA 1982 *Journal of Sound and Vibration* **81**, 337–358. Shock associated noise of supersonic jets from convergent–divergent nozzles.

17. J. M. SEINER, M. K. PONTON and R. S. BATY 1987 *private communication.*

18. C. K. W. TAM, J. M. SEINER and J. C. YU 1986 *Journal of Sound and Vibration* **110**, 309–321. Proposed relationship between broadband shock associated noise and screech tones.

19. A. POWELL 1953 *Proceedings of the Physical Society* **B66**, 1039–1057. On the mechanism of choked jet noise.

20. M. HARPER–BOURNE and M. J. FISHER 1973 *Proceedings (No. 131) of the AGARD Conference on Noise Mechanisms, Brussels, Belgium.* The noise from shock waves in supersonic jets.

21. A. POWELL 1953 *Aeronautical Quarterly* **4**, 103–122. On the noise emanating from a two–dimensional jet above the critical pressure.

22. A. KROTHAPALLI, Y. HSIA, D. BAGANOFF and K. KARAMCHETI 1986 *Journal of Sound and Vibration* **106**, 119–143. The role of screech tones on mixing of an underexpanded rectangular jet.

23. C. K. W. TAM and P. J. MORRIS 1985 *Journal of Sound and Vibration* **102**, 119–151. Tone excited jets, Part V: A theoretical model and comparison with experiment.

Analytical value of $\beta = 2.40482$	
Number of panels	$\beta_{\text{numerical}}$
8	2.5866
12	2.4765
20	2.4287
30	2.4151
40	2.4100

Table I. Boundary Element Calculations for a Circular Jet.

Figure Captions

Fig. 1. Sketch of Regions of Jet Cross Section.

Fig. 2. Sketch of Vortex-Sheet Shock Cell Model.

Fig. 3. Sketch of Boundary Divided into Elements.

Fig. 4. Variation of Shock Spacing with Fully-Expanded Jet Mach Number for Elliptic Jet. $L_a/L_b = 2.0$. ——— , present calculations, $N = 20$; $*$, analytic soution, [5].

Fig. 5. Variation of Screech Tone Frequency with Fully-Expanded Jet Mach Number for Elliptic Jet. $L_a/L_b = 2.0$.——— , present calculations, $N = 20$; $*$, analytic solution, [5]; $\triangle$, experimental values, [17]; - - - - , present calculations assuming constant jet aspect ratio.

Fig. 6. Variation of Shock Spacing with Fully-Expanded Jet Mach Number for Rectangular Jet. ——— , present calculations, $b/h = 5.83$, $N = 34$; $*$, analytic solution, [5]; $\triangle$, experimental values, $b/h = 5.83$, [19].

Fig. 7. Variation of Screech Tone Frequency with Fully-Expanded Jet Mach Number for Rectangular Jet. ——— , $b/h = 50/5$, - - - - , $b/h = 50/3$, present calculations, $N = 34$; $*$, analytic solution, [5]; experimental results, [20], $\triangle$, $b/h = 50/3$, $\square$, $b/h = 50/5$.

Fig. 8. Variation of Shock Spacing with Mixing Layer Thickness for Circular Jet. $M_j = 1.4$.

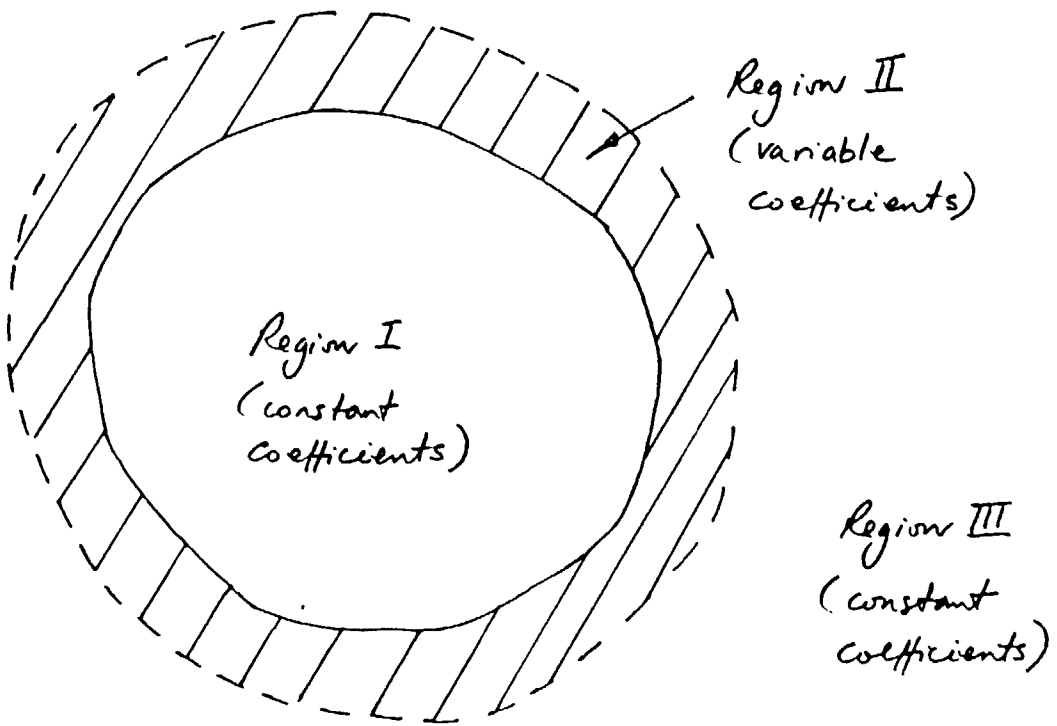

Fig. 1. Sketch of Regions of Jet Cross Section.

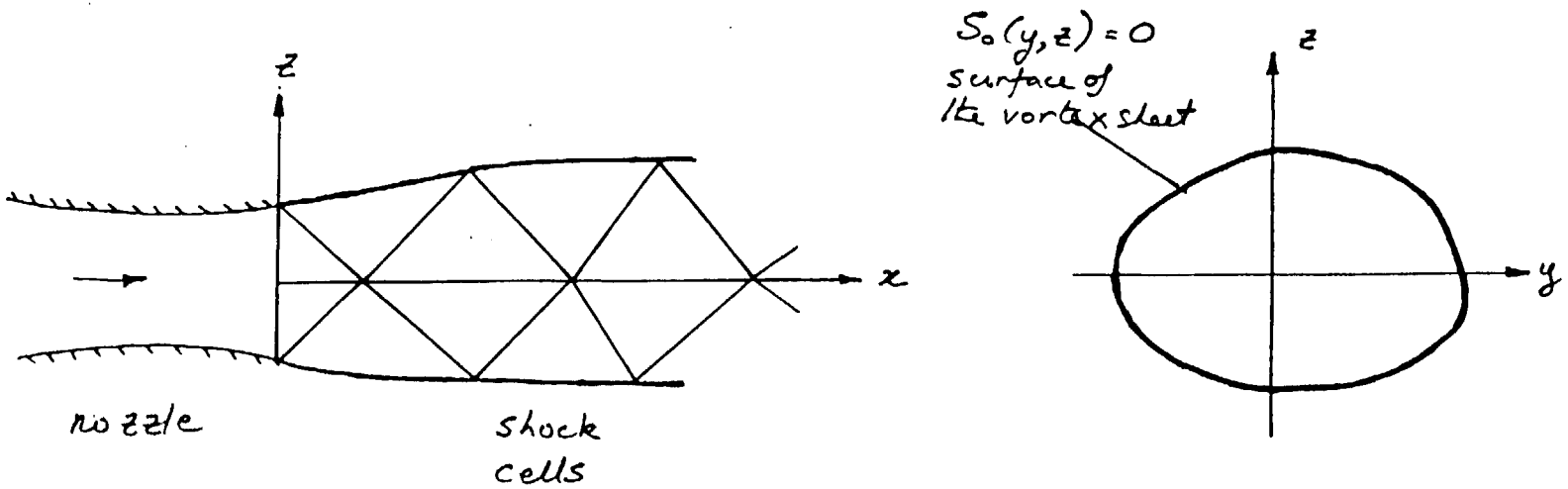

Fig. 2. Sketch of Vortex-Sheet Shock Cell Model.

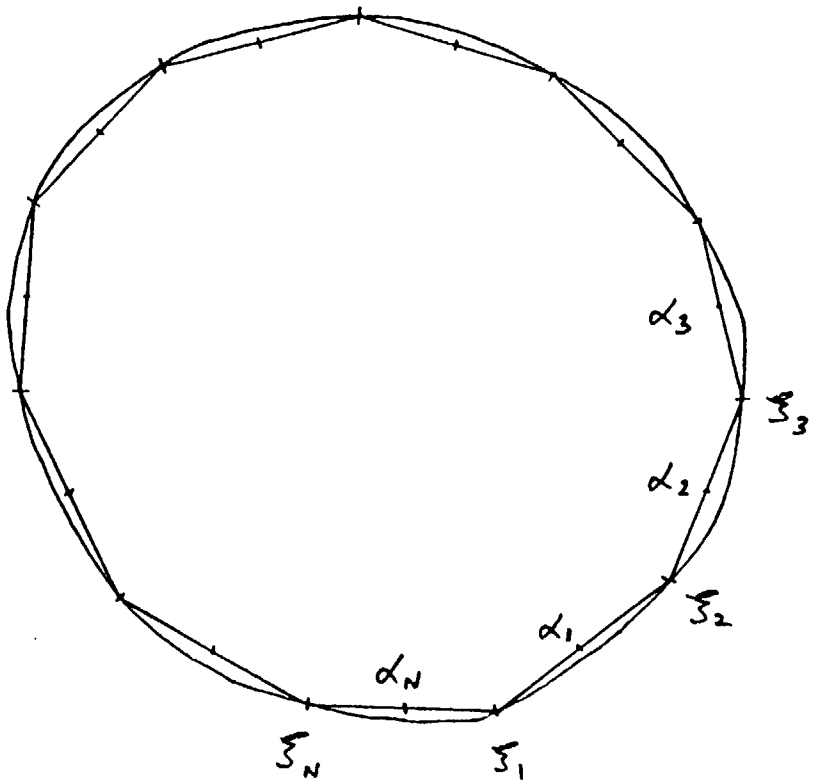

Fig. 3. Sketch of Boundary Divided into Elements.

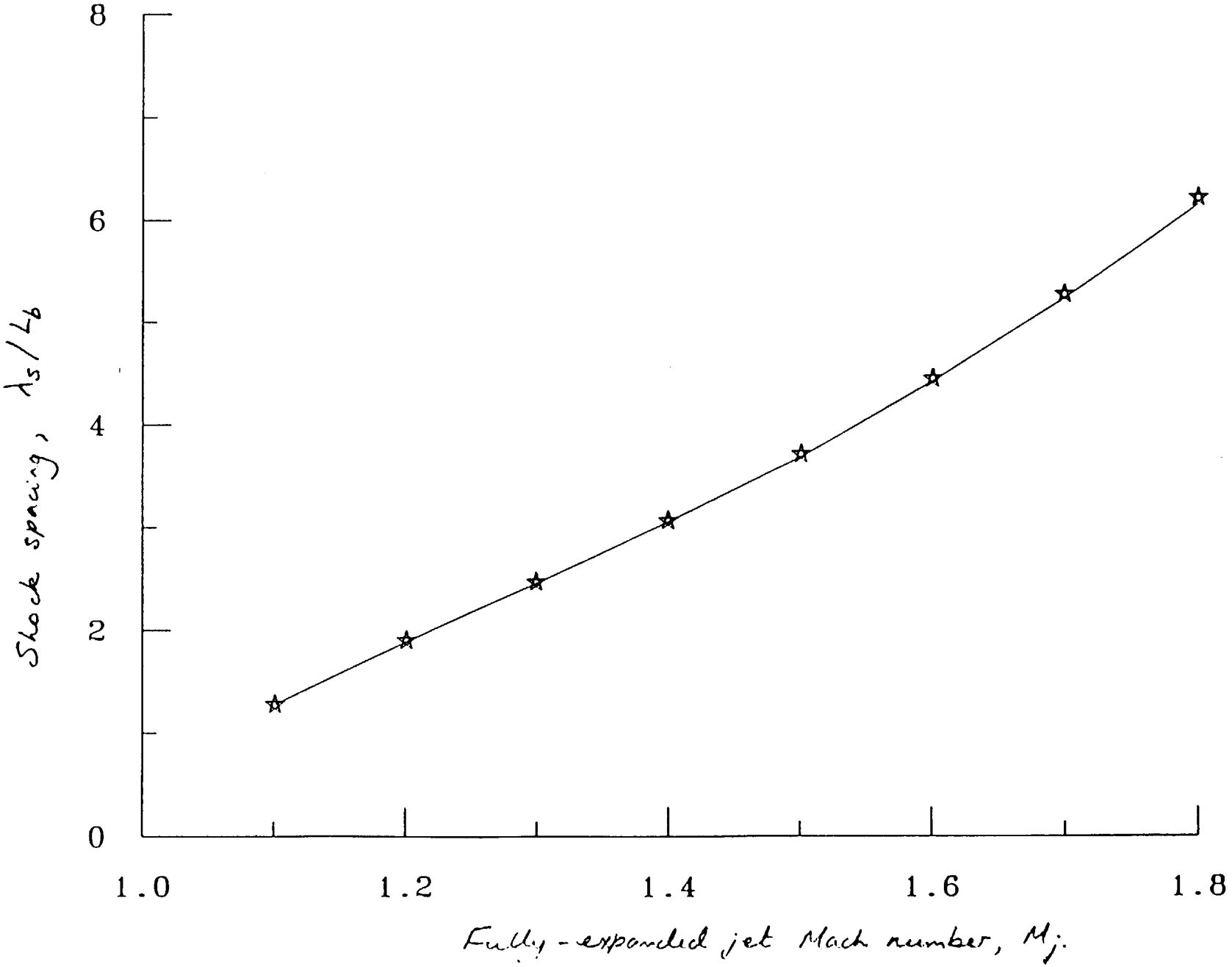

Fig. 4. Variation of Shock Spacing with Fully-Expanded Jet Mach Number for Elliptic Jet. $L_a/L_b = 2.0$. ——— , present calculations; * , analytic soution, [5].

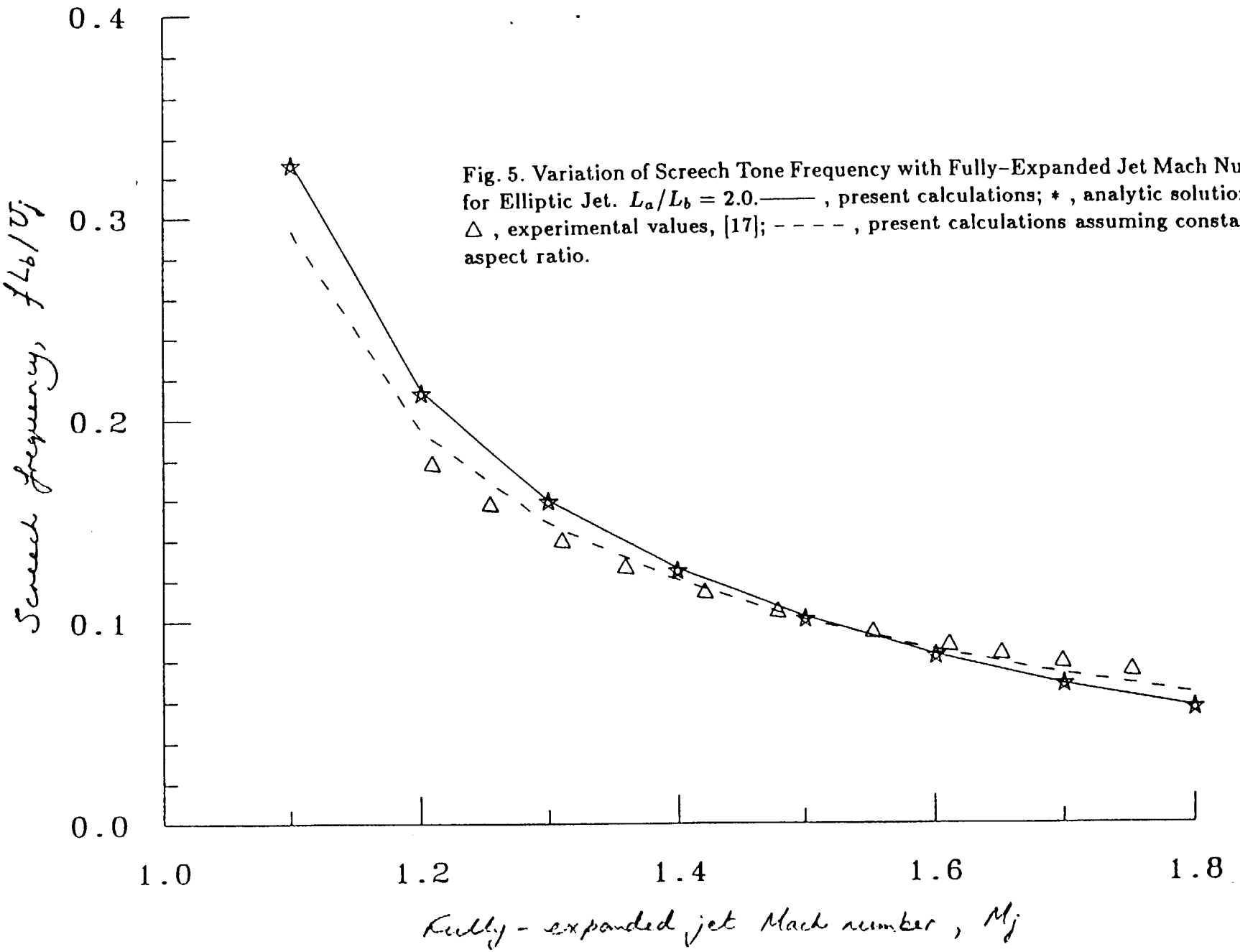

Fig. 5. Variation of Screech Tone Frequency with Fully-Expanded Jet Mach Number for Elliptic Jet. $L_a/L_b = 2.0$.——— , present calculations; * , analytic solution, [5]; △ , experimental values, [17]; - - - - , present calculations assuming constant jet aspect ratio.

Fig. 6. Variation of Shock Spacing with Fully-Expanded Jet Mach Number for Rectangular Jet. ——— , present calculations, $b/h = 5.83$; * , analytic solution, [5]; △ , experimental values, $b/h = 5.83$, [19].

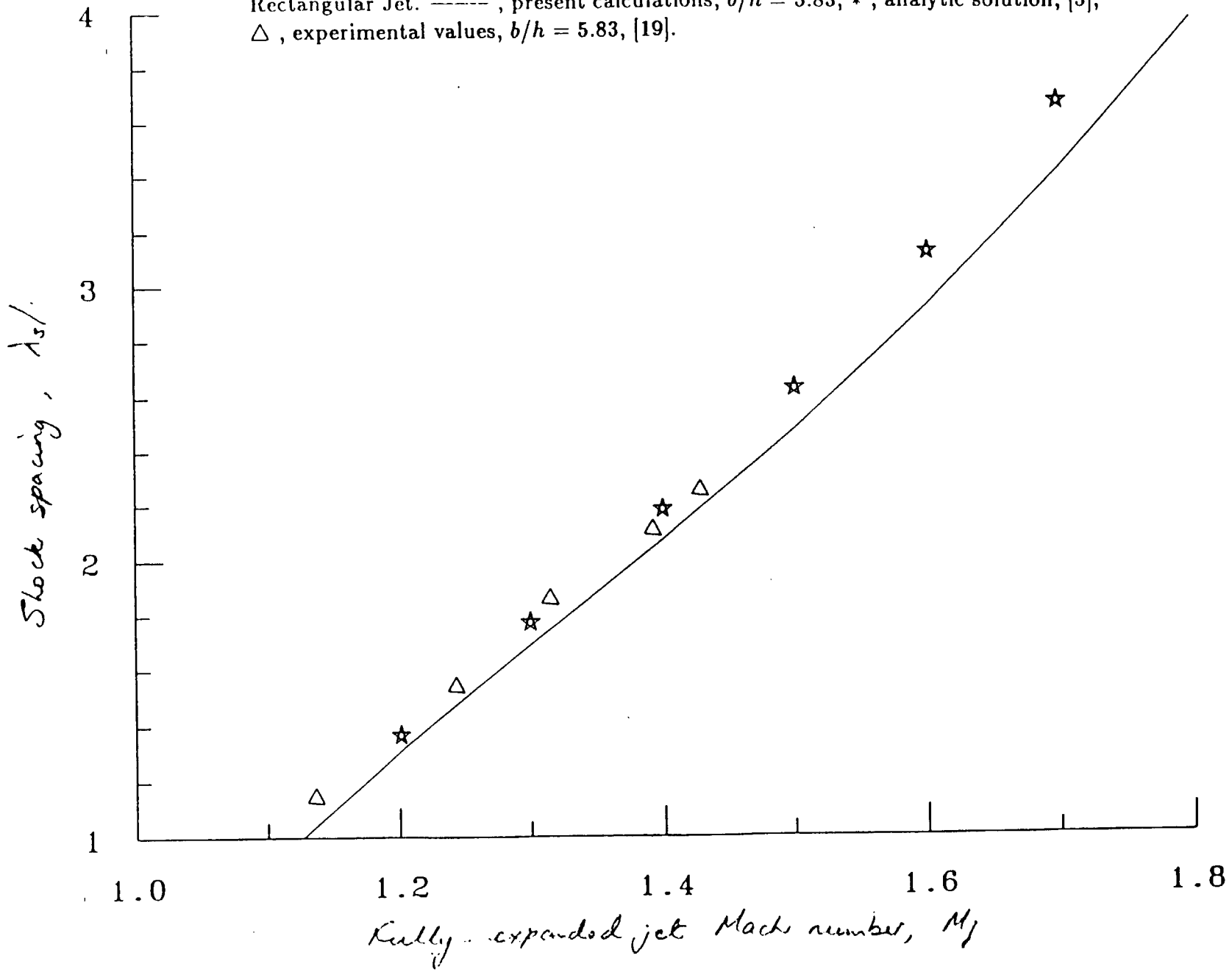

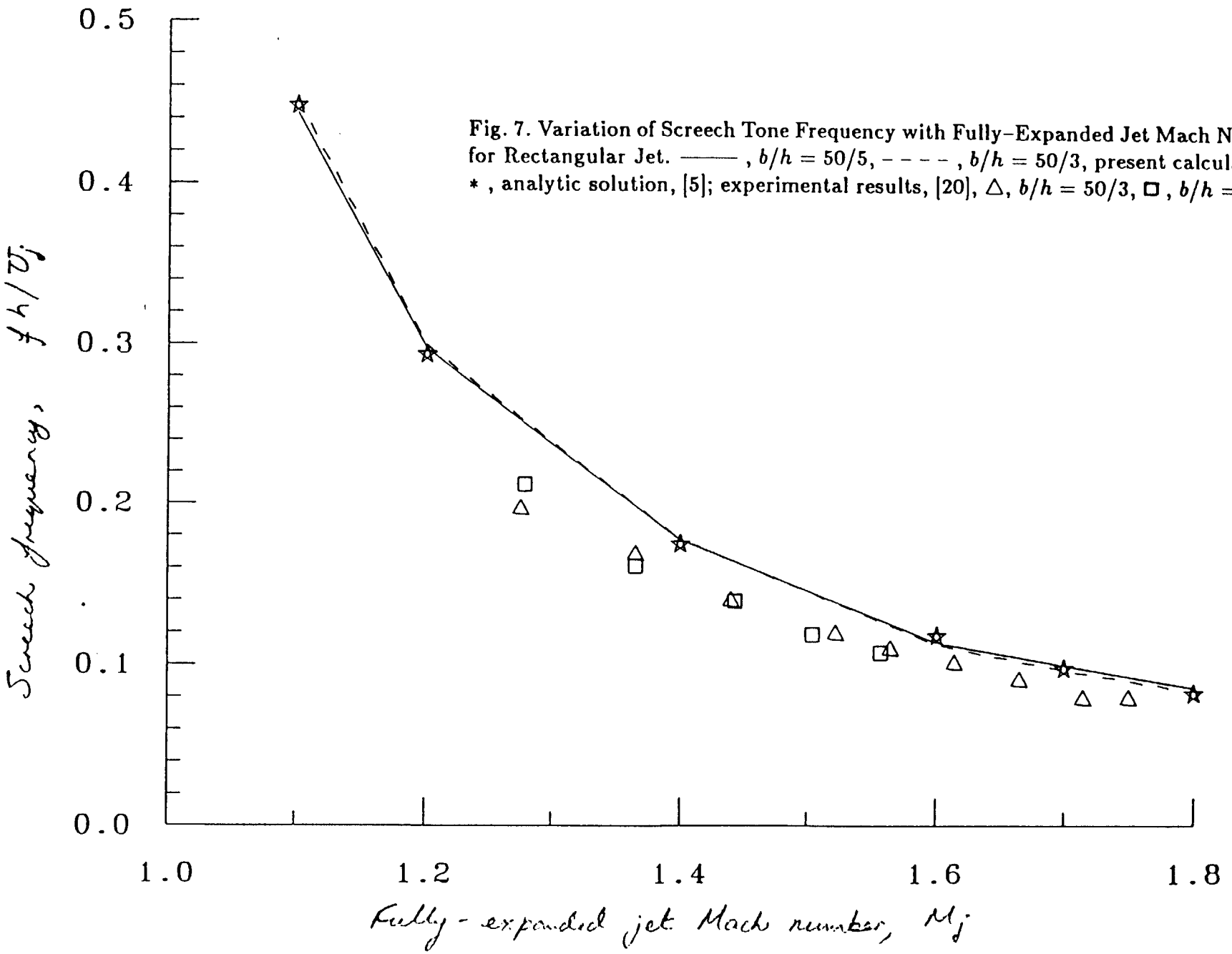

Fig. 7. Variation of Screech Tone Frequency with Fully–Expanded Jet Mach Number for Rectangular Jet. ——— , $b/h = 50/5$, - - - - , $b/h = 50/3$, present calculations; * , analytic solution, [5]; experimental results, [20], △, $b/h = 50/3$, □ , $b/h = 50/5$.

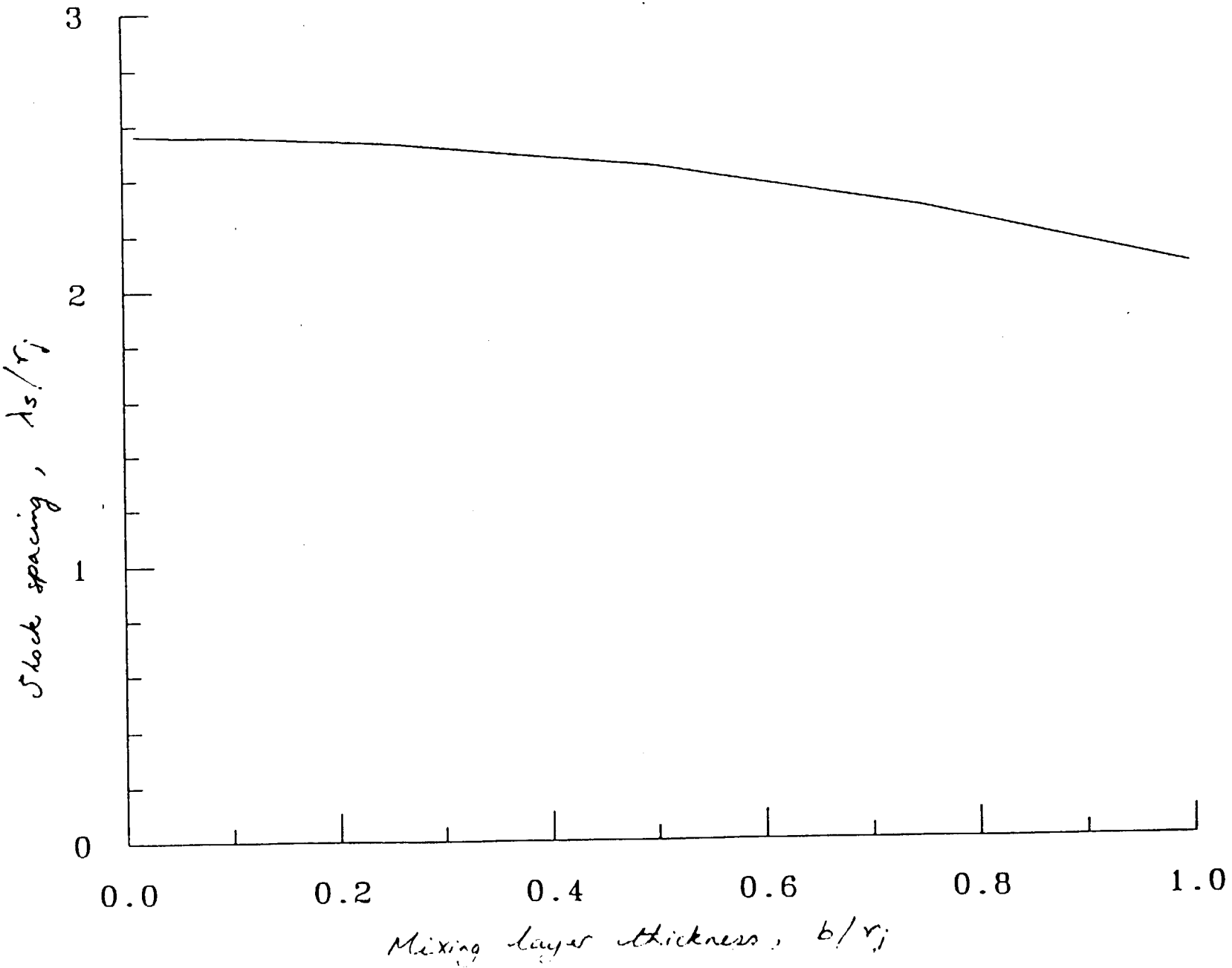

Fig. 8. Variation of Shock Spacing with Mixing Layer Thickness for Circular Jet. $M_j = 1.4$.

PAGE INTENTIONALLY BLANK

Appendix III

Instability Waves in Twin Supersonic Jets

P. J. Morris

INSTABILITY WAVES IN TWIN SUPERSONIC JETS

Philip J. Morris

Department of Aerospace Engineering

Penn State University

University Park, PA 16802 USA

Calculations are presented for the characteristics of instability waves in the initial mixing region of twin circular supersonic jets. Two models for the basic jet flow are used. In the first, the jets are modeled as two circular vortex sheets. In the second, realistic velocity and density profiles are used. It is shown that the unsteady flow fields of the two jets do interact before the time-averaged jets flows have merged. The normal modes or instability waves are classified by their symmetry properties in the twin jet case and their asymptotic behavior for large jet separations. Calculations of the growth rates and phase velocities are made for these modes as a function of jet separation and mixing layer thickness. The associated pressure distributions are also presented. In the realistic jet profile calculations the effect of jet separation is found to be relatively weak. For modes that are even about the symmetry plane between the two jets the pressure levels are found to increase near this plane as the jet separation decreases.

1.0 Introduction

When supersonic jets from convergent–divergent nozzles operate at off–design conditions they can produce intense screech tones. Powell (1953) made early observations of this phenomenon and proposed a feedback mechanism for the screech tone production. More recent experiments and analysis by Tam, Seiner and Yu (1986) showed that the feedback loop consists of downstream propagating large scale structures in the jet mixing layer that interact with the shock cell structure to generate upstream travelling acoustic waves. If these acoustic waves trigger additional flow disturbances at the jet lip with the correct phase then the feedback loop is established. Analyses, based on this model, have made excellent predictions of screech tone frequencies in both circular and non–circular jets; see Tam (1986) and Morris, Bhat and Chen (1989).

Seiner, Manning and Ponton (1988) showed experimentally that for two closely–spaced supersonic jets, operating off–design, the dynamic loads associated with the screech tone can reach levels, upstream of the jets' exits that could result in structural damage. Tam and Seiner (1987) noted that the screech tone frequency of the twin jets was slightly different to that of the single jet and that the acoustic intensity in the inter–nozzle region exceeded that of the direct sum of two non–interacting screeching jets. This suggests that there is a strong interaction between the unsteady flow and acoustic fields of the two jets. The analysis and calculations described in this paper help to quantify the effects of jet separation and operating conditions on the nature of this interaction.

Turbulent mixing in free shear flows is controlled by the dynamics of large scale coherent structures. The local characteristics of these structures may be described by linear instability theory. This has been demonstrated by the experiments of

Gaster, Kit and Wygnanski (1985), and Petersen and Samet (1988) among others. In their experiments they compared predictions of the amplitude and phase of the axial velocity fluctuations, based on linear stability theory, with phase–averaged measurements in an excited shear layer and a jet. The agreement between predictions and experiment was very good though only the local distributions and not the amplitude were predicted. This close agreement between the predictions of linear stability theory and the properties of the large–scale coherent structures has formed the basis for theories of turbulent mixing and supersonic jet noise. For example, Tam and Morris (1979), and Tam and Burton (1984a,b) predicted the noise radiation from instability waves in supersonic shear layers and jets and obtained very good agreement with experiment.

For supersonic jets the three main components of noise radiation are, turbulent mixing noise, broadband shock associated noise and screech. In each case, the essential component of the turbulence responsible for noise generation are the large scale structures. It should be noted that this is not the case for subsonic jets where a complete theory for noise generation and radiation is not available. Tam (1987) showed how predictions could be made for each noise component in a circular jet using an instability wave model for the large scale structures.

In the present paper the properties of the instability waves or large scale turbulent structures in the initial mixing region of twin circular supersonic jets are determined. Two models for the basic jet flows are used. In the first, the jets are modeled as two circular vortex sheets. In the second, realistic mean velocity and density profiles are used. Though the former model fails to provide quantitative results it does help to explain the observed modes of instability and interactions predicted by the more realistic model. The calculations examine whether the in-

stability growth rates, and hence the amplitudes of the large scale structures, are modified as the jet separation and operating conditions vary. In addition, the corresponding changes in the instability wave phase velocity are predicted. It is shown that the unsteady flow fields associated with the instability waves do interact before the time–averaged jet flows have merged. However, this interaction is relatively weak for the operating conditions considered. In Section 2 the general equations of motion and analytic solutions common to both models are developed. The details of the vortex sheet model and its predictions are then described in Section 3. Section 4 contains the numerical procedures and calculations for the realistic jet profiles. Finally, the role of these predictions in and their relationship to experimental observations of the twin plume resonance phenomenon are discussed.

2. ANALYSIS

Consider the two circular jets shown in Fig. 1. The time–averaged jet flows are assumed to be symmetric about the $x-z$ and $x-y$ planes, where the x–coordinate is normal to the jet exit planes. The centers of the jets are separated by a distance $2h$. Throughout this analysis the variables are non–dimensionalized with respect to the jet velocity u_j, jet density ρ_j and jet radius a_j. These values are taken to be the fully–expanded jet properties as defined by Tam and Tanna[11]. These values are described below. In the annular mixing regions of the two jets, before they have merged, there are three flow regions. In region I, the potential cores of the jets, the mean velocity and density are constant. Region III represents the stationary fluid surrounding the jets. In region II, the annular mixing region, the mean velocity $\bar{u}$ and density $\bar{\rho}$ are variable. Polar coordinate systems are introduced (r_1, θ_1) and (r_2, θ_2) with origins on the jet centerlines. The mean velocity and density of each jet are assumed to be a function of their radial coordinates only. This is the locally–

parallel flow approximation. The potential cores have radii R_1 and the outer edges of the mixing regions have radii R_2. The mean static pressure is assumed to be constant. The large scale coherent structures are modeled as instability waves. Their behavior is governed by the unsteady, linearized, compressible equations of motion. Thus, for example, in either polar coordinate system separable solutions for the pressure fluctuation are sought in the form:

$$p(\underline{x},t) = \hat{p}(r)\exp[i(kx + n\theta - \omega t)], \tag{2.1}$$

where k is an axial wavenumber, n is an azimuthal mode number, and ω is a radian frequency. The radial variation of the pressure fluctuation is then found to satisfy the equation:

$$\frac{d^2\hat{p}}{dr^2} + \left\{\frac{1}{r} - \frac{1}{\overline{\rho}}\frac{d\overline{\rho}}{dr} + \frac{2k}{\Omega}\frac{d\overline{u}}{dr}\right\}\frac{d\hat{p}}{dr} + \left\{k^2 - \overline{\rho}\Omega^2 M_j^2 + \frac{n^2}{r^2}\right\}\hat{p} = 0, \tag{2.2}$$

where,

$$\Omega = \omega - k\overline{u},$$

and $M_j^2 = u_j^2/c_j^2$, where c_j is the fully–expanded jet speed of sound. Equation (2.2) reduces to Bessel's equation in regions of constant mean velocity and density.

A solution for the pressure fluctuations outside the jet mixing layers in region III may be obtained in either polar coordinate system in the form

$$p(r,\theta,x,t) = \sum_{n=-\infty}^{\infty} B_n H_n^{(1)}(i\lambda_0 r)\exp[i(kx - \omega t + n\theta)], \tag{2.3}$$

where,

$$\lambda_0 = \{k^2 - \overline{\rho}_0\omega^2 M_j^2\}^{\frac{1}{2}}.$$

$\overline{\rho}_0$ is the non–dimensional mean density in the ambient medium which is equal to the jet static temperature ratio, T_j/T_0. The branch cuts for λ_0 are chosen such

that,

$$-\frac{1}{2}\pi \;\leq\; \arg\,\lambda_0 \;<\; \frac{1}{2}\pi.$$

This ensures that the solutions decay as $r \to \infty$ or are outgoing waves, for positive frequency. The symmetry properties of the mean velocity and density field, for example,

$$\overline{u}(y,z) \;=\; \overline{u}(-y,z) \;=\; \overline{u}(y,-z)$$

indicate that the eigensolutions should be odd or even about the $x-y$ and $x-z$ planes. From the latter symmetry property (the former symmetry property is used below) the general solution for the pressure fluctuations in the outer region may be written,

$$\begin{aligned} p(r_1,r_2,\theta_1,\theta_2,x,t) = \sum_{n=-\infty}^{\infty} B_n \Big\{ & H_n^{(1)}(i\lambda_0 r_2)e^{in\theta_2} \\ & \pm H_n^{(1)}(i\lambda_0 r_1)e^{in(\pi-\theta_1)} \Big\} \exp[i(kx-\omega t)], \end{aligned} \tag{2.4}$$

where the choice of sign depends on whether the solution is to be odd or even about the $x-z$ plane of symmetry.

It should be noted that this solution does not just represent the sum of the contributions from two, non–interacting, individual jets, though the form could then be the same. It is simply a convenient form of the separable solution in the outer region. The influence of the second jet is included when this general form of outer solution is matched with the solution in the interior of each jet. In the present case the fluctuations in each jet are affected not only by the outgoing solutions, that would exist for an individual, isolated jet, but by the incoming solutions from the second jet. These two contributions are included in the outer solution (2.4)

In order to match the outer solution (2.4) with the pressure fields in regions I and II it is convenient to write the solutions in region III in terms of only one of

the two polar coordinate systems. This may be accomplished using Graf's Addition Theorem [see, Tranter(1968)]. For example, we may write,

$$H_n^{(1)}(i\lambda_0 r_1)e^{in(\pi-\theta_1)} = \sum_{s=-\infty}^{\infty} H_{n+s}^{(1)}(2i\lambda_0 h)J_s(i\lambda_0 r_2)e^{is\theta_2}. \tag{2.5}$$

Then (2.4) may be written,

$$p(r_2,\theta_2) = \sum_{n=-\infty}^{\infty} e^{in\theta_2} \sum_{s=-\infty}^{\infty} B_s \beta_{sn}(i\lambda_0 r_2), \tag{2.6}$$

where,

$$\beta_{sn}(\xi) = \delta_{sn} H_s^{(1)}(\xi) \pm H_{n+s}^{(1)}(2i\lambda_0 h)J_n(\xi), \tag{2.7}$$

and δ_{sn} is the Kronecker delta function. It should be noted that

$$\beta_{-s,-n} = (-1)^s \beta_{sn}, \tag{2.8a}$$

and,

$$\beta_{-s,n} = (-1)^s \beta_{s,-n}. \tag{2.8b}$$

The influence of the second jet is seen in (2.7). The first term on the right hand side represents the outgoing waves from the jet at $y = -h$. The second term represents the incoming waves from the jet at $y = h$. For large h this latter term is very small and the interaction between the jets is very weak

The normal modes for the pressure fluctuation given by (2.6) may be separated further into modes that are odd or even about the $x-y$ plane. This is accomplished by first setting $s = -s$ and $n = -n$ and adding the resulting equation to (2.6). Then the pressure fluctuation may be written,

$$p(r_2,\theta_2) = \sum_{n=-\infty}^{\infty} \sum_{s=-\infty}^{\infty} \Big[F_s \cos(n\theta_2) + iG_s \sin(n\theta_2)\Big] \beta_{sn}(i\lambda_0 r_2), \tag{2.9}$$

where,

$$F_s = [B_s + (-1)^s B_{-s}]/2, \tag{2.10a}$$

and,

$$G_s = [B_s - (-1)^s B_{-s}]/2, \tag{2.10b}$$

A similar solution may be found for the pressure fluctuations in the potential core region. This may be written,

$$p(r_2, \theta_2) = \sum_{n=-\infty}^{\infty} \Big[A_n \cos(n\theta_2) + iC_n \sin(n\theta_2)\Big] J_n(i\lambda_1 r_2), \tag{2.11}$$

where,

$$\lambda_1^2 = k^2 - (\omega - k)^2 M_j^2. \tag{2.12}$$

With the form of the solutions known inside and outside the jet the eigenvalues k may be determined by matching these solutions at either the vortex sheet location or through the finite mixing layer. The former matching is described in the next section.

3. VORTEX SHEET MODEL

3.1 *Analysis*

In this representation of the jet flows the finite mixing layers are replaced by cylindrical vortex sheets of unit non-dimensional radius. Across the vortex sheet we require continuity of pressure and particle displacement. The matching conditions require that,

$$\Delta\left[\frac{dp/dr_2}{\bar{\rho}\Omega^2}\right] = 0 \quad \text{and} \quad \Delta[p] = 0, \tag{3.1}$$

where $\Delta[\ \ ]$ denotes the change in the argument across the vortex sheet. If the interior solutions given by (2.11) are matched with the exterior solutions, (2.9) for

all n we obtain, for the solutions that are even about the $x-y$ plane,

$$\sum_{s=\infty}^{\infty} F_s \left\{ \bar{\rho}_a \omega^2 \lambda_1 J_n'(i\lambda_1)\beta_{sn}(i\lambda_0) - (\omega-k)^2 \lambda_0 J_n(i\lambda_1)\beta_{sn}'(i\lambda_0) \right\} = 0, \qquad n = -\infty, \cdots, \infty, \tag{3.2}$$

where,

$$\beta_{sn}'(\xi) = \delta_{sn} H_s^{(1)'}(\xi) \pm H_{n+s}^{(1)}(2i\lambda_0 h) J_n'(\xi). \tag{3.3}$$

If we use the symmetry properties of β_{sn}, given by eqns. (2.8), and note that,

$$F_s = (-1)^s F_{-s}, \tag{3.4}$$

then the independent equations yielded by (3.2) may be written,

$$\sum_{s=1}^{\infty} F_s \left\{ \Gamma_n \delta_{sn} \pm \left[H_{n+s}^{(1)}(2i\lambda_0 h) + (-1)^s H_{n-s}^{(1)}(2i\lambda_0 h) \right] \right\} + F_0 \left\{ \Gamma_n \delta_{0n} \pm H_n^{(1)}(2i\lambda_0 h) \right\} \qquad n = 0,\ 1, \cdots, \infty, \tag{3.5}$$

where,

$$\Gamma_n = \frac{H_n^{(1)}(i\lambda_0) - \Lambda_n H_n^{(1)'}(i\lambda_0)}{J_n(i\lambda_0) - \Lambda_n J_n'(i\lambda_0)} \tag{3.6}$$

and,

$$\Lambda_n = \frac{(\omega-\alpha)^2 \lambda_0 J_n(i\lambda_1)}{\bar{\rho}_0 \omega^2 \lambda_1 J_n'(i\lambda_1)} \tag{3.7}$$

In the numerical calculations the series is truncated at $s = N$ and then (3.5) yields a set of $N+1$ homogeneous equations for F_s. These may be written in matrix form,

$$[\mathbf{A}]\mathbf{F} = 0, \tag{3.8}$$

where $\mathbf{F}$ is a vector of length $N+1$ of the unknown coefficients F_s. For a non-trivial solution to exist the determinant of this matrix must be zero. This provides the dispersion relationship between the wavenumber and frequency.

A similar set of equations may be derived for the unknown coefficients in the series representing the solutions that are odd about the $x-y$ plane. These may be written,

$$F_s = (-1)^s F_{-s}, \tag{3.4}$$

then the independent equations yielded by (3.2) may be written,

$$\sum_{s=1}^{\infty} G_s \left\{ \Gamma_n \delta_{sn} \pm \left[H^{(1)}_{n+s}(2i\lambda_0 h) + (-1)^s H^{(1)}_{n-s}(2i\lambda_0 h) \right] \right\} \tag{3.9}$$
$$n = 0,\ 1, \cdots, \infty.$$

The requirement of a non-trivial solution for G_s results in a dispersion relationship for the odd modes about the $x-y$ plane.

A similar expression to both eqns. (3.5) and (3.9) was obtained by Sedel'nikov (1967). He developed dispersion relationships for multilayer jets, several jets, and jets between parallel walls or in rectangular ducts. In each case the jet was represented by a vortex sheet. No roots of the dispersion relationship were determined. Written in the form of eqns. (3.5) and (3.9) the off-diagonal elements vanish for large jet separations and the eigenvalues are the zeroes of Γ_n. These eigenvalues correspond to the axisymmetric and helical normal modes of a single jet.

It is clear that this form of the equations does not hold for zero frequency. This case is of interest, as it may be used in a description of the shock cell structure of the jet. Tam and Tanna (1982) showed how a model for the shock cell structure could be posed as an initial-value problem in which the fully-expanded vortex sheet acts as a waveguide for the pressure perturbation at the jet exit. For the steady problem the matching conditions at the vortex sheet require that the pressure perturbation be zero at and outside the vortex sheet. Thus there is no communication between the two jets and the shock cell structure remains unchanged from the single jet case.

However, it should be noted that this is only true for jets into stationary air and some coupling between the steady shock cell structure could occur if the ambient air were in motion; see Morris(1988).

3.2 *Calculations*

There are many parameters and operating conditions that could be varied for the present configuration. Thus, the calculations have been limited to a set of operating conditions that correspond to available experiments. In the calculations for both the vortex sheet and the realistic mean profile representation of the jet the diameter of the jet is taken to be the fully- -expanded jet diameter. It may be argued, that in either the case of an over- or under–expanded jet, the jet plume will adjust its cross–section so as to preserve mass flux but equalize the mean static pressure. This gives the following relationship, assuming isentropic flow, between the fully–expanded and design jet dimensions.

$$r_d = \sqrt{\frac{M_j}{M_d}} \left\{ \frac{1 + \frac{\gamma-1}{2} M_d^2}{1 + \frac{\gamma-1}{2} M_j^2} \right\}^{\frac{\gamma+1}{4(\gamma-1)}}, \tag{3.10}$$

where r_d is the non–dimensional design jet radius and M_j and M_d are the fully–expanded and design jet Mach numbers respectively.

The instability wave calculations in the vortex sheet case provide an indication of the character of the results to be expected in the more realistic calculations that include the effects of finite mixing layer thickness. Four types of solution may be classified as shown in Table 1. In addition, each solution may be classified by the azimuthal mode number it approaches as the jets move further apart.

Figure 2 shows the variation of the axial growth rate, $-k_I$ as a function of the separation distance between the two jets' centerlines h. The instability wave frequency is 1.0 in each case. This corresponds to a Strouhal number of 0.318,

$(1/\pi)$, based on the fully–expanded jet diameter and velocity. The design and fully–expanded jet Mach numbers are 1.0 and 1.32 respectively and the jet is unheated. These conditions correspond to the experiments of Seiner, Manning and Ponton (1988). In the numerical evaluation of the dispersion relationships obtained from (3.5) and (3.9) a value of $N = 5$ was used. Calculations were also performed with $N = 9$ with no significant change in the calculations, even for small values of jet separation. For large separations the solutions approach those for the single jet and the growth rate increases with azimuthal mode number. Calculations are presented for mode numbers 0, 1 and 2. For a given mode number the most unstable mode type is a function of jet spacing. For example, consider the mode number 1. For $h > 1.6$ the type III mode is the most unstable, though its value does not differ greatly from the value at large h. For $h < 1.6$ the type I mode dominates. For the range of mode numbers and types considered, the mode number 1, type I mode appears to be most affected by small separations showing a large increase in axial growth rate. This mode is associated with a motion that is even about both $x - y$ and $x - z$ planes and is dominated by a pair of helical motions of opposite sense about each jet. This is the type B mode described by Seiner, Manning and Ponton (1988) which they found to be the dominant mode in their twin plume resonance experiments.

The prediction that the stability of the (1,I) mode is affected strongly by the jet separation and the interchange of dominance between modes of different types as the jet separation changes is encouraging, as it provides qualitative agreement with the observations of Seiner, Manning and Ponton (1988) and Wlezian (1987). However these results should be treated with some caution as they are based on the vortex sheet model for the jet. The dominant or preferred mode of a real jet is determined

by the total growth of a given frequency disturbance through the developing shear layer. In the next section more realistic profiles are used to describe the jet flow.

4. REALISTIC JET FLOW MODEL

4.1 Analysis

In this case the mean velocity and density vary in Region II in a smooth, realistic manner. The matching between the potential core and ambient flow solutions must be performed using a numerical solution in the mixing layer.

In the potential core the solution for the pressure fluctuation takes the form given by (2.11). Consider, for example the modes that are even about the $x-y$ plane. For $n = -\infty, \cdots, \infty$ (2.2) may be integrated from $r = R_1$ to $r = R_2$ with initial conditions,

$$\hat{p} = J_n(i\lambda_1 R_1) \quad \text{and} \quad \frac{d\hat{p}}{dr} = i\lambda_1 J_n'(i\lambda_1 R_1). \tag{4.1}$$

The corresponding numerical solutions at $r = R_2$ are denoted by $\hat{p}_n$ and $\hat{p}_n'$. These solutions may be matched with the exterior solutions for all n. That is,

$$A_n \hat{p}_n = \sum_{s=-\infty}^{\infty} F_s \beta_{sn}(i\lambda_0 R_2), \tag{4.2}$$

and

$$A_n \hat{p}_n' = \sum_{s=-\infty}^{\infty} i\lambda_0 F_s \beta_{sn}'(i\lambda_0 R_2). \tag{4.3}$$

Following the same approach used in Section 3, based on the symmetry properties of $\hat{p}_n$, β_{sn} and F_s, a dispersion relationship may be derived from an identical system of equations to (3.5). However, in this case the Γ_n and Λ_n are defined by,

$$\Gamma_n = \frac{H_n^{(1)}(i\lambda_0 R_2) - \Lambda_n H_n^{(1)\prime}(i\lambda_0 R_2)}{J_n(i\lambda_0 R_2) - \Lambda_n J_n'(i\lambda_0 R_2)} \tag{4.4}$$

and,

$$\Lambda_n = i\lambda_0 \hat{p}_n / \hat{p}_n'. \tag{4.5}$$

For modes that are odd about the $x-y$ plane the dispersion relationship may be obtained from (3.9) with Γ_n and Λ_n defined by eqns.(4.4) and (4.5) respectively.

4.2 Calculations

In the subsequent calculations it is assumed that the mean velocity and density of the jet flows take the same form as in the single jet case: up to the location where the jet edges meet. The mean velocity is assumed to take the form:

$$\overline{u}(r,x) = \begin{cases} 1 & r \le g(x) \\ \exp\left[-\ln(2)\eta^2\right] & r > g(x). \end{cases} \tag{4.6}$$

where,

$$\eta = [r - g(x)]/b(x). \tag{4.7}$$

$g(x)$ is the radius of the potential core and $b(x)$ is the half–width of the mixing layer.

The mean density is related to the mean velocity through a Crocco relationship,

$$\overline{\rho} = \left[\frac{(\gamma-1)}{2}\overline{u}(1-\overline{u})M_j^2 + \overline{u} + T_0(1-\overline{u})\right]^{-1}, \tag{4.8}$$

where T_0 is the non–dimensional ambient temperature.

From the mean axial momentum integral equation a relationship may be found between the potential core radius and the half–width of the mixing layer,

$$g(x) = -\beta_1 b + \sqrt{b^2(\beta_1^2 - 2\beta_2) + 1}, \tag{4.9}$$

where,

$$\beta_1 = \int_0^\infty \overline{\rho}\,\overline{u}^2\, d\eta,$$

and

$$\beta_2 = \int_0^\infty \overline{\rho}\,\overline{u}^2 \eta d\eta.$$

At some axial location the edges of the two jets will touch on the symmetry plane and the present analysis, that assumes that the mean flow is axisymmetric relative to each jet's centerline, is no longer valid. In the present calculations the edge of the jet is taken to be the location at which the axial velocity given by (4.6) equals 0.01. This corresponds to a value of η of 2.58. Thus the present calculations are for values of jet thickness such that,

$$g(b) + 2.58b \leq h. \tag{4.10}$$

A variable step–size fourth–order Runge–Kutta algorithm is used to integrate (2.2) from the edge of the potential core to $\eta = 2.58$. This gives the values of $\hat{p}_n$ and $\hat{p}'_n$. As in the vortex sheet calculations the upper limit in the series representations is taken to be $N = 5$. Calculations have also been performed with $N = 9$ with negligible change in the largest elements of F_s or G_s.

The vortex sheet calculations, shown in Fig. 2, indicate that for large separations the higher azimuthal mode numbers have higher axial growth rates. Additional calculations show that, for the present operating conditions, the maximum axial growth rate occurs for $n = 3$. A similar result is obtained for small values of local thickness $b(x)$. However, as the jet mixing layer thickens, the higher order azimuthal modes become damped more quickly. Figure 3 shows the variation of the axial growth rate $-k_I$ as a function of thickness $b(x)$ for a large jet separation $h/r_d = 5.0$, for the first three azimuthal modes. In this and subsequent calculations the fully–expanded jet Mach number is 1.32, the design jet Mach number is 1.0, and the jet is unheated. Figure 3 shows how the growth rate of the $n = 2$ mode rapidly

decreases. The helical mode $n = 1$ has a larger growth rate than the axisymmetric mode $n = 0$ for the all values of jet thickness considered. In the subsequent calculations only the two lowest mode numbers will be examined. The calculations shown in Figure 3 give results that are identical to the single jet case.

As the separation decreases so the growth rates of the various mode numbers and types move away from their large separation value. Figure 4 shows this variation for mode numbers 0 and 1 and the four mode types. The jet thickness is $b = 0.2$ and the Strouhal number $St = 0.3$. The change in the axial growth rate is relatively small for jet separations greater than 2 radii. For these conditions the most unstable mode at the closest separation achievable, before the jets' edges merge, is the (1,IV) mode. This mode is dominated by two helical instabilities that are out of phase that give a solution that is odd about both the $x - y$ and $x - z$ planes. However, at other separations other modes are the most unstable.

The relative instability of the various modes at a given separation has been found to be nearly independent of jet mixing layer thickness. For example, Figure 5 shows the variation of axial growth rate with $b(x)$ for the (0,I) and (0,III) modes. The single jet, $n = 0$ value is shown for comparison. In this case, with $h/r_d = 1.9$, the (0,III) mode is the most unstable at all jet thicknesses.

Before considering the eigenfunctions for the various modes of instability the effect of wave frequency will be considered. Figure 6 shows the variation of axial growth rate $-k_I$ with Strouhal number for the same modes shown in Fig. 5. The mixing layer thickness $b = 0.2$. Except for the lower Strouhal numbers the (0,III) mode is more unstable than the (0,I) mode or the $n = 0$ single jet mode. At this jet thickness the most unstable frequency occurs for a Strouhal number of approximately 0.45 and is relatively independent of jet separation or mode type.

The real part of the wavenumber is also affected by the jet separation. The trend in all the cases considered involves an increase in k_R for the even modes about the $x-z$ plane and a decrease in k_R for the odd modes as the jet separation decreases. However, the changes are relatively small involving typically a 10% change from the single jet value. For example, Figure 7 shows the variation with mixing layer thickness of the phase velocity, given by ω/k_R, for the same modes shown in Figure 5. The phase velocity for the (0,I) mode, that is even about the $x-z$ plane is lower than the single jet or large separation value. Conversely, the (0,III) mode, that is odd about the $x-z$ plane takes a higher value. It should be noticed that for larger thicknesses, where the instability wave is reaching its maximum amplitude or neutrally stable condition, there is effectively no change in the phase velocity. In this region the phase velocity is approximately 0.73. Thus the observed shift in the screech frequency for the twin jets is linked to a change in the shock cell spacing rather than a modification to the phase velocity of the large scale structures. Seiner, Manning and Ponton (1988) did observe a 10 to 15% increase in the shock cell spacing. The reason for this increase is unclear as, in the absence of ambient flow, the shock cell structure of the two jets should be independent. However, insufficient aerodynamic data for the twin jets is available at present to help to explain this observation.

The pressure distributions associated with each mode of instability may be constructed by obtaining the coefficients F_s or G_s for a given eigenvalue. An inverse iteration technique is used to obtain these values. That is,

$$[\mathbf{A}]\mathbf{F}^{k+1} = \sigma\mathbf{F}^{k}, \tag{4.11}$$

where σ is a scaling factor and $[\mathbf{A}]$ is given by (3.8). An initial guess for $\mathbf{F}^0$ is taken to be $\{1,1,\cdots,1\}^T$. This algorithm has been found to give convergence in

two iterations for the cases considered. The interior coefficients may then be found from (4.2).

For convenience in the present calculations only the pressure field outside the edge of the jet has been determined. Equation (2.3), rewritten in terms of modes that are odd or even about the $x-y$ plane, is used to calculate the pressure. For example, Figure 8 shows contours of equal pressure level for the (0,I) mode and $h/r_d = 1.9$. The phase, given by $kx - \omega t$ in (2.4) has been set to zero. It can be seen that the pressure field remains nearly axisymmetric. However, in the region between the two jets there is a loss of axisymmetry. In this region the amplitude of the pressure is nearly uniform and equal to the maximum amplitude achieved at the edge of the jet. The shaded region shows the region of maximum amplitude. This is the case for all the modes that are even about the $x-z$ plane.

A measure of the azimuthal mode content for each mode of instability and type is given by the relative magnitudes of the coefficients F_* and G_*. Table 2 shows how these amplitudes vary with jet separation for the (1,III) mode. For each separation the $n = 1$ helical mode is dominant. However, for $h/r_d = 1.5$ the $n = 0$ mode amplitude rises to 67% of that of the $n = 1$ mode and the $n = 2$ mode rises to 16% of the $n = 1$ mode.

5. DISCUSSION

The present calculations have shown how the growth rates of instability waves or large structures in the initial mixing region of twin supersonic jets are affected by the jet separation. This interaction is caused by a coupling of the waves unsteady flow fields even before the time–averaged jet flows have merged. At a given operating condition the mode number and type that is most unstable is a function of the jet separation. However, the quantitative change in the local growth rates are relatively

small until the separation between the jet centerlines approaches the jet diameter: that is $h/r_d \rightarrow 1$. Though this may be achieved in theory in the case of the vortex sheet model, similar calculations for the realistic jet profiles are limited to very small mixing layer thicknesses. At larger thicknesses the jets merge rendering the present analysis invalid.

The influence of the jet separation on the eigenvalues can be seen from (3.5) to (3.8). The elements of the matrix **A** consist of two components: those that depend on h, the jet separation, and those that do not. In fact, the easiest way to construct the matrix elements numerically is to first note that the components that depend on h form a symmetric matrix. The other terms, that only occur on the diagonal, may then be added. As the separation increases the relative magnitude of the terms that depend on h decrease rapidly, as Hankel functions, relative to the remaining components. Eventually, only the terms given by Γ_n, that occur on the diagonal, are significant. The numerator in (3.6) can be seen to be the dispersion relationship for azimuthal mode number n for a single jet. Thus the single jet eigenvalues constitute the zeroes of the determinant of matrix **A** for large jet separations.

It should be noted that the amplitude achieved by an instability wave depends on the integrated growth of the wave with axial distance and the local variation in the shape of the eigenfunction. Thus, relatively small changes in the local growth rate can result in large changes in the eventual amplitude of the wave. For example, using the data shown in Fig. 5, and assuming that db/dx is given by the single jet value for the same operating conditions, the amplitude of the (0,III) mode is 24% larger for $h/r_d = 1.9$ compared to $h/r_d = 5.0$ at the location where the jets merge in the former case. However, as mentioned earlier, the rate of spread in the twin jet case may be decreased by the co-flowing, entrained air between the jets. This would

increase the relative amplitude at the merger location. In addition, the pressure levels between the jets are much higher in the twin jet case for modes I and II as shown in Fig. 8. However, it is not clear whether changes of this order of magnitude would be sufficient to explain the observed changes in the near–field pressure levels when the twin jets resonate.

The present analysis has considered only a part of the feedback cycle associated with twin jet screech. The instability wave's growth into the merged jet region must be determined. In this region the merged jet would resemble more closely a developing rectangular jet. In this case certain normal modes, particularly the flapping mode about the $x - y$ plane might be enhanced. The interaction between the instability waves and the shock cell structure in the jet that gives rise to the upstream propagating acoustic wave must then be described. It should be noted that existing theories of jet screech are unable to predict the amplitude even for single circular jets. Experimentally, the occurrence and amplitude of jet screech are very sensitive to small changes in the detailed geometry of the jet model and laboratory. So a prediction of the occurrence of resonance or its amplitude is extremely difficult.

To assist in the extension of the present calculations to other sections of the feedback loop further experimental data on the aerodynamic development of the twin jets is required. This includes the modification to the rate of growth of the jet mixing layers, mean flow contours in the merged jet region, and measurements of the entrained flow between the jets.

Though the present analysis does not answer all the questions regarding the complex phenomenon of twin jet resonance, it has shown how an instability wave analysis can provide some insight into the interaction of twin supersonic jets.

This work has been supported by NASA Langley Research Center under NASA Grant NAG–1–657. The technical monitor is Dr. J. M. Seiner

6. REFERENCES

GASTER. M., KIT, E. & WYGNANSKI, I. 1985 Large scale structures in a forced turbulent mixing layer, *J. Fluid Mech.* **150**, 23–39.

MORRIS, P. J. 1988 A note on the effect of forward flight on shock spacing in circular jets, *J. Sound Vib.* **121**, 175–177.

MORRIS, P. J., BHAT, T. R. S. & CHEN, G., 1989 A linear shock cell model for jets of arbitrary exit geometry, *J. Sound Vib.* **132**, 199–211.

PETERSEN, R. A. & SAMET, M. M. 1988 On the preferred mode of jet instability, *J. Fluid Mech.* **194**, 153–173.

POWELL, A. 1953 On the noise emanating from a two–dimensional jet above the critical pressure, *Aero. Quart.* **4**, 103-122.

SEDEL'NIKOV, T. K. 1967 The dispersion relations for multilayer jets and for several jets, *Phys. Aero. Noise* ed. Rimskiy–Korsakov, Nauka Press, Moscow. (Trans. 1969 *NASA* TTF–538.)

SEINER, J. M., MANNING, J. C., & PONTON, M. K. 1988 Dynamic pressure loads associated with twin supersonic plume resonance, *A.I.A.A. J.* **26** 954–960.

TAM, C. K. W. 1986 On the screech tones of supersonic rectangular jets," *AIAA Paper 86–1866*

TAM, C. K. W. 1987 Stochastic model theory of broadband shock associated noise from supersonic jets, *J. Sound Vib.* **116**, 265- -302.

TAM, C. K. W. & BURTON, D. E. 1984a Sound generated by instability waves of supersonic flows. Part 1. Two–dimensional mixing layers, *J. Fluid Mech.*, *138*, 249–271.

TAM, C. K. W. & BURTON, D. E., 1984*b* Sound generated by instability waves of supersonic flows. Part 2. Axisymmetric jets, *J. Fluid Mech.* **138**, 273–295.

TAM, C. K. W. & MORRIS, P. J. 1980 The radiation of sound by the instability waves of a compressible plane turbulent shear layer, *J. Fluid Mech.* **98**, 349–381.

TAM, C. K. W. & SEINER, J. M. 1987 Analysis of twin supersonic plume resonance, *A.I.A.A. Paper 87–2695.*

TAM, C. K. W., SEINER, J. M., & YU, J. C. 1986 Proposed relationship between broadband shock associated noise and screech tones, *J. Sound Vib.* **110**, 309–321.

TAM, C. K. W. & TANNA, H. K. 1982 Shock associated noise of supersonic jets from convergent–divergent nozzles, *J. Sound Vib.* **81**, 337–358.

TRANTER, C. J. 1968 *Bessel Functions with Some Physical Applications*, English Universities Press, Sec. 2.6.

WLEZIAN, R. W. 1987 Nozzle geometry effects on supersonic jet interaction, *A.I.A.A. Paper 87–2694.*

$x-y$ plane	$x-z$ plane	Mode
even	even	I
odd	even	II
even	odd	III
odd	odd	IV

Table 1. Classification of Normal Modes.

Mode number	Relative amplitude		
	$h/r_d = 3.0$	$h/r_d = 2.0$	$h/r_d = 1.5$
0	0.016	0.199	0.199
1	1.000	1.000	1.000
2	0.001	0.098	0.155
3	0.000	0.008	0.019

Table 2. Variation in relative mode amplitude with jet separation, Mode (1,III). $M_j = 1.32,\ M_d = 1.0,\ St = 0.3,\ b = 0.2.$

Figure Captions

'Fig. 1 Schematic of twin jet cross section and coordinate systems.

Fig. 2 Variation of the axial growth rate $-k_I$ with jet spacing. $M_j = 1.32$, $M_d = 1.0$, $St = 0.318$. ——, Mode I; - - - -, Mode II; — - —, Mode III; ····· Mode IV.

Fig. 3 Variation of the axial growth rate $-k_I$ with jet mixing layer thickness. $M_j = 1.32$, $M_d = 1.0$, $St = 0.3, h/r_d = 5.0$. ——, n=0; - - - -, n=1; — - — , n=2.

Fig. 4 Variation of the axial growth rate $-k_I$ with jet spacing. $M_j = 1.32$, $M_d = 1.0$, $St = 0.3$, $b = 0.2$. ——, Mode I; - - - -, Mode II; — - - —, Mode III; ····· Mode IV.

Fig. 5 Variation of the axial growth rate $-k_I$ with jet mixing layer thickness. $M_j = 1.32$, $M_d = 1.0$, $St = 0.3$. ——, $n = 0$, $h/r_d = 5.0$; - - - -, (0,I), $h/r_d = 1.9$; — - — , (0,III), $h/r_d = 1.9$.

Fig. 6 Variation of the axial growth rate $-k_I$ with Strouhal number. $M_j = 1.32$, $M_d = 1.0$, $b = 0.2$. For legend see Fig. 5.

Fig. 7 Variation of the phase velocity, ω/k_R, with jet mixing layer thickness. $M_j = 1.32$, $M_d = 1.0$, $St = 0.3$. —— , $n = 0$, $h/r_d = 5.0$; - - - -, (0,I), $h/r_d = 1.9$; — - — , (0,III), $h/r_d = 1.9$.

Fig. 8 Contours of equal pressure level, Mode (0,I). $M_j = 1.32$, $M_d = 1.0$, $St = 0.3$, $h/r_d = 1.9$. ——, outer edge of the jet. Contours from -.025 to -.175 in steps of -.025.

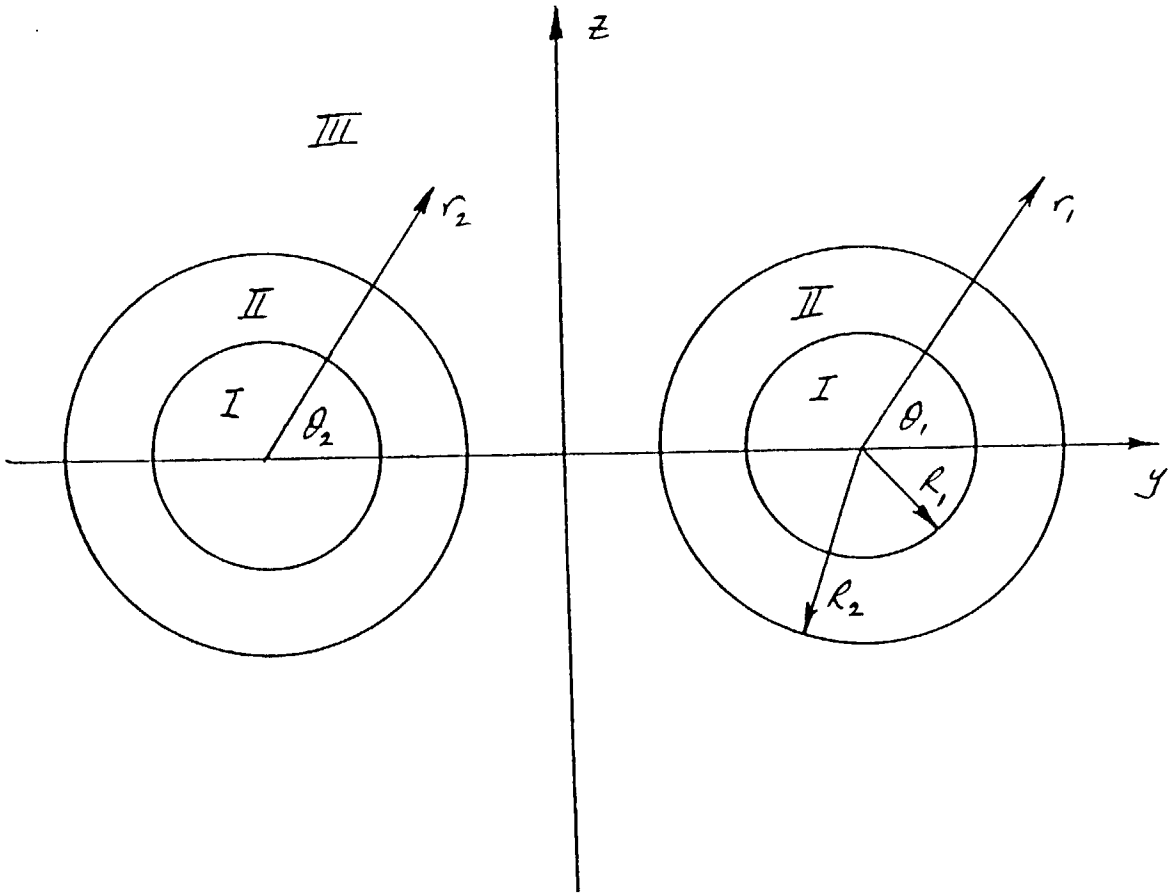

Fig. 1 Schematic of twin jet cross section and coordinate systems.

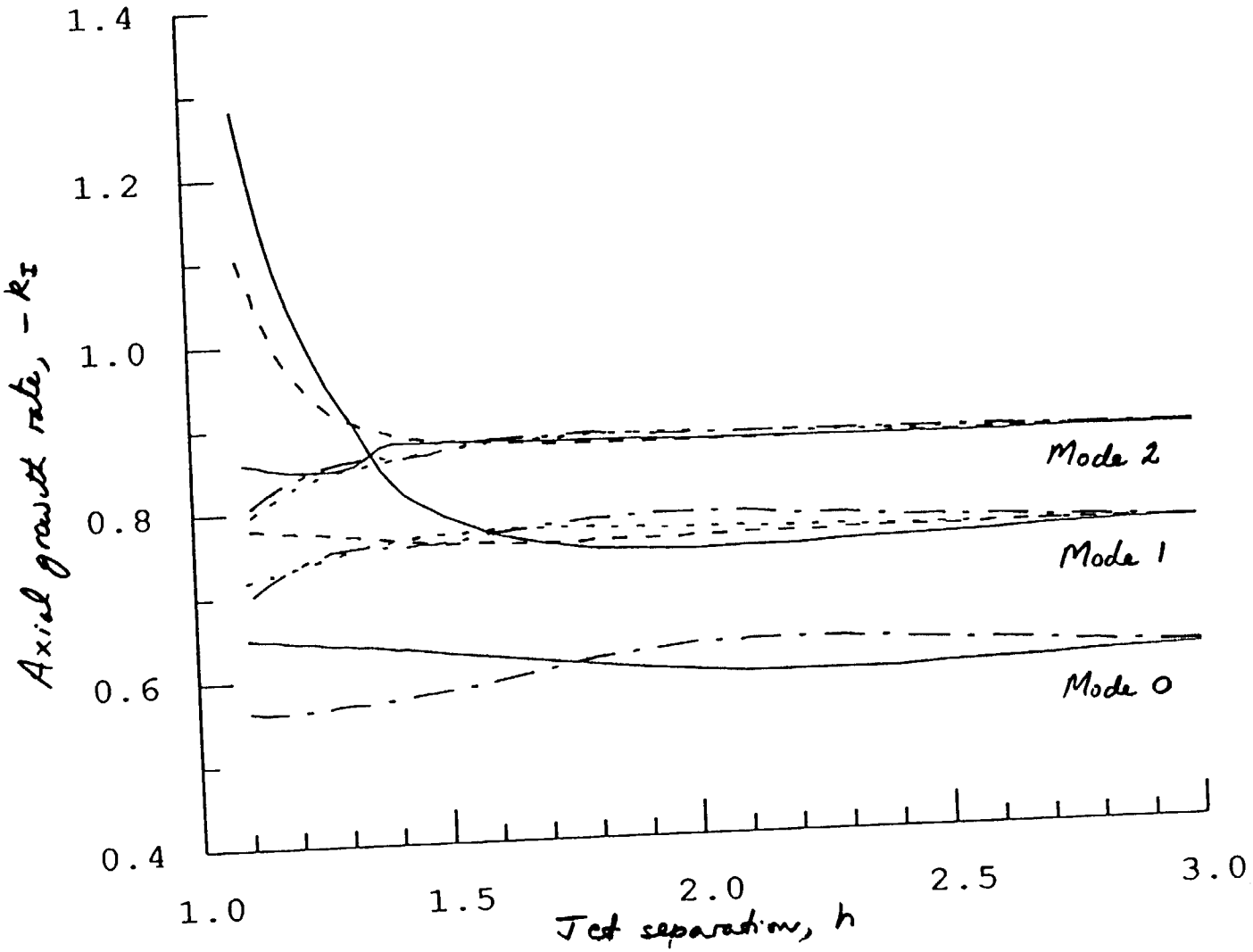

Fig. 2 Variation of the axial growth rate $-k_I$ with jet spacing. $M_j = 1.32$, $M_d = 1.0$, $St = 0.318$. ——, Mode I; - - - -, Mode II; —— - ——, Mode III; ····· Mode IV.

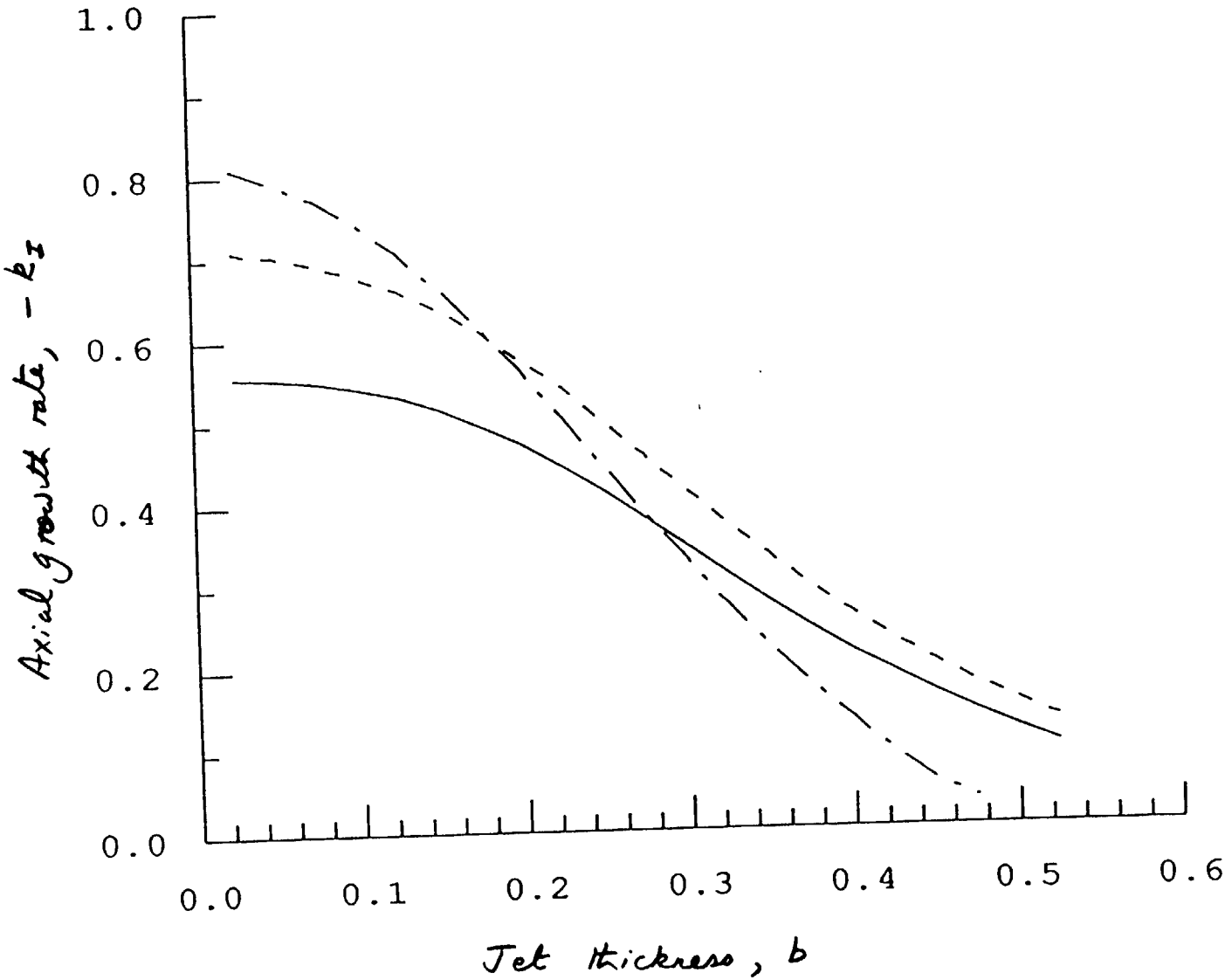

Fig. 3 Variation of the axial growth rate $-k_I$ with jet mixing layer thickness. $M_j = 1.32$, $M_d = 1.0$, $St = 0.3, h/r_d = 5.0$. ——, n=0; - - - -, n=1; —— - ——, n=2.

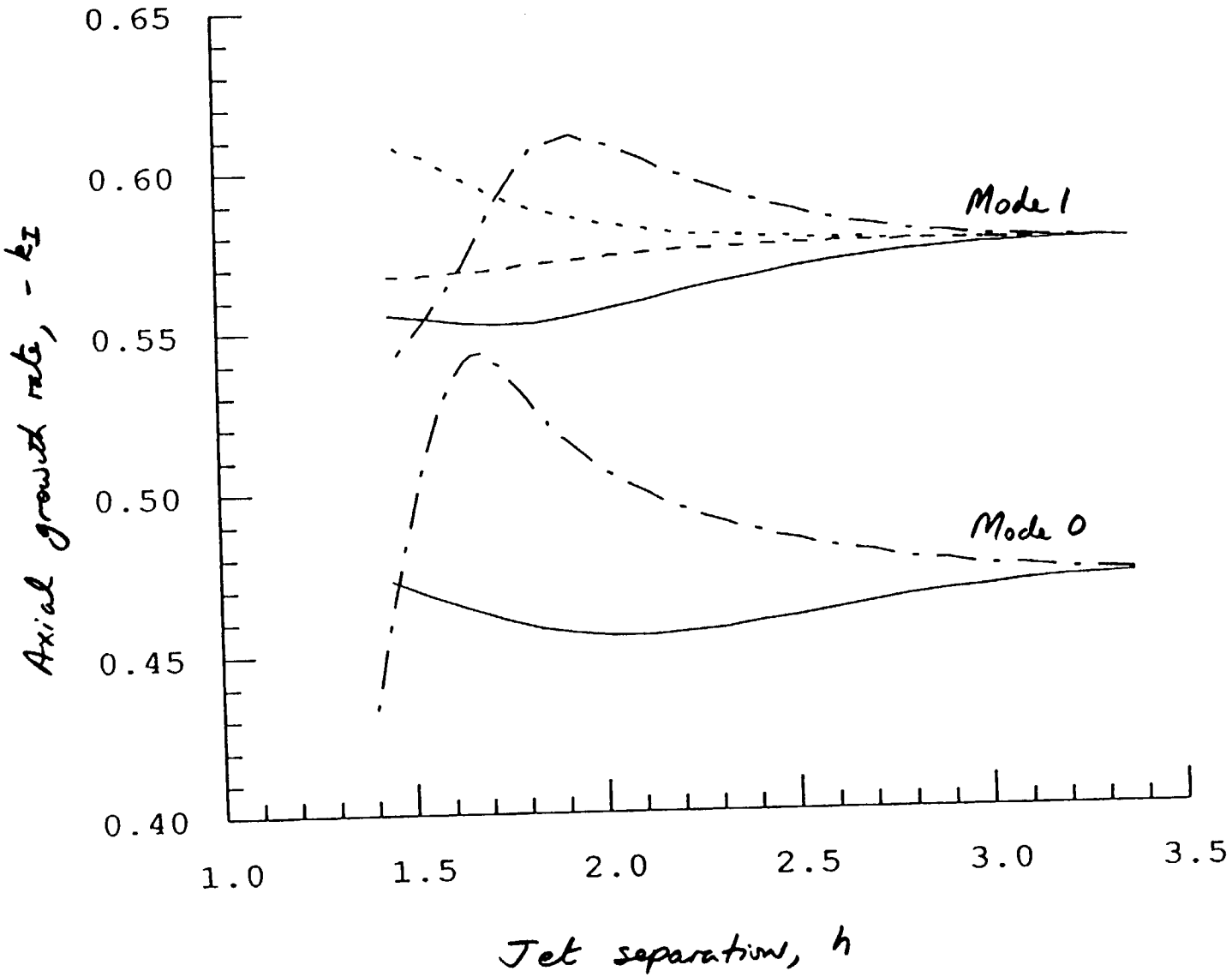

Fig. 4 Variation of the axial growth rate $-k_I$ with jet spacing. $M_j = 1.32$, $M_d = 1.0$, $St = 0.3$, $b = 0.2$. ——, Mode I; - - - -, Mode II; — - - —, Mode III; ..... Mode IV.

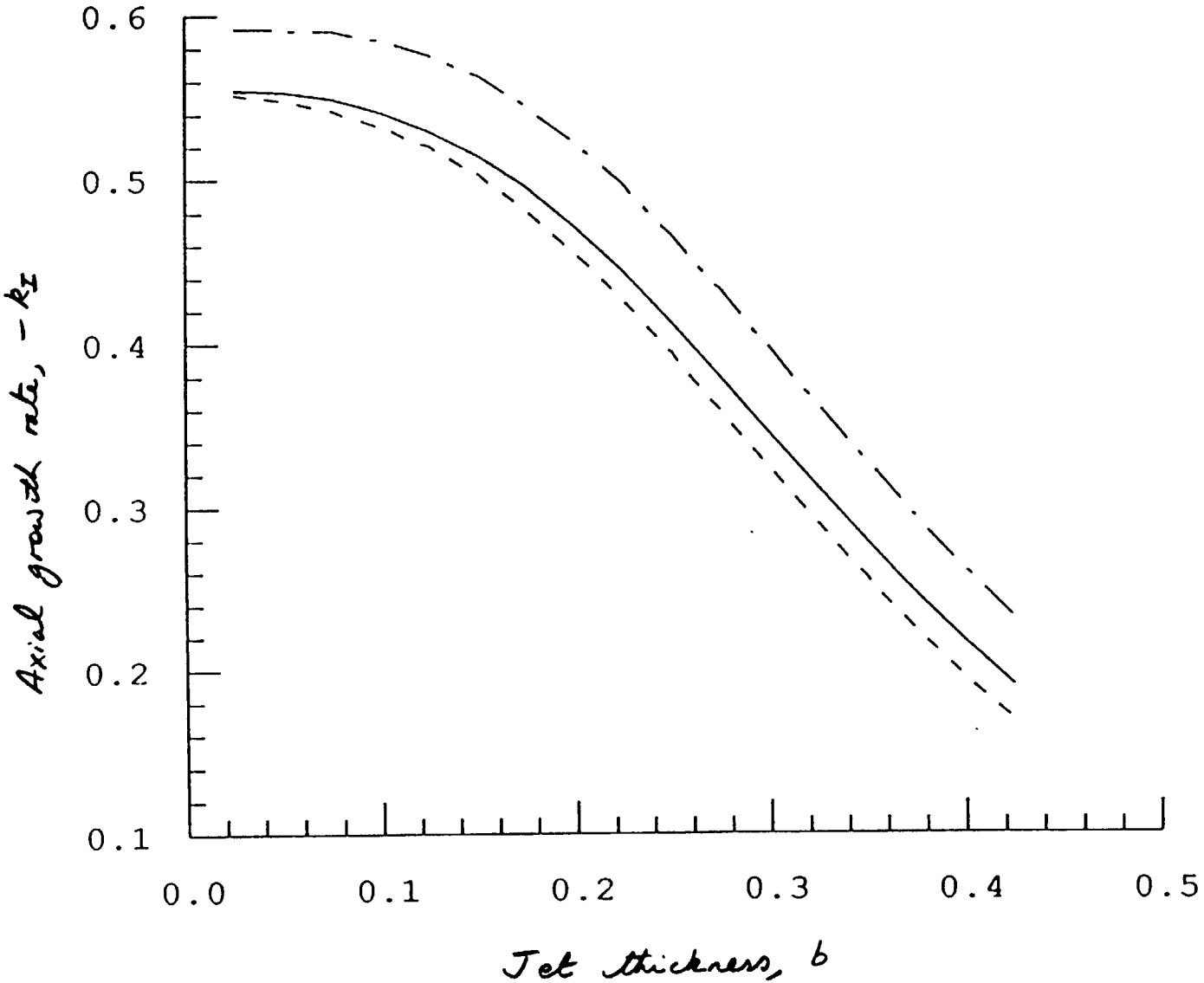

Fig. 5 Variation of the axial growth rate $-k_I$ with jet mixing layer thickness. $M_j = 1.32$, $M_d = 1.0$, $St = 0.3$. ——, $n = 0$, $h/r_d = 5.0$; - - - -, (0,I), $h/r_d = 1.9$; —— - ——, (0,III), $h/r_d = 1.9$.

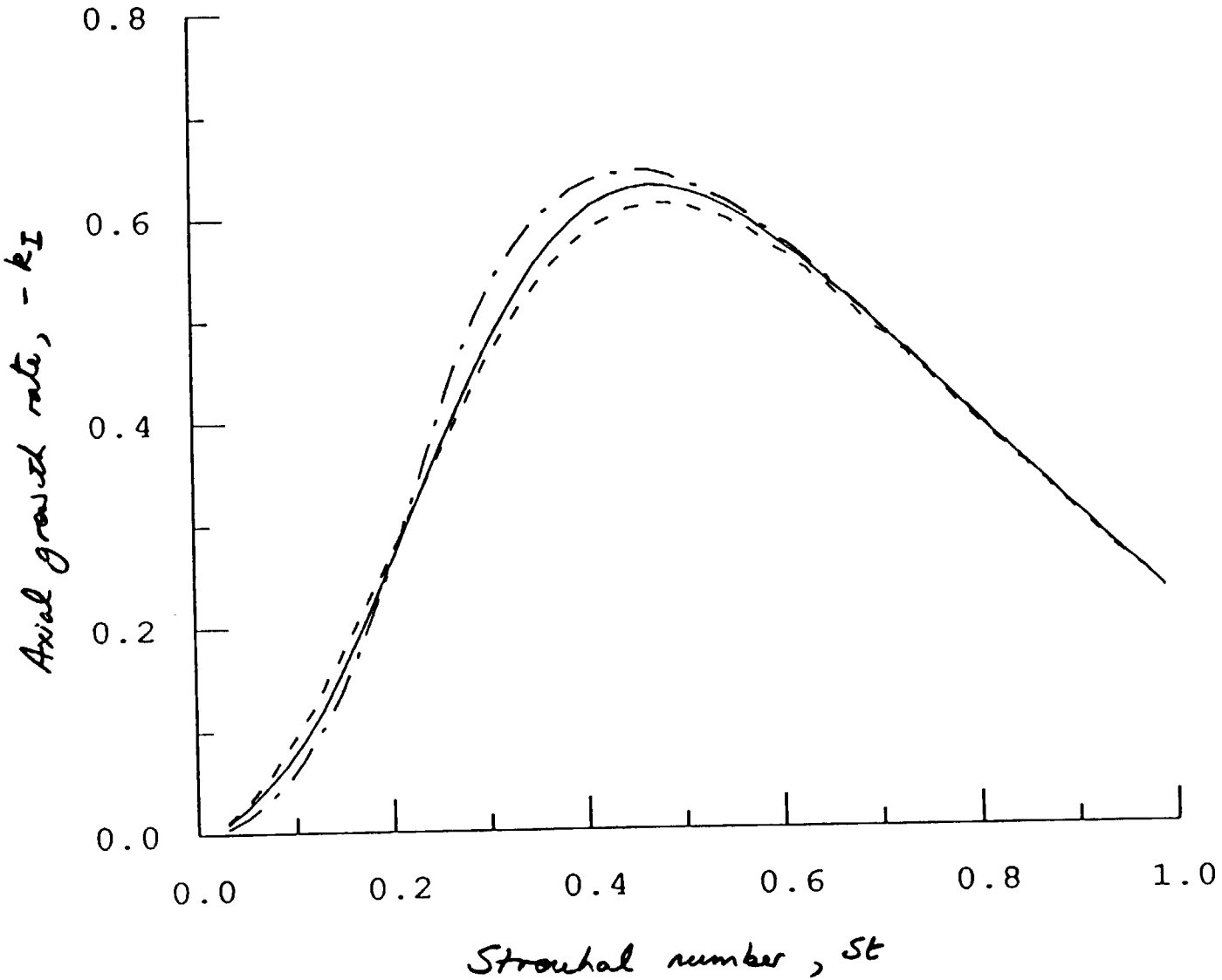

Fig. 6 Variation of the axial growth rate $-k_I$ with Strouhal number. M_j = 1.32, $M_d = 1.0$, $b = 0.2$. For legend see Fig. 5.

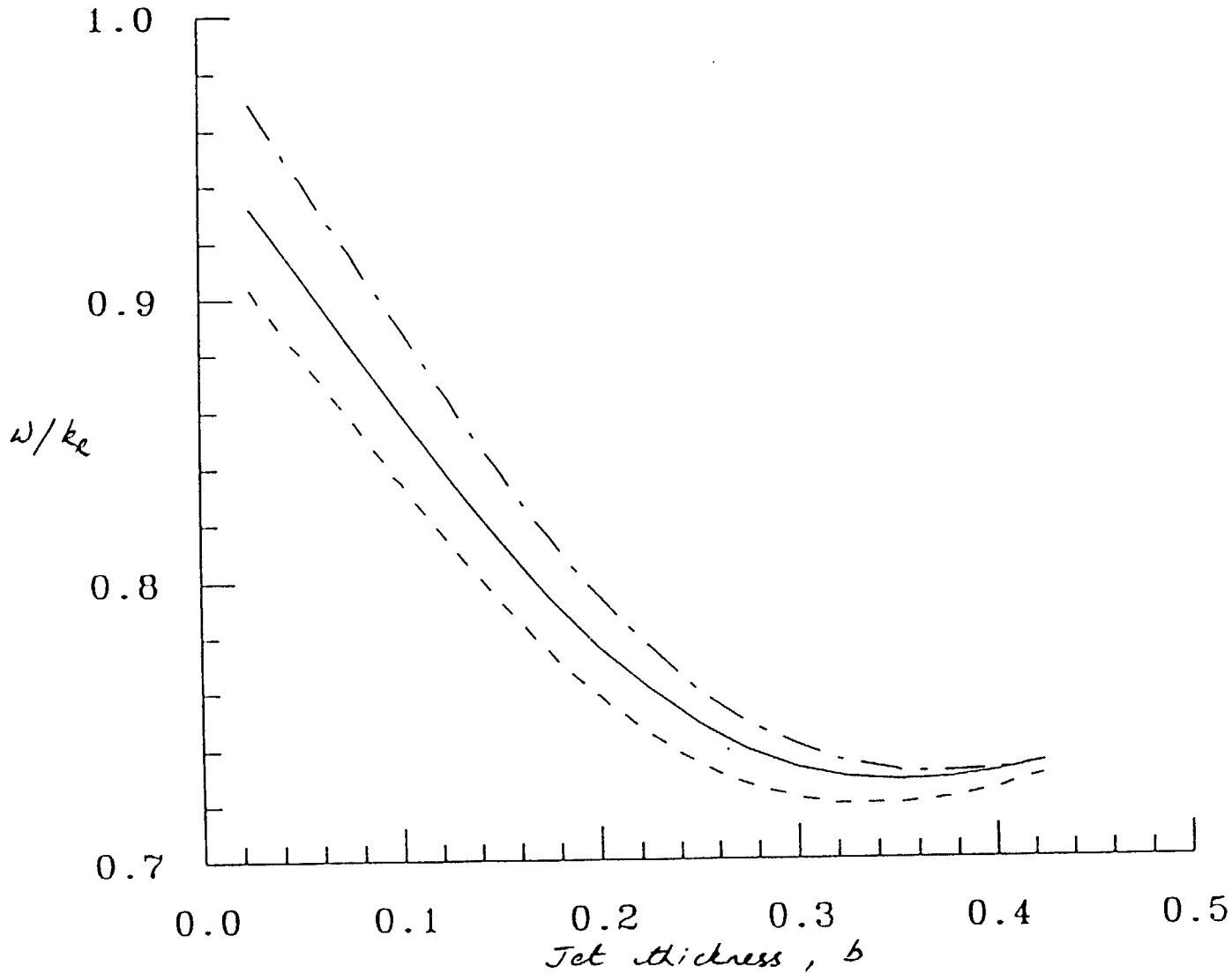

Fig. 7 Variation of the phase velocity, ω/k_R, with jet mixing layer thickness. M_j = 1.32, $M_d = 1.0$, $St = 0.3$. ——— , $n = 0$, $h/r_d = 5.0$; – – – –, (0,I), $h/r_d = 1.9$; ——– – ——, (0,III), $h/r_d = 1.9$.

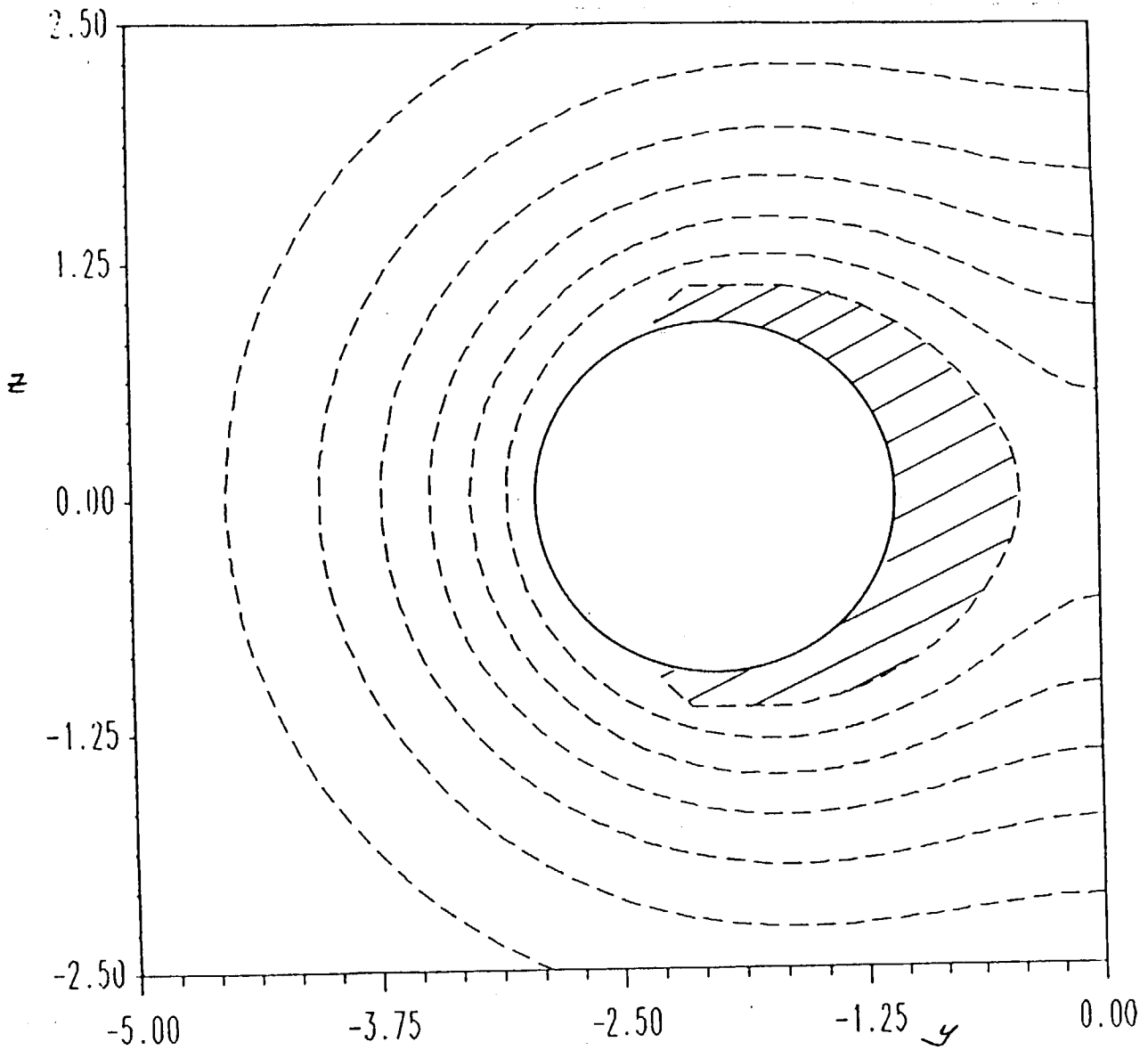

Fig. 8 Contours of equal pressure level, Mode (0,I). $M_j = 1.32$, $M_d = 1.0$, $St = 0.3$, $h/r_d = 1.9$. ——, outer edge of the jet. Contours from -.025 to -.175 in steps of -.025.